Electromagnetic Techniques for Vibration Damping and Isolation

Lead Guest Editor: Efrén Díez-Jiménez
Guest Editors: Toshihiko Sugiura, Rocco Rizzo, María J. Gómez-García, and Andrew Fleming

Electromagnetic Techniques for Vibration Damping and Isolation

Electromagnetic Techniques for Vibration Damping and Isolation

Lead Guest Editor: Efrén Díez-Jiménez
Guest Editors: Toshihiko Sugiura, Rocco Rizzo, María J. Gómez-García, and Andrew Fleming

Contents

Editorial

Electromagnetic Techniques for Vibration Damping and Isolation

Efren Diez-Jimenez [ID],[1] **Toshihiko Sugiura,**[2] **Rocco Rizzo,**[3] **Maria-Jesus Gómez-García** [ID],[4] **and Andrew Fleming**[5]

[1]*Mechanical Engineering Area, Signal Theory and Communications Department, Universidad de Alcalá,*
 Ctra. Madrid-Barcelona, Km 33,66, Alcalá de Henares 28805, Spain
[2]*Department of Mechanical Engineering, Faculty of Science and Technology, Keio University, Yokohama, Japan*
[3]*Department of Energy and Systems Engineering, University of Pisa, Largo Lucio Lazzarino, 56122 Pisa, Italy*
[4]*Department of Mechanical Engineering, Universidad Carlos III de Madrid, Leganés, Spain*
[5]*Precision Mechatronics Laboratory, School of Electrical Engineering and Computer Science, University of Newcastle,*
 Callaghan, Australia

Correspondence should be addressed to Efren Diez-Jimenez; efren.diez@uah.es

Electromagnetic devices for vibration damping and isolation are becoming a real alternative to traditional mechanical vibration and isolation methods. Performance of new magnetic materials in combination with optimization tools allows the development of efficient and tunable vibration damping and/or isolation techniques. Moreover, damping and isolation by electromagnetic means can be clean and environmentally friendly since there is no need of using fluids; thus, they can be applied in clean, harsh, and/or extreme temperature environments such as space, aerospace, electric vehicles, and microfabrication industries. Nevertheless, there are still critical issues to be solved like optimization of masses, performance, and cost, ageing of the devices, reduction of external electromagnetic interferences, or frequency tuning.

The aim of this special issue was to collect research articles on electromagnetic devices for vibration damping and isolation in civil and mechanical engineering applications. Articles describing original theoretical research as well as new experimental results have been gathered. The research results were product oriented; i.e., it must consider the requirements of a particular application and demonstrate significant, unique, or economically differential factors in respect to other techniques for a particular application.

This special issue has attracted more than ten submissions from researchers from all around the world. Five of them have been accepted and included in this special issue of *Shock and Vibration* journal. The selection of the high-level papers was conducted as a rigorous peer-review process by the international, well-recognized experts in the appropriate fields presented in each paper. Thus, each manuscript has been evaluated as single, original work. Special attention to the applicability and market competitiveness of the devices has been considered.

In the article "Multiphysics Model of an MR Damper including Magnetic Hysteresis" by M. Kubík and J. Goldasz, researchers analysed and modelled the two primary sources of hysteresis acting on a magnetorheological (MR) damper: hydro(mechanical) hysteresis, which can be related to flow dynamic mechanisms, and magnetic hysteresis which is an inherent property of ferromagnetic materials forming the magnetic circuit of the actuators. In the paper, the authors present a hybrid multiphysics model of a flow-mode MR actuator which considered both types of hysteresis. The model relies on the information which can be extracted primarily from material datasheets and engineering drawings, and it was verified against measured data. Moreover, they use the model in a parameter sensitivity study to

examine the influence of magnetic hysteresis and other relevant factors on the output of the actuator.

The article submitted by E. Palomares et al. entitled "Modelling Magnetorheological Dampers in Preyield and Postyield Regions" presents a review of different magnetorheological damper models used, which includes characterisation, modelling, and comparison. The analyses cover the behaviour from preyield to postyield regions of the MR fluid. The performance of the different models was assessed by means of experimental tests and simulations in a simple and straightforward semiactive control case study. The results obtained proved that most models usually fail in predicting accurate low-velocity behaviour (before iron chains yield), and this may lead to bad estimations when used in control schemes due to modelling errors and chattering.

The third paper describes an active mount that combines a passive rubber mount and an electromagnetic actuator which has been examined for use in naval shipboard equipment. The design specification of an active mount such as required force, displacement, and frequency characteristics is identified for the self-excited pump system, and then an electromagnetic actuator active mount is designed considering the shape of the passive rubber mount and shock resistance. From the results of applying the proposed electromagnetic active mount, a vibration reduction of about 20 dB for the motor equipment was observed for the excited frequency components of 1600 rpm and its two harmonic components. This interesting article is entitled as "Experimental Approach to Active Mounts Using Electromagnetic Actuator and Rubber with Consideration of Shock Resistance for Naval Shipboard Equipment," and it was submitted by Y. Shin et al.

The review article on "Passive Electromagnetic Devices for Vibration Damping and Isolation" by E. Díez-Jiménez et al. summarizes an interesting type of electromagnetic dampers. Passive electromagnetic devices present good damping capacity, lower cost, null power consumption, and higher reliability. In this review, advantages and drawbacks were highlighted in addition to application fields and technology readiness level of most recent developments. Besides, a general introductory section relates the present key considerations that any engineer, electrical or mechanical, needs to know for a deep comprehension and correct design of this type of devices.

The last published article is entitled "Energy Dissipation Mechanism and Control Model of a Digital Hydraulic Damper" by C. Wang et al. In this article, a digital hydraulic damper was described. This device can adjust the whole buffering capacity to be adaptable to the impacting load on time during the buffering process. In this paper, the mechanism of energy dissipation in the digital hydraulic damper and the whole damping process are studied. Based on an energetic dissipation model, the control of the process was given, which laid a theoretical foundation for detailed structural design and control optimization.

We hope that this special issue updates scientific evidences in electromagnetic techniques for vibration damping and isolation, contributing to an adequate scientific and industrial dissemination of the topic.

Conflicts of Interest

The editors declare that they have no conflicts of interest.

Acknowledgments

Efren Diez-Jimenez
Toshihiko Sugiura
Rocco Rizzo
Maria-Jesus Gómez-García
Andrew Fleming

Research Article

Energy Dissipation Mechanism and Control Model of a Digital Hydraulic Damper

Cheng-long Wang ⓘ **, ZhiWei Qiu** ⓘ **, QingLiang Zeng** ⓘ **, Yanxi Liu** ⓘ **, and Genyuan Miao** ⓘ

Shandong University of Science and Technology, College of Mechanical and Electronic Engineering, 266590 Qingdao, China

Correspondence should be addressed to QingLiang Zeng; qlzeng@sdust.edu.cn

In order to achieve the high efficiency and stable cushioning effect under the uncertain impacting situation, a digital hydraulic damper is developed which can adjust the whole buffering capacity so as to be adaptable to the impacting load on time during the buffering process. In the paper, the mechanism of energy dissipation in the digital hydraulic damper and the whole damping process are studied. The relationship between the energy dissipation process and the control process is given. Firstly, the energy dissipation process of the digital throttling unit is studied, and the mathematical model of energy losses of the digital hydraulic damper unit and the energy dissipation model of the whole digital damper are established. The energy dissipation model of the digital hydraulic buffer is proposed. Secondly, the effect on energy losses caused by the three elements of the digital damper, which are the sudden extension of cross section, form of orifice, and form of cone valve port, is analyzed. Finally, based on the energy dissipation model, the control model of the energy dissipation process is given, which lays a theoretical foundation for detailed structural design and control optimization.

1. State of the Art

As a kind of safety protection device, the hydraulic damper has been widely used in various occasions. The basic working principle is that the energy generated by the impacting body is consumed by means of throttle section which can produce liquid resistance.

Jiang [1] studied the gradual throttling hydraulic buffer, and the role of gradient throttle hydraulic buffer in a tracked vehicle suspension system is analyzed. Wang et al. [2] studied the structure design, optimization, and dynamic characteristics of multiorifice hydraulic buffer. Wang and Shen [3] simulated and analyzed the viscoelastic damper; an optimum method of clay buffer design was proposed. Qi [4] made a comparative study of the experiment and simulation of the viscoelastic buffer, which indicates high feasibility of the application of the viscoelastic material in the recoil mechanism. Wang et al. [5] studied the cushioning characteristics of viscoelastic buffer, which shows that the use of viscoelastic damper can

increase the energy absorption rate and improve the stability. Baochen et al. [6] studied and analyzed the buffer characteristics of throttle bar buffer and verified the rationality of the selection method of K.

For the buffer, the prompt response and the smooth buffering process should be improved on the basis of guaranteeing the buffer efficiency and amount of absorbed shocking energy. In order to realize the above goals, a digital hydraulic buffer is proposed by Wang et al. [7]. In the buffer as shown in Figure 1, the throttle valve and high-speed on-off valve are connected in series to form a digital magnetic throttle unit, and the digital throttle valve group is composed of several groups of digital magnetic throttle units in parallel; high-speed on-off valve controlled by PID is used to complete the variable throttle control.

For the digital hydraulic buffer, in order to achieve the high efficiency and stable cushioning effect under the uncertain impact load, the following problems should be solved: firstly, for the digital throttling unit, the key point
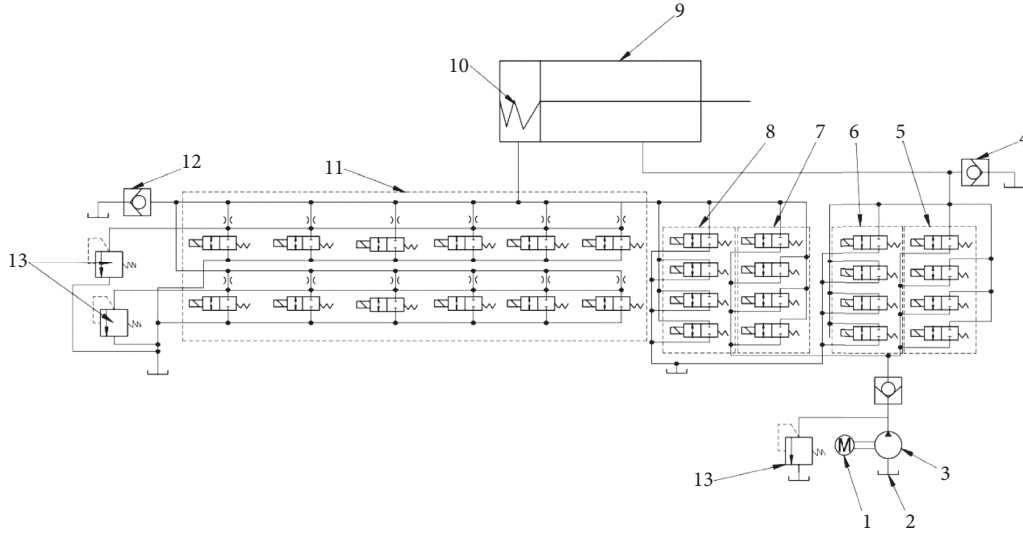
FIGURE 1: Digital buffer hydraulic system. (1) Motor; (2) tank; (3) gear pump; (4) check valve for rod chamber; (5) group of oil inlet control valves for rod chamber; (6) group of oil outlet control valves for the rod chamber; (7) group of oil inlet control valves for the rodless chamber; (8) group of oil outlet control valves for the rodless chamber; (9) cylinder; (10) reset spring; (11) digital throttle unit; (12) check valve for the rodless chamber; (13) safety valve.

is how to ensure the appropraite PWM (pulse width modulation) and value of energy dissipation during the buffering process, and secondly, how to control the whole buffering capacity so as to make it adaptable to the impacting load on time during the buffering process.

In order to achieve the above objectives, the energy dissipation process of the digital throttling unit needs to be studied. On this basis, the energy dissipation model and the control model of the digital hydraulic buffer should be proposed, which will provide a theoretical foundation for detailed structural design and control optimization.

Aiming at the problem of energy dissipation, Hong et al. [8–10] studied the flow coefficient and flow field variation law of various valve ports. Zhang et al. [11] have carried out the experimental research on the flow co-efficient of the orifice of flat plate valve, conical valve, ball valve, and slide valve and put forward the optimum design for the structural design of various orifices from the flow coefficient point of view. Wu [12, 13] analyzed the flow characteristics of servo valve in the laminar and turbulent state by means of experiment. Srikanth and Bhasker [14] studied the formation and development of vortices in the flow field of hydraulic valves based on the dynamic grid technology. Pace et al. [15] studied the flow coefficient of the spool valve orifice and the liquid change of the internal flow field. Liu et al. [16] studied the wake flow field of cone flow meter. Yu et al. [17] studied the effect of orifice chamfer on the flow field characteristics of perforated plate flow meter. Gao [18] carried out finite element analysis on the flow field of the complex flow passage and various throttle holes. Wang et al. [19] studied the causes of cavitations' generation and influencing factors of the hydraulic poppet valve port. Fu and Du [20] studied the cavitations' phenomenon in high-speed flow of throttle

groove. Vallet et al. [21] studied the hydraulic pressure of the hydraulic spool and the flow coefficient of the valve orifice.

Among the above research, the mechanism of energy losses in the whole damping system and the whole damping process has not been systematically studied. The relationship between the energy dissipation process and the control process is not mentioned. In our research, the energy dissipation process of the digital throttling unit is studied, and the influence of the sudden extension of digital damper unit, valve opening, and extension on energy losses is analyzed. Energy dissipation model of the digital hydraulic buffer is proposed, and the correlative model of energy dissipation and control processes is established, which lays a theoretical foundation for detailed structural design and control optimization.

2. Energy Dissipation Mechanism of the Digital Hydraulic Damper

A digital hydraulic damper consists of several digital magnetic throttle units which are made up of the high-speed on-off valve and the throttle valve. The throttle valve and the high-speed on-off valve are connected in series so as to form the digital throttling unit shown in Figure 2, which consists of the throttle valve body, coil, valve core, gas spring, keeper, and pole shoe. A number of digital magnetic throttle units are combined together in parallel to form a digital throttle valve group. When the oil passes through the unit, there are local pressure losses and frictional pressure losses, and a damping force is created so as to buffer the impacting object until it stops.

As shown in Figure 3, when the fluid flows through the digital throttling unit, there are three kinds of energy losses which are local pressure losses at sudden change cross
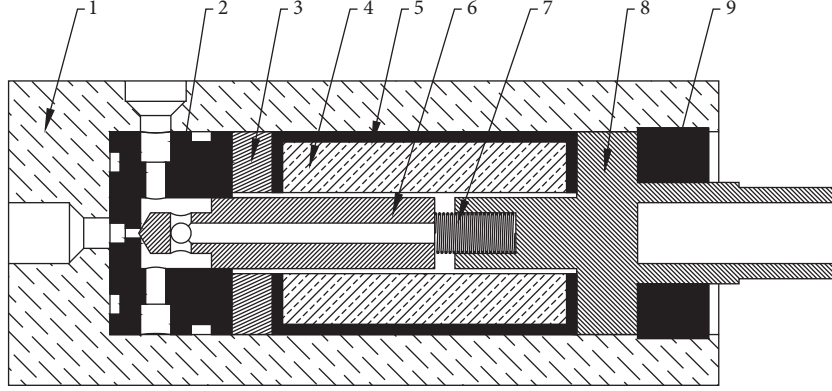
FIGURE 2: Digital magnetic throttle unit. (1) Integrated valve block; (2) valve body; (3) ring iron; (4) coil; (5) yoke; (6) spool; (7) reset spring; (8) iron core; (9) fastening ring.
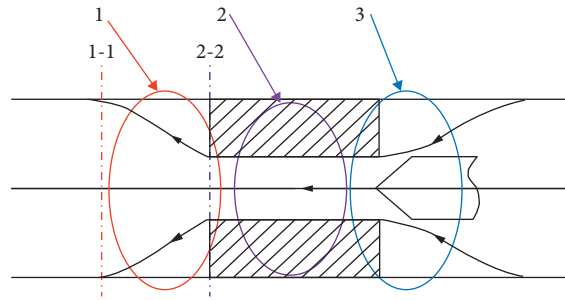
FIGURE 3: Energy losses of digital damping unit. (1) Local pressure losses at sudden change cross section; (2) friction pressure losses through the orifice; (3) local pressure losses through the cone valve port.

section, frictional pressure losses through the orifice, and local pressure losses through the cone valve port. A mathematical model for the energy losses of the unit is analyzed according to the above three factors.

2.1. Mathematical Model for the Energy Losses of the Unit.
The flow rate of the digital damper unit depends on the flow capacity of the conical valve orifice. In a pulse width modulation (PWM) period, the average flow rate through the valve orifice is proportional to the PWM of the input signal. The average flow rate of the digital damper unit is as follows:

$$\overline{q} = \tau C_d A_2 \sqrt{\frac{2\Delta p_2}{\rho}}. \tag{1}$$

In the formula, $\overline{q}$ is the average flow rate of the digital damper unit, τ is the PWM of pulse, which is equal to t_p/t_f, where t_p is the pulse width of PWM and t_f is the pulse period of PWM, C_d is the flow coefficient, A_2 is the area of throttle hole at section 2-2, and Δp_2 is the pressure difference of the conical valve orifice.

2.1.1. Local Pressure Losses at Sudden Change Cross Section.
In Figure 3, local pressure losses at sudden change cross section are illustrated when the fluid flows into the orifice of the digital magnetic throttle unit. h_m (local pressure

losses at sudden change cross section) can be described as follows:

$$h_m = \left(1 - \frac{A_2}{A_1}\right)^2 \frac{v_2^2}{2g} = \zeta \frac{v_2^2}{2g}. \tag{2}$$

In formula (2), A_2 is the area of section 2-2, A_1 is the area of section 1-1, v_2 is the average velocity of flow in section 2-2, ζ is the partial loss coefficient which is equal to $1 - (A_2/A_1)^2$ and g is the gravity acceleration. According to formula (2),

$$v_2 = \frac{\overline{q}}{A_2} = \frac{\tau C_d A_2}{A_2} \sqrt{\frac{2\Delta p_2}{\rho}}. \tag{3}$$

The energy losses at cross section changes are as follows:

$$h_m = \frac{\zeta \Delta p_2}{\rho g} \left(\frac{\tau C_d}{1}\right)^2. \tag{4}$$

2.1.2. Frictional Pressure Losses through the Orifice.
According to the Navier–Stokes equation, the pressure losses Δp_1 flow through the distance of 1 are as follows:

$$\Delta p_1 = \frac{32\mu l v_2}{d^2}. \tag{5}$$

In formula (5), μ is the kinematic viscosity of the fluid, d is the diameter of the throttle hole, and v_2 is the velocity of the fluid in the throttle hole. According to formulas (3) and (5), it shows that the pressure losses are as follows:

$$\Delta p_1 = \frac{32\mu l\tau C_\mathrm{d}}{d^2}\sqrt{\frac{2\Delta p_2}{\rho}}. \tag{6}$$

2.1.3. Local Pressure Losses through the Cone Valve Port.
The buffering process is realized by means of a number of parallel digital damper units. If the number of opened digital magnetic throttle units is n at the moment, then the average flow $\overline{q}$, which flows through the port of the cone spool, is as follows:

$$\overline{q} = \frac{Av}{n}. \tag{7}$$

In formula (7), A is the cross-sectional area of the digital hydraulic damper piston which is shown in Figure 1, and v is the motion velocity of the piston at this moment. Pressure losses caused by the cone spool of the digital magnetic throttle unit are as follows:

$$\Delta p_2 = \frac{\rho}{2}\left(\frac{Av}{n\tau C_\mathrm{q}A_2}\right)^2. \tag{8}$$

2.1.4. Energy Dissipation Model of the Digital Hydraulic Damper.
In summary, total losses of each digital damping unit in the digital hydraulic damper include three parts which are losses in the sudden extension section, losses along throttle orifice, and local losses at cone valve orifice. The mathematical model of total losses per digital damping unit (water column height) can be described as follows:

$$h = \frac{\Delta p_1}{\rho} + \frac{\Delta p_2}{\rho} + h_\mathrm{m} = \frac{32\mu l\tau C_\mathrm{d}}{\rho d^2}\sqrt{\frac{2\Delta p_2}{\rho}}$$
$$+ \frac{1}{2}\left(\frac{Av}{n\tau C_\mathrm{q}A_2}\right) + \frac{\zeta \Delta p_2}{\rho g}\left(\frac{\tau C_\mathrm{d}}{1}\right)^2. \tag{9}$$

Here, the energy dissipation model of the whole system is given as follows:

$$H = \sum hi, \quad i = 1, 2, 3, \ldots, n. \tag{10}$$

2.2. Simulation Analysis of Energy Losses of Digital Damping Unit.
In this section, the three factors affecting the energy losses of the digital damping unit are mainly studied, which are, namely, the sudden extension channel with chamfer, sections with different proportions of sudden extension, and conical spool with different angles. Focusing on the three factors, the simulation analysis is done.

The flow field modeling of the channel with sudden extension can be established according to Figure 4 and Table 1. The flow channel of the digital damping unit is shown in Figure 4, which has a damping hole. The diameter of the hole is 0.5 mm and the length of the hole is 0.75 mm.
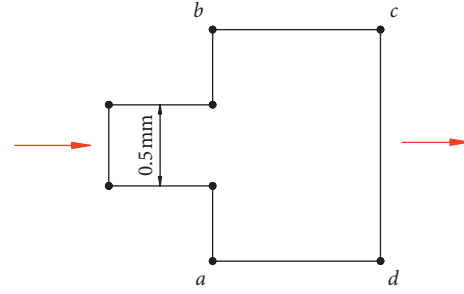
Figure 4: Structure of channel with sudden extension.

The size of sections with different proportions of sudden extension is obtained according to Table 1.

Here, 45# hydraulic oil is used in the simulation and the specific simulation parameters are shown in Table 2.

The flow field modeling of the conical valve core is established according to Figures 5 and 6 and Table 3. The conical valve core in Figures 5 and 6 has the same opening height. The height is 0.3 mm. The size of the conical spool with different angles is obtained according to Table 3.

2.3. Influence of Extension of Cross Section with Different Ratios.
After the fluid flows through the sudden extension of cross section, the flow field diagram shown in Figure 7 is formed. It can be seen that the jet flow phenomenon occurs in the cross section with different sudden extension proportions, resulting in the existence of the wall recirculation zone and the jet recirculation zone. The key factor of energy losses is swirls of various changes in the recirculation zone. Since the recirculation zone between the jets is small, it can be neglected. Here, L is the length of the recirculation zone and v is the flow velocity of the recirculation zone. The starting point of the sudden extension of cross section is taken as the coordinate origin, and coordinate map of the flow field of the section is established. The coordinates of vortex center of the recirculation zone of the upper and lower walls are represented by O_1 and O_2.

From Figure 8 and Table 4, it can be seen that the pressure is changed seriously when the sudden spread ratio is equal to 1.5. From Figures 9–15, it can also be seen that with the increase of the sudden spread ratio, scale of the vortex and the negative pressure region is increased. However, from Figure 16 and 17, it can be seen that the sudden spread ratio is inversely proportional to the turbulent kinetic energy and velocity of the vortex center reflux. In summary, the scale of the vortex is not the key factor of energy losses. The key factors which determine the energy losses in the sudden spread of the cross section are the reflux speed and turbulent kinetic energy in the reflux zone. The smaller the sudden spread ratio, the greater the confluence velocity and turbulent kinetic energy in the reflux zone. And the more complex the

TABLE 1: Structure size of sections with different proportions of sudden extension.

Name	Coordinate (unit: mm)			
Cross sections with proportion of sudden extension	a	b	c	d
1.25	(0, 0)	(0.625, 0)	(0.625, 0.75)	(0, 0.75)
1.5	(0, 0)	(0.75, 0)	(0.75, 0.75)	(0, 0.75)
1.75	(0, 0)	(0.875, 0)	(0.875, 0.75)	(0, 0.75)
2	(0, 0)	(1, 0)	(1, 0.75)	(0, 0.75)

TABLE 2: Simulation parameters.

Model	Viscosity (kg/m·s)	Density (kg/m³)	Inlet velocity (m/s)
45#hydraulic oil	0.04	890	15
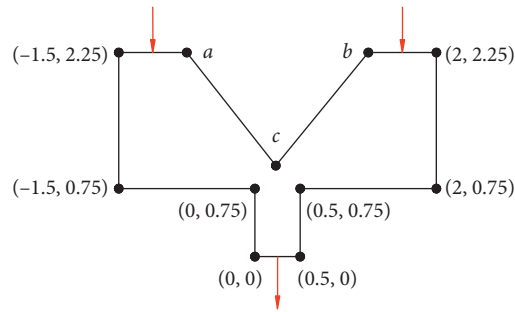
FIGURE 5: Structural sketch of 60° conical valve core.
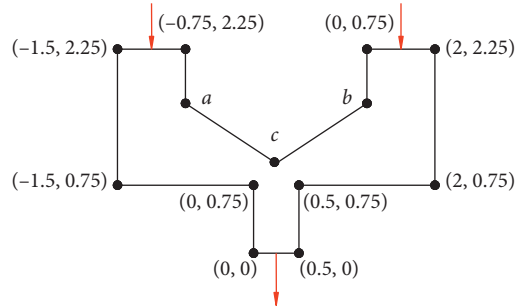
FIGURE 6: Structural sketch of 90° and 120° conical valve core.

TABLE 3: Structural size of the conical spool with different angles.

Name	Coordinate (unit: mm)		
Angle	a	b	c
60	(−0.807, 2.25)	(1.193, 2.25)	(0.25, 0.617)
90	(−0.75, 1.05)	(0.75, 1.05)	(0.25, 0.8)
120	(−0.75, 0.733)	(0.75, 0.733)	(0.25, 0.906)

structure of the vortex in the reflux zone, the more intense the motion and the greater the local pressure losses. From Figure 18, it can also be verified that the pressure difference between inlet and outlet is inversely proportional to the sudden spread ratio, and the flow coefficient is proportional to the sudden spread ratio. It

shows that the larger the sudden spread ratio, the smaller the energy losses.

2.4. Chamfer Effect on Energy Losses of Sudden Extension of Cross Section. From Figures 19 and 20 and Table 5, it can
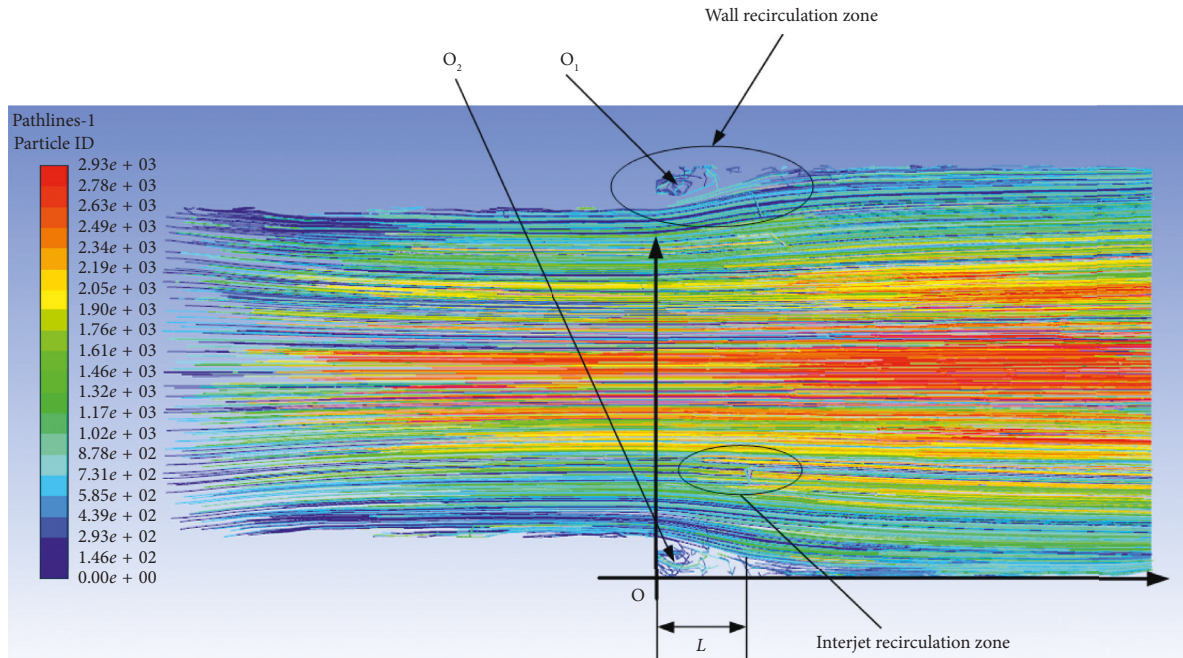
FIGURE 7: Flow field diagram of the sudden extension of cross section.
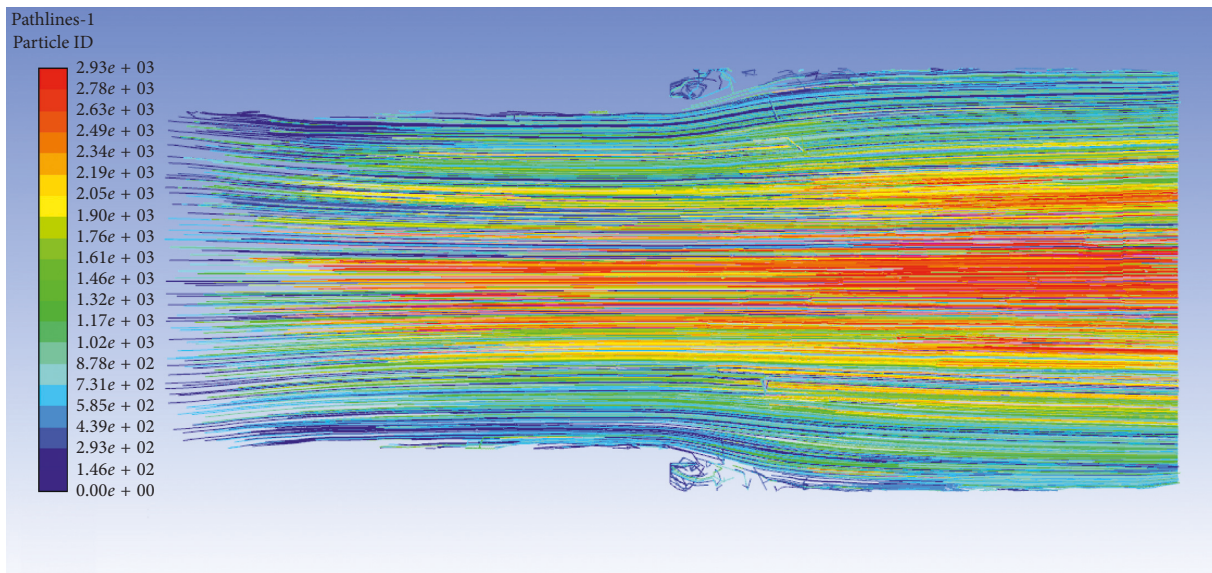
FIGURE 8: Sudden extension ratio is 1.25.

TABLE 4: Characteristics of sudden extension reflux zone in cross section.

Inlet condition	Vortex position	Vortex structure	Reflow zone length
15 m/s	O_1 (0.067D, 0.067D)	Complex structure and intense movement	0.33D
	O_1 (0.18D, 0.16D)	Stable reattachment vortex	0.94D
	O_1 (0.4D, 0.33D)	Stable reattachment vortex	1.33D
	O_1 (0.62D, 0.31D)	Stable reattachment vortex	1.54D

D is the diameter of the damping hole.
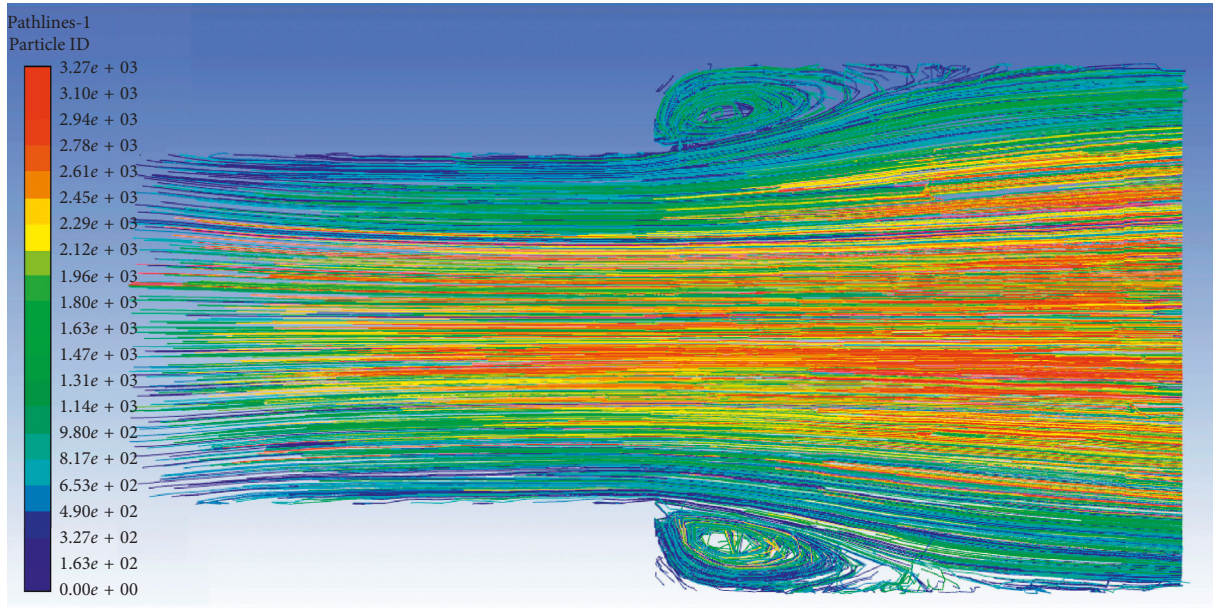
FIGURE 9: Sudden extension ratio is 1.5.
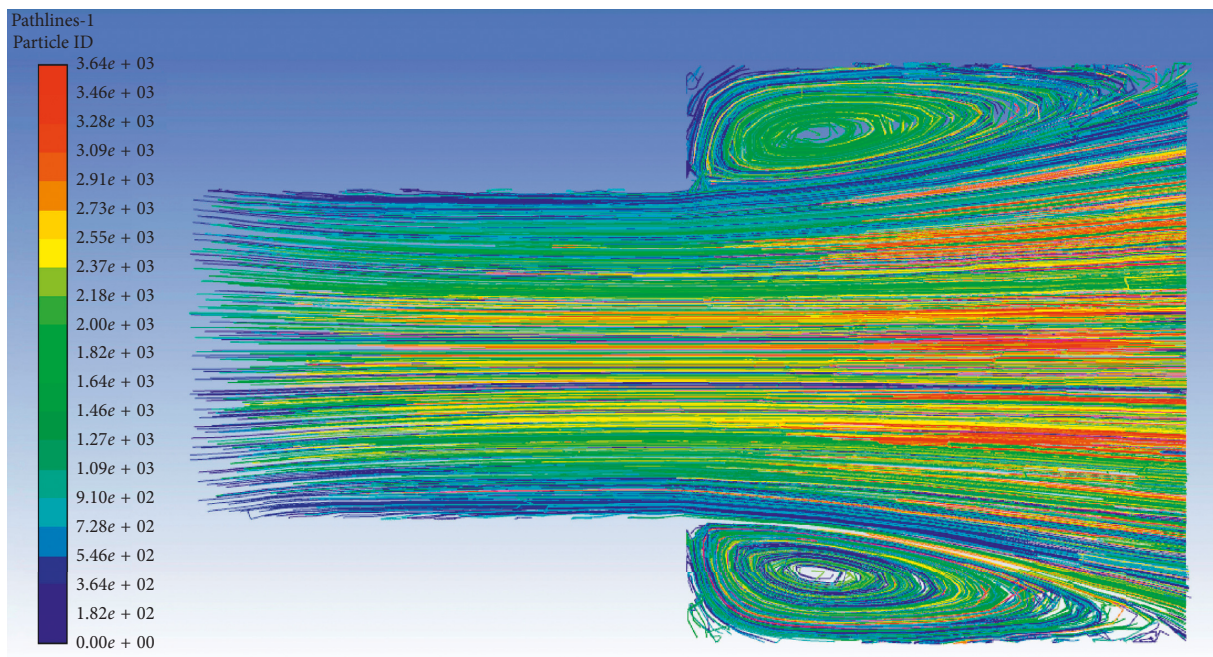
FIGURE 10: Sudden extension ratio is 1.75.

be seen that if there is a chamfer at extension of cross section, the size of the vortex at the extension of cross section will be reduced, and the negative pressure zone will also be reduced. From Figures 21 and 22, the same result can be obtained. From Figure 23, it can be seen that the turbulent kinetic energy of extension of cross section with chamfer is lower than that of the sudden extension

of cross section without chamfer. From Figure 24, it can be seen that the reflux velocity of vortex center of the sudden extension of cross section with chamfer is lower than that of the sudden extension of cross section without chamfer.

The pressure losses at the sudden extension of cross section are mainly due to the fact that the streamline
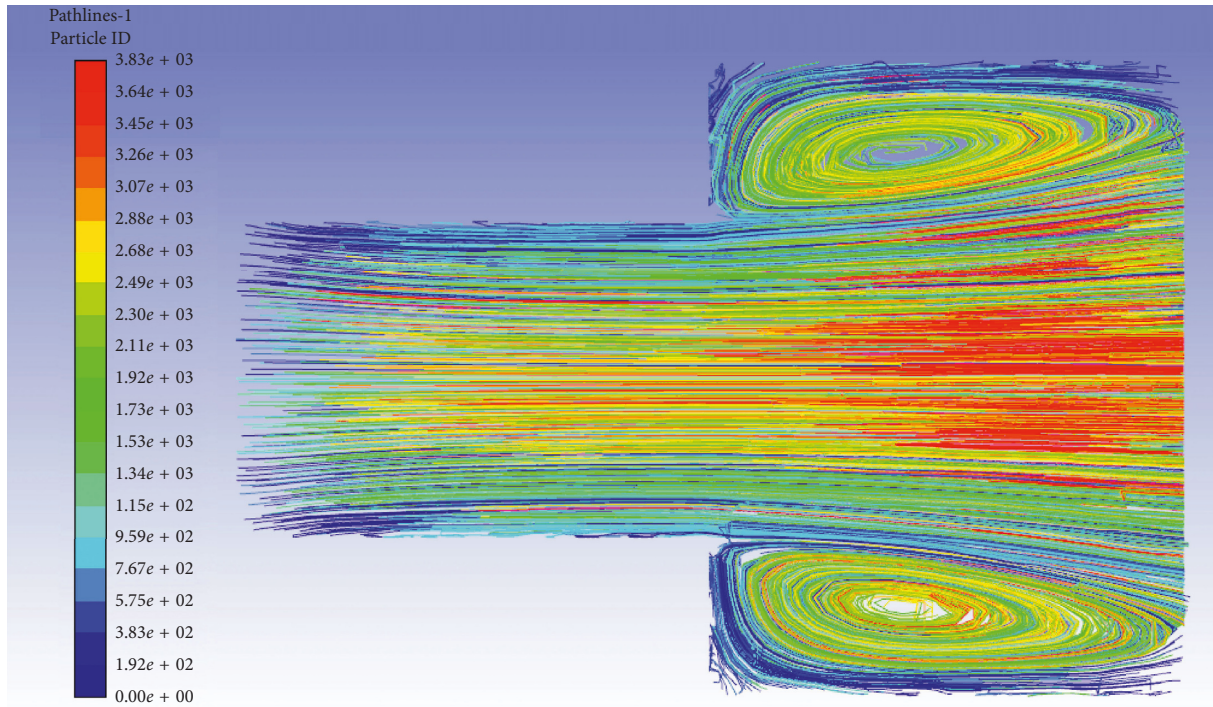
FIGURE 11: Sudden extension ratio is 2.
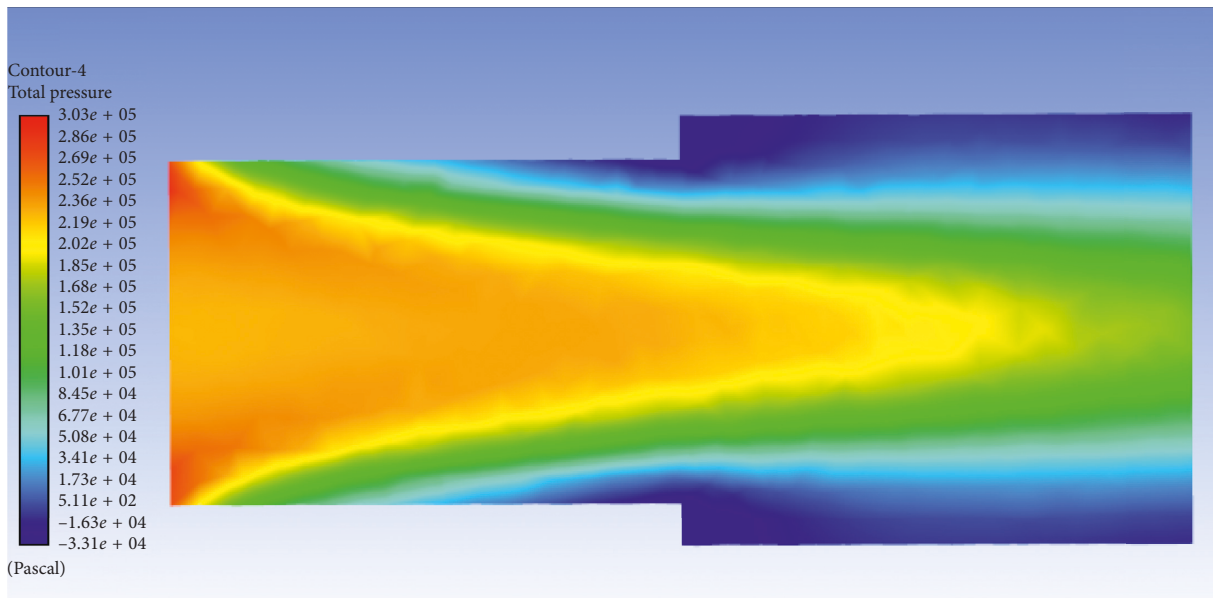
FIGURE 12: Pressure nephogram (sudden expansion ratio is 1.25).

cannot be bent, which will cause the vortex at the sudden extension of cross section and then cause pressure losses and energy losses. The flow coefficient of the sudden extension of cross section with chamfer is 0.47, and that of the sudden extension of cross section without chamfer is 0.49, which increases the flow capacity by 4.25%.

Sudden spread with chamfer will make the streamline at the sudden extension of cross section more smoothly, which is conducive to reducing the size of the vortex, reducing the velocity and turbulent kinetic energy in the wall reflux zone, and reducing pressure losses and energy losses.
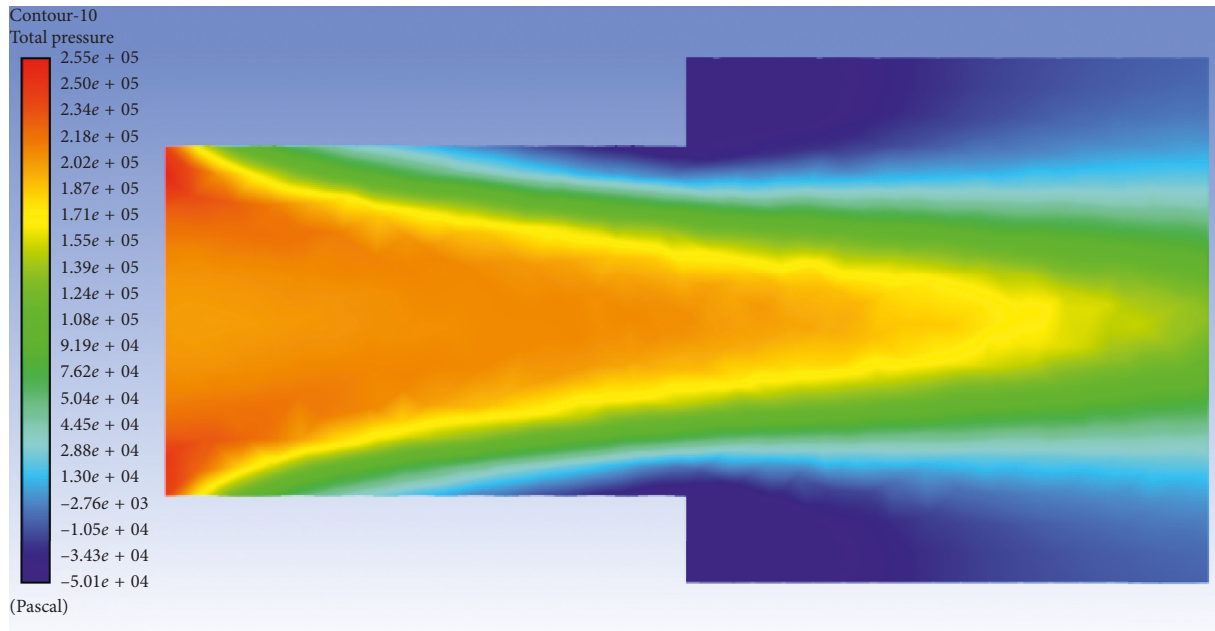
Figure 13: Pressure nephogram (sudden expansion ratio is 1.5).
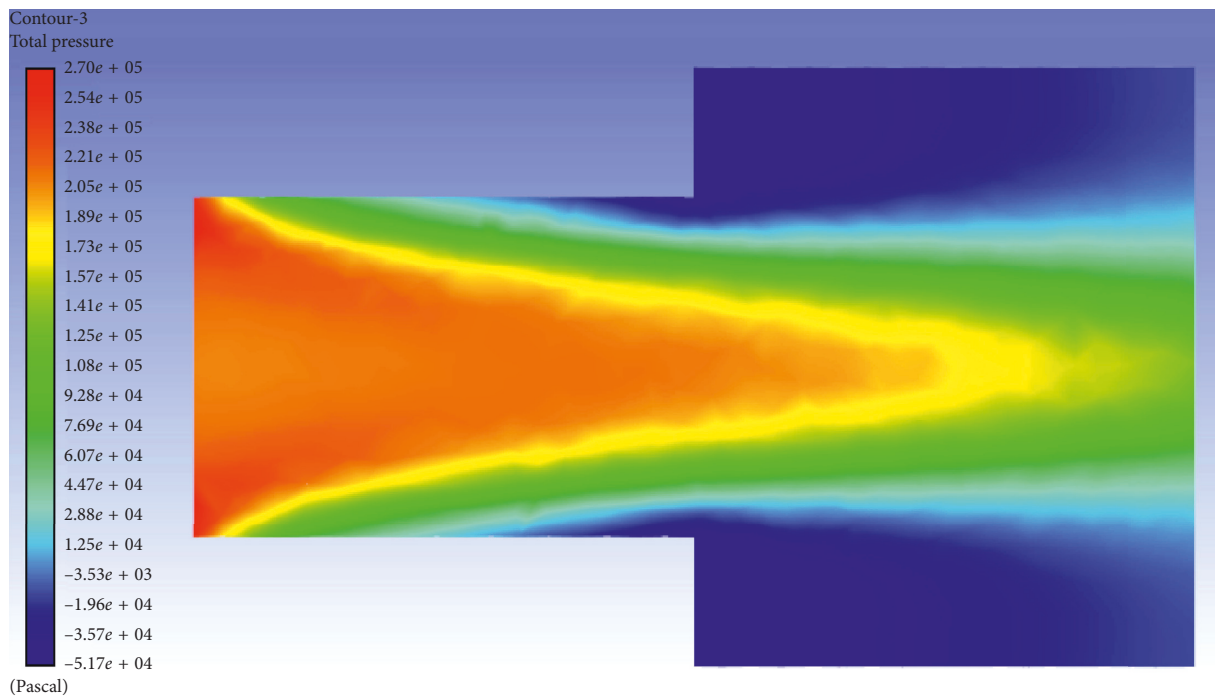
Figure 14: Pressure nephogram (sudden expansion ratio is 1.75).

2.5. Effect of Core Angle on Energy Losses of Poppet Valve. From Figures 25–27, it can be seen that the angle of the poppet valve core is inversely proportional to the size of the vortex at valve port and the edge of valve port at the same opening height. From Figures 28–30, it can be seen that there is a fluid separation phenomenon at the tip of the poppet valve core. The larger the angle of the poppet valve core is, the weaker the fluid separation phenomenon is. The larger the angle of the core, the larger the high pressure zone at the core outlet. From Figures 31–35, it can also be seen that with the increase of the core angle, the turbulent kinetic energy region decreases, the turbulent intensity decreases, and the
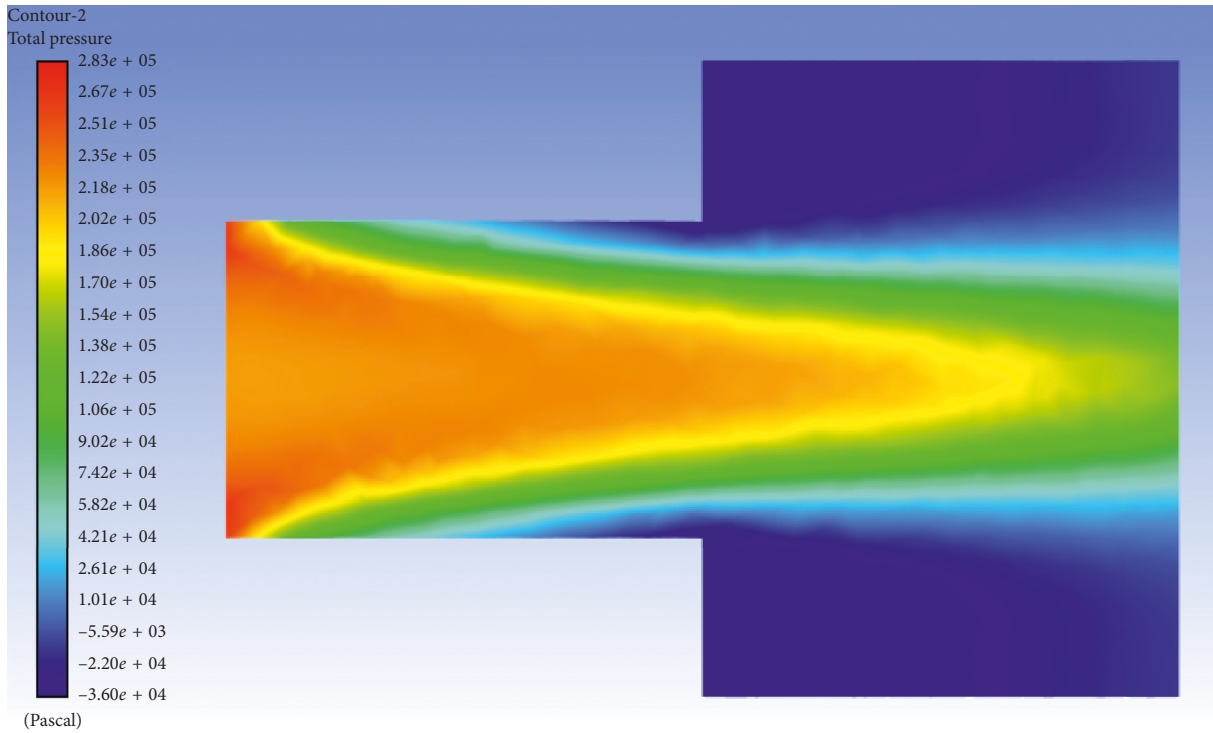
FIGURE 15: Pressure nephogram (sudden expansion ratio is 2).
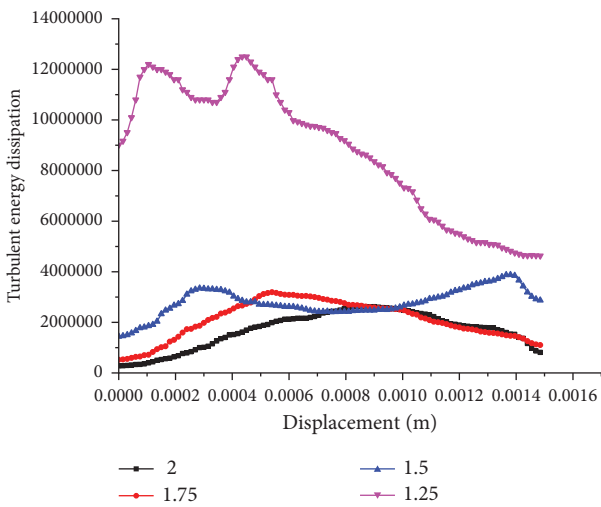
FIGURE 16: Turbulent energy distribution at the sudden extension of cross section.
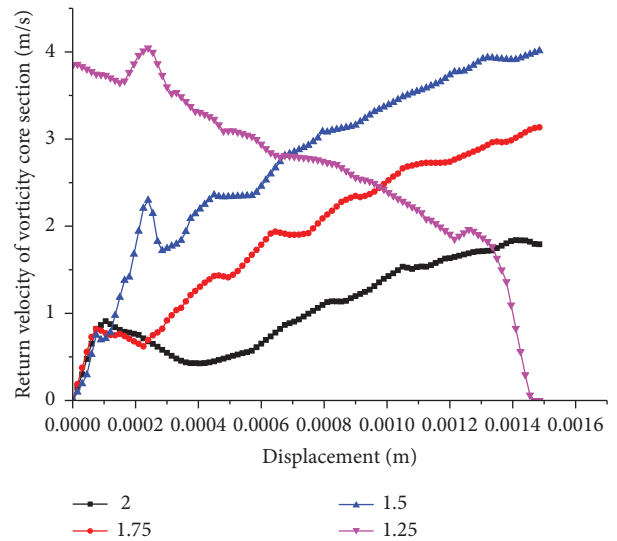
FIGURE 17: Velocity distribution in the recirculation zone of vortex core section.

energy losses in the region decrease. With the increase of the angle of the core, the negative pressure on the wall of poppet valve becomes smaller and the flow velocity decreases, and the pressure change rate and the flow velocity change rate become smaller. Large negative pressure will accelerate the vortex velocity in the wall reflux zone, and the flow field changes more complex, resulting in greater pressure losses and energy losses.

In summary, energy losses at the poppet valve port include the energy losses at the edge of the valve port and energy losses at the tip of the valve core. When the poppet valve core is opened at the same height, the smaller the angle of the poppet valve core is, the faster the fluid flows through the poppet valve core, which accelerates the vortex flow in the edge area of the valve port, enhances the turbulence
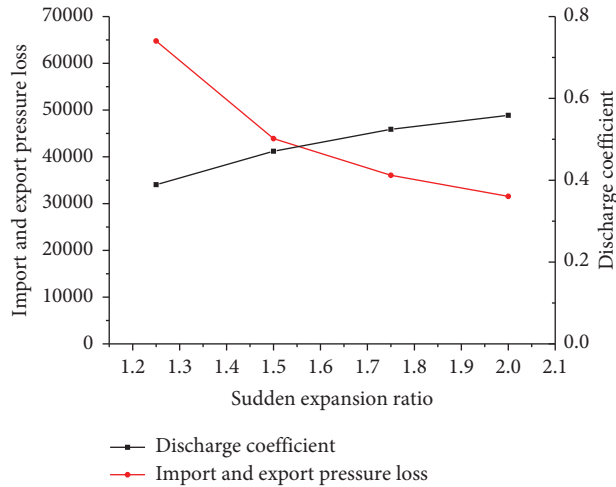
FIGURE 18: Flow coefficient of different sudden extension ratios and the pressure difference between import and export.
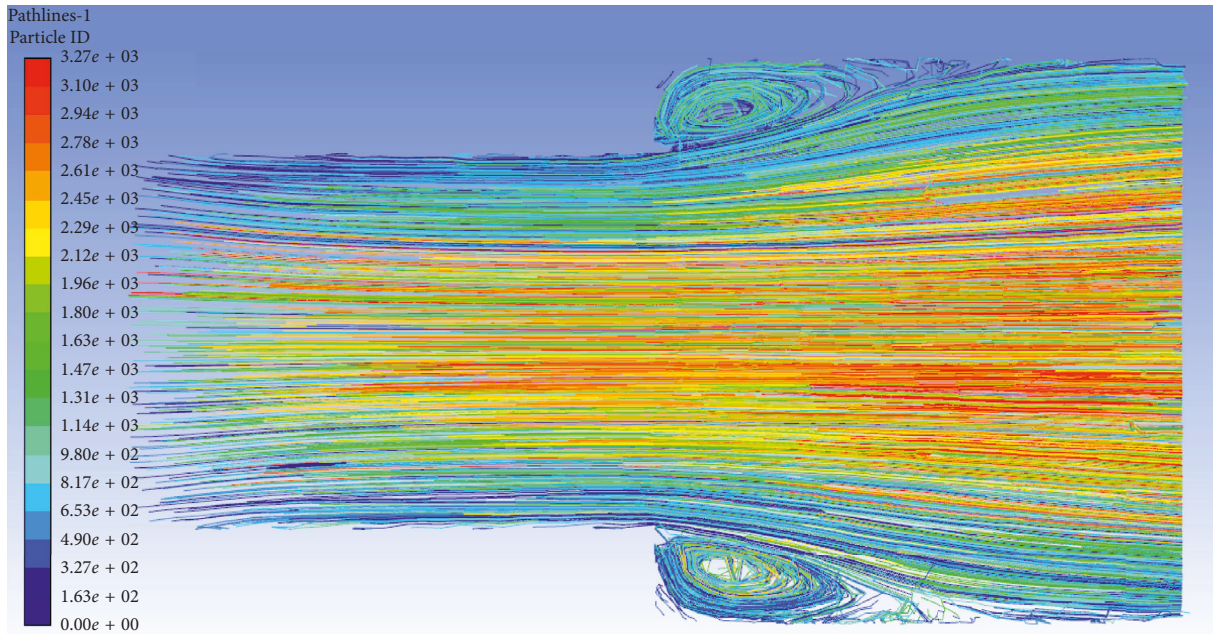
FIGURE 19: Without chamfer (sudden spread ratio is 1.5).

intensity, and increases the energy losses. The flow separation phenomena will occur in the tip area of the poppet valve core with circular cross section, which makes the separation vortex occur in the tip area of the valve core and increases its energy losses. With the increase of the angle, the energy losses decrease.

3. Control Model of Energy Dissipation Process

According to the energy dissipation model of the whole system proposed in Section 2, it can be seen that the key factors are as follows: pulse width modulation (PWM) of the digital damper unit, number of digital damper units, chamfer on the sudden extension of cross section of the digital damper unit, sudden extension of cross section with different ratios of the digital damper unit, and cone spool with different angles of the digital damper unit. All of them affect the energy dissipation process.

Theoretically, the above five parameters should be controlled during the process of the digital damper. Theoretically, the above five parameters should be controlled during the damping process. In this paper, PWM and number of digital damper units are the present adjustable parameters. Only the PWM of digital damping elements and the number of digital damping elements are designed as the adjustable parameters at present.

The work equation is as follows: $W = FS$. Under the same energy absorption situation, the force on the piston
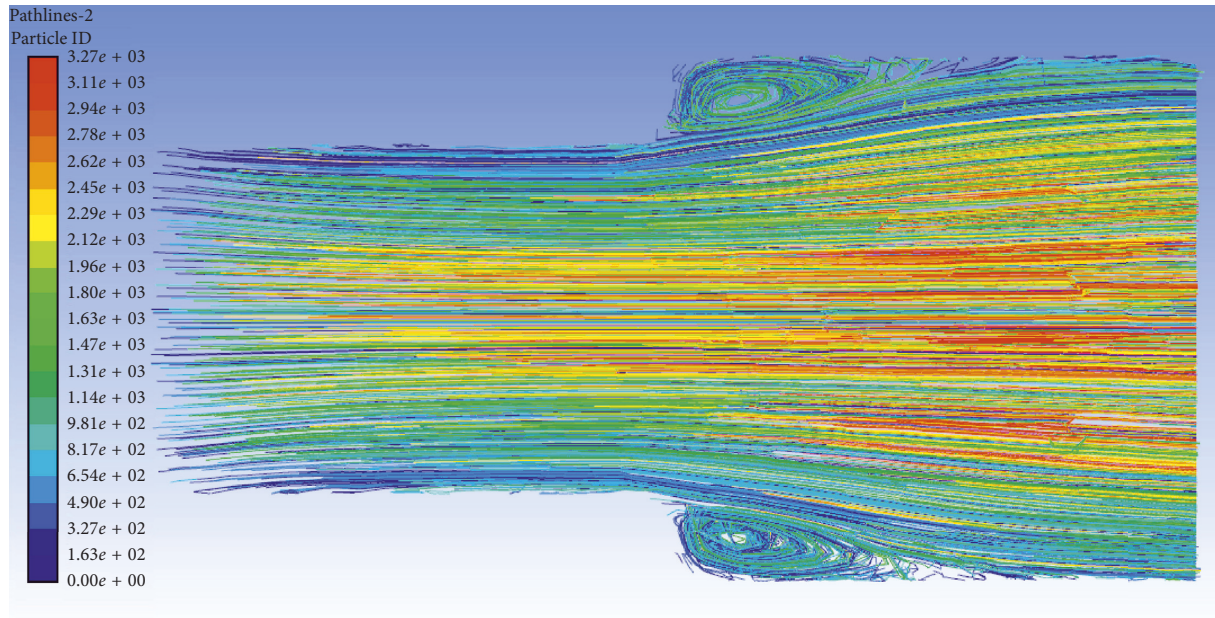
FIGURE 20: With chamfer (sudden spread ratio is 1.5).

TABLE 5: Sudden spread ratio of 1.5 with or without chamfer reflux zone.

Entry condition	Type	Center location of vortex	Vortex structure	Length of reflux zone
15 m/s	Without chamfer	O_1 (0.18D, 0.16D)	Stable reattachment vortex	0.94D
	With chamfer	O_1 (0.2D, 0.13D)	Stable reattachment vortex	0.8D

D is the diameter of the damping hole.
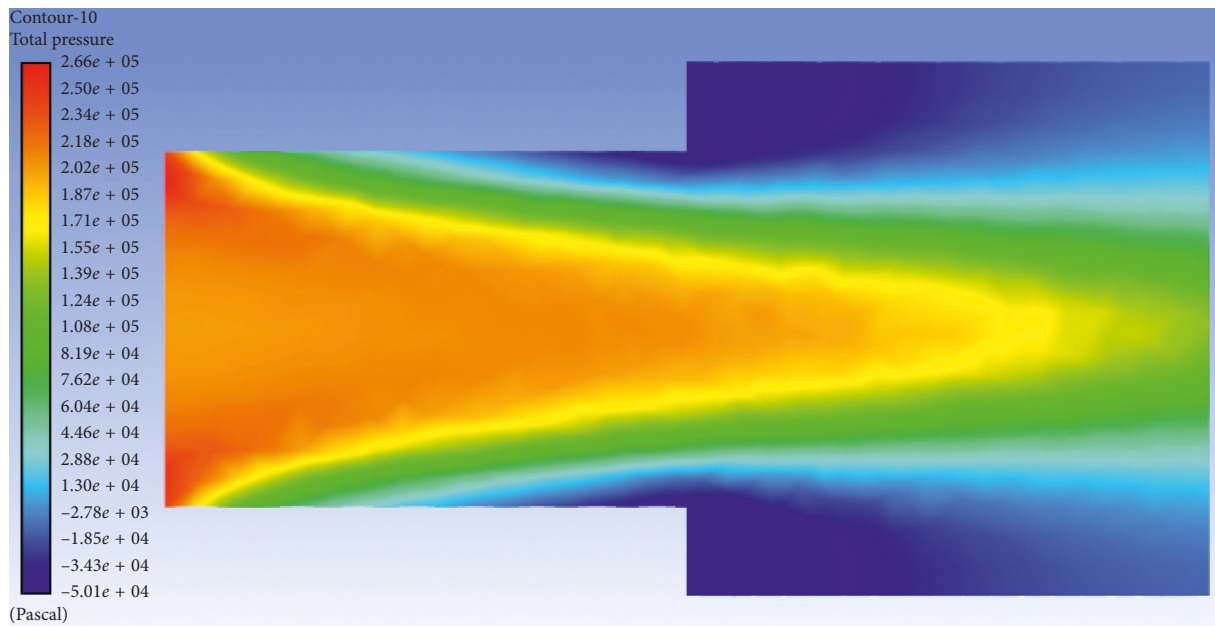
FIGURE 21: Pressure nephogram without chamfer (sudden spread ratio is 1.5).

rod of the damper is inversely proportional to the displacement of the piston in the damper cylinder. In the formula, W is the total energy absorbed by the hydraulic damper, F is the force on the piston rod in the damper cylinder during the buffering process, and S is the displacement of the piston in the damper cylinder during the buffering process.

Two control modes are designed for the digital hydraulic damper, which are the minimum pressure mode and the minimum displacement mode. For the minimum pressure
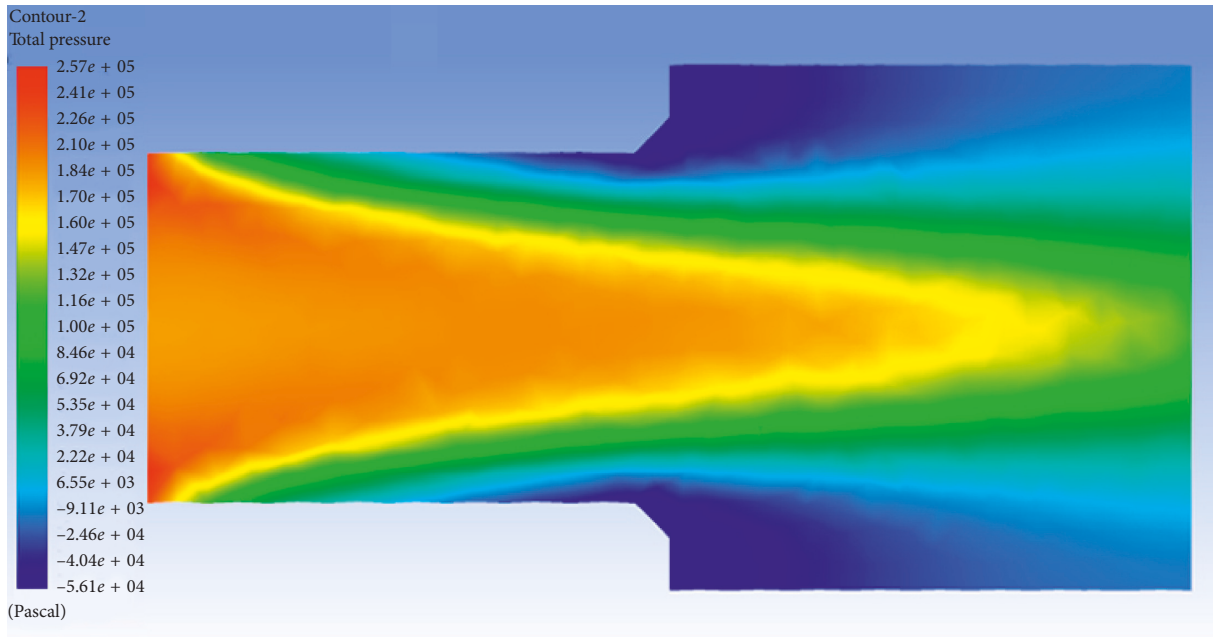
FIGURE 22: Pressure nephogram with chamfer (sudden spread ratio is 1.5).
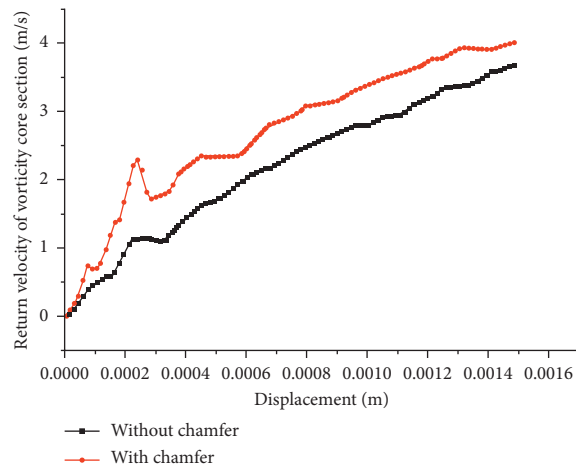
FIGURE 23: Velocity distribution in the reflux zone of vortex center.
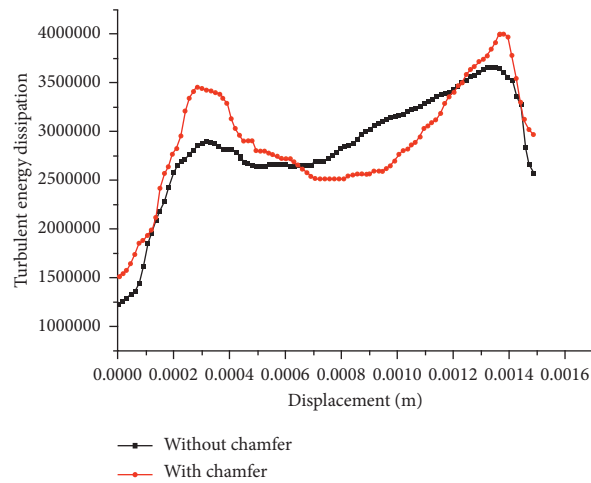
FIGURE 24: Distribution of turbulent kinetic energy at extension of cross section.
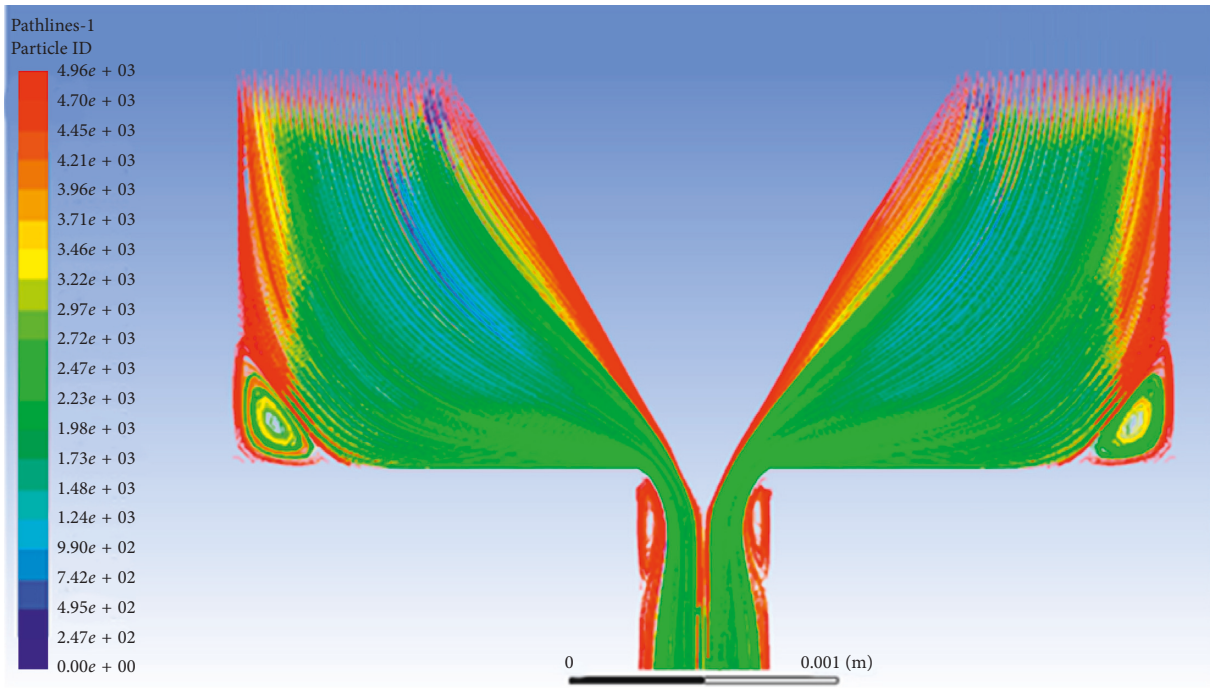
FIGURE 25: Flow streamline when the poppet valve core angle is 60°.
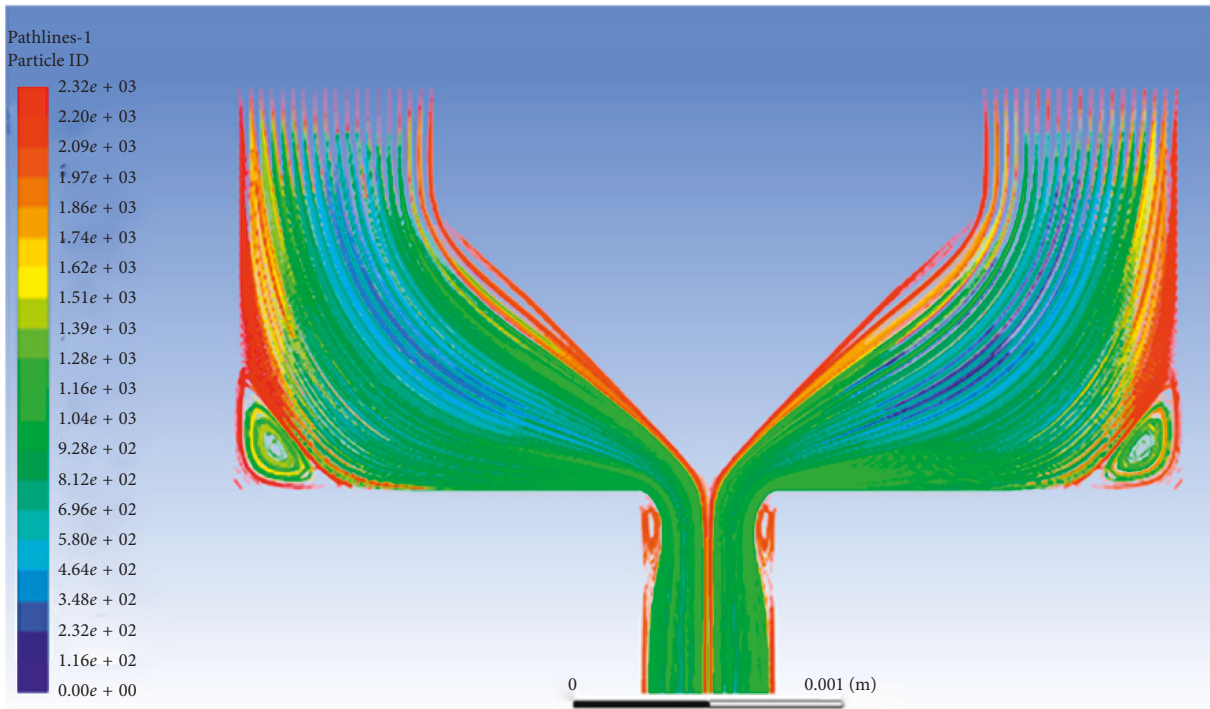
FIGURE 26: Flow streamline when the poppet valve core angle is 90°.

mode, the force on the piston rod in the damper cylinder should be minimal under the situation of maximum allowable displacement. For the minimum displacement mode, the displacement of the piston in the damper cylinder should be minimal under the situation of maximum allowable stress.

The energy dissipation process of the whole system is based on different working modes so as to determine the appropriate buffering pressure value. Here, the buffering pressure value is described with F in Figure 36. The digital hydraulic damper is equipped with speed sensor and
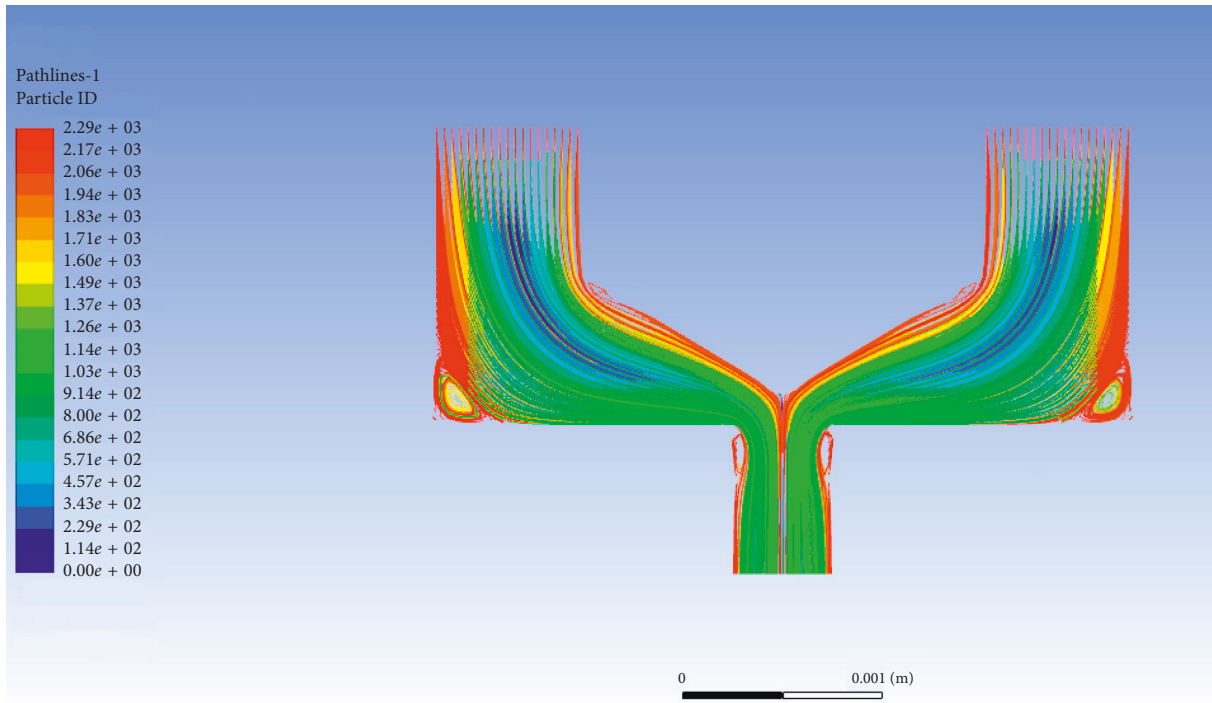
FIGURE 27: Flow streamline when the poppet valve core angle is 120°.
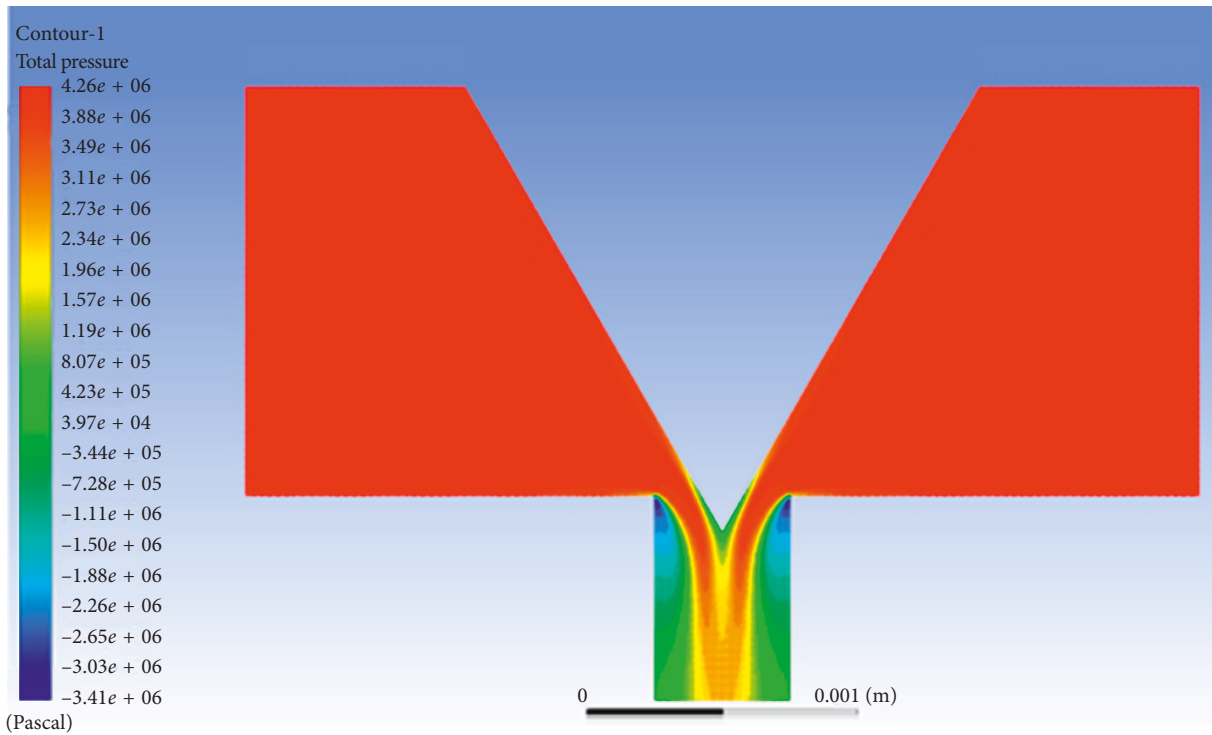
FIGURE 28: Pressure nephogram of a poppet valve core angle of 60°.

pressure sensor that are used to detect the impact velocity and the pressure in the rodless chamber of the damper cylinder, respectively. The speed of the whole moving parts is described with V in Figure 36.

The control process is shown in Figure 36. When the impacting body contacts the piston rod of the digital hydraulic damper, the velocity of the piston, piston rod, and impacting body will be the same. The velocity of the impacting body is
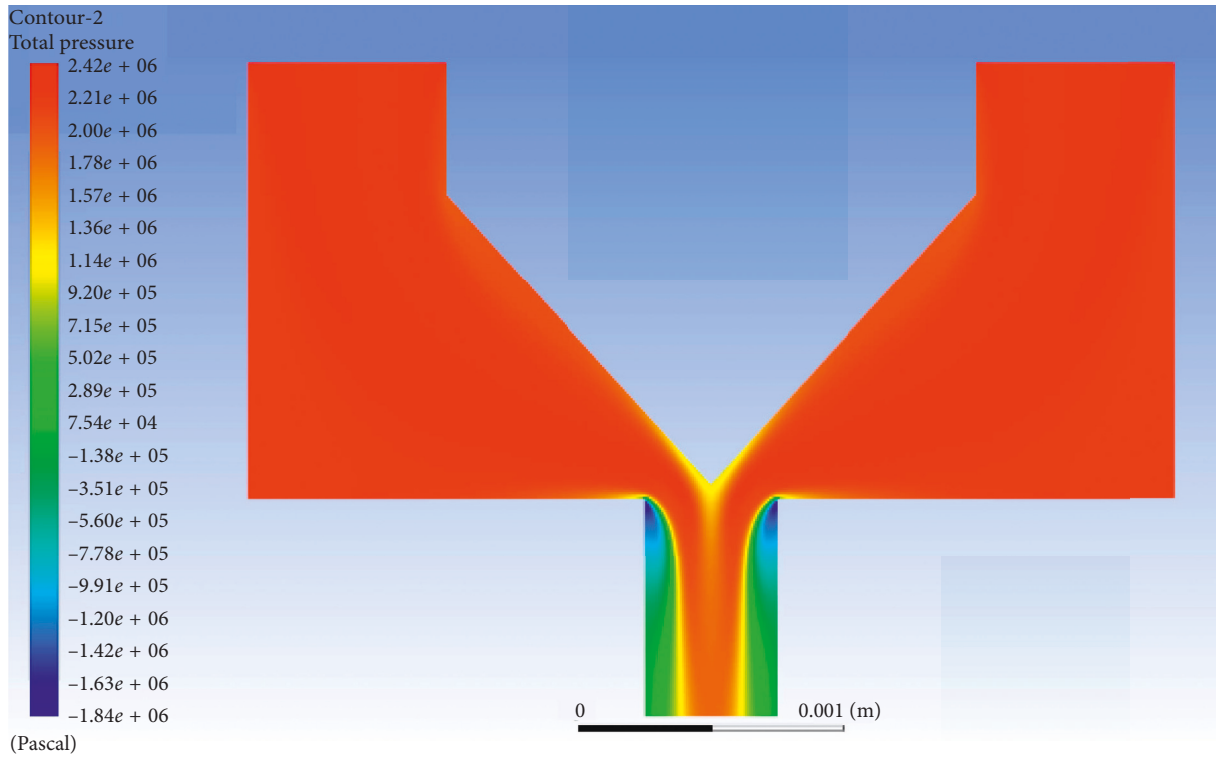
Figure 29: Pressure nephogram of a poppet valve core angle of 90°.
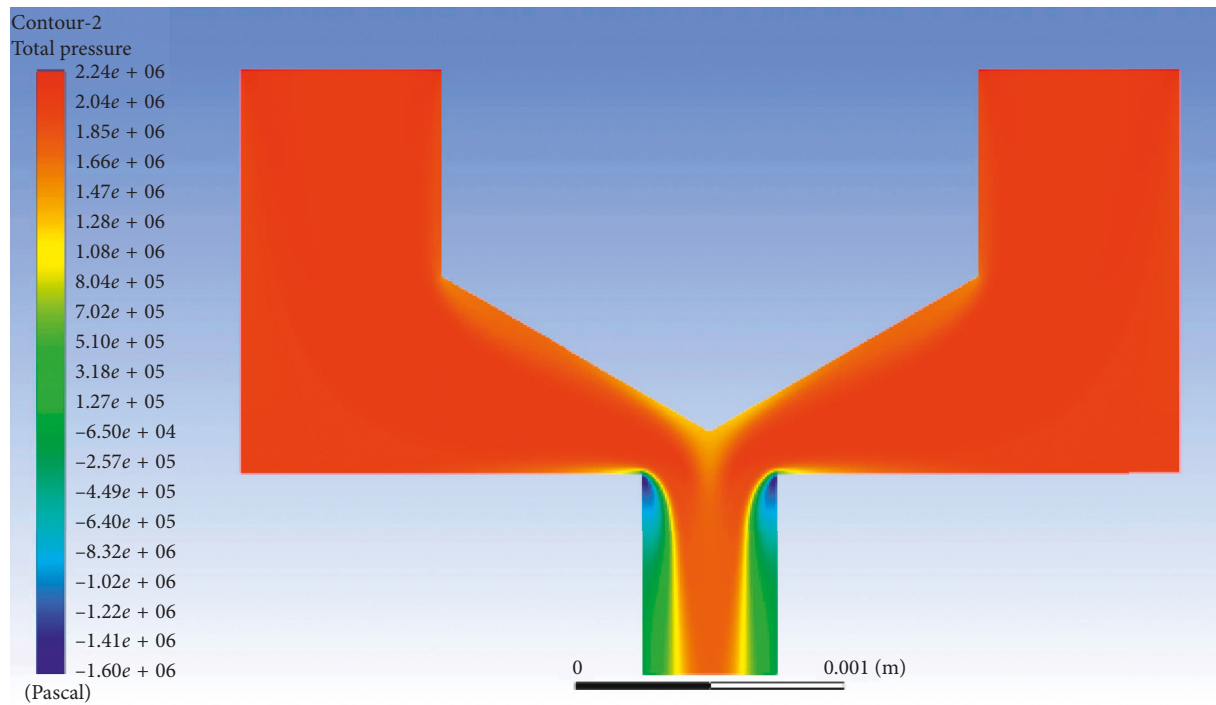
Figure 30: Pressure nephogram of 120° flow field.

detected by the velocity sensor in real time. The pressure of the rodless chamber of the damper cylinder is detected by the pressure sensor in real time. After the averaging value

processing, PWM of the digital damping unit and numbers of the digital damping units are controlled by the digital throttling control algorithm. According to the digital

Contour-1
Turbulent kinetic energy (k)

1.74e + 03
1.65e + 03
1.56e + 03
1.47e + 03
1.39e + 03
1.30e + 03
1.21e + 03
1.13e + 03
1.04e + 03
9.55e + 02
8.58e + 02
7.81e + 02
6.84e + 02
6.08e + 02
5.21e + 02
4.34e + 02
3.48e + 02
2.61e + 02
1.74e + 02
8.74e + 01
6.83e + 01

$[m^2/s^2]$

0   0.001 (m)
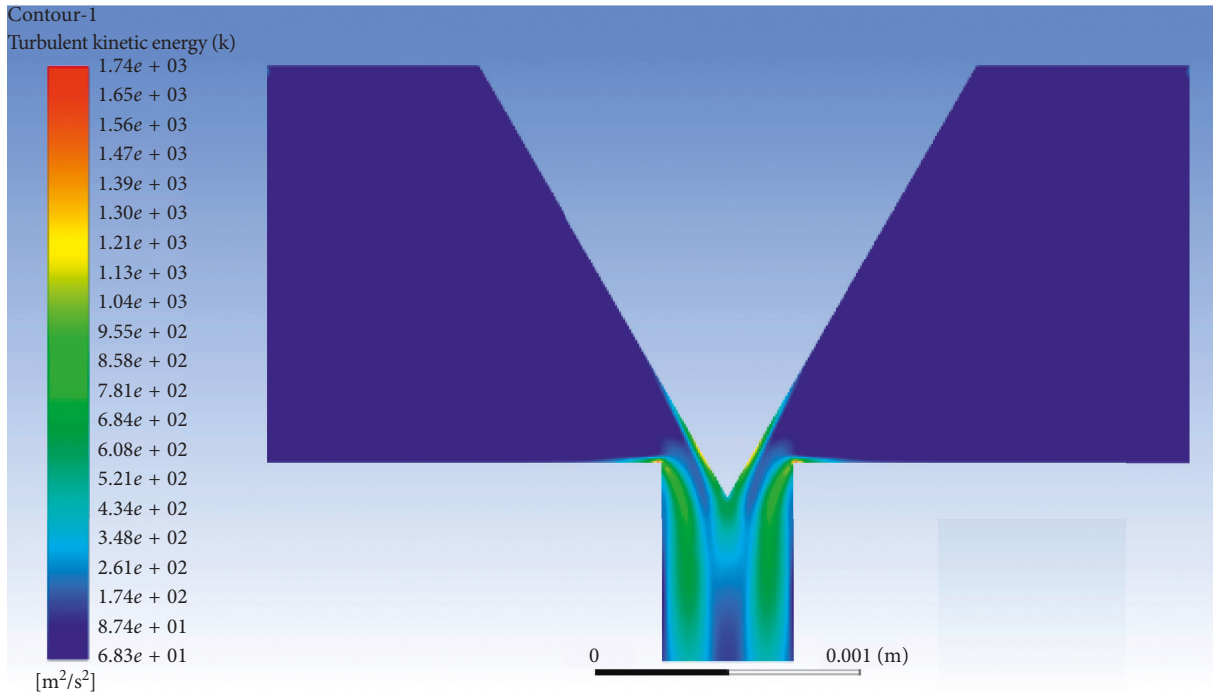
FIGURE 31: Turbulent kinetic energy distribution nephogram of a poppet valve core angle of 60°.

Contour-1
Turbulent kinetic energy (k)

1.24e + 03
1.18e + 03
1.12e + 03
1.05e + 03
9.91e + 02
9.20e + 02
8.68e + 02
8.06e + 02
7.44e + 02
6.82e + 02
6.20e + 02
5.56e + 02
4.96e + 02
4.34e + 02
3.72e + 02
3.10e + 02
2.46e + 02
1.86e + 02
1.25e + 02
6.26e + 02
7.27e − 01

$[m2/s^2]$

0   0.001 (m)
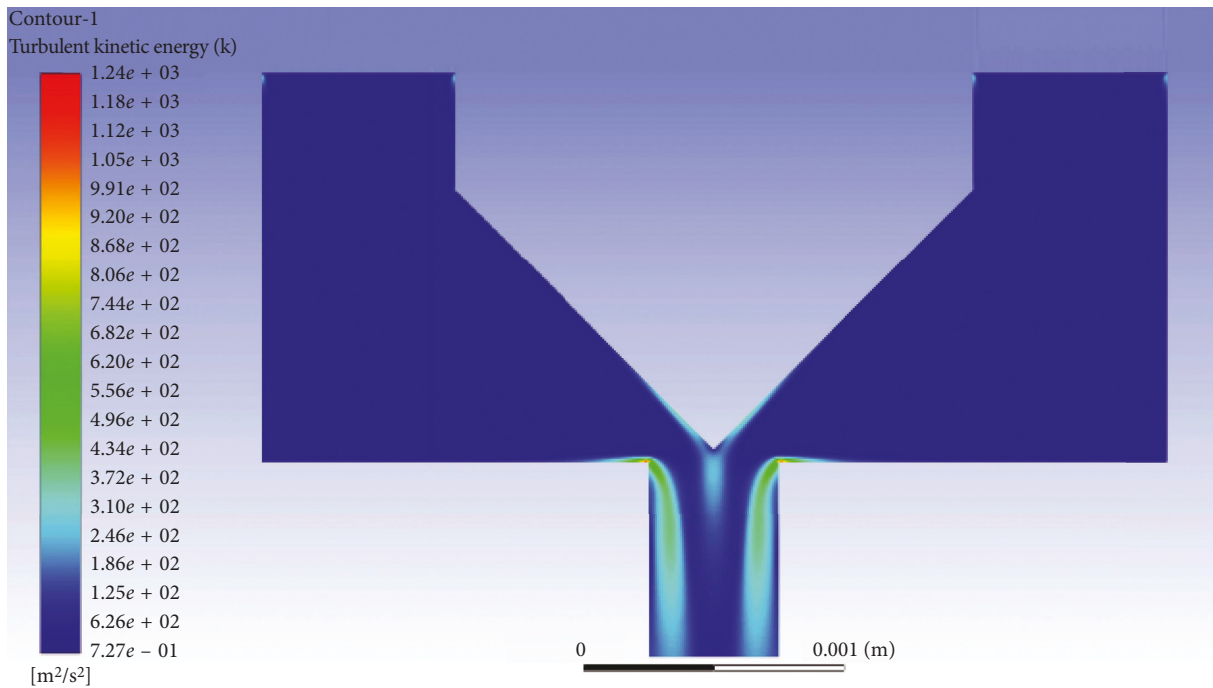
FIGURE 32: Turbulent kinetic energy distribution nephogram (90°).

throttling control algorithm, the throttle area of the device can be adjusted in real time according to the moving situation of the impacting body so as to obtain the best total throttle area. Then, the value of the pressure and the buffering displacement of the digital hydraulic damper can be adjusted so as to achieve the purpose of smooth control and timely buffering.

4. Conclusion

In this paper, the mathematical model of energy losses of digital damper unit and the energy dissipation model of the whole digital damper are established. Based on the energy dissipation model, the energy dissipation mechanism of a
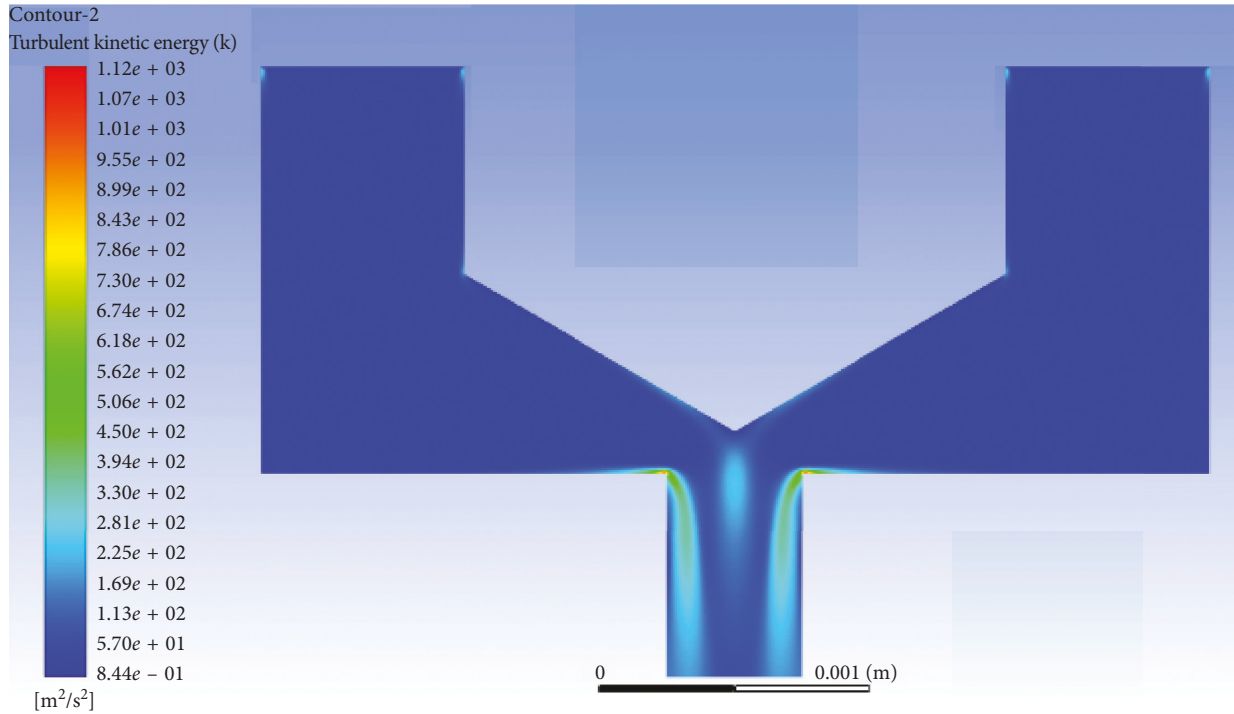
FIGURE 33: Turbulent kinetic energy distribution nephogram (120°).
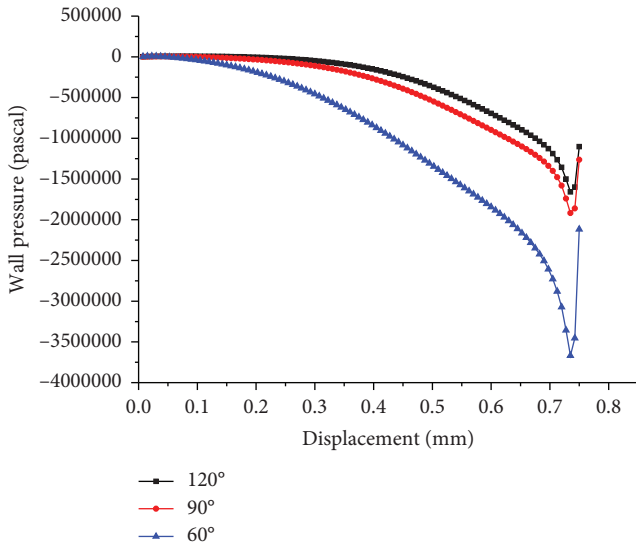
FIGURE 34: Pressure distribution on the wall of poppet valve port.
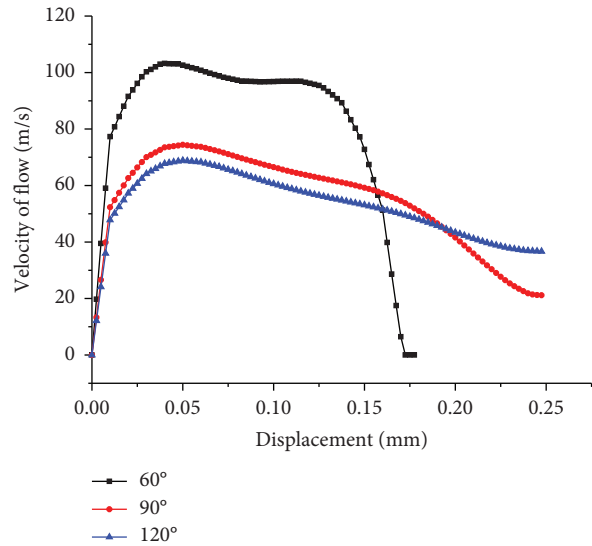
FIGURE 35: Velocity distribution at poppet valve port.

single digital damper unit is studied. The effect on energy losses caused by the three elements of the digital damper, which are local pressure losses at sudden change cross section, frictional pressure losses through the orifice, and local pressure losses through the cone valve port, is analyzed. On the basis of the study of energy dissipation mechanism, the control model of the energy dissipation process is given, which lays a theoretical foundation for the realization of better effect during the buffering process.

In the future works, the effect on energy losses, which is caused by local pressure losses at sudden change cross section, frictional pressure losses through the orifice, and local pressure losses through the cone valve port, will be tested physically by means of a test rig so as to verify the simulation models. An optimized structure of the digital damper unit will be given according to the testing and simulation data, and an optimized energy dissipation control process model will be given.
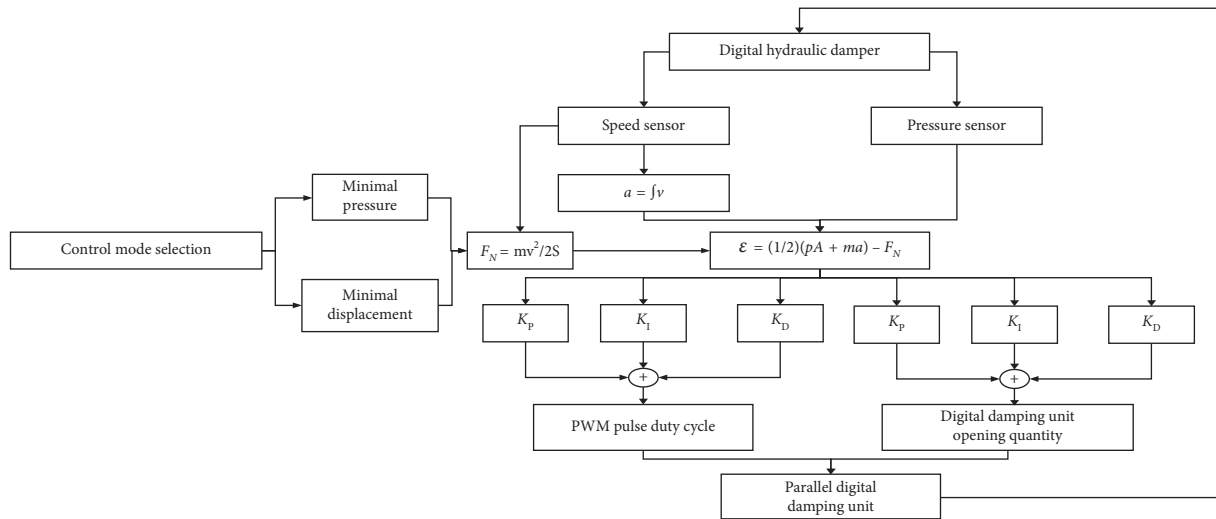
FIGURE 36: Control model of the energy dissipation process.

Data Availability

The data used to support the findings of this study are included within the article.

Conflicts of Interest

The authors declare that they have no conflicts of interest.

Acknowledgments

References

[1] L. Jiang, *Gradual Throttling Hydraulic Absorber Structural Design Optimization and Researchon Dynamic Characteristics*, Shenyang Ligong University, Shenyang, China, 2016.

[2] C. Wang, Z. Qiu, Q. Zeng, and T. Wang, "Design and buffering characteristics study of a porous hydraulic buffer," *Machine Tool and Hydraulics*, vol. 46, no. 9, pp. 93–96, 2018.

[3] P. Wang and G. Shen, "Energy absorption performance of the multi-unit VehicleImpact on clay buffer," *Urban Mass Transit*, vol. 19, no. 6, pp. 80–85, 2016.

[4] M. Qi, *Study on Dynamic Characteristics of Viscoelastic Buffer*, Nanjing University of Science and Technology, Nanjing, China, 2014.

[5] D. Wang, T. Su, H. Wang et al., "The influence of the viscoelatic elastomer damper to the firing accuracy of the large caliber machine gun," *Journal of Ordnance Equipment Engineering*, vol. 38, no. 12, pp. 13–16, 2017.

[6] H. A. O. Baochen, W. Sun, and X. Pan, "Study on the buffer characteristics of artillery hydraulic buffer," *Journal of Ordnance Equipment Engineering*, vol. 39, no. 9, pp. 54–58, 2018.

[7] C.-L. Wang, Z.-W. Qiu, Q.-L. Zeng, Y.-X. Liu, and G.-Y. Miao, "An active-control digital hydraulic damper: design, modeling and simulation," in *Proceedings of the 11th International Fluid Power Conference*, Aachen, Germany, March 2018.

[8] J. I. Hong, X. fu, and H. Yang, "Analysis and calculation on typical shape orifice areas in hydraulic valves," *Machine Tool & Hydraulics*, no. 5, p. 1416, 2003.

[9] J. I. Hong, D.-S. Wang, D. Ding, Z. Tan, and X. Liu, "Calculation method of orifice area of spool valve with notches," *Journal of Lanzhou University of Technology*, vol. 34, no. 3, pp. 48–51, 2008.

[10] J. I. Hong, J. Zhang, D. Wang, W. Zhang, and X. Liu, "Flow coefficient of rectangular notch throttle orifice in spool valve," *Journal of Lanzhou University of Technology*, vol. 36, no. 3, pp. 47–50, 2010.

[11] T. Zhang, Y. Yang, and X. He, "Research on flow coefficient of water hydraulic throttles," *Machine Tool & Hydraulics*, no. 2, pp. 120–122, 2002.

[12] D. Wu, *Modeling and Experimental Evaluation of a Load-Sensing and Pressure Compensated Hydraulic System*, University of Saskatchewan, Saskatoon, Canada, 2003.

[13] D. Wu, R. Burton, and G. Schoenau, "An empirical discharge coefficient model for orifice flow," *International Journal of Fluid Power*, vol. 3, no. 3, pp. 13–19, 2002.

[14] C. Srikanth and C. Bhasker, "Flow analysis in valve with moving grids through CFD techniques," *Advances in Engineering Software*, vol. 40, no. 3, pp. 193–201, 2009.

[15] L. Pace, M. Ferro, F. Fraternale, M. D. Vedova, A. Caimano, and P. Maggiore, "Comparative analysis of a hydraulic servovalve," *International Journal of Fluid Power*, vol. 14, no. 2, pp. 53–62, 2013.

[16] W. Liu, T. Zhang, Y. Xu, and L. Bai, "Analysis on flow field in cone wake flow field," *Journal of Tianjin University (Science and Technology)*, vol. 48, no. 10, pp. 929–936, 2015.

[17] H. Yu, T. Zhang, and W. Xu, "Influence of orifice chamfering on the flow field characteristic of multi-hole orifice flowmeter," *Journal of Electronic Measurement and Instrumentation*, vol. 29, no. 9, pp. 1356–1364, 2015.

[18] D. Gao, *Numerical Simulation and Visualization Study on the Flow Field of Complicated Flow Channel in Hydraulic Techniques*, Yanshan University, Qinghuangdao, China, 2011.

[19] J. Wang, Z. Wu, S. Cen, and X. Wang, "Flow field analysis and structural optimizationof hydraulic poppet valve based on

ANSYS," *Machine Tool & Hydraulics*, vol. 39, no. 13, pp. 128–130, 2011.

[20] X. Fu and X. Du, "Cavitation observation and flow-field analysis of high-speed flowinside throttling groove," *Machine Tool & Hydraulics*, no. 7, pp. 29–31, 2006.

[21] C. Vallet, J. Ferrari, and J. F. Rit, "Single phase CFD inside a water safety valve," in *Proceedings of The Asme2010 Pressure Vessels and Piping Division/K-Pvp Conference*, pp. 335–342, American Society of Mechanical Engineers, Washington, DC, USA, July 2010.

Review Article

Review of Passive Electromagnetic Devices for Vibration Damping and Isolation

Efren Diez-Jimenez [ID],[1] Rocco Rizzo,[2] Maria-Jesus Gómez-García,[3]
and Eduardo Corral-Abad[3]

[1]*Mechanical Engineering Area, Signal Theory and Communications Department Universidad de Alcalá,
 Ctra. Madrid-Barcelona, Km 33,66, Alcalá de Henares 28805, Spain*
[2]*Department of Energy and Systems Engineering, University of Pisa, Largo Lucio Lazzarino, 56122 Pisa, Italy*
[3]*Department of Mechanical Engineering, Universidad Carlos III de Madrid, Leganés, Spain*

Correspondence should be addressed to Efren Diez-Jimenez; efren.diez@uah.es

Passive electromagnetic devices for vibration damping and isolation are becoming a real alternative to traditional mechanical vibration and isolation methods. These types of devices present good damping capacity, lower cost, null power consumption, and higher reliability. In this work, a state-of-the-art review has been done highlighting advantages and drawbacks, application fields, and technology readiness level of most recent developments. In addition, a general introductory section relates presents key considerations that any engineer, electrical or mechanical, needs to know for a deep comprehension and correct design of these types of devices.

1. Introduction

Vibrations generate significant problems and issues in mechanical systems such as fatigue, fracture, and energy loss [1, 2]. Therefore, it is essential to damp the vibrations for overall performance and durability of machines and mechanisms. Performance of new magnetic materials in combination with optimization tools allows the development of efficient and tuneable vibration damping and/or isolation techniques. Moreover, electromagnetic damping and isolation can be clean and environmentally friendly since there is no need of using fluids (except in magneto-rheological dampers). Thus, they can be applied in clean, harsh, and/or extreme temperature environments such as space, aerospace, electric vehicles, or microfabrication industries. As they provide damping through contactless magnetic forces, most friction and wear issues of conventional dampers also disappear, increasing their reliability. Nevertheless, there are still critical issues to be solved like design optimization, performance, cost, device ageing,

reduction of external electromagnetic interferences, or frequency tuning.

In this paper, two different types of electromagnetic damping devices can be found: active and passive. Active devices are those devices that measure vibrations in real time and react accordingly under an active control system decision. Those devices present an outstanding customized performance. However, they require control systems, electric power systems, and sensors that increase the total complexity, price, and energy consumption while decreasing the reliability of the device. On the other hand, passive devices are designed and manufactured to respond in a certain manner against vibration without the need of active feedback and control. They are flexible and can be tuned in design or during assembly, but not during operation. These types of devices have a lower cost and higher reliability at the expense of lower performance under certain vibration variations. In this article, we focus on passive electromagnetic devices for vibration, damping, and isolation (PEDVDI) because of their larger applicability. Main

challenges of PEDVDI are to provide at least the same damping capacity in terms of damping coefficients and stiffness within the same mass, lifetime, and reliability of conventional mechanical dampers, and of course, with a competitive price.

Applications of electromagnetic devices require gathering different engineering disciplines. They are typically designed and manufactured by electrical engineers. Electrical engineers test the devices and provide performance of the device in some general known variables. However, the final applications of the devices which sometimes need specific performance values are typically developed and selected by mechanical engineers. It is thus important to link properly these two fields in order to obtain more efficient and optimized devices.

One of the main objectives of this article is to summarize and show general information of all types of passive electromagnetic devices applied in vibration damping and vibration isolation. PEDVDI have been categorized as follows: eddy current dampers (ECD), electromagnetic shunt dampers (EMSD), magnetic negative-stiffness dampers (MNSD), and passive magnetorheological dampers (PMRD). This provides a wide view of the existing technologies for a proper application selection. A second aim of this article is to collect and present recent and outstanding research articles on passive electromagnetic devices for vibration damping and isolation in civil and mechanical engineering and space applications. A comparison of the performance and application field is given, highlighting its main differences, pros, and cons.

In addition to the technology review part itself, a general introductory section relates main considerations and design key parameters that any engineer, electrical or mechanical, needs to know for a deep comprehension of any PEDVDI performance. Therefore, the article may be used as a design guide for specific applications. Moreover, as it describes the general design for each technology, it can be used as starting point for new designs.

This paper is organized as follows: Section 2 relates to general design considerations of PEDVDI, Section 3 describes the review of the different technologies explored: ECD in Section 3.1, Section 3.2 is the review for EMSD, and Section 3.3 shows the review of MNSD. The papers end with the review of PMRD described in section 3.4. Finally, general conclusions are listed in Section 4.

2. General Design Considerations of Electromagnetic Dampers and Isolators

When designing PEDVDI, three types of materials are mainly used: paramagnetic, soft ferromagnetic, and hard ferromagnetic. Paramagnetic materials are weakly affected by external static magnetic fields. Common paramagnetic materials used in designs are aluminium, copper, titanium, or polymers. However, when selecting paramagnetic materials, their electrical conductivity must be carefully considered, as we will describe later. Even if they are inert to static external magnetic fields, they can severely react to alternant magnetic fields if they are good conductors. If a paramagnetic material is inside a static magnetizing field H, its magnetic polarization M is negligible, acting as if they were air or vacuum.

On the contrary, ferromagnetic materials do react against external magnetic fields H. If an external magnetic field is applied to a ferromagnetic material, it gets magnetized, increasing significantly its volumetric magnetization M, and thus the total magnetic flux density B, i.e., more magnetic field accumulated within the same volume. Magnetic behaviour of the ferromagnetic materials is not linear, but it follows a hysteresis curve (Figure 1).

Based on the value of remanence B_R and coercivity H_C, we can determine whether the sample under study is a hard or a soft magnetic material. Those materials with large remanence and large coercive field are called hard magnetic materials because they are hard to demagnetize. Inversely, soft magnetic materials have very low remanence and low coercive field, and thus they are easily demagnetizable.

Soft magnetic materials have a thin hysteresis curve, so they are typically applied in applications where polarities change very often, such as in transformers and motor windings. Soft magnetic materials can sustain relatively small electrical losses. The hysteresis loop width tells much about the losses. Hard magnetic materials have a very wide hysteresis curve, which makes them practical in applications where they exert their magnetic field on soft magnetic materials. Their slope of demagnetization at the zero line is very shallow and does not steepen until it goes far to the left of the zero line. If hard magnetic materials changed polarity very often, the hysteresis losses would be huge. Hysteresis losses can be used in magnetic dampers as a mechanism to transform and dissipate kinetic energy, as shown in Section 3.4.

General values of electromagnetic properties for different engineering materials are listed in Table 1.

In mechanical engineering applications, we used magnetic materials to exert forces between themselves to provide an output torque like in motors or damping forces as in PEDVDI. Magnetic forces between two magnetic elements depend on the strength and orientation of the magnetic field that element 1 applies on element 2 and on the strength and direction of the magnetization of element 2 [3–6]. The force that element 1 exerts on 2 depends on the gradient of its volumetric magnetization M and on the magnetic field generated by the element 2:

$$\overrightarrow{F_{12}} = \nabla \left(\overrightarrow{m_2} \cdot \overrightarrow{B_{\text{applied by 1}}} \right) = \nabla \left(\overrightarrow{M_2} \cdot \text{Vol}_2 \cdot \mu_0 \cdot \overrightarrow{H_{\text{applied by 1}}} \right). \tag{1}$$

Thus, the larger is its magnetization the larger will be the forces acting on it. Materials with very large magnetization values suffer larger forces under the same external magnetic field. Inside up, materials with very large magnetization generate larger external magnetic fields. Therefore, in first term, the larger is the magnetization of the elements, the larger will be the forces of/on the device. Moreover, the magnetic field strength that a certain element generates in its surroundings is inversely proportional to the cube of distance. Hence, it is very important to approximate magnetic elements as much as possible in order to increase magnetic
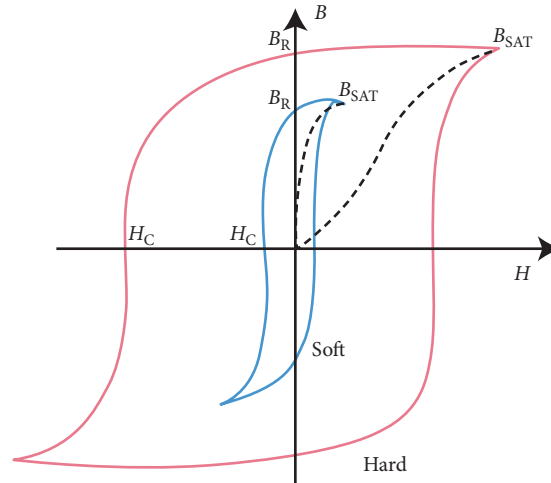
FIGURE 1: Diagram of B–H hysteresis curve for a hard and a soft ferromagnetic material.

TABLE 1: Magnetic properties of different engineering materials.

Material type	Coercivity, bHc (kA/m)	Remanence, Br (T)	Relative permeability	Saturation, bsat (T)
Ferrite magnet	150–250	0.35–0.4	1.2–1.9	0.35–0.4
Alnico magnet	30–151	0.7–1.11	1.2–1.9	0.7–1.2
Neodymium-iron magnet	675–1090	0.87–1.5	1.05	0.87–1.5
Samarium-cobalt magnet	493–790	0.83–1.15	1.05	3000
Iron	0.006–0.080	0.01–0.06	150–2000	1.6–2.15
Nickel	0.056–2.01	0.01–0.15	100–600	0.4–0.6
Cobalt	0.80–71.62	0.02–0.2	70–250	0.7–0.9
Co-Fe alloy (49% Co)	0.07–0.09	0.1–0.3	8000–15000	2.2–2.4
Ni-Fe alloy (75% Ni)	0.001–0.002	0.05–0.2	60000–250000	0.6–0.8
Ni-Fe alloy (50% Ni)	0.005–0.010	0.03–0.15	7000–100000	1.5
Electrical steel	0.032–0.072	0.5–0.8	3000–4000	1.6–2
Stainless steel 304/316	1–3	0.001–0.002	1.003–1.012	0.025–0.03
Stainless steel 430	0.5	0.8	750	1.4
Copper OFCH	—	—	0.99	—
Aluminium 7075	—	—	1.004	—
Titanium grade 5	—	—	1.0001	—
PTFE Teflon	—	—	1	—
Polyimide	—	—	1	—
Nylon	—	—	1	—

forces. Air gaps between moving elements must be always minimized.

There are two main methods to achieve large magnetizations inside a certain volume: nonpermanent magnetization of soft ferromagnetic materials and permanent magnetization of hard ferromagnetic materials. Nonpermanent magnetization is generally obtained through magnetizing fields generated by currents circulating through coils or windings in the device. This option is not affected by other phenomena provided that the current is maintained, so it is a reliable method. Its major issue is that it requires a continuous power consumption and current control.

Permanent magnetization of hard ferromagnetic materials has a main advantage which is that it does not require continuous currents flowing since magnetization is done once in factory. However, other problems must be considered. For example, as the magnetization is permanent,

forces between magnets will always appear even in non-desired orientations, so it is important to analyse the magnetic forces at each of the motion positions. Permanent magnetizations usually have lower flux density on the materials in comparison with fully saturated soft ferromagnetic materials. Permanent magnets, if once fully magnetized, retains magnetism permanently, but its intensity does not remain constant and normally decreases gradually with elapse of time. This change is known as permanent magnet ageing, which is caused either naturally or by external disturbance. The external disturbance mentioned before can be classified into the following four types according to characteristics: magnetic circuit reluctance change, external field application, mechanical shock, and temperature change [7].

For extreme applications like in space or in cryogenic environments, other aspects also affect significantly to

permanent magnetizations. Radiation, as found in space applications, can permanently demagnetize magnets [8]. Therefore, special cares as correct selection of materials, even if they have lower remanence or radiation shielding, must be considered. Temperature also plays a main role when analysing permanent magnetization. For all permanent magnets, increasing temperature means to lose their magnetization. Some materials like SmCo may resist higher temperatures than others, but high temperatures always imply permanent magnetization issues. In contrast, lower temperatures usually increase permanent magnetizations for most of the materials [9, 10]. Nevertheless, at lower temperatures, permanent magnets get more brittle, so applications with very large magnetic forces may need wall reinforcement of magnetic pieces.

As stated, magnetic forces are generated by applying external magnetic fields to magnetized volumes. This surely implies that volumetric magnetization changes, according to the material hysteresis curve. When having permanent magnets in a device, they should be checked for possible demagnetisation caused by external magnetic fields. Normally, only a simple check is needed at the end of the analysis. The check is made accordingly: to find the highest possible temperature inside a magnet and to find the lowest possible field value inside a magnet given by a finite element method (FEM) model. This lowest parametric model values should be treated as average values inside a magnet. Then, by using the BH-curve of the used magnet material, check that the point of the lowest field value is above the knee point (point where magnetizations changes are significant and irreversible) [11].

Another main point to analyse in electromagnetic devices is the eddy current generation and its associated issues and/or benefits. When magnets move through the inner conductor, the moving magnetic field induces an eddy current in the conductor. The flow of electrons in the conductor immediately creates an opposing magnetic field, generating Lorentz forces, which result in damping of the magnet motion and produces heat inside the conductor. The amount of energy transferred to the conductor in the form of heat is equal to change in kinetic energy lost by the magnets.

Power loss due to eddy currents in a conductive sheet per unit of mass can be calculated as

$$P = \frac{\pi^2 \sigma B_p^2 d^2}{6\,D} \cdot f^2, \tag{2}$$

where P is the power lost per unit mass (W/kg), B_p is the moving magnetic field peak (T), d is the sheet thickness (m), σ is the electric conductivity of the conductive sheet (S/m), D is the conductive sheet density (kg/m^3), and f is the oscillation frequency (Hz), or variation, of the applied magnetic field. Thus, power losses depend directly on material conductivity, quadratically with the applied magnetic field on the conductive element and on geometrical dimensions. The component of the magnetic field that affects for the eddy current generation is the one perpendicular to the sheet. This must be considered when designing towards eddy current motion damping.

Equation (3) is valid only under the so-called quasistatic conditions, where magnet motion frequency is not fast enough to generate the skin effect, i.e., the electromagnetic wave fully penetrates into the material. In relation to very fast-changing fields, the magnetic field does not penetrate completely into the material. However, increased frequency of the same field value will always increase eddy currents, even with nonuniform field penetration. The skin depth or penetration depth, δ, is defined as the depth where the current density is just $1/e$ (about 37%) with respect to the value at the surface. Penetration depth for a good conductor can be calculated from the following equation [12]:

$$\delta = \frac{1}{\sqrt{\pi f \mu \sigma}}, \tag{3}$$

where δ is the penetration depth (m), f is the frequency (Hz), μ is the material magnetic permeability (H/m), and σ is the material electrical conductivity (S/m). Penetration depths for different materials are plotted on Figure 2. As design criteria, penetration depth at a certain frequency must be in the same order than the characteristic geometric value of the conductive elements. This allows to maximize eddy current generation and so the damping forces.

Eddy current generation can be linked with mechanical damping. In a viscous damper, mechanical power losses can be expressed as

$$P = F_D \cdot v, \tag{4}$$

where F_D is the damping force and v is the moving mass speed. By linking eddy current power losses and mechanical power losses, we can state that

$$\frac{\pi^2 \sigma B_p^2 d^2}{6\,D} \cdot f^2 = F_D \cdot v. \tag{5}$$

An oscillatory linear motion frequency is directly proportional to linear speed amplitude as $v = A \cdot 2 \cdot \pi \cdot f$, where A is the displacement amplitude. Thus, we can determine that the damping force-speed ratio is a constant c depending on the eddy current electromagnetic behaviour as

$$c_{\text{ed}} = \frac{F_D}{v} = \frac{\sigma B_p^2 d^2}{24\,D \cdot A^2}. \tag{6}$$

Therefore, in order to maximize damping coefficient, several parameters must be optimized. If the magnetic field applied is larger, damping coefficient will increase quadratically. As already stated, maximizing a generated magnetic field can be done by selecting a material with large magnetization and by reducing distances between magnetic field generator magnet and conductive element. By reducing motion amplitude, damping coefficient can also be larger. Opposite considerations must be taken when trying not to damp motion but to allow it smoothly.

Magnetic forces are volumetric forces that depend on the magnetization and magnetic field directions and orientations. Some designs may require forces in radial, tangent or longitudinal directions in order to damp or to transmit forces. However, for most of the cases, only one direction of the forces is required while other two directions must be constraint or locked. If they are not locked, undesired motions can appear. Earnshaw's theorem states that a
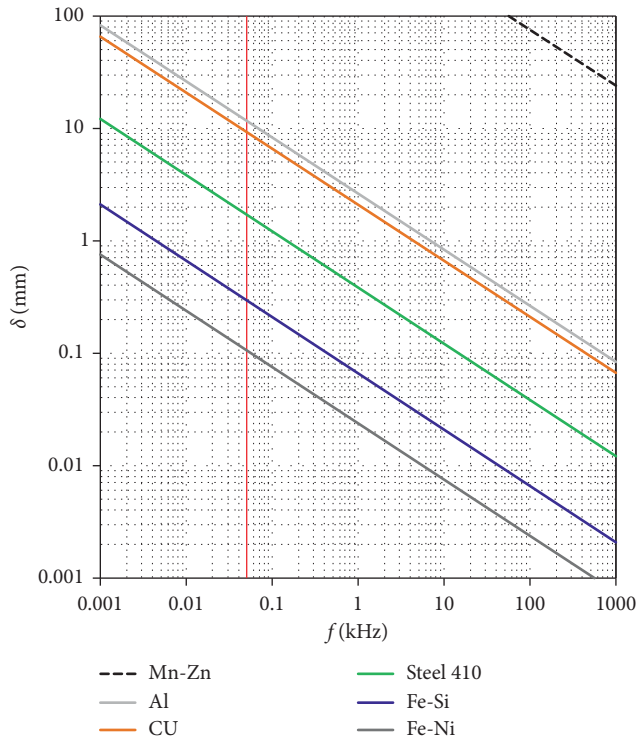
Figure 2: Skin depth vs. frequency for some materials at room temperature; red vertical line denotes 50 Hz frequency [13].

collection of permanent magnets cannot be maintained in a stable stationary equilibrium configuration by themselves, thus mechanical constraints must be included in any device. These mechanical constrains or kinematic pairs generate undesired frictions. Therefore, in order to minimize the loads on these kinematic pairs, symmetrical magnetic configurations and balanced assemblies are highly recommended. This means to include pairs of magnets instead of odd number of magnets with counter directions and symmetrical magnetic mass configurations.

We can summarize some key considerations when designing electromagnetic dampers and isolators as

(i) The larger the magnetization of the elements, the larger will be the forces

(ii) Air gaps between moving elements must be always minimized

(iii) Permanent magnets must be analysed in all their motion positions

(iv) Remanence of permanent magnets is affected by mechanical shocks and external fields

(v) Temperature is also a critical aspect for permanent magnet remanence

(vi) Demagnetization of permanent magnet pair has to be analysed and prevented

(vii) Eddy current damping depends quadratically on applied magnetic field

(viii) Penetration depth at a certain frequency must be analysed in eddy current damping

(ix) Magnetic assemblies have to be symmetric and magnetically balanced, if possible

(x) Simple and standard magnet shapes like cylinders, ring, or blocks on prototypes must be selected.

Along next sections, we will overview different types of PEDVDI analysing their characteristics and constructive properties and also their application fields and performance.

3. Passive Electromagnetic Technologies for Vibration Damping and Isolation

3.1. Eddy Current Dampers. Eddy current dampers (ECDs) are based on the interaction between a nonmagnetic conductive material and a time varying magnetic field in their relative motion. Eddy currents are generated either by movement of the conductive material through a stationary magnet or by strength or position change of the magnetic field source. This induces a magnetic field with opposite polarity to the applied field and a repulsive electromotive force (EMF) which is dependent on the applied field change rate, as shown in Section 2. Due to the conductive material internal resistance, induced currents are dissipated into heat and the energy transformed from the system is removed [14].

General design of an ECD is depicted in Figure 3. It consists of a set of permanent magnets, typically made of NdFeB or SmCo because of their large magnetic quality, which are aligned in front of conductive elements made in aluminium or copper (preferred as its conductivity is the largest). Design and device optimization are currently done through numerical simulations on the magnetic field distribution and eddy current, generally FEM based.

There are three main points to consider during design phase in order to enhance the damping coefficient of an ECD. First is to properly orient permanent magnets poles in respect to the conductive elements. Magnetic field vector components must be perpendicular to the conductive plane as much as possible because eddy currents are generated by those components. However, there are cases where magnet polarization capacity prevents an optimal magnets layout, for example, radial magnetizations could be an optimal choice for cylindrical devices, but radial polarized magnets are not as strong as axial polarized ones yet. Second point is to maximize the magnetic field variation, i.e., to maximize the peak-to-peak value of the applied magnetic field. This maximization can be done by combining reduced air gaps, long displacement variations, large magnetic quality of permanent magnets, and large magnet sizes. An alternative to large magnets could be to assemble more magnets but with reduced sizes. In this way, eddy currents generated per magnet will be smaller but multiplied by the number of magnets. From a certain point, increasing the size of the magnets does not increase the applied magnetic field; therefore, there is an optimized size wherein it is worthier to

(a)

(b)
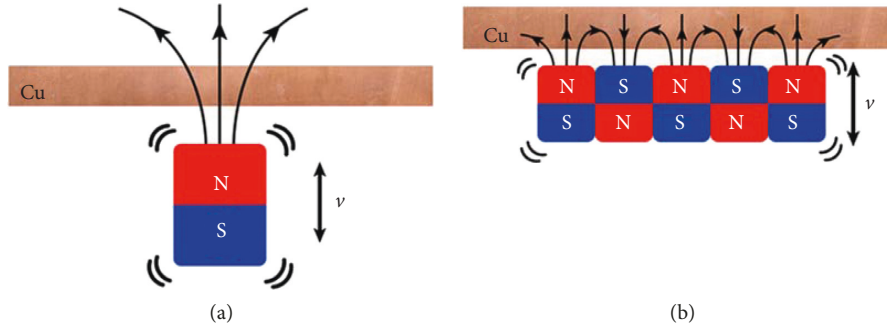
FIGURE 3: ECD common configurations: (a) Single magnet against conductive element. (b) Multipole magnets against conductive element.

add other magnets with alternative polarizations instead of increasing the own magnet size.

Third method, and most relevant, to enhance damping coefficient is to increase cinematically the motion of the permanent magnets towards faster, i.e., larger variation frequency, magnet motions. We consider this method as the most relevant because there are multiple mechanical options to enhance or multiply magnet's motion towards a maximization of the variation of the magnetic field. A common method is to couple a mechanical speed multiplication stage between vibration source and magnets frame. Mechanical speed multiplication selection will depend on the vibration source type of displacement. It has been typically done by using track-pinion elements or lever arms [15] for linear vibration oscillations and planetary speed multipliers for rotational vibrations. This last type of devices is profusely commercialized in aerospace applications [16, 17]. These commercial elements operate at temperature ranging from -40 to $+70°$C, having a significant variation in damping depending on the operational temperature. The variation of damping coefficient with respect to temperature is typically $-0.5\%/°$C. The main disadvantage of using mechanical multipliers is that this part may need maintenance, lubrication, and of course contact, limiting those advantages provided by the eddy current dampers. In addition, mechanical issues like large hysteretic forces or gear backlash prevent their use in low-amplitude vibration damping applications like for microvibrations [18, 19]. To solve those issues, an outstanding and unique eddy current magnetic damper with mechanical multiplication has been proposed and successfully tested [20]. This commercialized device includes an innovative multiplication stage made through linear magnetic gearing instead of mechanical that prevents almost all issues appearing in conventional mechanical multiplication stages while providing excellent results both at room and high temperature environments, with a damping coefficient of 35000 Ns/m for a 19 kg device [21]. This eddy current damper has one of the best specific damping coefficients ever demonstrated, 1842 Ns/m·kg, making it very adequate for cars or aircrafts. Damper tested in [20] has an operational temperature range from -40 to $+250°$C with a very low complexity of its moving parts. The major con is that magnetic parts generates magnetic contamination in its surroundings.

There are multiple research articles related to ECDs. Ahn [22] presents a design procedure of an ECD for a linear

motor motion stage. This device overcomes the disadvantages of the spring type mechanism such as resonance and assembly difficulties due to the spring. However, the design is simple and constraint to the specific linear motor stage. In [23], the eddy current damping is applied in a passive tuned mass damper using a Halbach array of magnets against a copper plate. They demonstrated that plate thickness severely affects the damping coefficient passing from 25 Ns/m for a 4 mm plate thickness to more than 35 Ns/m if the plate is 20 mm for a constant speed. Berardengo et al. [24] presented a new type of adaptive tuned mass damper based on shape memory alloys and eddy current damping. The former element is used to adapt the Eigen frequency of the device, while the latter to tune the damping. Again damping coefficient is highly affected by geometrical parameters and layouts. This can be an advantage during the design process, since it gives flexibility to the designers but it can lead to nondesired performance if some geometric values are modified during assembly or operation.

Besides the studies conducted in the previous references, other applications like in civil engineering, rotors applications, precision instrumentation, robotics, or automotive can also be found. For example, Jo et al. [25] proposed to include ECD in an air-bearing precision stage to improve the vibration isolation characteristics. A Halbach magnet array was devised to increase the density of the magnetic flux of the ECD because a stronger magnetic field generates a greater damping force. In this case, vibrations lower than 100 Hz are damped; however, vibrations above are not damped efficiently. This is explained because ECD damping coefficient decreases with frequency as also found in previous references. ECD can also be found working independently or in combination with tuned mass dampers (TMD) [26, 27] or magnetorheological dampers [28]. In any case, references [22–28] are far from a product-oriented design and they remained just as interesting proof-of-concept prototypes.

The main commercial application field for eddy current dampers is aerospace mechanism where cleanness and reliability are critical requirements. Since it is rather difficult to implement maintenance and the operational environment is severe in aerospace, the damping device should be advanced in long function fatigue life, high reliability, and good applicability in vacuum and heat transformation conditions. Eddy current dampers with instinct natures, such as

noncontact, nonleakage, and easy implementation, become a candidate to suppress vibrations of in the aerospace application system. There are different constructions and designs for ECD depending on the manufacturer. While the design and "temperature factors" may vary from manufacturer to manufacturer, the basic principle of using a high-speed magnetic damper and a gearbox to increase the damping rate and torque capacity is almost universal [29, 30]. Previous studies report rotational eddy current dampers demonstrating damping coefficients ranging between 24 and 1000 Nms/rad. The specific damping coefficient of these devices ranges between 1000 and 2000 Ns/m·kg. Damping coefficient varies with frequency, decaying significantly for greater than 50 Hz frequencies. Therefore, they are adequate for low-frequency damping but not very performant above those frequencies. They both use a single magnet against a copper plate and both they calculate equivalent viscous damping coefficient from hysteresis force-displacement curve.

Other product-oriented applications can also be found. For high-resolution and precision instruments, such as scanning tunnelling microscopy (STM) and atomic force microscopes (AFM), the effective isolation of environmental vibrations plays a key role. Different types of eddy current dampers have been presented and analysed in the literature. A comparison of one- and two-stage spring-suspended systems with magnetic eddy current damping showed acceptable vibration isolation levels [31]. The advantage of using eddy current dampers is avoiding the use of grease-lubricated elements near the probe, which may damage the instrumentation. Most of the recent STM and AFM use magnetic eddy current damping for low-frequency vibration isolation [32, 33]. Typical values of damping coefficient for eddy current dampers applied in instrumentations vary from 0.25 Ns/m to 5 Ns/m. For scientific on-ground instrumentation, specific damping coefficient is not relevant. ECD in [33] was used in the pressure ranges between 10^{-7} Pa and 10^{-9} Pa, showing a significant vibration displacement attenuation going from 50 nm at 16 Hz in the input to just 50 pm at 16 Hz after using ECD. Major pitfall of ECDs in STM and AFM is the magnetic contamination that ECDs may induce in the system and in the samples.

Moreover, active electromagnetic dampers used in automotive vehicle suspension systems have also drawn so much attention in recent years, due to the developments in power electronics, permanent magnet materials, and microelectronic systems. One of the main drawbacks of these electromagnetic dampers is that they are not fail-safe in case of power failure. A passive damping element can make the active electromagnetic dampers fail-safe. ECD has the potential to be used in electromagnetic dampers, providing passive damping for a fail-safe hybrid electromagnetic damper. ECD for automotive applications has demonstrated a damping coefficient 1880 Ns/m for a weight of 3.25 kg [34], which leads to a specific damping density of 578 Ns/m·kg. However, a comparison of the ECD presented in [34] with the off-the-shelf passive dampers reveals that the size and cost of the ECD are higher than those of passive oil dampers. Moreover, the ECD cost is more than twice of a commercial

passive damper, due to the high cost of rare earth magnets. This is why it is essential to optimize the selection of shapes and sizes also for decreasing cost and not only to increase performance, as recommended in Section 2.

On the contrary, ECD has not been widely used for civil engineering applications because its performance remains rather limited due to its low density of energy dissipation. ECD can offer advantages in building vibration damping compared with other damping devices, such as friction damping and viscous fluid damping. A notable advantage is that the eddy current dampers may operate in outdoor under severe temperature conditions. Additionally, there is no fluid inside the damper and the damping generation is independent of friction, potentially increasing eddy current damper longevity and lowering maintenance requirements [35, 36]. In those studies, it was demonstrated that the linear damping assumption in the analytical model is only valid for a limited range of low velocity and this velocity. It is important, thus, to determine the aimed frequency range when designing ECD, because for high frequencies, they are not so performant. However, for large-scale massive structures, the required damping will be of several orders of magnitude larger than that for eddy current dampers applied in mechanisms. It is therefore more practical and economical to apply eddy current dampers as a damping element for a resonant-type absorber or tuned mass damper. The auxiliary mass weights of a TMD are just a small fraction (commonly 0.5–2%) of the controlled modal mass of the primary structure, and the damping required to mitigate the vibration of the auxiliary mass of a TMD is greatly reduced. A ECD optimized for TMD has demonstrated damping coefficients of 321.34 Ns/m, with a mass of 2 kg.

Last but not least, EDC can be found in manufacturing applications [37], specifically in robotic milling. This type of machining has become a new choice for machining of large complex structure parts. However, due to its serial structure, the industrial robot has several limitations such as low stiffness that causes a low accuracy in the machining due to chatter vibrations. In order to mitigate these chatter vibrations, a novel ECD has been designed for vibration suppression in the robotic milling process [38]. The ECD proposed is a multipole set of magnets against a cooper plate oriented to damp two vibrations directions. The damping coefficient measured in this element is 165.6 Ns/m with 0.6 kg mass, which leads to a specific damping coefficient of 276 Ns/m·kg. The results showed that the peaks of the tool tip FRFs caused by the milling tool modes were damped by 22.1% and 12.4% respectively, in the vertical axis, which increase the precision of the milling process and increase the reliability of the tool.

As a conclusion, ECDs can increase the damping property of the structures they are attached to in a broader frequency range over the classic tuned mass dampers. Also, they are clean and temperature resistant and they are not quite sensitive to the change of structural modal frequencies, thus having good robustness. Moreover, ECDs are passive dampers and do not require complex control laws, and therefore they are easy to be implemented. These advantages

make ECDs a good choice for vibration attenuation in mechanical systems.

3.2. Electromagnetic Shunt Dampers.

An electromagnetic shunt damper (EMSD) is essentially an electromagnetic motor/generator that is connected to a shunt circuit (Figure 4), in which the electromagnetic motor converts mechanical oscillation into electrical energy, whereas the shunt circuit design controls the characteristic behaviour of EMSDs [39, 40]. The main features of EMSDs are as follows: easy design, passive control, energy harvesting, and motion multiplication.

Analogy between mechanical and electrical systems allows flexible EMSD designs by adjusting the external electric shunt circuit, which is generally compact in size and allows an easy element replacement. When EMSDs are combined with gear components, as in [41], EMSDs can transform linear motion to rotary motion and provide a great damper force with a small size/weight. In addition, unlike conventional dampers that dissipate kinetic energy into heat, EMSD converts kinetic to electrical energy through the electromechanical coupling effect, where electrical energy can be potentially harvested and reused for other functions if necessary. However, the optimal performance of EMSD is inevitably constrained by the inherent resistance of motor coils and circuit elements (such as inductors and capacitors) in practical applications.

There are two main practical advantages of this passive damper system. First is that the vibration energy is not merely dissipated but it can be reutilized. In [42], researchers demonstrated that by using EMSDs, vibrations were attenuated while energy is transferred to an electric circuit for its use. Secondly, vibration energy transferred to the damper can be transported easily through wires. This permits to locate the dissipation in other places far from the vibration origin. For example, in [43], an EMSD showed that it is capable of isolating the first-order and the third-order vibrations (larger than 80 Hz) far away from the vibration source. In applications where on-place thermal generation is a critical issue, like cryogenic or space applications, having the possibility to select the most adequate dissipation location is an interesting feature. On the other hand, EMSDs present several limitations; for example, the presence of inherent resistance considerably caps the maximum damping and causes the divergence of the damper performance from the design. Moreover, power generation performance of a EMSD working as an energy harvester is limited by resonance excitation as shown in [44]; therefore, other methods as multigenerator methods or multiresonance modes have to be applied. Marinkovic and Koser [45] showed wide bandwidth energy harvested from vibrations by using multigenerator method; however, its damping capacity at frequencies lower than 20 Hz is much reduced, acting as a bandwidth pass filter. Multiresonance mode method was used in [46] showing a device with 2 degrees of freedom that has two resonant peaks which may be tuned independently maintaining fairly uniform power output over a frequency range.
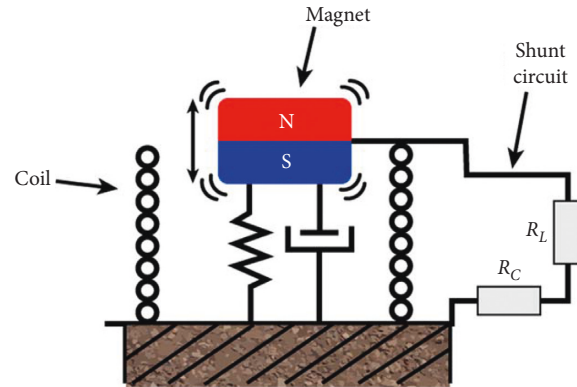
FIGURE 4: EMSD common configuration: a permanent magnet oscillates along a coil generating electricity from the vibration damping. This electricity is then reoriented to a load resistance to be dissipated externally or to be used or accumulated for other applications.

Main application fields for EMSDs are microvibration [47], low-frequency energy harvesting [48–52], mostly for microelectronics applications, and regenerative shock absorbers mostly for vehicle applications [53–57]. Other applications like human motion energy harvesting or combined with tuned mass absorbers [58–60] can be also found. In any case, all the developments found are limited to the laboratory demonstrator or applications and far from its extensive commercialization.

Recent studies for EMSDs applied as microelectronics energy harvesting are divided into three groups according to their objectives and approaches. The main point is to reduce the harvester resonant frequency in order to collect low-frequency vibration energy from the environment. Also, broadening current technology harvester bandwidth to increase the utilization of the random vibration energy is sought [61]. It is impossible to make a perfect harvester with low resonant frequency, wide frequency band, and good output performances at the same time.

In [62], power harvesting is simply achieved from relative oscillation between a permanent magnet allowed to move freely inside a tube-carrying electrical coil with two-end stoppers and directly connected to the vibration source. The proposed harvester with free/impact motion shows a nonresonant behaviour in which the output power continuously increases with the input frequency and/or amplitude. In addition, the allowable free motion permits significant power harvesting at low frequencies. Hence, proposed harvester is well suited for applications involved in variable large amplitude-low-frequency vibrations such as human-powered devices. Another example of nonresonant magnetomechanical low-frequency vibration energy harvester can be found in [63]. In this article, energy harvester converts vibrations into electric charge using a guided levitated magnet oscillating inside a multiturn coil that is fixed around energy harvesters exterior. In this case, the fabricated energy harvester is hand-held and the prototype generates a normalized power density of approximately $0.133 \, \text{mW/cm}^3 \, \text{g}^2$ at 15.5 Hz.

Regenerative shock absorbers are based on electromagnetic rotary or linear motors connected to a shunt resistance operating as generators. Motors are linked to the vibration source directly or through a mechanical multiplication stage as for eddy current dampers. Three drive modes of the regenerative shock absorber systems can be found: direct drive mode, indirect drive mode, and hybrid drive mode [64]. The direct drive system has attracted substantial amount of interests due to its compact design and simple manufacturing. The direct drive mode directly connects vibration source to magnet stator to generate electricity. Direct drive regenerative shock absorbers provide damping coefficient between 1500 and 2000 Ns/m.

Microvibration on board a spacecraft is an important issue that affects payloads requiring high pointing accuracy. Although isolators have been extensively studied and implemented to tackle this issue, their application is far from being ideal due to the several drawbacks that they have, such as limited low-frequency attenuation for passive systems or high power consumption and reliability issues for active systems. In [65], a novel 2-collinear-DoF strut with embedded electromagnetic shunt dampers (EMSD) is modeled and analysed and the concept is physically tested. The combination of high-inductance components and negative-resistance circuits is used in the two shunt circuits to improve EMSD microvibration mitigation and to achieve an overall strut damping performance that is characterised by the elimination of the resonance peaks. EMSD operates without requiring any control algorithm and can be comfortably integrated on a satellite due to the low power required, the simplified electronics, and the small mass.

EMSDs demonstrate a unique feature when handling the damped vibration energy because it can be transported and/or stored as electrical energy. This makes EMSDs a very interesting type of dampers for microelectronics and vehicle applications. However, their wide implementation in industry has been limited by their low specific damping capacity as well as by the fact the performance is highly dependent on the vibration frequency.

3.3. Magnetic Negative-Stiffness Dampers.

Negative-stiffness elements have been identified as unique mechanisms for enhancing acoustical and vibrational damping. Examples of negative-stiffness mechanisms include mechanical systems with negative spring constants and materials with negative moduli [66–69]. Negative-stiffness elements contribute to damping behaviour because they tend to assist rather than resist deformation as a result of internally stored energy [70]. Negative-stiffness isolators employ a unique and completely new mechanical concept in low-frequency vibration isolation. Vertical-motion isolation is provided by a stiff spring that supports a weight load, combined with a negative-stiffness structure. The net vertical stiffness is made very low without affecting the static load-supporting capability of the spring. Reducing the net vertical stiffness implies that resonant frequency is highly reduced since resonant frequency is proportional to the root square of the stiffness.

Generally, negative-stiffness spring is made by two bars hinged at the centre, supported at their outer ends on pivots, and loaded in compression by compressive forces [69, 71–73]. Both bars are brought to almost buckling operation point. The equilibrium positions of the buckled beam correspond to local minimum and maximum of the strain energy curve. Since the beam stiffness corresponds to the spatial derivative of its strain energy, the buckled beam exhibits negative stiffness over a certain interval [74].

Permanent magnets are an easy and reliable way of obtaining negative-stiffness springs. By using magnets poles, it is possible to tune operation range where the stiffness becomes negative [75]. A common setup is to locate magnets in unstable equilibrium point by facing equal poles, north against north and south against south, as shown in Figure 5(a). In this way, magnet repulsion will act with negative stiffness for displacements above and below the preload equilibrium point, compensating coil spring positive stiffness of the and thus, minimizing effective stiffness in the operation point (Figure 5(b)). By minimizing dynamic stiffness, the resonance frequency is lower and therefore, vibration damping capacity in higher frequencies is enhanced.

The main advantage of negative-stiffness dampers is that the resonance frequency is lower; therefore, it is very suitable not only for low-frequency vibration damping but also to enhance damping in higher frequencies significantly. By using magnetic negative springs, the system can be more reliable and long-lasting since one of the main problems of mechanical negative springs is the fatigue of the structures. Magnets will not suffer from fatigue or permanent plastic deformation; therefore, creating negative springs through magnetic forces is worthwhile. Application fields for magnetic negative-stiffness dampers (MNSD) are the same as those for negative-stiffness dampers made with structural elements: precision manufacturing, optical and scientific instrumentation, vehicles seat, and rotary machinery.

Among the most interesting developments, we found a magnetic vibration isolator with the feature of high-static-low-dynamic stiffness which is developed in [76, 77]. The device was constructed by combining a magnetic negative-stiffness spring with a spiral flexure spring for static load support. The magnetic spring comprised three magnetic rings configured in attraction, and it was used to reduce the resonant frequency of the isolator. Experimental results demonstrated that the magnetic negative-stiffness spring can reduce the resonant frequency in more than a half while it can expand the isolation frequency band.

Two novel designs of negative-stiffness dampers based on magnetism were designed, optimized, manufactured, and tested in [78, 79]. The two designs from those studies can efficiently integrate negative stiffness and eddy current damping in a simple and compact design. The proof-of-concept experiments were conducted through the scaled prototypes cyclic loading on a vibration machine. Nonlinearity in negative stiffness was observed in both configurations. Nonlinear problems in the vibratory system are hard to solve analytically, and many efforts have been

(a)

(b)
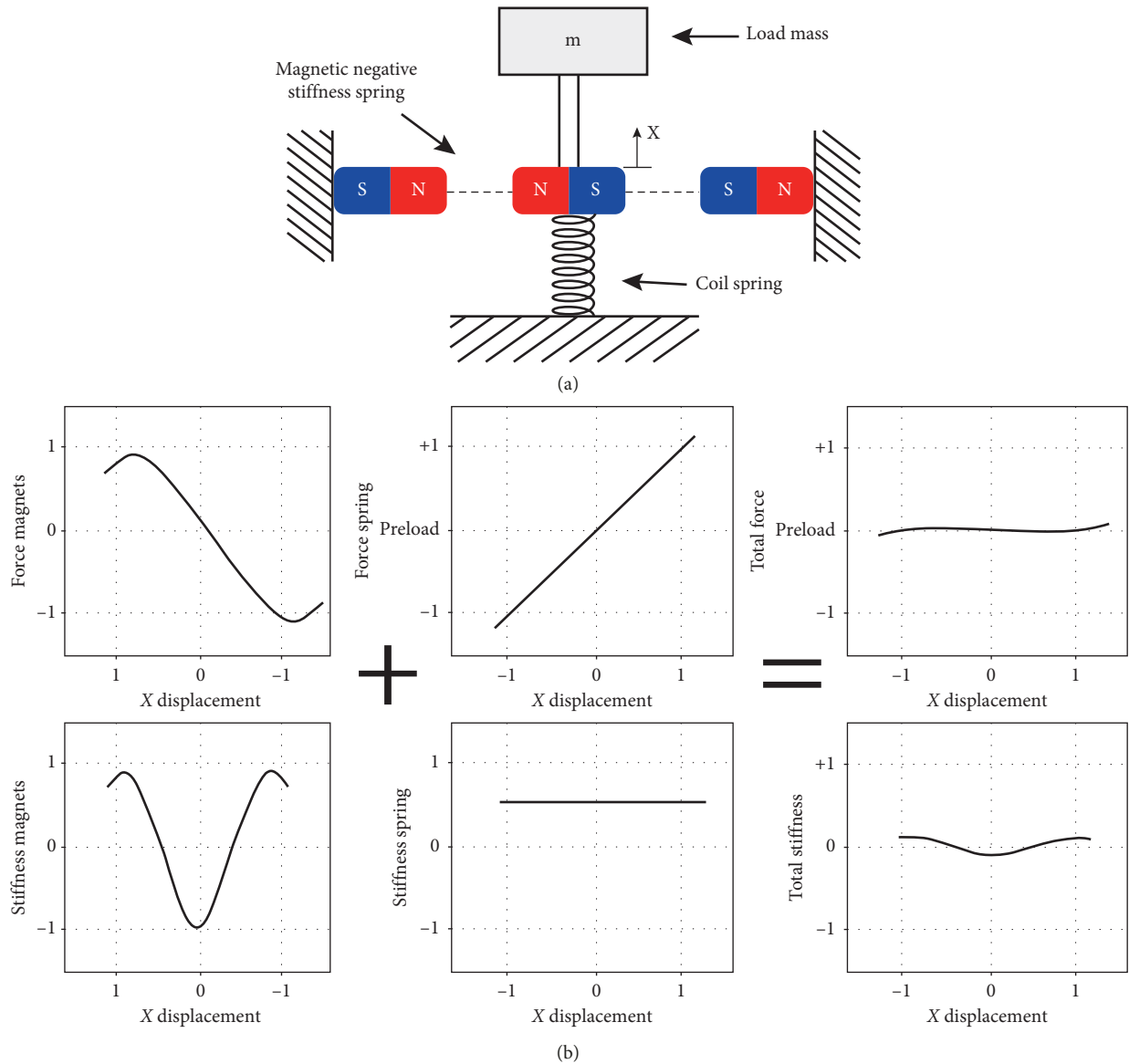
Figure 5: (a) Magnetic negative-stiffness spring configuration with coil spring for static forces. (b) Normalized forces and stiffness against normalized displacements for magnetic spring, coil spring, and its addition.

devoted to its solution [80–82]. Designs in [78, 79] exhibited the hardening and softening patterns of negative stiffness, respectively, with increasing displacement. Compared with the existing designs of negative-stiffness systems, unique features of the proposed designs include symmetrical negative-stiffness behaviour; integrated damping characteristic; and a compact design that can be installed in any direction. Proposed designs have a great potential to replace semiactive or active dampers in diverse vibration suppression or isolation applications.

To suppress rotor systems vibration, a vibration absorber combining together negative stiffness and positive stiffness is proposed in [83]. Firstly, the magnetic negative-stiffness producing mechanism using ring-type permanent magnets is presented and negative-stiffness characteristics are analysed. Then, absorber-rotor system principles and

nonlinear dynamic characteristics are studied numerically. Experiments are carried out to verify the numerical conclusions. The results show that the proposed vibration absorber is effective in order to suppress the rotor system vibration, the negative-stiffness nonlinearity affects the vibration suppression effect, and the negative stiffness can broaden the effective vibration control frequency range of the absorber.

A special application of magnetic negative-stiffness dampers has been found to isolate low-frequency seismic noise from the ground in the fields such as gravitational wave detecting [84, 85]. The ultra-low-frequency isolator is made by a magnetic spring composed of a pair of ring magnets in parallel with the conventional pendulum. The magnetic spring can produce magnetic torque to cancel the gravitational torque of the pendulum and hence to reduce
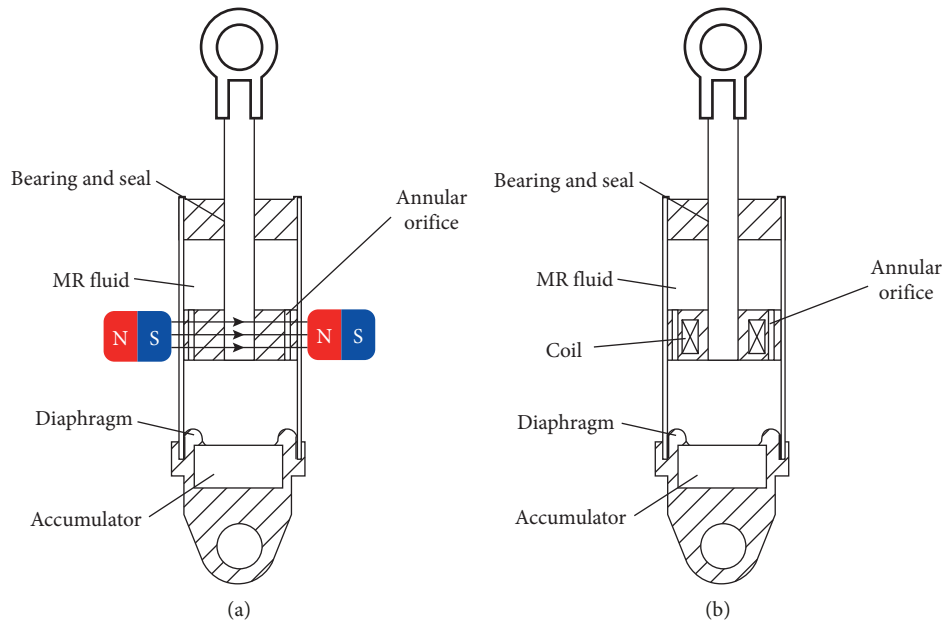
FIGURE 6: Permanent magnet-based magnetorheological damper (a) compared with active magnetorheological damper (b).

the resonance frequency. In this case, resonance frequency can be up to ten times lower, hence multiplying low-frequency vibration damping capacity.

MNSD can significantly decrease the resonance frequency while keeping the same static load capacity, therefore enhancing vibration damping capacity in higher frequencies.

3.4. Permanent Magnet-Based Magnetorheological Dampers. Similar to passive hydraulic dampers, a magnetorheological (MR) damper consists of a fluid that moves between different chambers via small orifices in the piston, converting "shock" energy into heat. However, in an MR damper, an electrical circuit is introduced in the piston assembly. As electrical current is supplied to the damper, a coil inside the piston creates a magnetic field and instantaneously changes the properties of the MR fluid in the piston annular orifice. Consequently, the dampers resistance can be continuously changed in real time by modulating the electrical current to the damper. Magnetorheological dampers are typically active elements since they need current circulating through the coils in order to generate the magnetic field [86–90]. This goes against passive devices benefits promoted in this article, so in this section, we will only focus on a passive special type of MR damper which is the permanent magnet-based MR dampers (PMRD).

Electromagnetic coils to generate the magnetic field intensity from the input current activate most of the proposed or developed MR dampers. So, to obtain the desired damping force, various control-related devices such as current amplifiers, signal converters, and signal processors are absolutely required. Furthermore, coil and wire modules of the current make the damper structure more complicated and difficult to assemble. In order to improve the commercial feasibility, self-powered MR dampers have been developed featuring energy harvesting by piston movement.

However, they are not convincing powerless options. In this sense, in PMRD, damping force is tuned by a permanent magnet instead of electromagnetic coil circuits typically used to drive MR dampers [91]. PMRD consists of a ferromagnetic piston that is magnetically activated through a permanent magnet external motion (Figure 6). Damping force variation of PMRD is realized by the magnetization area or magnet flux dispersion variation, not by the input current magnitude. Thus, the PMRD input variable is totally different from the conventional MR damper.

The major advantage of PMRD is the specific damping coefficient magnitude since they can reach values as high as oil viscous dampers while keeping a tuning capacity of their performance. In comparison, with active MR dampers, the reduced power consumption is the second main benefit when PMRD was chosen for certain applications. The main drawback for this kind of devices is that most of them need magnetorheological fluid for its operation, eliminating all the benefits associated to oil-free devices, for example, cleanness, maintenance free, and reliability. In fact, PMRD are hybrid devices between oil dampers and PEDVDI. The fields of application for this type of device are mainly automotive elements like dampers [92], clutches [93, 94], or brakes [95] and also prosthetic mechanical systems. However, most of studies found in the literature are still laboratory prototypes, and as far as we are concerned, there is no commercialized device based on this technology.

A novel type of tunable magnetorheological PMRD damper based only on the location of a permanent magnet incorporated into the piston was designed, built, and tested in [96]. It was observed that the damping force reached up to 390 N according to the piston location. The maximum damping coefficient is 21428 Ns/m for an estimated mass of 1 kg. To reduce the nonlinearity of on the magnet location, a modified structure of the sidebar was utilized in the piston. It

Table 2: Summary and main conclusions of PEDVDI review.

Type	Fields of application	Advantages	Drawbacks
ECD	Aerospace, civil engineering, precision instrumentation, robotics, and automotive	Contactless damping, best specific damping coefficient, cleanness, temperature resistant	Magnetic contamination and heat generation
EMSD	Microvibration and low-frequency energy harvesting	Dissipation transportable and energy harvesting	Performance restricted to resonance frequency
MNSD	Precision manufacturing, optical and scientific instrumentation, vehicles seat, and rotary machinery	Reduced resonance frequency, enhancement of damping at higher frequencies, and easy manufactory, reliability	No direct damping capacity
PMRD	Automotive elements like dampers, clutches, or brakes	High specific damping coefficient	Oil contamination

Type	Characteristic parameters	Development level
ECD	Damping coefficient from 1 to 35000 Ns/m; specific damping coefficient between 1000 and 2000 Ns/m·kg	Commercialized products
EMSD	Damping coefficient from 1 to 10000 Ns/m; energy harvesting density from 0.1 to 10 mW/cm^3	Laboratory demonstrator
MNSD	Reduced resonance frequency up to ten times	Laboratory demonstrator
PMRD	Damping coefficient from 1 to 50000 Ns/m; specific damping coefficient between 10000 and 20000 Ns/m·kg	Laboratory demonstrator

was experimentally shown that a linear variation of the damping force can be obtained based on the sidebars curved shape. It was also reported in a previous study on this damper that its response time is relatively slow compared with a conventional MR damper using an electromagnetic coil [97]. It should be remarked that the damping force can decrease a lot, perhaps due to the slow response time of the magnet when the excitation frequency is increased.

Sato [98] presents a power-saving magnetizing device for magnetorheological fluids. This device encompasses a permanent magnet for magnetizing the device, instead of an electromagnet that consumes electric power. The permanent magnet applies a magnetic field to the device through a specially designed magnetic yoke. The field intensity can be controlled by moving the magnet. When the magnetic field is controlled by a permanent magnet, thrust that attracts the magnet into the yoke normally acts on the magnet and consumes the power holding and moving the magnet.

As stated, PMRD has also been oriented for its applications in prosthetics. The development presented in [99] is a special damper mechanism proposed to make a prosthetic leg which can derive from on mode to off by using permanent magnet only. The mechanism design is undertaken, and the damping force is analysed in order to validate the effectiveness of the proposed damper system for the patient's motion without the control device. The system can provide up to 1500 Ns/m when it is "on" while the "off" damping coefficient is not larger than 55 Ns/m, demonstrating a very high variation capacity given by the permanent-based actuation.

PRMDs are hybrid devices combining the high specific damping capacity of oil dampers with the electromagnetic damping modulation capacity. The main drawback for this type of devices is that they need magnetorheological fluid for its operation, eliminating all the benefits associated to oil-free devices, for example, cleanness, maintenance free, and reliability.

4. Conclusion

Passive electromagnetic devices for vibration damping and isolation are becoming a real alternative to traditional mechanical vibration and isolation methods. Passive devices are designed and manufactured to respond in a certain manner against vibration without the need of active feedback and control. These types of devices present good damping capacity, lower cost, null power consumption, and higher reliability.

We have presented e a general description of all types of passive electromagnetic devices applied in vibration damping and vibration isolation. Those devices have been categorized as follows: eddy current damper (ECD), electromagnetic shunt damper (EMSD), magnetic negative-stiffness damper (MNSD), and passive magnetorheological damper (PMRD). We have analysed their topologies and pros and cons in the fields of applications, and we have given some characteristic parameter values. All this information has been summarized in Table 2 (advantages and drawbacks are described comparatively with other types of PEDVDI).

In addition to the technology review part itself, a general introductory section relates main considerations and design key parameters that any engineer, electrical or mechanical, needs to know for a deep comprehension of any PEDVDI performance.

Therefore, the article may be also used as a design guide for specific applications. Moreover, as it describes the general design for each technology, it can be used as a starting point for new designs. A practical list of key considerations when designing electromagnetic dampers and isolators is given in the general design considerations of electromagnetic dampers and isolator section.

Conflicts of Interest

The authors declare that they have no conflicts of interest.

Acknowledgments

References

[1] R. Palomera-Arias, *Passive Electromagnetic Damping Device for Motion Control of Building Structures*, Massachusetts Institute of Technology, Cambridge, MA, USA, 2005.

[2] N. Z. Meymian, N. Clark, J. Subramanian et al., *Quantification of Windage and Vibrational Losses in Flexure Springs of a One Kw Two-Stroke Free Piston Linear Engine Alternator*, SAE Technical Paper Series, PA, USA, 2019.

[3] I. Valiente-Blanco, E. Diez-Jimenez, and J.-L. Pérez-Díaz, "Alignment effect between a magnet over a superconductor cylinder in the Meissner state," *Journal of Applied Physics*, vol. 109, no. 7, article 07E704, 2011.

[4] E. Diez-Jimenez, J.-L. Perez-Diaz, and J. C. Garcia-Prada, "Local model for magnet–superconductor mechanical interaction: experimental verification," *Journal of Applied Physics*, vol. 109, no. 6, article 063901, 2011.

[5] E. Diez-Jimenez, J. L. Perez-Diaz, and J. C. Garcia-Prada, "Mechanical method for experimental determination of the first penetration field in high-temperature superconductors," *IEEE Transactions on Applied Superconductivity*, vol. 22, no. 5, article 9003106, 2011.

[6] J.-L. Pérez-Díaz, J. C. García-Prada, E. Díez-Jiménez et al., "Non-contact linear slider for cryogenic environment," *Mechanism and Machine Theory*, vol. 49, no. 7, pp. 308–314, 2012.

[7] N. Makino and M. Mishima, "Ageing of permanent magnet," *Journal of the Instrument Technology*, vol. 7, no. 1, pp. 22–27, 1957.

[8] A. Samin, M. Kurth, and L. R. Cao, "An analysis of radiation effects on NdFeB permanent magnets," *Nuclear Instruments and Methods in Physics Research Section B: Beam Interactions with Materials and Atoms*, vol. 342, pp. 200–205, 2015.

[9] E. Diez-Jimenez, J. L. Perez-Diaz, C. Ferdeghini et al., "Magnetic and morphological characterization of Nd2Fe14B magnets with different quality grades at low temperature 5–300 K," *Journal of Magnetism and Magnetic Materials*, vol. 451, pp. 549–553, 2018.

[10] E. Diez-Jimenez, J. L. Perez-Diaz, F. Canepa, and C. Ferdeghini, "Invariance of the magnetization axis under spin reorientation transitions in polycrystalline magnets of

Nd2Fe14B," *Journal of Applied Physics*, vol. 112, no. 6, article 063918, 2012.

[11] S. Ruoho, *Demagnetisation of Permanent Magnets in Electrical Machines*, Helsinki University of Technology, Espoo, Finland, 2006.

[12] R. Wangsness, *Electromagnetic Fields*, Wiley, Hoboken, NJ, USA, 2007.

[13] Zureks, "Skin effect," Wikipedia, 2019.

[14] J.-S. Bae, J.-H. Hwang, J.-S. Park, and D.-G. Kwag, "Modeling and experiments on eddy current damping caused by a permanent magnet in a conductive tube," *Journal of Mechanical Science and Technology*, vol. 23, no. 11, pp. 3024–3035, 2010.

[15] C. Yilmaz and N. Kikuchi, "Analysis and design of passive band-stop filter-type vibration isolators for low-frequency applications," *Journal of Sound and Vibration*, vol. 291, no. 3–5, pp. 1004–1028, 2006.

[16] Avior Control Technologies Inc, *Durango Eddy Current Damper Product Catalog*, Avior Control Technologies Inc, Longmont, CO, USA, 2019.

[17] CDA-InterCorp, *Eddy Current Damper Application Data Catalog*, CDA-InterCorp, MA, USA, 2019.

[18] J. L. Pérez-Díaz, I. Valiente-Blanco, C. Cristache, and E. Díez-Jiménez, *Enhanced Magnetic Vibration Damper with Mechanical Impedance Matching*, WIPO, Geneva, Switzerland, 2015.

[19] J. Pérez-Díaz, I. Valiente-Blanco, and C. Cristache, "Z-Damper: a new paradigm for attenuation of vibrations," *Machines*, vol. 4, no. 2, p. 12, 2016.

[20] I. Valiente-Blanco, C. Cristache, J. Sanchez-Garcia-Casarrubios, F. Rodriguez-Celis, and J.-L. Perez-Diaz, "Mechanical impedance matching using a magnetic linear gear," *Shock and Vibration*, vol. 2017, Article ID 7679390, 9 pages, 2017.

[21] J. L. Perez-Diaz, I. Valiente-Blanco, C. Cristache et al., "A novel high temperature eddy current damper with enhanced performance by means of impedance matching," *Smart Materials and Structures*, vol. 28, no. 2, article 025034, 2019.

[22] H.-J. Ahn, "Eddy current damper type reaction force compensation mechanism for linear motor motion stage," *International Journal of Precision Engineering and Manufacturing-Green Technology*, vol. 3, no. 1, pp. 67–74, 2016.

[23] T. van Beek, H. Jansen, K. Pluk, and E. Lomonova, "Optimisation and measurement of eddy current damping in a passive tuned mass damper," *IET Electric Power Applications*, vol. 10, no. 7, pp. 641–648, 2016.

[24] M. Berardengo, A. Cigada, F. Guanziroli, and S. Manzoni, "Modelling and control of an adaptive tuned mass damper based on shape memory alloys and eddy currents," *Journal of Sound and Vibration*, vol. 349, pp. 18–38, 2015.

[25] J.-H. Jo, C.-H. Seo, H.-Y. Kim, Y.-H. Jeon, and M.-G. Lee, "Design and application of an eddy-current damper for improving stability in positioning systems," *Journal of the Korean Society of Manufacturing Technology Engineers*, vol. 27, no. 3, pp. 194–202, 2018.

[26] W. Wang, D. Dalton, X. Hua, X. Wang, Z. Chen, and G. Song, "Experimental study on vibration control of a submerged pipeline model by eddy current tuned mass damper," *Applied Sciences*, vol. 7, no. 10, p. 987, 2017.

[27] W. Shi, L. Wang, Z. Lu, and H. Gao, "Study on adaptive-passive and semi-active eddy current tuned mass damper with variable damping," *Sustainability*, vol. 10, no. 2, p. 99, 2018.

[28] A. Asghar Maddah, Y. Hojjat, M. Reza Karafi, and M. Reza Ashory, "Reduction of magneto rheological dampers stiffness by incorporating of an eddy current damper," *Journal of Sound and Vibration*, vol. 396, pp. 51–68, 2017.

[29] Q. Pan, T. He, D. Xiao, and X. Liu, "Design and damping analysis of a new eddy current damper for aerospace applications," *Latin American Journal of Solids and Structures*, vol. 13, no. 11, pp. 1997–2011, 2016.

[30] S. Starin and J. Neumeister, "Eddy current damper simulation and modeling," in *Proceedings of the 14th European Space Mechanisms & Tribology Symposium*, Konstanz, Germany, September 2011.

[31] M. Schmid and P. Varga, "Analysis of vibration-isolating systems for scanning tunneling microscopes," *Ultramicroscopy*, vol. 42–44, pp. 1610–1615, 1992.

[32] Omicron Nanotechnology GmbH Catalog, 2019.

[33] S. B. Chikkamaranahalli, R. R. Vallance, B. N. Damazo, and R. M. Silver, "Damping mechanisms for precision applications in UHV environment," *American Society for Precision Engineering*, vol. 1-2, 2006.

[34] B. Ebrahimi, M. B. Khamesee, and F. Golnaraghi, "Eddy current damper feasibility in automobile suspension: modeling, simulation and testing," *Smart Materials and Structures*, vol. 18, no. 1, article 015017, 2008.

[35] L. Zuo, X. Chen, and S. Nayfeh, "Design and analysis of a new type of electromagnetic damper with increased energy density," *Journal of Vibration and Acoustics*, vol. 133, no. 4, article 041006, 2011.

[36] Z. W. Huang, X. G. Hua, Z. Q. Chen, and H. W. Niu, "Modeling, testing, and validation of an eddy current damper for structural vibration control," *Journal of Aerospace Engineering*, vol. 31, no. 5, article 04018063, 2018.

[37] J.-S. Bae, J.-S. Park, J.-H. Hwang, J.-H. Roh, B.-d. Pyeon, and J.-H. Kim, "Vibration suppression of a cantilever plate using magnetically multimode tuned mass dampers," *Shock and Vibration*, vol. 2018, Article ID 3463528, 13 pages, 2018.

[38] F. Chen and H. Zhao, "Design of eddy current dampers for vibration suppression in robotic milling," *Advances in Mechanical Engineering*, vol. 10, no. 11, article 168781401881407, 2018.

[39] Y. Luo, H. Sun, X. Wang, L. Zuo, and N. Chen, "Wind induced vibration control and energy harvesting of electromagnetic resonant shunt tuned mass-damper-inerter for building structures," *Shock and Vibration*, vol. 2017, Article ID 4180134, 13 pages, 2017.

[40] J.-Y. Li and S. Zhu, "Versatile behaviors of electromagnetic shunt damper with a negative impedance converter," *IEEE/ASME Transactions on Mechatronics*, vol. 23, no. 3, pp. 1415–1424, 2018.

[41] M. C. Smith, "Synthesis of mechanical networks: the inerter," *IEEE Transactions on Automatic Control*, vol. 47, no. 10, pp. 1648–1662, 2002.

[42] P. Wang and X. Zhang, "Damper based on electromagnetic shunt damping method," *International Journal of Applied Electromagnetics and Mechanics*, vol. 33, no. 3-4, pp. 1425–1430, 2010.

[43] B. Yan, X. Zhang, and H. Niu, "Vibration isolation of a beam via negative resistance electromagnetic shunt dampers," *Journal of Intelligent Material Systems and Structures*, vol. 23, no. 6, pp. 665–673, 2012.

[44] C. Wei and X. Jing, "A comprehensive review on vibration energy harvesting: modelling and realization," *Renewable and Sustainable Energy Review*, vol. 74, pp. 1–18, 2017.

[45] B. Marinkovic and H. Koser, "Demonstration of wide bandwidth energy harvesting from vibrations," *Smart Materials and Structures*, vol. 21, no. 6, article 065006, 2012.

[46] S.-J. Jang, E. Rustighi, M. J. Brennan, Y. P. Lee, and H.-J. Jung, "Design of a 2DOF vibrational energy harvesting device," *Journal of Intelligent Material Systems and Structures*, vol. 22, no. 5, pp. 443–448, 2011.

[47] A. Stabile, G. S. Aglietti, G. Richardson, and G. Smet, "Design and verification of a negative resistance electromagnetic shunt damper for spacecraft micro-vibration," *Journal of Sound and Vibration*, vol. 386, pp. 38–49, 2017.

[48] K. J. Kim, F. Cottone, S. Goyal, and J. Punch, "Energy scavenging for energy efficiency in networks and applications," *Bell Labs Technical Journal*, vol. 15, no. 2, pp. 7–29, 2010.

[49] C. B. Williams, C. Shearwood, M. A. Harradine, P. H. Mellor, T. S. Birch, and R. B. Yates, "Development of an electromagnetic micro-generator," *IEE Proceedings-Circuits, Devices and Systems*, vol. 148, no. 6, p. 337, 2002.

[50] P. GlynneJones, M. J. Tudor, S. P. Beeby, and N. M. White, "An electromagnetic, vibration-powered generator for intelligent sensor systems," *Sensors and Actuators A: Physical*, vol. 110, no. 1–3, pp. 344–349, 2004.

[51] C. R. Saha, T. O'Donnell, H. Loder, S. Beeby, and J. Tudor, "Optimization of an electromagnetic energy harvesting device," *IEEE Transactions on Magnetics*, vol. 42, no. 10, pp. 3509–3511, 2006.

[52] R. Torah, P. Glynne-Jones, M. Tudor, T. O'Donnell, S. Roy, and S. Beeby, "Self-powered autonomous wireless sensor node using vibration energy harvesting," *Measurement Science and Technology*, vol. 19, no. 12, article 125202, 2008.

[53] E. Asadi, R. Ribeiro, M. B. Khamesee, and A. Khajepour, "Analysis, prototyping, and experimental characterization of an adaptive hybrid electromagnetic damper for automotive suspension systems," *IEEE Transactions on Vehicular Technology*, vol. 66, no. 5, pp. 3703–3713, 2017.

[54] R. Wang, R. Ding, and L. Chen, "Application of hybrid electromagnetic suspension in vibration energy regeneration and active control," *Journal of Vibration and Control*, vol. 24, no. 1, pp. 223–233, 2018.

[55] Z. Zhang, X. Zhang, W. Chen et al., "A high-efficiency energy regenerative shock absorber using supercapacitors for renewable energy applications in range extended electric vehicle," *Applied Energy*, vol. 178, pp. 177–188, 2016.

[56] S. Guo, Y. Liu, L. Xu, X. Guo, and L. Zuo, "Performance evaluation and parameter sensitivity of energy-harvesting shock absorbers on different vehicles," *Vehicle System Dynamics*, vol. 54, no. 7, pp. 918–942, 2016.

[57] Y. Fukumori, R. Hayashi, R. Matsumi, Y. Suda, and K. Nakano, "Study on independent tuning damping characteristic by coupling of electromagnetic dampers for automobiles," in *Proceedings of the SAE Technical Paper Series*, pp. 0148–7191, Detroit, MI, USA, March 2015.

[58] J.-J. Bae and N. Kang, "Development of a five-degree-of-freedom seated human model and parametric studies for its vibrational characteristics," *Shock and Vibration*, vol. 2018, Article ID 1649180, 15 pages, 2018.

[59] T. Inoue, Y. Ishida, and M. Sumi, "Vibration suppression using electromagnetic resonant shunt damper," *Journal of Vibration and Acoustics*, vol. 130, no. 4, article 041003, 2008.

[60] H. Sun, Y. Luo, X. Wang, and L. Zuo, "Seismic control of a SDOF structure through electromagnetic resonant shunt tuned mass-damper-inerter and the exact H2 optimal solutions," *Journal of Vibroengineering*, vol. 19, no. 3, pp. 2063–2079, 2017.

[61] Y. Tan, Y. Dong, and X. Wang, "Review of MEMS electromagnetic vibration energy harvester," *Journal of Microelectromechanical Systems*, vol. 26, no. 1, pp. 1–16, 2017.

[62] A. Haroun, I. Yamada, and S. Warisawa, "Micro electromagnetic vibration energy harvester based on free/impact motion for low frequency-large amplitude operation," *Sensors and Actuators A: Physical*, vol. 224, pp. 87–98, 2015.

[63] A. Nammari, L. Caskey, J. Negrete, and H. Bardaweel, "Fabrication and characterization of non-resonant magneto-mechanical low-frequency vibration energy harvester," *Mechanical Systems and Signal Processing*, vol. 102, pp. 298–311, 2018.

[64] R. Zhang, X. Wang, and S. John, "A comprehensive review of the techniques on regenerative shock absorber systems," *Energies*, vol. 11, no. 5, 2018.

[65] A. Stabile, G. S. Aglietti, G. Richardson, and G. Smet, "Concept assessment for a 2-collinear-DOF strut prototype with embedded electromagnetic shunt dampers," in *Proceedings of the Esmats 2017*, pp. 20–22, Hatfield, UK, September 2017.

[66] C. Han, X. Liu, M. Wu, and W. Liang, "A new approach to achieve variable negative stiffness by using an electromagnetic asymmetric tooth structure," *Shock Vibration*, vol. 2018, Article ID 7476387, 11 pages, 2018.

[67] H. Yao, Z. Chen, and B. Wen, "Dynamic vibration absorber with negative stiffness for rotor system," *Shock and Vibration*, vol. 2016, Article ID 5231704, 13 pages, 2016.

[68] L. Meng, J. Sun, and W. Wu, "Theoretical design and characteristics analysis of a quasi-zero stiffness isolator using a disk spring as negative stiffness element," *Shock and Vibration*, vol. 2015, Article ID 813763, 19 pages, 2015.

[69] Y. Shen, X. Wang, S. Yang, and H. Xing, "Parameters optimization for a kind of dynamic vibration absorber with negative stiffness," *Mathematical Problems in Engineering*, vol. 2016, Article ID 9624325, 10 pages, 2016.

[70] L. Kashdan, C. Seepersad, M. Haberman, and P. S. Wilson, "Design, fabrication and evaluation of negative stiffness elements," in *Proceedings of the 20th Annual International Solid Freeform Fabrication Symposium*, SFF, Austin, TX, USA, August 2009.

[71] H. Junshu, M. Lingshuai, and S. Jinggong, "Design and characteristics analysis of a nonlinear isolator using a curved-mount-spring-roller mechanism as negative stiffness element," *Mathematical Problems in Engineering*, vol. 2018, Article ID 1359461, 15 pages, 2018.

[72] R. Li, C. Du, F. Guo, G. Yu, and X. Lin, "Performance of variable negative stiffness MRE vibration isolation system," *Advances in Materials Science and Engineering*, vol. 2015, Article ID 837657, 8 pages, 2015.

[73] D. Huang, W. Li, G. Yang, M. He, and H. Dang, "Vibration analysis of a piecewise-smooth system with negative stiffness under delayed feedback control," *Shock and Vibration*, vol. 2017, Article ID 3502475, 14 pages, 2017.

[74] C.-M. Lee, V. N. Goverdovskiy, and A. I. Temnikov, "Design of springs with "negative" stiffness to improve vehicle driver vibration isolation," *Journal of Sound and Vibration*, vol. 302, no. 4-5, pp. 865–874, 2007.

[75] W. Wu, X. Chen, and Y. Shan, "Analysis and experiment of a vibration isolator using a novel magnetic spring with negative stiffness," *Journal of Sound and Vibration*, vol. 333, no. 13, pp. 2958–2970, 2014.

[76] G. Dong, X. Zhang, S. Xie, B. Yan, and Y. Luo, "Simulated and experimental studies on a high-static-low-dynamic stiffness isolator using magnetic negative stiffness spring," *Mechanical Systems and Signal Processing*, vol. 86, pp. 188–203, 2017.

[77] Y. Zheng, X. Zhang, Y. Luo, B. Yan, and C. Ma, "Design and experiment of a high-static-low-dynamic stiffness isolator using a negative stiffness magnetic spring," *Journal of Sound and Vibration*, vol. 360, pp. 31–52, 2016.

[78] X. Shi and S. Zhu, "Simulation and optimization of magnetic negative stiffness dampers," *Sensors and Actuators A: Physical*, vol. 259, pp. 14–33, 2017.

[79] X. Shi and S. Zhu, "Magnetic negative stiffness dampers," *Smart Materials and Structures*, vol. 24, no. 7, article 072002, 2015.

[80] I. Pakar and M. Bayat, "Analytical study on the non-linear vibration of Euler-Bernoulli beams," *Journal of Vibroengineering*, vol. 14, no. 1, pp. 216–224, 2012.

[81] M. Bayat, M. Shahidi, A. Barari, and G. Domairry, "The approximate analysis of nonlinear behavior of structure under harmonic loading," *International Journal of Physical Sciences*, vol. 5, no. 7, 2010.

[82] S. C. Somé, V. Gaudefroy, and D. Delaunay, "Estimation of bonding quality between bitumen and aggregate under asphalt mixture manufacturing condition by thermal contact resistance measurement," *International Journal of Heat and Mass Transfer*, vol. 55, no. 23-24, pp. 6854–6863, 2012.

[83] H. Yao, Z. Chen, and B. Wen, "Dynamic vibration absorber with negative stiffness for rotor system," *Shock and Vibration*, vol. 2016, Article ID 5231704, 13 pages, 2016.

[84] Y. Zheng, X. Zhang, C. Ma, Z. Zhang, and S. Zhang, "An ultra-low frequency pendulum isolator using a negative stiffness magnetic spring," *International Journal of Applied Electromagnetics and Mechanics*, vol. 52, no. 3-4, pp. 1313–1320, 2016.

[85] M. Wang, X. Chen, and X. Li, "An ultra-low frequency two DOFs' vibration isolator using positive and negative stiffness in parallel," *Mathematical Problems in Engineering*, vol. 2016, Article ID 3728397, 15 pages, 2016.

[86] K. S. Arsava and Y. Kim, "Modeling of magnetorheological dampers under various impact loads," *Shock and Vibration*, vol. 2015, Article ID 905186, 20 pages, 2015.

[87] G. Hu, F. Liu, Z. Xie, and M. Xu, "Design, analysis, and experimental evaluation of a double coil magnetorheological fluid damper," *Shock and Vibration*, vol. 2016, Article ID 4184726, 12 pages, 2016.

[88] J. Ding, X. Sun, L. Zhang, and J. Xie, "Optimization of fuzzy control for magnetorheological damping structures," *Shock and Vibration*, vol. 2017, Article ID 4341025, 14 pages, 2017.

[89] X. Yuan, T. Tian, H. Ling, T. Qiu, and H. He, "A review on structural development of magnetorheological fluid damper," *Shock and Vibration*, vol. 2019, Article ID 1498962, 33 pages, 2019.

[90] S. Zhu, L. Tang, J. Liu, X. Tang, and X. Liu, "A novel design of magnetorheological damper with annular radial channel," *Shock and Vibration*, vol. 2016, Article ID 8086504, 7 pages, 2016.

[91] W. H. Kim, J. H. Park, S. Kaluvan, Y.-S. Lee, and S.-B. Choi, "A novel type of tunable magnetorheological dampers operated by permanent magnets," *Sensors and Actuators A: Physical*, vol. 255, pp. 104–117, 2017.

[92] P. Xiao, Q. Wang, L. Niu, and H. Gao, "Research on suspension system with embedded-permanent-magnet magnetorheological damper based on V-model," *Proceedings of the Institution of Mechanical Engineers, Part C: Journal of Mechanical Engineering Science*, vol. 230, no. 10, pp. 1602–1614, 2016.

[93] R. Rizzo, A. Musolino, and H. C. Lai, "An electrodynamic/ magnetorheological clutch powered by permanent magnets," *IEEE Transactions on Magnetics*, vol. 53, no. 2, pp. 1–7, 2017.

[94] R. Rizzo, A. Musolino, F. Bucchi, P. Forte, and F. Frendo, "A multi-gap magnetorheological clutch with permanent magnet," *Smart Materials and Structures*, vol. 24, no. 7, article 075012, 2015.

[95] E. Diez-Jimenez, A. Musolino, M. Raugi, R. Rizzo, and L. Sani, "A magneto-rheological brake excited by permanent magnets," *Applied Computational Electromagnetics Society*, vol. 34, no. 1, pp. 186–191, 2019.

[96] T. H. Lee, C. Han, and S. B. Choi, "Design and damping force characterization of a new magnetorheological damper activated by permanent magnet flux dispersion," *Smart Materials and Structures*, vol. 27, no. 1, article 015013, 2018.

[97] T.-H. Lee and S.-B. Choi, "On the response time of a new permanent magnet based magnetorheological damper: experimental investigation," *Smart Materials and Structures*, vol. 28, no. 1, article 014001, 2019.

[98] Y. Sato, "Power-saving magnetizing device for magnetorheological fluid control using permanent magnet," *IEEE Transactions on Magnetics*, vol. 50, no. 11, pp. 1–4, 2014.

[99] S.-B. Choi, A.-R. Cha, J.-Y. Yoon, and T.-H. Lee, "Design of new prosthetic leg damper for above knee amputees using a magnetorheological damper activated permanent magnet only," in *Proceedings of the Active And Passive Smart Structures And Integrated Systems XII*, p. 107, Denver, CO, USA, March 2018.

Research Article

Multiphysics Model of an MR Damper including Magnetic Hysteresis

M. Kubík [ID][1] **and J. Goldasz** [ID][2,3]

[1]*Faculty of Mechanical Engineering, Brno University of Technology, Brno, Czech Republic*
[2]*Faculty of Electrical and Computer Engineering, Cracow University of Technology, Kraków, Poland*
[3]*Technical Center Kraków, BWI Group, Kraków, Poland*

Correspondence should be addressed to M. Kubík; michal.kubik@vutbr.cz

Hysteresis is one of key factors influencing the output of magnetorheological (MR) actuators. The actuators reveal two primary sources of hysteresis. The hydro(mechanical) hysteresis can be related to flow dynamics mechanisms and is frequency- or rate-dependent. For comparison, the magnetic hysteresis is an inherent property of ferromagnetic materials forming the magnetic circuit of the actuators. The need for a good quality hysteresis model has been early recognized in studies on MR actuators; however, few studies have provided models which could be used in the design stage. In the paper we reveal a hybrid multiphysics model of a flow-mode MR actuator which could be used for that purpose. The model relies on the information which can be extracted primarily from material datasheets and engineering drawings. We reveal key details of the model and then verify it against measured data. Finally, we employ it in a parameter sensitivity study to examine the influence of magnetic hysteresis and other relevant factors on the output of the actuator.

1. Introduction

Magnetorheological (MR) dampers are fairly well-known devices utilizing MR fluids which, when subjected to magnetic stimuli of sufficient strength, generate yield stress [1]. So far, the unique technology has been commercialized in semiactive passenger vehicle suspensions, powertrain mounts [2], or optical finishing [3]. Low power consumption, fast and reversible responses, and high dynamic range have made the devices attractive for use in vibration control systems in particular [4]. As MR dampers are generally operated in real-time control systems, their dynamic performance is equally important as or more important than their steady-state characteristics. Steady-state characteristics only provide the evidence of an actuator or a damper meeting the required force/torque range (or force/torque) targets. Their dynamic behaviour needs to be quantified at the same time if it is used in a real-life control process. Thus, understanding the contributions of various factors complicating the force or torque build-up dynamic process is critical for the development of a realistic application. Briefly,

with MR actuators, there is ample evidence of several factors complicating the force/torque generation process, namely, mechanical/hydraulic hysteresis, magnetic hysteresis, control circuit dynamics such as eddy currents, driver dynamics, temperature, flow losses, friction, and nonlinear relationship between the material's yield stress and the induced flux [5–7]. These factors influence the device's ability to generate the output force/torque and need to be accounted, for instance, for in the control algorithm development process.

In this study, we pay particular attention to modeling the damper's hysteretic behaviour. In general, MR devices reveal two primary sources of hysteresis. The (hydro-)mechanical hysteresis can be related to the damped dynamics of a heavy slug of MR fluid (MRF) bouncing against compliant columns of MRF in fluid chambers. The effect is rate- or frequency-dependent, and its magnitude varies with the current applied, too. It disappears as the mechanical excitation frequency approaches zero [8]. The magnetic hysteresis is different. It is present in all electromagnetic devices, e.g., electromagnetic solenoids [9], motors [10], and magnetorheological actuators [11]. First of all, it is the inherent

property of ferromagnetic materials forming the magnetic circuit of the MR valve; the hysteresis of carbonyl iron-(CIP-) based MFRs is virtually nonexistent [12]. Next, it does not vanish as the inducing current frequency approaches DC limit. Also, temperature, load history, and mechanical stresses have a negative influence on the hysteresis and magnetization characteristics of ferromagnetic materials [13]. For instance, it is a common practice to subject machined ferromagnetic components to heat treatment for internal stress and hysteresis as well as coercive force reduction.

The need for a good quality hysteresis model has been early recognized in studies on MR actuators, and the reader should refer, e.g., to Zheng et al. [14] for a review of suitable phenomenological models as well as to the well-known study of Spencer et al. [15]. In general, the posteriori parametric models were obtained by examining the force-position and force-velocity relationships by fitting by model response to the actuator's output. Such models are suitable for control studies only. In the device's development process, other approaches are required. In that aspect, many MR-related research studies neglected the particular contributor's presence. The topic, however, has been well identified in the field of conventional solenoid actuators where various models were developed to copy the hysteretic behaviour of the actuators. For instance, Mayergoyz [16] applied the Preisach model to model the hysteretic behaviour of a solenoid actuator. In the Preisach model, the hysteresis is the sum of elementary hysteresis loops. Next, Coleman and Hodgdon [17] developed a first-order differential equation that links the field strength H and the flux density B. One model whose parameters can be related to physical properties of ferromagnetic materials is the Jiles–Atherton (J–A) model [18, 19]. The model was extended to include both the impact of eddy currents and temperature on hysteresis and magnetisation curves [20, 21]. All of the above models can be vectorized. Tellinen [22] proposed a simple scalar model for handling the hysteresis based on the limiting hysteresis loop from physical measurements of ferromagnetic materials. With MR actuators, however, although the significance of a good quality hysteretic model has been recognized early, the topic does not seem to have deserved enough attention. Significant contributions include Han et al. [23] who examined the field dependent hysteresis of ER fluids. The authors used the familiar Preisach approach. Moreover, Han et al. [7] used the Preisach model to identify the hysteresis of an MR fluid. Yadmellat and Kermani developed a model of an MR clutch in which the developed hysteresis model was assessed against the Preisach operator [24]. For comparison, in their early study using the Coleman-Hodgdon model, An and Kwon modelled the hysteretic behaviour of an MR clutch, and by examining the torque-current loops showed that the hysteresis is an important contributor to the device's output [25]. The model parameters were identified from physical measurements (of magnetisation characteristics) of the materials forming the magnetic circuit of the clutch. Next, Jędryczka et al. presented a finite-element (FE) model of an MR clutch based on the J-A approach [26]. Moreover, Guo et al. presented a transient multidomain model of a flow-mode damper based on the J-A approach and then verified it against the novel FE vector hysteresis technique [27]. The inverse J-A model was recently examined by Zheng et al. [14] to copy the transient behaviour of an MR flow-mode damper. Goldasz et al. [28] proposed an extension of the Bouc–Wen model in an attempt to separate the magnetic hysteresis from the mechanical one. The authors proposed a simple lumped parameter model of the actuator including a hysteretic operator. The model was verified against selected sinusoidal AC excitation inputs and provided acceptable accuracy for practical purposes. Still, when compared to the vast number of research studies using parametric phenomenological hysteretic models, the topic does not seem intensively studied as already mentioned. That may be due to few existing comprehensive electromagnetic models of such actuators.

Another aspect is dynamics. Clearly, the insight into the dynamics of MR actuators should be provided through transient models. Such a comprehensive model would attempt to copy not only the dynamics of the fluid flow through the valve and the flux dynamics but account for the physics outside the control valve as well. Suitable lumped parameter models usually utilize a network of elements representing physical domains of interest (hydraulic, thermal, electric, and magnetic) and connections (interfaces) between them [2]. For example, the electrical circuit of the actuator can be represented in the form of a resistor-nonlinear inductor network model [5]. Their main disadvantage is the necessity of using various simplifying assumptions, e.g., uniform yield stress/flux, fully developed flow, etc. On the contrary, continuum multiphysics (magnetics and flow dynamics) models utilize fewer assumptions and can be exercised on realistic geometries, however, at a significant computational expense [29].

As such, in the paper, we propose a hybrid multiphysics model of the magnetorheological damper which separates the magnetic hysteresis of the magnetic circuit of the actuator from that of the mechanical hardware. Briefly, the electromagnetic domain is modelled using the vector hysteresis FE model (present in Ansys Maxwell) based on the extension of well-known Maxwell equations [30], and the hydraulic section is described through dimensionless biplastic Bingham approach [31].

The paper is organized as follows. First, we present an MR damper geometry and key material properties. Then, in the following section, we reveal key details of the FE model of the actuator such as magnetic hysteresis and the coupled lumped parameter hydromechanical model. Next, we show measurements of magnetic hysteresis loops and a comparison of the measurements against the FE electromagnet model. Finally, we show results of a parametric study (also involving the hybrid model) in an attempt to examine the hysteresis influence on the output of the MR actuator and then draw conclusions.

2. Magnetorheological Damper

In the study, an MR flow-mode damper configuration having a single coil assembly in the electromagnet and one annular

flow path in the control valve is of research interest. The damper is presented in Figure 1. The hydraulic tube houses (1) the piston (2), the piston rod (3), the floating piston (4) and the rod guide assembly (5). The piston separates the MR fluid volume into rebound chamber volume and the compression chamber volume. The floating piston separates the fluid from the gas chamber. The MR valve located in the piston control controls the fluid flow between the rebound and compression chamber and vice versa. The MR valve is a conventional control valve by design. It consists of the piston core (6), the sleeve (7), the nonmagnetic flanges or plates (8), the coil assembly (9), and the connecting wires (10) for connecting to an external power supply. It is the most common single-tube MR damper configuration.

The MR valve's magnetic circuit (6, 7) is manufactured out of annealed low-carbon steel 11SMn30 (see the components in blue in Figure 1). The bronze (yellow) flanges (8) define the mutual position of the piston core and sleeve. The distance between the outer diameter of the annulus and the inner diameter of the sleeve defines the annular gap height. The coil assembly (9) incorporates $N = 120$ turns of copper (purple) wire (0.5 mm diameter).

The connecting wires are routed through the thru-hole in the piston rod (3) made of steel 42CrMo4 (AISI 4140). The floating piston, the rod guide, and the remaining components are manufactured out of steel S235JR (green). The MR damper is filled with the fluid MRF132-DG by Lord Corp; see the magnetisation curve in Figure 2(c). The damper key dimensions, rheological properties of MR fluid, and gas chamber details are shown in Table 1. The magnetisation curves of the annealed low-carbon steel 11SMn30 were determined using the measurement system Remagraph C-500. The obtained virgin & hysteresis data can be seen in Figures 2(a) and 2(b).

The coercitivity and remanence of the 11SMn30 material sample were determined from the measured hysteresis: $H_c = 209$ A/m and remanence $B_r = 1.09$ T. The material's bulk conductivity was set at 5.8 MS/m. Based on similar measurements of the rod material (42CrMo4), we set its coercivity to $H_c = 1250$ A/m and the bulk conductivity to 4.5 MS/m.

3. Modeling

In the section, we present modeling details. Specifically, we highlight the transient magnetic FE model of the MR valve including hysteresis followed by a description of a monotube damper lumped parameter model. The lumped parameter model is coupled with the transient FE model through the yield stress-flux density interface. We consider the integrated model as illustrated in Figure 3. In the presented layout, the electromagnetic circuit (described in Section 3.1) is driven by the voltage u supplied by the current driver. The resulting output flux density B_g is then converted into the materials' (fluid) field-induced yield stress τ_0 (extracted from the material's datasheet or rheological measurements). Given the input velocity v_r or displacement and the yield stress, we then calculate the output force according to the equations in Section 3.2.

3.1. Transient Magnetic Model with Magnetic Hysteresis. To model the electromagnetic circuit of the MR valve, we applied the vector hysteresis modeling feature available in Ansys Maxwell R19. For isotropic material and 2D/3D problems, the vector play model was recognized to be more computationally efficient than a vector Preisach model [30, 33]. In general, the play model assumes a decomposition of the applied field H into the reversible component H_{re} and the irreversible one H_{ir}. Then, the resulting flux density

$$B = B_{re} + B_{ir} = \mu_0 M (H_{re}) + \mu_0 H_{ir}, \qquad (1)$$

where B_{re} is the reversible component of flux density and B_{ir} is the irreversible component. The magnetization M varies with the reversible field component along an anhysteretic curve. The process can be visualized as in Figure 4. The parameters for the model can be identified from the major hysteresis loop. The major hysteresis loop incorporates two branches, the ascending branch and the descending branch, and they can be calculated from each other, the Maxwell model utilizes only one branch of particular *B-H* loops. The algorithm for constructing the major and symmetric minor hysteresis loops is given in [34].

To develop the FE model, we assumed the valve to be axially symmetrical around the centerline in a cylindrical coordinate system. The geometry of the MR damper piston (valve) was simplified for the transient simulations (Figure 5(a)). The discretized model can be observed in Figure 5(b). As shown, the geometry was discretized using triangular elements. The element length-based refinement with the maximum length of 0.5 mm was applied to the coil core and the sleeve. Next, the value of 0.7 mm was applied to the piston rod and the hydraulic tube, and the criterion of 0.2 mm was applied to the MR fluid region in the active zone.

To accomplish transient field simulations, the FE model was coupled to the external circuit revealed in Figure 6(a). The lumped circuit documents an ideal current source (input) in series with a resistor (coil winding) and the FE valve object (as represented by the nonlinear inductor). The model is subjected to prescribed current waveforms, and the resulting flux density in the annulus B_g is extracted from the simulation results. The flux density B_g presented in the next sections was calculated by averaging flux density of the middle of the annulus. The information is required for coupling the FE model with the damper hydraulics.

The figure also shows the curve fit to the experimental data for the steel 11SMn30 (Figure 6(b)). The agreement is satisfactory except for low magnetic field strength and on the initial magnetization curve only. The core and sleeve components were assigned the *B-H* properties of the 11SMn30 alloy and the MRF component that of MRF132-DG available from Lord Corp. Also, the rod component was assigned the material properties of the 42CrMo4 steel alloy as mentioned above. Finally, all data in subsequent simulations were obtained using the fixed step-size solver with the following settings: constant time step was 0.05 ms, nonlinear residual was $1e-7$, time integration method was Backward Euler.

(a)

(b)
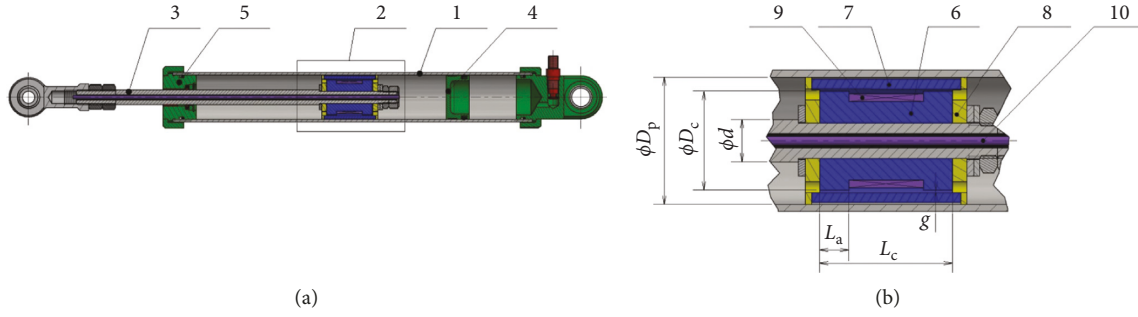
FIGURE 1: Magnetorheological damper. (a) MR damper. (b) Piston (control valve).

(a)

(b)

(c)
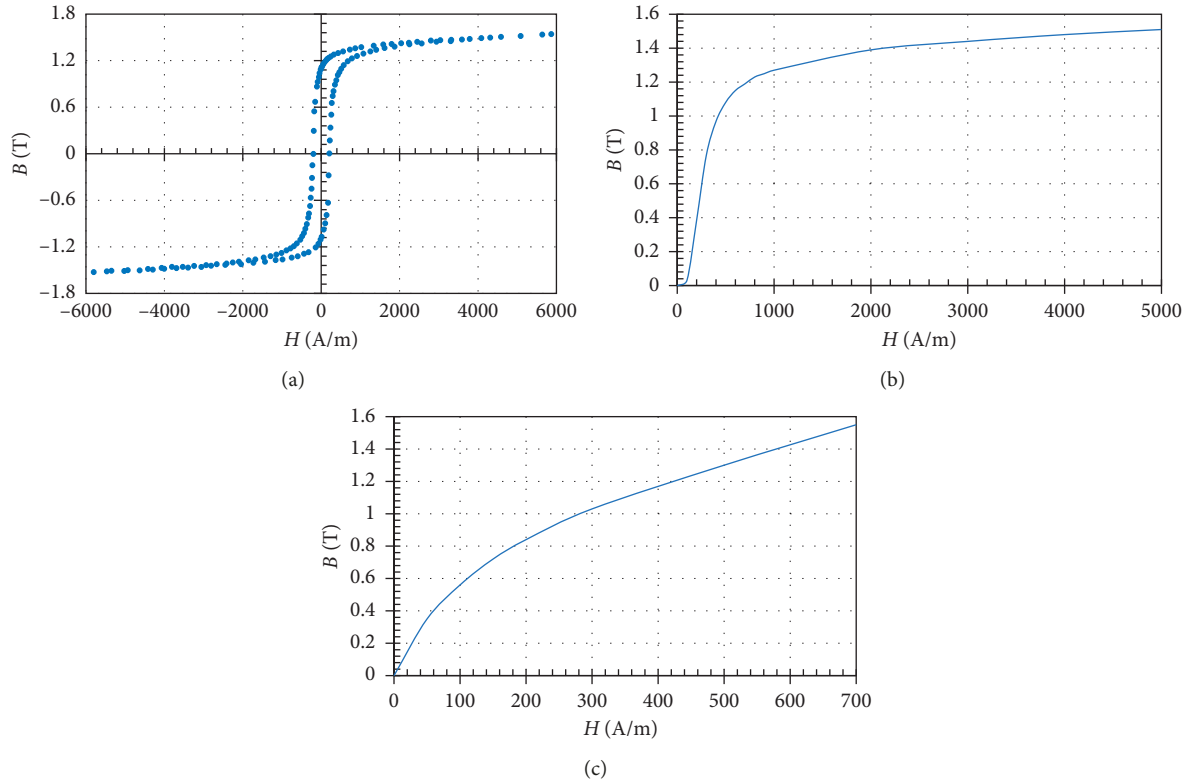
FIGURE 2: Virgin and hysteresis magnetization curves. (a) Hysteresis curve of 11SMn30. (b) Static curve of 11SMn30. (c) Static curve of MRF 132-DG [32].

TABLE 1: MR damper dimensions and material properties.

Name	Value	Symbol	Unit
Geometry and weight			
Piston rod outer diameter	12	d	mm
Piston outer diameter	36	D_p	mm
Annular gap height	0.65	h	mm
Active zone length	16	L_a	mm
Core length	37	L_c	mm
Piston stroke	150	L_s	mm
Internal diameter of the gap	28	D_c	mm
Floating piston weight	0.07	m_f	kg
MR fluid properties (MRF-132DG [32])			
MR fluid viscosity at 40°C	0.114	μ	Pa·s
MR fluid isothermal bulk modulus	1500	β	MPa
MR fluid density	3090	ρ	kg·m^{-3}

TABLE 1: Continued.

Name	Value	Symbol	Unit
Air content in the MR fluid	0.01	α	—
Gas chamber			
Gas volume (at midstroke)	46000	V_{g0}	mm^3
Gas temperature	40	T	°C
Initial gas pressure	30	P_{g0}	bar
Initial floating piston position	20	x_g	mm
Others			
Initial rebound chamber (upper) MR fluid volume	63333	V_{r0}	mm^3
Initial compression (lower) chamber MR fluid volume	71250	V_{c0}	mm^3
Coil turns	120	N	—
Coil resistance	1.0	R_c	Ω
Nondimensional viscosity ratio (est.)	0.1	γ	—
Yield stress number (est.)	0.5	δ	—
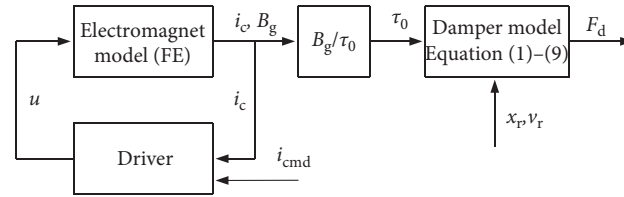
FIGURE 3: Block diagram of the proposed model.
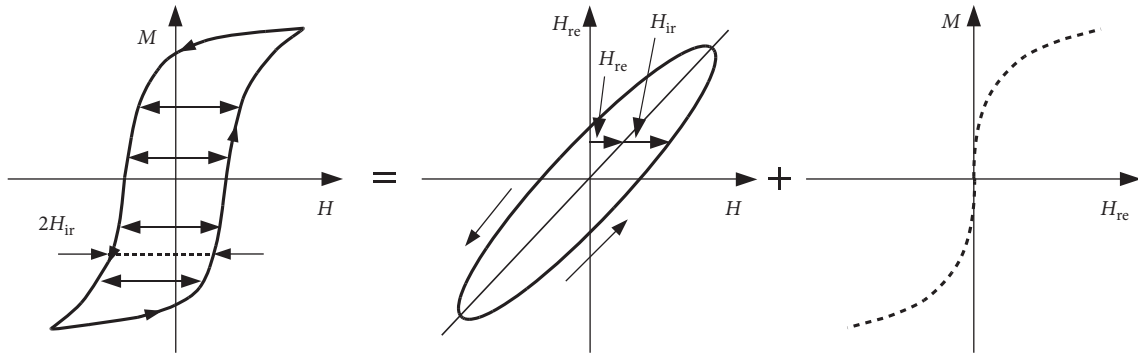
FIGURE 4: Magnetic field decomposed into reversible/irreversible components [35].

(a)

(b)
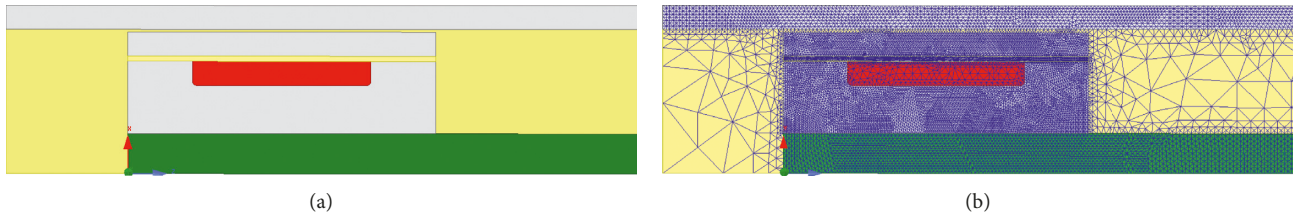
FIGURE 5: Simplified geometry of the piston unit and mesh. (a) Geometry. (b) Mesh.

3.2. Hydromechanical Model. To illustrate or reveal the effect of fluctuating (transient) magnetic field on the output of the actuator, a capable damper model is required. Modeling the behaviour of MR dampers has been clearly the subject of intensive research, to name only [36–38]. However, we chose to proceed further with the model of Goldasz and Sapinski in [2]. The approach is flexible, incorporates most key physical phenomena occurring in the MR valve and outside of it, and was successfully verified against several MR piston valve configurations (monotube damper, valve: single coil, single annular flow path, magnetic flux bypass feature). Therefore, in the sections that follow, we describe details of the lumped parameter model of the damper and the coupling method with the FE transient model.

(a)

(b)
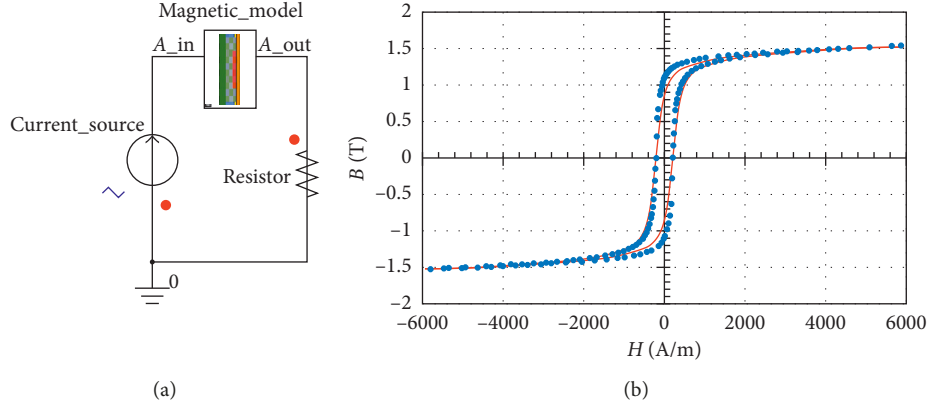
FIGURE 6: External circuit model and magnetisation curve: 11SMn30 (curve fit vs data). (a) External circuit. (b) *B-H* plot.

3.2.1. MR Damper Model: Theoretical Background. The schematic geometry of the damper is revealed in Figure 7. In the presented illustration, the piston separates the upper (rebound) fluid chamber from the fluid below it (compression chamber). The pressure in the upper chamber is P_r, and its (initial) volume is V_r (V_{r0}). Accordingly, the pressure in the compression chamber is P_c, and its (initial) volume is V_c (V_{c0}). The gas pressure is P_g (P_{g0}), and the (initial) gas volume below the floating piston is referred to as V_g (V_{g0}). At static conditions, the pressure in each chamber is equal to P_{g0}. The cross-sectional area of the piston is A_p and that of the rod A_r. As the piston rod moves, it displaces the floating piston (separating the lower fluid chamber and the pressurised gas). The floating gas cup mass is m_g, and its displacement is x_g. The friction forces against the rod guide and the floating piston are F_{fg} and F_{fr}, respectively. We assume one annular flow path in the MR valve; dimensions: h is the gap height; w is the circumferential width (at perimeter); $A_g = wh$ is the flow channel area. The flow rate through the annulus is referred to as Q_a. Finally, we refer to the displacement of the piston rod as x_r and to that of the cylinder tube as x_t (not shown).

The fluid's behaviour is quantified with the viscosity μ, the density ρ, the compressibility β, and the field-induced yield stress τ_0. The non-Newtonian rheology of the MR fluid is described using the biplastic Bingham model [31].

We assume that the damper model would account for the following phenomena: MR effect (using the biplastic Bingham model mentioned above), compressibility of fluid, dynamics of the fluid element ("slug") motion when forced through the annulus, entrance and exit losses in the annulus, floating piston mass inertia, and seal friction. Elasticity of the cylinder tube, various effects due to heating, and the dependency of seal friction on the damper internal pressure are not accounted for.

First, the gas pressure in the volume below the floating piston can be modeled by assuming the adiabatic process ($n = 1.4$). The gas pressure P_g is then dependent on the position of the floating piston x_g in the following manner:

$$P_g = P_{g0}\left(\frac{V_{g0}}{V_{g0} + A_p x_g}\right)^n. \tag{2}$$
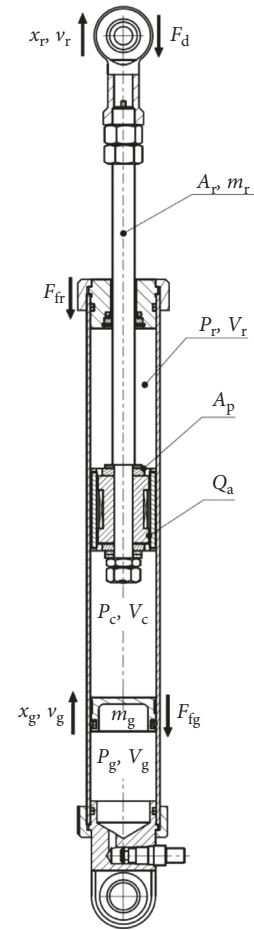
FIGURE 7: Damper model schematic layout.

The pressure variation in the chambers below/above the piston is modeled assuming isothermal processes and the conservation of mass approach [39]. Next, the dynamics of the mass of fluid is considered by examining the motion of the fluid mass in the annular channel. The resulting system of ordinary differential equation in the state-space form which describes the mutual relationships between the rebound pressure chamber P_r, the compression chamber pressure P_c, the floating piston motion velocity v_g, and the

volumetric flow rate through the annulus Q_a is shown below

$$\dot{P}_r = \beta \frac{(A_p - A_r)v_p - Q_a}{V_r}, \tag{3}$$

$$\dot{P}_c = \beta \frac{(v_g - v_p)A_p + Q_a}{V_c}, \tag{4}$$

$$\dot{v}_g = \frac{1}{m_g} \left[A_p(P_c - P_g) - F_{fg}\text{sign}(v_g) \right], \tag{5}$$

$$\dot{Q}_a = \frac{A_g}{\rho L}(P_r - P_c - \Delta p_a). \tag{6}$$

As already mentioned, the behaviour of the energized MR fluid is described by incorporating the field-dependent losses into the pressure drop Δp_a which is described in detail in Section 3.2.3; the reader should refer to [2, 39] for a more detailed derivation of the equations and the experimental verification method. The pressure term also incorporates the local flow losses Δp_e. The local flow losses as the fluid enter/exits the annulus are accounted for using the semiempirical equation [40]:

$$\Delta p_e = K \frac{\rho Q_a}{2A^2} |Q_a|, \tag{7}$$

$$K_{SE} = K_{cor} \left(1 - \frac{A_g}{A_p}\right)^2, \tag{8}$$

$$K_{SC} = K_{cor} \left(1 - \frac{A_g}{A_p}\right)^{0.75}, \tag{9}$$

where K/K_{SE} is the pressure loss coefficient for the sudden enlargement (exit from the gap), K/K_{SC} is the pressure loss coefficient for the sudden contraction (entrance to the annular gap), and K_{cor} is the correction factor. Finally, considering the forces acting on the piston yields the following relationship:

$$F_d = (A_p - A_r)P_r - P_c A_p + F_{fr} + F_{fg}. \tag{10}$$

The friction force in MR damper is assumed to be the sum of Stribeck, Coulomb, and viscous components [40]. As already mentioned, the effects of viscosity change with temperature (heating) are not included.

We solve the system of equations (2)–(10) using the multidomain modeling package Simscape which extends Simulink with tools for object oriented modeling and simulating multiphysics systems [40]. Our model as shown in Figure 8 consists of mechanical, hydraulic, and physical signals domains. Using that environment, the MR damper model was developed with isothermal hydraulic double-acting cylinder components, adiabatic gas blocks, and friction components. The MR fluid behaviour as copied specifically by equation (6) was defined by means of a custom component based on the biplastic

Bingham model approach [31] in series with the local loss model.

To allow simulations of the transient performance of the damper, the model was coupled to the FE model in Ansys Maxwell through the magnetic flux density vs yield stress relationship, $\tau_0 = \tau_0(B_g)$. The interface assumes zero delay between the electromagnetic response of the circuit and the MRF response. MRF measurements indicate the response time of the fluid to be below 0.6 ms; therefore, that particular contribution is omitted in the developed equation set.

3.2.2. Magnetorheological Valve Model. In this section, we describe the biplastic Bingham computing scheme for determining the pressure drop across the magnetorheological valve. Specifically, the relationship between the flow rate through the annulus Q_a and the pressure drop Δp_a is needed. The biplastic scheme is preferred rather than the conventional Bingham approach as it is more flexible and allows for a more effective modeling of low velocity features in the annulus, e.g., magnetic bypass [2]. Using the dimensionless representation of the scheme in terms of the pressure number G and the plasticity S, we express the relationship between the flow rate Q_a and the pressure drop across the annulus Δp_a as

$$\Delta p_a = \frac{2\tau_2 L_a}{h}G(S) = \frac{2\tau_0 L_a}{h(1 - \gamma(1 - \delta))}G(S), \tag{11}$$

where

$$\begin{cases} G = -\frac{h\Delta p_a}{2 L_a \tau_2}, \\ \\ S = \frac{12\mu Q_a}{wh^2\tau_2}. \end{cases} \tag{12}$$

The two additional parameters, γ and δ, are referred to as the artificial viscosity ratio and the (nondimensional) bypass number (yield stress ratio), respectively. As the biplastic model was well studied in prior research papers, the reader should refer there for in-depth details and the parameter estimation method. Briefly, δ controls the intercept force at the zero piston velocity, and γ influences the curve's slope below the knee-point of the force-velocity characteristics [2]. The two parameters of the biplastic model are related to the valve's geometry rather than material properties. The estimation procedure was highlighted, e.g., in [36]. For example, based on prior knowledge, the value of δ (0.5) was selected for a valve with no leakage flow path in the annulus. Using the model, we classify the valve's behaviour into two flow regimes: preyield ($G \leq 1$) and postyield ($G > 1$). The transition point coordinates at which the behaviour of the pseudomaterial changes from the preyield regime to the postyield regime are equal to $G = 1$, $S_0 = \gamma(2 - 3\delta + \delta^3)$. Briefly, when in the postyield regime, the relationship between G and S can be expressed as
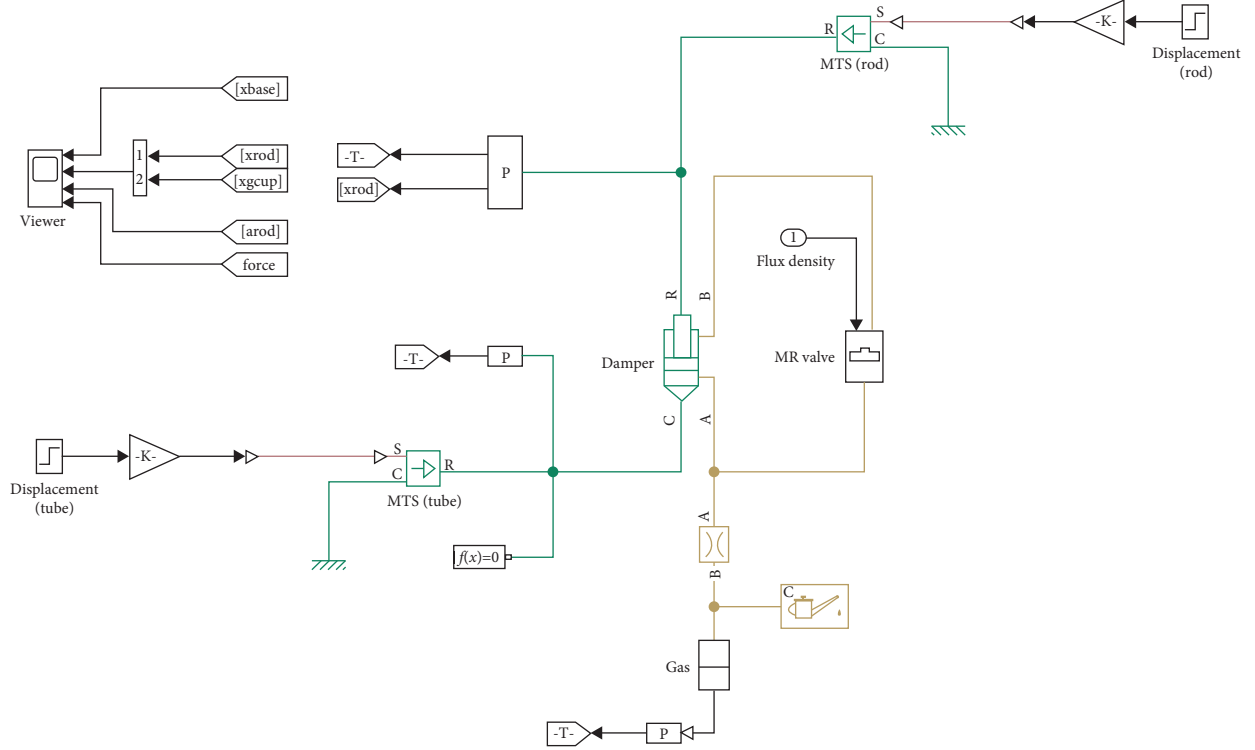
Figure 8: High-level Simscape model layout.

$$G = \frac{1}{6}\left[3\left(1 - \gamma(1 - \delta)\right) + S\right]\left[2\,\cos\left(\frac{1}{3}a\,\tan 2\,(y, x)\right) + 1\right],$$

(13)

$$\begin{cases} y = 12\sqrt{-81b^2 + 12ba^3}, \\ x = -108b + 8a^3, \\ a = \frac{3}{2}\left(1 - \gamma(1 - \delta)\right) + \frac{1}{2}S, \\ b = \frac{1}{2}\left(1 - \gamma\left(1 - \delta^3\right)\right), \end{cases}$$

(14)

whereas in the preyield regime, the relationship between the pressure drop and the flow rate through the annulus is governed by the following formula:

$$G = \delta\frac{1}{6}\left[\frac{S}{\gamma\delta} + 3\right]\left[2\,\cos\left(\frac{1}{3}a\,\tan 2\,(y_1, x_1)\right) + 1\right],$$

(15)

where

$$\begin{cases} y_1 = 6\sqrt{3}\,\sqrt{27\dfrac{S}{\gamma\delta} + 9\left(\dfrac{S}{\gamma\delta}\right)^2 + \left(\dfrac{S}{\gamma\delta}\right)^3}, \\ x_1 = -27 + 27\dfrac{S}{\gamma\delta} + 9\left(\dfrac{S}{\gamma\delta}\right)^2 + \left(\dfrac{S}{\gamma\delta}\right)^3. \end{cases}$$

(16)

The two model parameters (γ, δ) can be identified from real damper experimental data or CFD (computational flow dynamics) simulations. Finally, equation (11) can be modified to include the contribution of the nonenergized region above the coil of the length $L_c - L_a$ through

$$\Delta p_a = \frac{2\tau_2 L_a}{h}G(S) + \frac{12\mu\left(L_c - L_a\right)Q_a}{wh^3}.$$

(17)

4. Magnetic Flux Measurements

For the specific electromagnet geometry, we performed a series of measurements for extracting the flux density information with respect to the control (exciting) current input. The goal was to verify the FE model. Therefore, in this section, we reveal the experimental procedure for acquiring the magnetic flux relationship against the exciting current and present the obtained data.

4.1. Test Rig Configuration.
The magnetic flux density was measured in the middle of the air gap with the ultrathin Hall transverse probe (STB1X-0201) and the magnetometer F. W. Bell 5180 at the sampling frequency of 100 Hz. The coil current magnitude coil was simultaneously acquired by means of the Fluke i30s current clamp. The MR damper coil was excited using two laboratory power supplies: (1) Manson SDP2603 device for lower amplitude current excitations and (2) G. W. Instek PST-3202 power supply for higher current inputs. The two signals are recorded simultaneously using the front-end Dewetron USB-50-USB2-8 data acquisition module connected to the laptop (Figure 9).

The procedure was performed as follows: (1) current increase up to the maximum prescribed current I_{max}, which was followed by decreasing the current down to 0 A, (2) input voltage polarity change, (3) repeat Step 1, (4) repeat
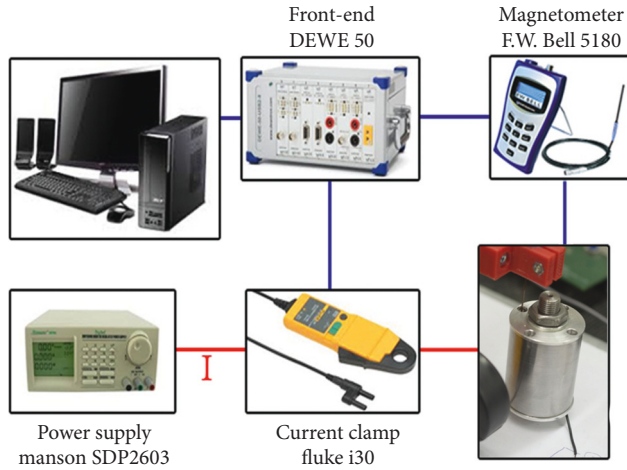
FIGURE 9: Test rig configuration.

Step 2, and (5) repeat Step 1. Using the highlighted procedure, the magnetic flux density was measured for the maximum current levels $I_{max} = \{0.5, 1, 2, 3, 4, 5\}$ A, respectively.

The measurements of magnetic flux in the annular gap were performed without the MR fluid. Note that the relative permeability of the Hall sensor ($\mu_r = 1$) placed in the thin annulus with MR fluid would distort the accuracy of the experiment as the flux flows around the probe as illustrated in Figure 10. In the simulations, we assume the presence of MR fluid would not degrade the accuracy of the model.

4.2. Results. The obtained data are revealed in Figure 11 as plots of flux density vs coil current.

Observations of the plots of flux density vs current reveal the presence of hysteresis and nonlinear behaviour with the actuator approaching the saturation at the highest current level ($I_{max} = 5$ A).

5. Modelling Results

The series of modelling experiments was split into two stages. First, we validate the transient FE model against the experimental data, and then we study the behaviour of the hydraulic model.

5.1. FE Model Verification: Air Gap, No MR Fluid. Here, the FE model of the damper described in Section 3.1 was verified against the obtained air gap flux density measurements. The comparison of the obtained data against the model output can be observed in Figure 12 as plots of flux density vs coil current. Due to the low current change rate, the eddy currents were neglected in the model, and only the hysteresis contribution was studied.

Again, observations of the plots reveal satisfactory agreement with the model anywhere except for the smallest exciting current. Overall, the plots prove the rationality of the proposed approach.

5.2. Hysteresis Assessment of the MR Valve. Due to reasons explained in Section 4.1, direct assessment of the hysteretic behaviour of the MR valve with the fluid in the annulus was not possible with the available laboratory equipment. However, CIP- (carbonyl powder iron-) based MR fluids show virtually zero hysteresis [12]. Therefore, the presence of the fluid in the annulus only modifies the flux density-current relationship through its (nonlinear) magnetisation characteristics. Hence, it is reasonable to proceed further under the assumption that electromagnet model of the actuator was validated, and it would be accurate also in the scenarios in which the MR annulus would be filled with the fluid. Due to the magnetic circuit saturation above 2 A, we reveal the results for the exciting currents up to 2 A (Figure 13). The nonlinear contribution of the fluid is evident in the presented results.

Next, we examine the behaviour of the valve model for the two following variants:

(i) Hysteresis (core loss) ON, eddy currents ON (solid line)

(ii) Hysteresis (core loss) ON, eddy currents OFF (dashed line)

The hysteresis model was applied to all 11SMn30 components (core, sleeve). As presented in Figure 14, the calculated remanent flux density is relatively independent of the previous magnetic history within the examined coil current range from 0.5 A to 2 A, and the effect of eddy currents is rather insignificant in the examined case as already revealed in Figure 14.

Furthermore, we repeated the flux density calculations for one selected electric current level ($I_{max} = 2$ A) for the following three model variants:

(i) Hysteresis switched OFF, eddy currents switched OFF (dashed line)

(ii) Hysteresis ON, eddy currents OFF (dotted line)

(iii) Hysteresis ON and eddy currents ON (solid line)

The results are revealed in Figure 15. It is now apparent that the hysteresis has the biggest impact on the initial
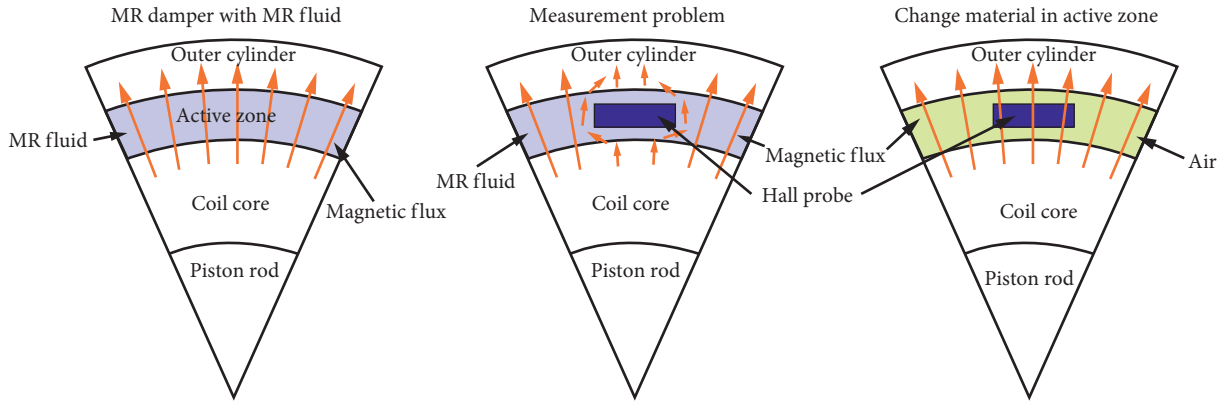
FIGURE 10: Illustration of the measurement problem with Hall sensor in the annular gap in the presence of MR fluid [41].
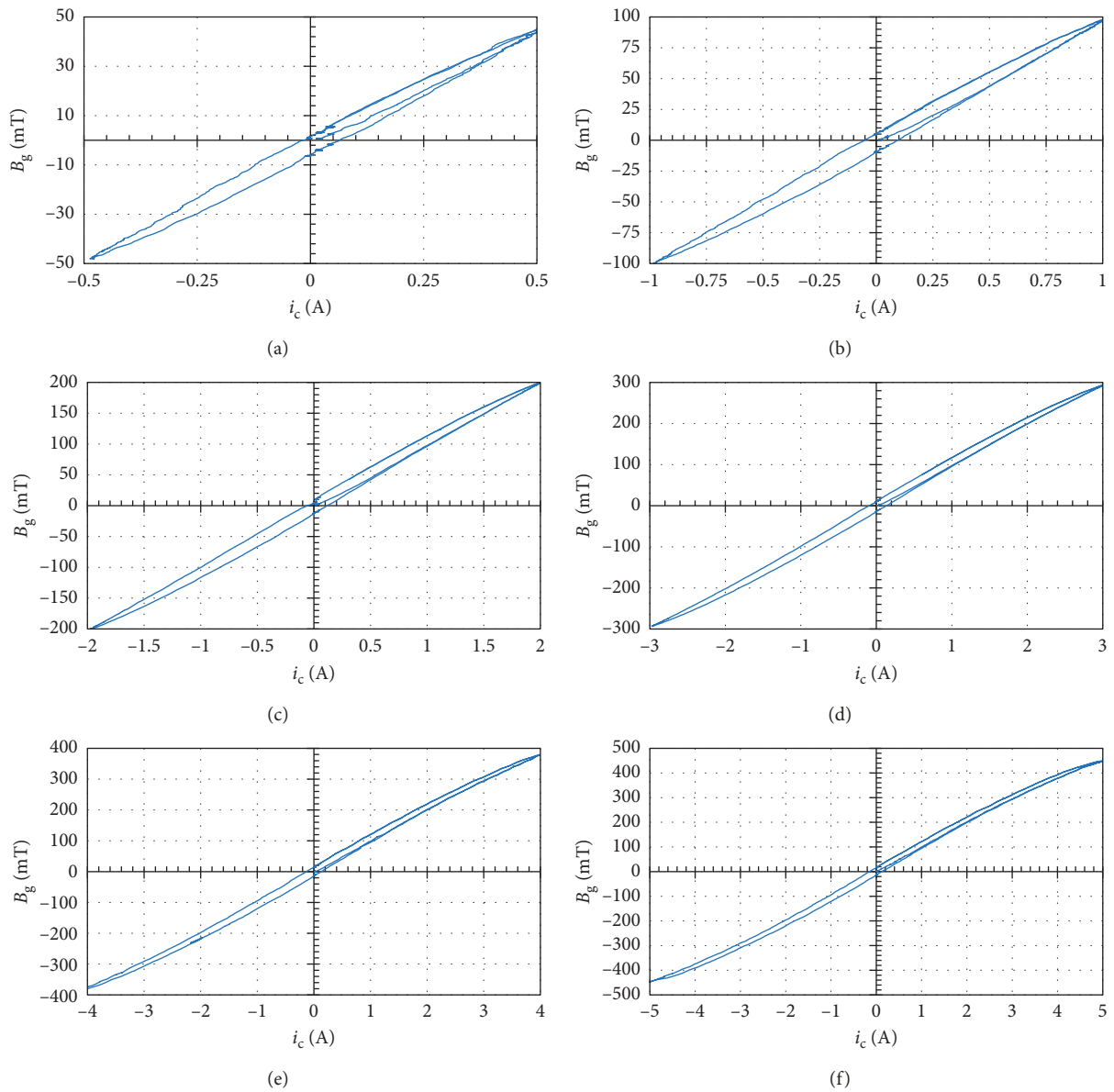
FIGURE 11: Flux density measurements: air gap, no MR fluid. (a) $I_{max} = 0.5$ A. (b) $I_{max} = 1.0$ A. (c) $I_{max} = 2.0$ A. (d) $I_{max} = 3.0$ A. (e) $I_{max} = 4.0$ A. (f) $I_{max} = 5.0$ A.
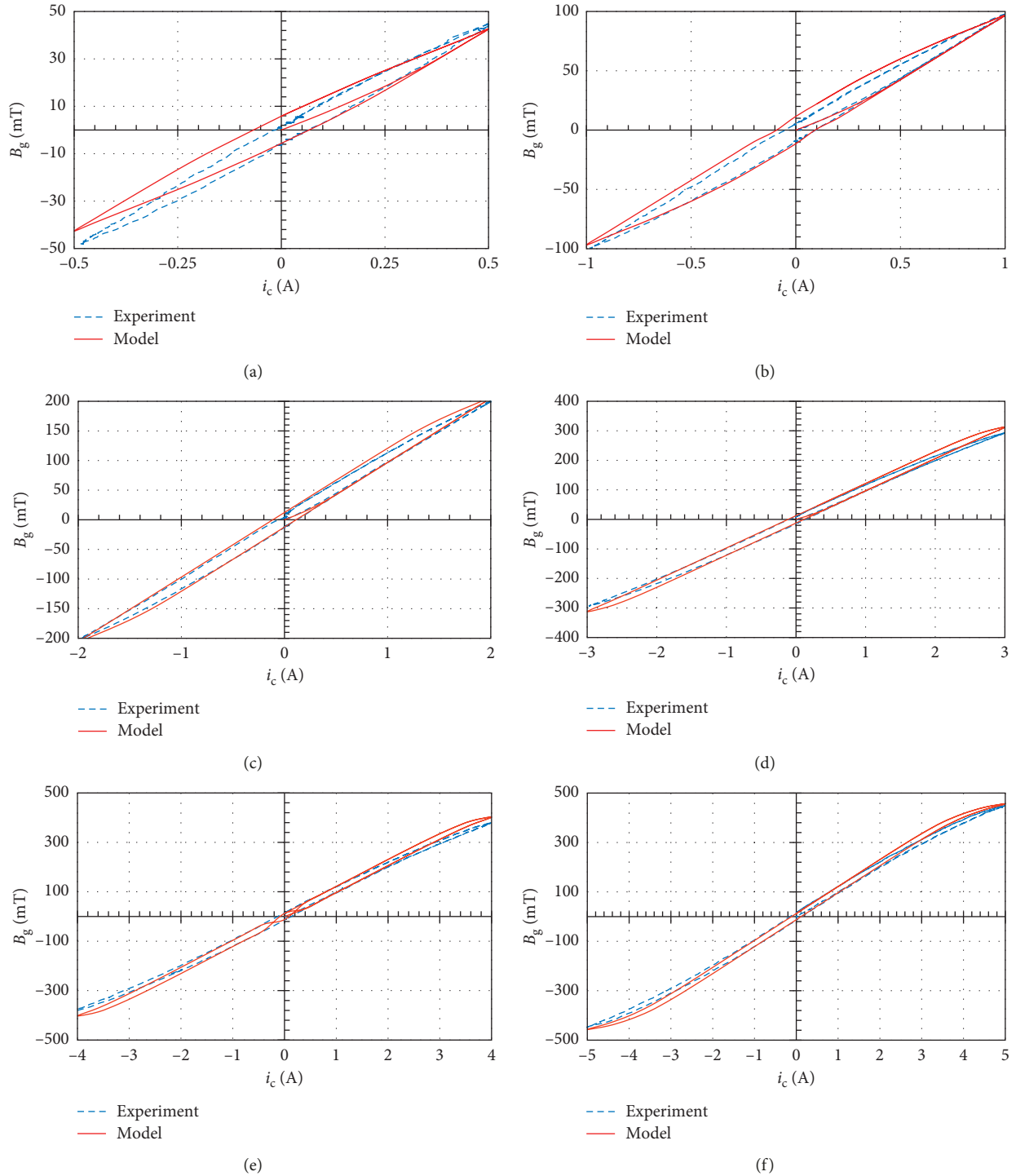
FIGURE 12: Air gap flux density: measurements vs FE model. (a) $I_{max} = 0.5$ A. (b) $I_{max} = 1.0$ A. (c) $I_{max} = 2.0$ A. (d) $I_{max} = 3.0$ A. (e) $I_{max} = 4.0$ A. (f) $I_{max} = 5.0$ A.

output of the actuator (up to 100 mT), and the contribution of the eddy currents is negligible within the examined time scale. The eddy currents have little effect on the output flux density in the examined case (Figure 15). Clearly, the first and second scenarios are only hypothetical ones and unseen

in real MR devices. However, they were included in the simulation for the purpose of isolating the contribution of a specific phenomenon.

Now, the obtained flux density output can be converted into the resulting yield stress and then used in all subsequent
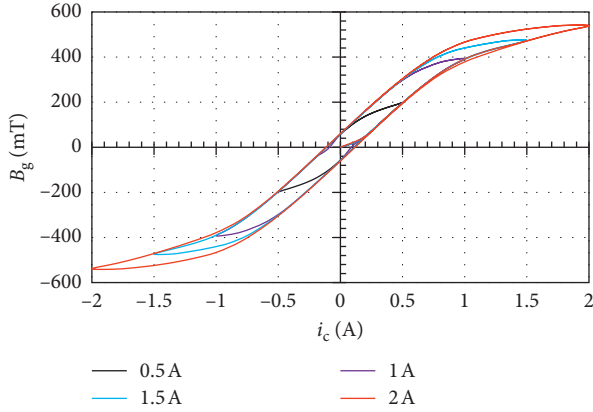
FIGURE 13: MR fluid contribution: calculated flux density vs. exciting current.
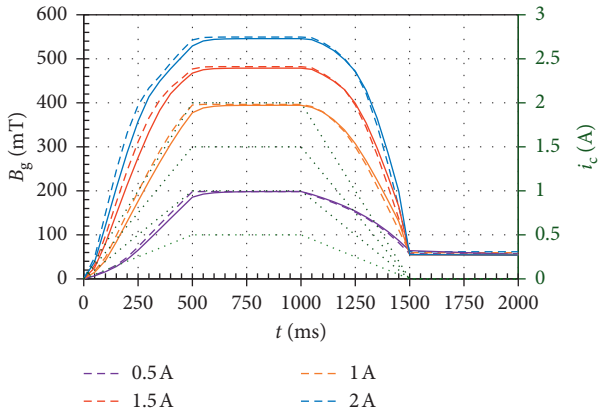
FIGURE 14: Time history of (gap) magnetic flux density: hysteresis ON (dashed line), hysteresis ON and eddy currents OFF (solid line), and electric current (dotted line).
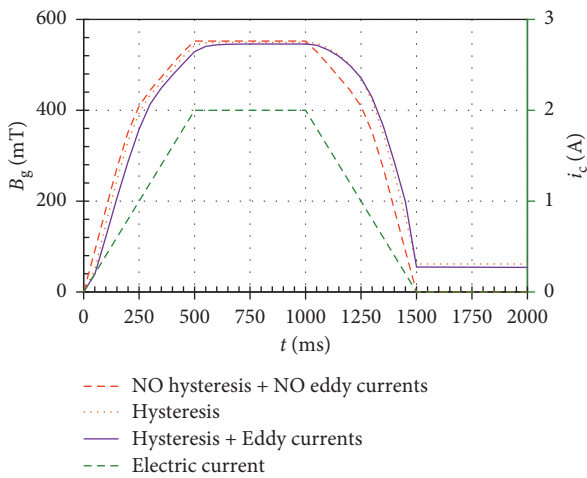
FIGURE 15: Time history: (gap) magnetic flux density, $I_{max} = 2$ A.

damper simulations (Figure 16). As seen in the calculated data, the residual flux results in the field-induced yield stress of appr. 2.23 kPa.
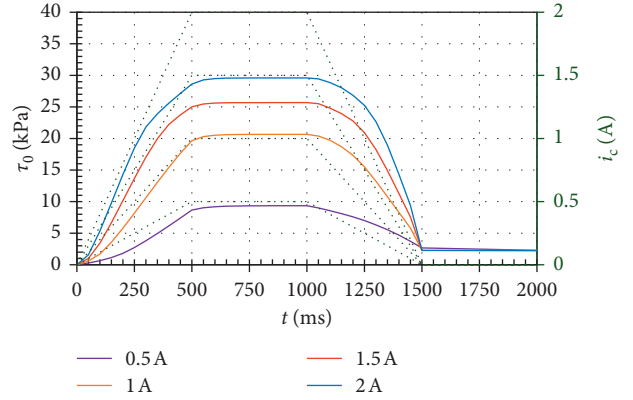
FIGURE 16: Time history: yield stress (full line) and electric current (dotted green line).

5.3. Damper Response to Sinusoidal Displacement Inputs.
Using the set of equations (1)–(9) in Section 3.2.1 and (10)–(16) in Section 3.2.2 as well as the above yield stress map in Figure 16, we then modelled the response of the damper subjected to sinusoidal displacement inputs at fixed (constant) current levels. This was merely for demonstrating the force output of the damper corresponding to the pre-scribed current levels. The calculated results are highlighted as plots of force vs velocity and force vs displacement for the peak velocity $V_r = 0.3$ m/s in Figure 17. In the calculated example, the stroking amplitude X_r was 30 mm. Note that the data are shifted by the gas force proportional to the product of the gas pressure P_g and the piston rod area A_r (equal to 339 N). Hysteresis due to compressibility of the fluid (increasing with the current/flux level), force oscillations at piston motion reversal points, can be also observed in the generated plots, too.

Moreover, the influence of remnant flux can be seen in Figure 18. In the figure, we present the results of off-state (zero current) simulations with and without de-magnetization cycle. In the revealed example, the damper was subjected to a sinusoidal displacement input at the peak velocity $V = 0.3$ m/s. The blue loops reveal the damper response after demagnetization, and the red loops copy the off-state behaviour of the damper which was previously excited at $I_{max} = 2$ A. The presence of the remanent flux (appr. 54 mT) results in the contribution of 140 N.

5.4. Damper Response to Control Current Step Inputs.
The optimal performance of a S/A (semiactive) control system with an MR damper requires understanding its dynamic behaviour. In controller design studies as well as vehicle simulation, a need for modeling the MR damper system dynamics arises quite often; the time delay between the force and the control signal due to, e.g., eddy currents degrades the system performance. Therefore, in this section, we reveal the results of a series of simulations in which the influence of eddy currents, magnetic hysteresis, and hydromechanical hysteresis (due to compressibility of the fluid) is considered. In the simulations, we assumed a fast controller [6] capable of driving the coil to within 2 ms of the commanded values.
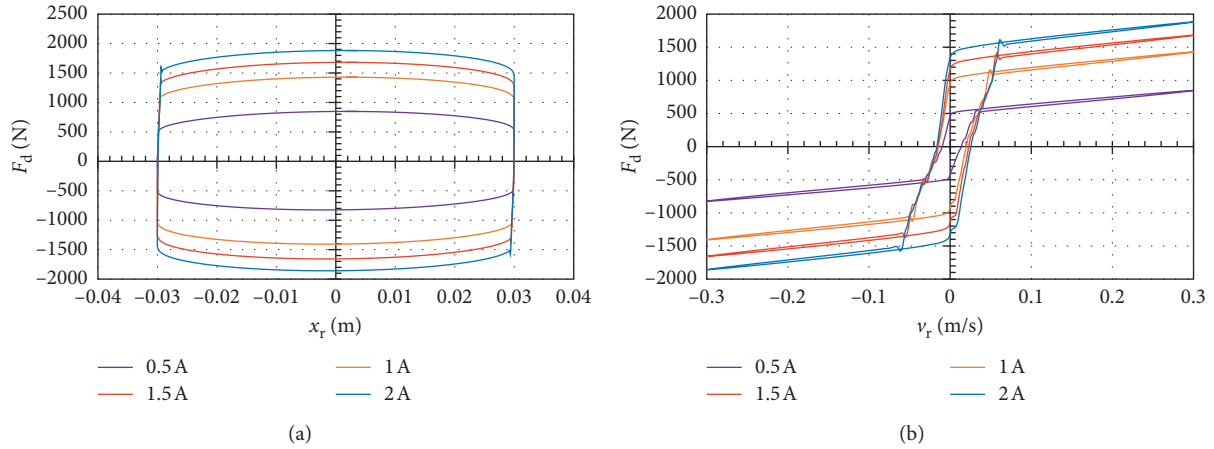
FIGURE 17: Fixed current: force vs. velocity and force vs. stroke, $V_r = 0.3$ m/s. (a) F_d vs x_r. (b) F_d vs v_r.
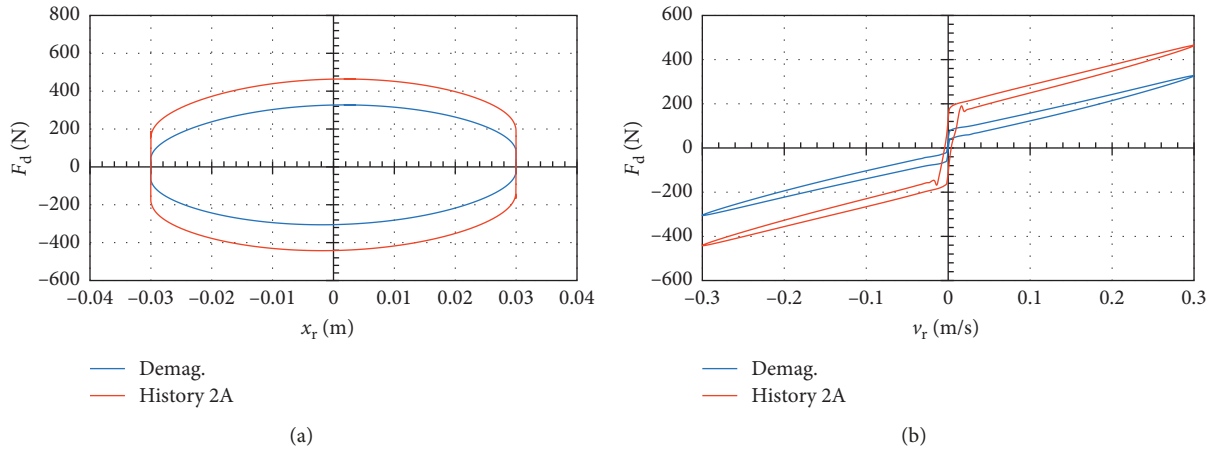
FIGURE 18: Off-state force: demagnetized (blue) and following 2 A current excitation, no demagnetization (red). (a) F_d vs x_r. (b) F_d vs v_r.

The output is highlighted in Figure 19. As seen, the actuator's off-state output is degraded by the presence of a static (residual) flux. The actuator is capable of reaching zero flux only in the hysteresis-free scenario.

In Figure 20, we further examined the force output varying the coercivity from 0 A/m to 200 A/m. It has no effect on the force output in the current (flux) rise stage; however, in the current drop case (Figure 20(b)), its contribution became evident as the actuator never reached the initial force of 240 N (prior to the current excitation).

5.5. Sensitivity to Gap Height: Parametric Study.
Next, the following series of numerical experiments involved studying the contribution of the MR valve's geometry on the residual force (and flux) output. The model setup incorporated the hysteresis loss model only and no eddy current mechanism. Throughout the experiment series, the coercivity H_c was varied from 120 A/m to 600 A/m, and the gap size h from 0.65 mm to 1.0 mm. The generated B-H loop set (core material) is revealed in Figure 21.

The calculated results are shown in Figure 22 for the maximum electric current of 2 A. The exciting current input
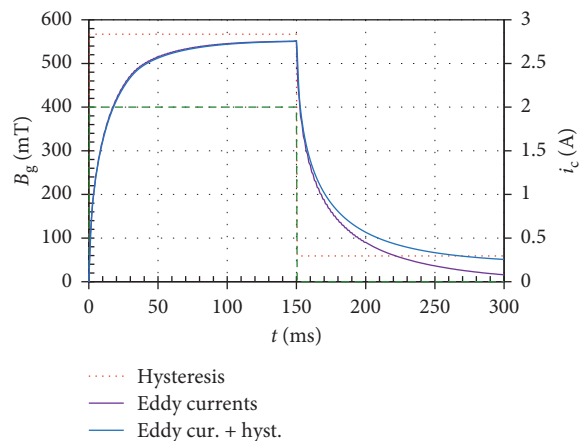
FIGURE 19: Transient FE model: time history of magnetic flux density and electric current (dashed green line).

is identical with that in Figure 14. The coercivity influences the course of the magnetic flux density over time. The greater the coercive force applied, the slower the slope of magnetic induction observed. Moreover, the material coercivity also affects the maximum achievable magnetic flux induction.

(a)

(b)
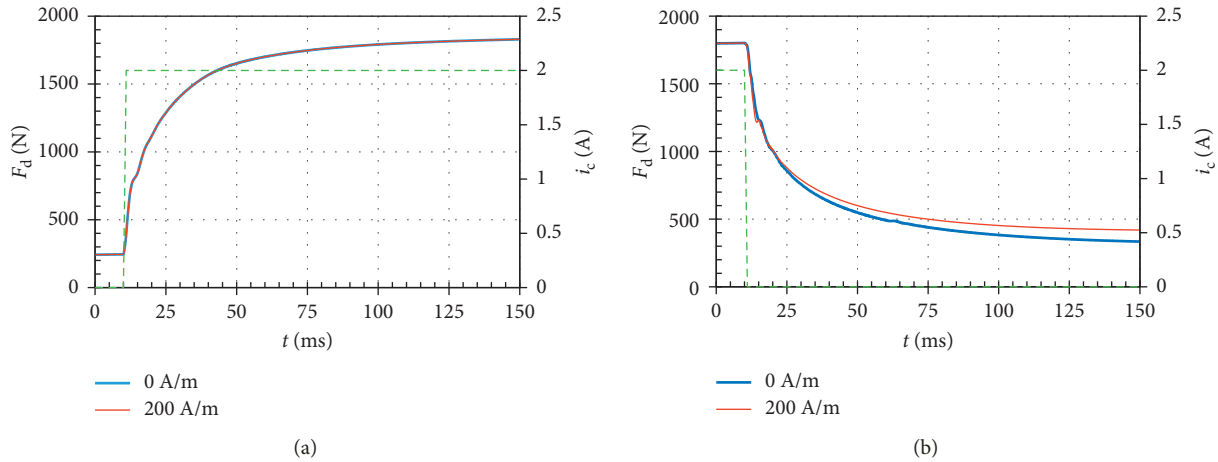
FIGURE 20: Force time history: damper response to current step input, $I_{max} = 2\,A$ (electric current course highlighted by the green dashed line). (a) Current rise. (b) Current drop.
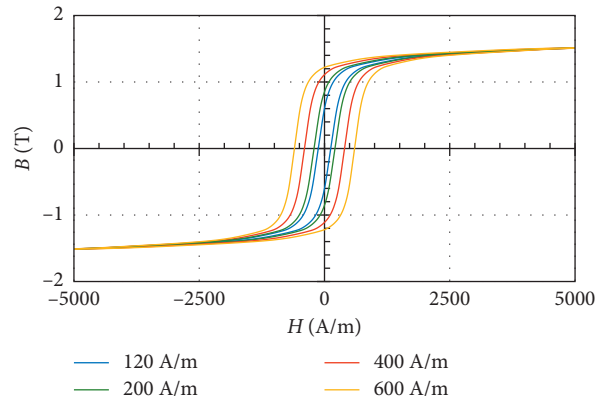
FIGURE 21: Coercivity: impact on the core material magnetisation characteristics (11SMn30).

Note that the greater the coercive force, the lower the maximum magnetic flux density generated. However, the difference is minor on the order of several percent. The difference in maximum magnetic flux density can also be due to the different shape of the generated hysteresis B-H curve by Ansys Electronics. This effect will have to be further studied in follow-up research. However, one other conclusion can be drawn: the remanent flux density follows the coercivity change. The greater the coercivity, the greater the remanent flux density induced.

The relationship of the remanent flux density vs coercivity within the range from 120 to 600 A/m is linear (Figure 23). The remanent flux density decreases as the annular gap height is increased.

Furthermore, it was of research interest to compare the impact of the material coercivity on the ratio B_{max}/B_{rem}, where B_{max} is the gap maximum flux density, as there is a significant influence of the annular gap size on the calculated flux density ratio at low material coercivity levels (Figure 24). It is evident that the gap height does not affect the flux density ratio at higher coercivity levels. This ratio follows the turn-up ratio change of the MR damper (Figure 25). The increase of gap size and the coercivity degradation

significantly increase the turn-up ratio K_f of MR damper. However, the maximum damping forces decrease at the same time as illustrated in Figure 26.

5.6. Parameter Sensitivity Study: Transient Response. In this section, we present the results of a parameter sensitivity study. Here, we examine the influence of the coercive force H_c, the electric conductivity σ, and the piston velocity v_r on the damping force under constant velocity excitation ($V_r = 0.3\,m/s$) and current step inputs.

5.6.1. Influence of Material Coercitivity. To examine the contribution of the coercivity H_c, we simulated the damper model response to current step inputs within the range from 120 A/m to 600 A/m. In each scenario, we assumed the material's electric conductivity σ equal to 1 MS/m (which is typical to some silicon steel alloys or soft magnetic composites) and the presence of eddy currents. The FE results from the transient model are shown in Figure 27. The coil current step input is also shown in Figure 27 (green dashed line).

(a)

(b)

(c)
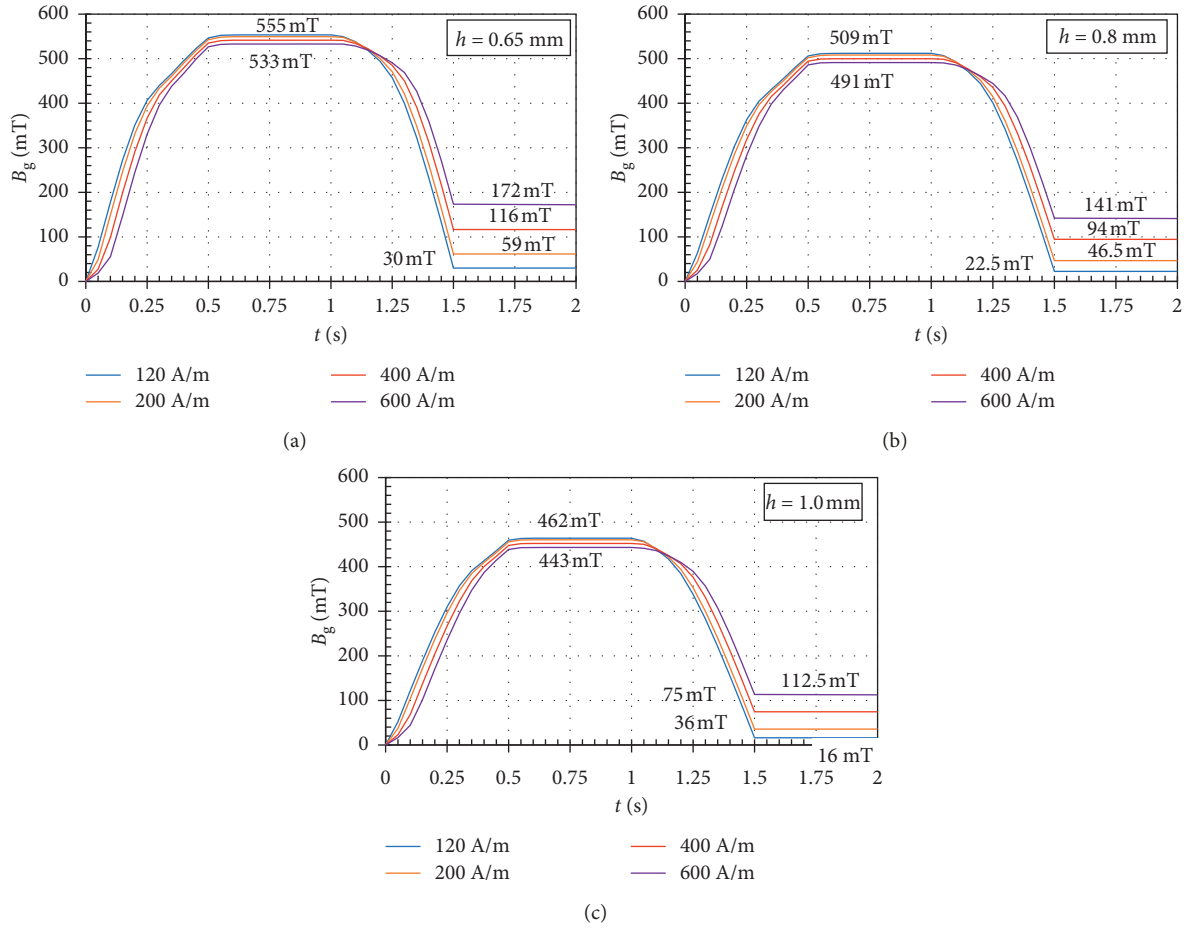
FIGURE 22: Influence of gap height and coercivity on magnetic flux density. (a) $h = 0.65$ mm. (b) $h = 0.8$ mm. (c) $h = 1.0$ mm.
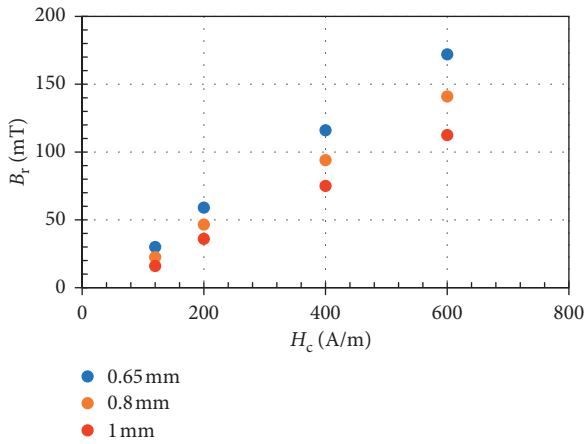
FIGURE 23: Remanent flux density variation with coercivity and gap size.
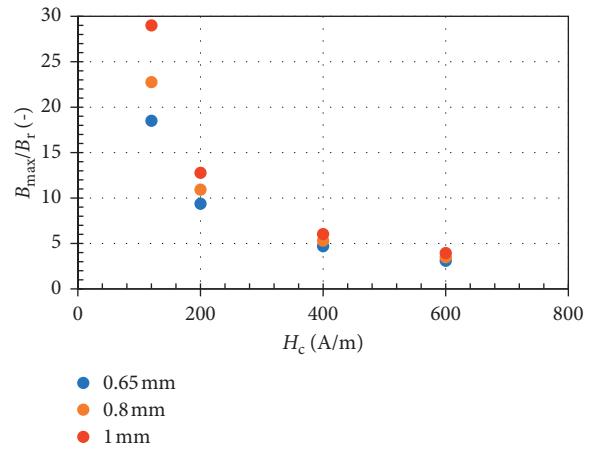
FIGURE 24: Maximum-to-remanent flux density ratio vs material coercivity.

The corresponding time histories of the damping force following the current (flux) rise/decay are revealed in Figure 28.

5.6.2. Influence of Electric Conductivity.

It is well known that the ferromagnetic material's electric conductivity has a rather dramatic effect on the eddy currents induced in

solenoid structures. Here, we simulate the transient response of the damper subjected to 2 A current step inputs. The value of 5.8 MS/m is typical of low-carbon steel alloys, whereas 1 MS/m characterizes some soft magnetic composite materials. The resulting time history is revealed in Figure 29. As shown, as the conductivity decreases, the eddy currents are reduced, and the response of the damper becomes faster.
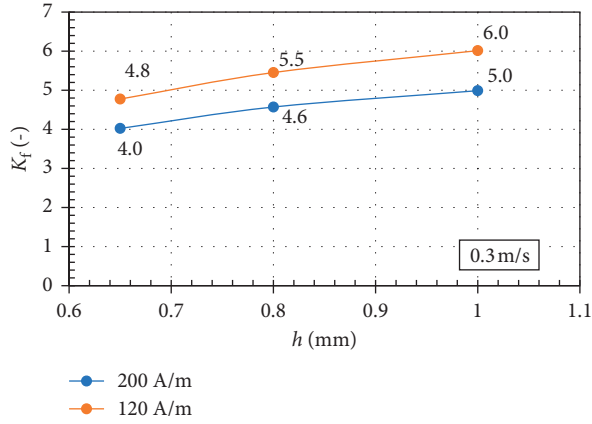
FIGURE 25: Turn-up ratio variation with gap height and coercivity, $V_r = 0.3$ m/s.
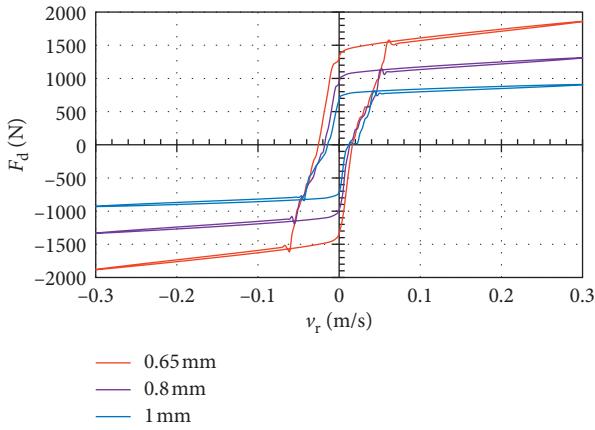
FIGURE 26: Gap height influence on damping force output, $I_{max} = 2$ A $V_r = 0.3$ m/s.
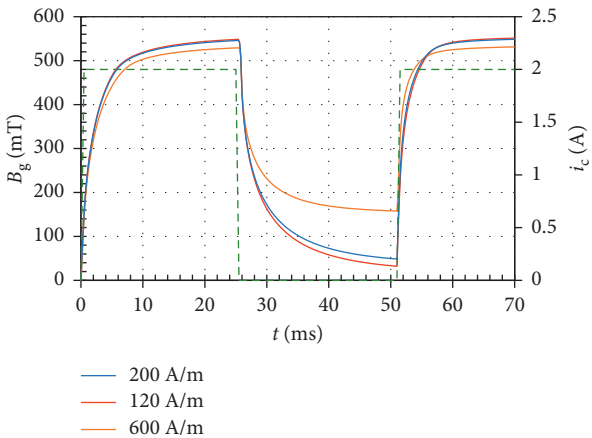
FIGURE 27: Coercivity H_c: (gap) averaged magnetic flux density time history.

5.6.3. Influence of Piston Velocity. Setting the electrical conductivity to 1 MS/m and the coercivity to 200 A/m, we then tested the influence of the piston velocity on the force. In the presented examples, the force output time histories were normalized for better comparison. The obtained results

imply that the slower the piston velocity for control current rise, the slower the magnitude of the force change rate generated. After exceeding the piston velocity of 0.2 m/s, the actuator response in the current rise stage is independent of the piston velocity (Figure 30). However, the exact velocity value will depend on the particular damper design. For comparison, the actuator response in the current drop stage is independent of the prescribed piston velocity.

Apart from the eddy currents, the main source of slower force rise is the compressibility of the MR fluid itself. Three different values of MR fluid bulk modulus were tested to illustrate this effect (Figure 31).

The primary response time of force (63.3% of final force) was calculated from the simulated data (Figure 30) (Figure 32). The primary response time for control current rise is influenced by the piston velocity. The lower the piston velocity, the lower the primary response time. However, the primary response time for control current drop is independent of piston velocity. It is noteworthy that similar trends were experimentally determined in other research studies [42, 43].

6. Conclusions and Summary

In this paper, we present the results of a modeling study involving a multiphysics model of a flow-mode MR damper. The model allows integrating an FE electromagnet model of the device with a hydraulic lumped parameter model of the device. The modeling approach relies only on the information which can be extracted from engineering drawings (geometry), material data sheets (material properties), and therefore, it can be used in studies on the performance of real actuators or virtual prototypes.

The electromagnet was verified experimentally. Based on the obtained data, we conclude that the model is capable of predicting the magnetic hysteretic behaviour of the MR valve. The results concerning the hydraulic model are simulated; however, it should be noted that the model is based on a well-established and experimentally verified theory [39]. To demonstrate the usefulness of the model, we applied it in a parametric study, in which the contribution of various geometric parameters and material properties to the output of the actuator was studied and analyzed. For instance, we can conclude the following.

(i) Residual magnetic flux is directly related to the current history and the annular gap height

(ii) Larger annular gaps induce lower remanent (residual) flux density and then less undesired force increase (Figures 22 and 23)

(iii) Valves with larger annular gaps height reveal higher turn-up ratio (dynamic range), however, at the expense of maximum damping forces (Figures 25 and 26)

(iv) Turn-up ratio (dynamic range) varies with the coercivity and gap height (Figure 25)

(v) Demagnetizing current cycles are required to reduce/eliminate the residual flux (and the force increment due to the residual flux)

(a)

(b)

(c)
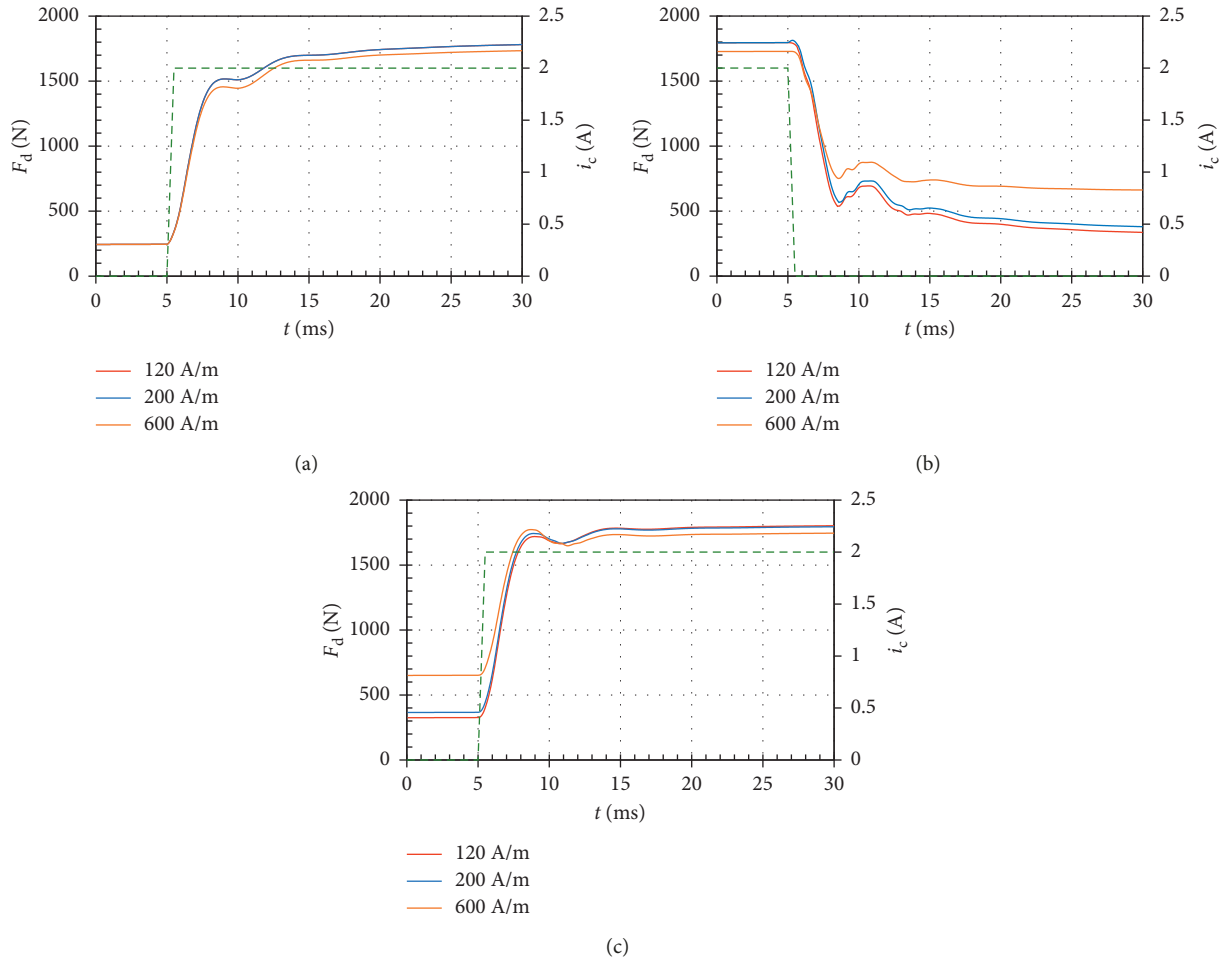
FIGURE 28: Impact of the coercivity H_c. Full line: damping force time history; green dashed line: current step input. (a) Force vs time: current rise (initial condition = demag.). (b) Force vs time: current drop. (c) Force vs time: current rise (no demag.).
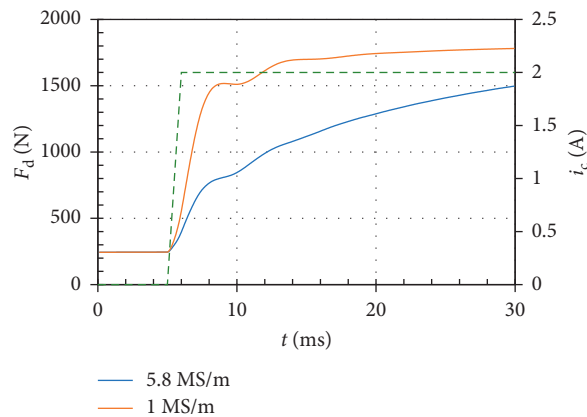
FIGURE 29: Core material's electric conductivity: Full line: damping force time history; green dashed line: current step input. $H_c = 200$ A/m, $V_r = 0.3$ m/s.

(vi) The electrical conductivity has a major influence on the dynamic behaviour of the actuator (Figure 29)

(vii) The piston velocity influences the actuator's response time. Low piston velocities degrade the response time in the current rise stage (Figures 30 and 32). It is likely due to the compressibility of the fluid (Figure 31).

The collected data enhance understanding the key mechanisms governing the flux/force output of MR
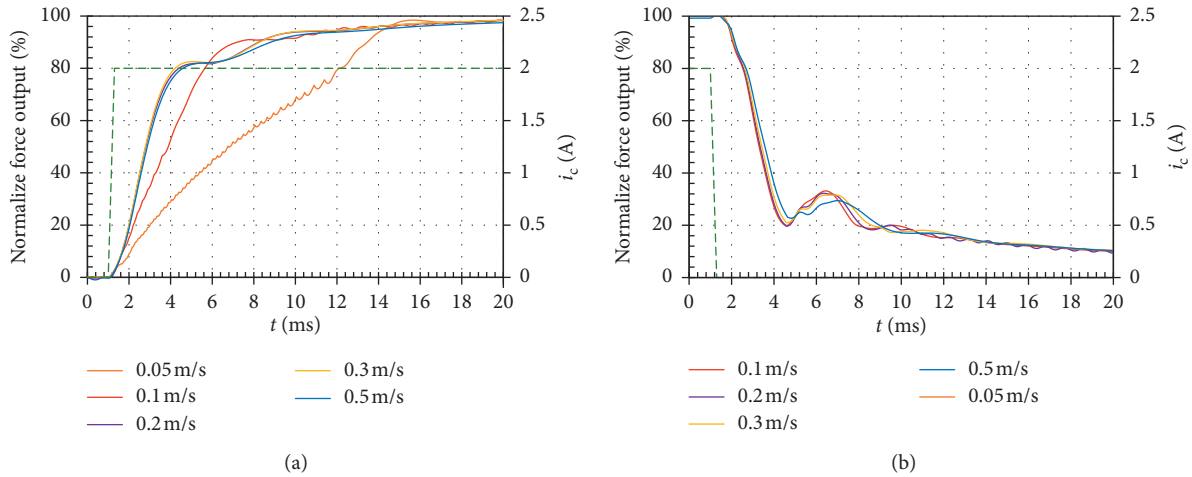
Figure 30: Influence of piston velocity for control current rise and drop (green dashed line) on the force output (full line). (a) Current rise. (b) Current drop.
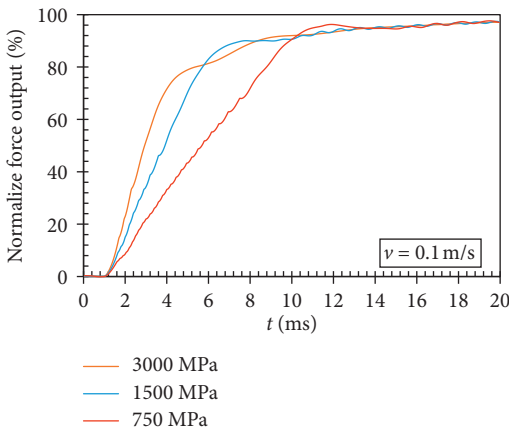
Figure 31: Influence of MR fluid bulk modulus on the force output at velocity 0.1 m/s.
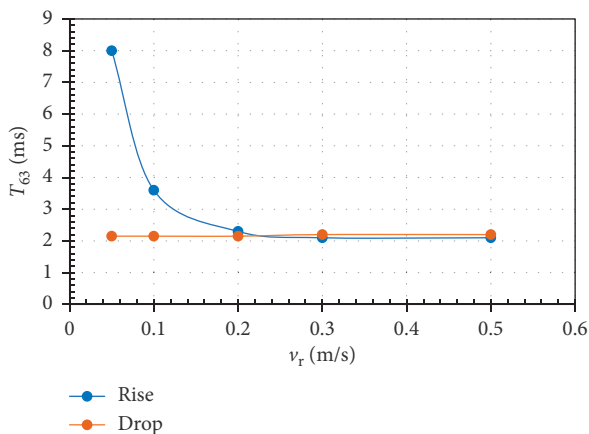
Figure 32: Influence of piston velocity on the primary response time for the rise and drop control current.

actuators. They allow for a clear separation of various contributors to the static and dynamic behaviour of such devices. In our opinion, the proposed model can be a useful tool as it incorporates major key phenomena occurring in the actuator including magnetic hysteresis and remanence/coercivity, eddy currents, compressibility, and fluid inertia (hydraulic hysteresis), the MR effect. It allows separating the magnetic hysteresis from the hydromechanical one so that the two phenomena can be examined separately.

Data Availability

The data used to support the findings of this study are available from the corresponding author upon request.

Conflicts of Interest

The authors declare that they have no conflicts of interest.

Acknowledgments

References

[1] J. Rabinow, "The magnetic fluid clutch," *Electrical Engineering*, vol. 67, no. 12, p. 1167, 1948.

[2] J. Goldasz and B. Sapinski, *Insight into Magnetorheological Shock Absorbers*, Springer, Cham, Switzerland, 2015.

[3] W. Kordonski and A. Shorey, "Magnetorheological (MR) jet finishing technology," *Journal of Intelligent Material Systems and Structures*, vol. 18, no. 12, pp. 1127–1130, 2007.

[4] M. R. Jolly, J. W. Bender, J. D. Carlson, and L. Drive, "Properties and applications of commercial magneto-rheological fluids," *Journal of Intelligent Material Systems and Structures*, vol. 10, no. 1, pp. 5–13, 1999.

[5] A. Farjoud and E. A. Bagherpour, "Electromagnet design for magneto-rheological devices," *Journal of Intelligent Material Systems and Structures*, vol. 27, no. 1, pp. 51–70, 2016.

[6] Z. Strecker, J. Roupec, I. Mazurek, O. Machacek, M. Kubik, and M. Klapka, "Design of magnetorheological damper with short time response," *Journal of Intelligent Material Systems and Structures*, vol. 26, no. 14, pp. 1951–1958, 2015.

[7] Y.-M. Han, S.-B. Choi, and N. M. Wereley, "Hysteretic behavior of magnetorheological fluid and identification using Preisach model," *Journal of Intelligent Material Systems and Structures*, vol. 18, no. 9, pp. 973–981, 2007.

[8] A. Sternberg, R. Zemp, and J. C. de la Llera, "Multiphysics behavior of a magneto-rheological damper and experimental validation," *Engineering Structures*, vol. 69, pp. 194–205, 2014.

[9] C. P. Riley, "Effect of magnetic hysteresis in solenoid valve operation," *Sensor Letters*, vol. 11, no. 1, pp. 9–12, 2013.

[10] Y. Chuang, S. Niu, S. L. Ho, W. Fu, and L. Li, "Hysteresis modeling in transient analysis of electric motors with AlNiCo magnets," *IEEE Transactions on Magnetics*, vol. 51, no. 3, pp. 1–4, 2015.

[11] J. Gołdasz, B. Sapinski, and Ł. Jastrzębski, "Assessment of the magnetic hysteretic behaviour of MR dampers through sensorless measurements," *Shock and Vibration*, vol. 2018, Article ID 3740208, 21 pages, 2018.

[12] J. de Vicente, G. Bossis, S. Lacis, and M. Guyot, "Permeability measurements in cobalt ferrite and carbonyl iron powders and suspensions," *Journal of Magnetism and Magnetic Materials*, vol. 251, no. 1, pp. 100–108, 2002.

[13] K. C. Pitman, "The influence of stress on ferromagnetic hysteresis," *IEEE Transactions on Magnetics*, vol. 26, no. 5, pp. 1978–1980, 1990.

[14] J. Zheng, Y. Li, Z. Li, and J. Wang, "Transient multi-physics analysis of a magnetorheological shock absorber with the inverse Jiles–Atherton hysteresis model," *Smart Materials and Structures*, vol. 24, no. 10, pp. 1–16, 2015.

[15] B. F. Spencer Jr., S. J. Dyke, M. K. Sain, and J. D. Carlson, "Phenomenological model for magnetorheological dampers," *Journal of Engineering Mechanics*, vol. 123, no. 3, pp. 230–238, 1997.

[16] I. D. Mayergoyz, "Dynamic Preisach models of hysteresis," *IEEE Transactions on Magnetics*, vol. 24, no. 6, pp. 2925–2927, 1988.

[17] B. D. Coleman and M. L. Hodgdon, "A constitutive relation for rate-independent hysteresis in ferromagnetically soft materials," *International Journal of Engineering Science*, vol. 24, no. 6, pp. 897–919, 1986.

[18] D. C. Jiles and D. L. Atherton, "Theory of ferromagnetic hysteresis," *Journal of Magnetism and Magnetic Materials*, vol. 61, no. 1-2, pp. 48–60, 1986.

[19] D. C. Jiles, J. B. Thoelke, and M. K. Devine, "Numerical determination of hysteresis parameters for the modeling of magnetic properties using the theory of ferromagnetic hysteresis," *IEEE Transactions on Magnetics*, vol. 28, no. 1, pp. 27–35, 1992.

[20] A. Raghunathan, Y. Melikhov, J. E. Snyder, and D. C. Jiles, "Modeling the temperature dependence of hysteresis based on Jiles-Atherton theory," *IEEE Transactions on Magnetics*, vol. 45, no. 10, pp. 3954–3957, 2009.

[21] K. Chwastek, "Frequency behaviour of the modified Jiles–Atherton model," *Physica B: Condensed Matter*, vol. 403, no. 13–16, pp. 2484–2487, 2008.

[22] J. Tellinen, "A simple scalar model for magnetic hysteresis," *IEEE Transactions on Magnetics*, vol. 34, no. 4, pp. 2200–2206, 1998.

[23] Y. M. Han, S. C. Lim, H. G. Lee, S. B. Choi, and H. J. Choi, "Hysteresis identification of polymethylaniline-based ER fluid using Preisach model," *Materials & Design*, vol. 24, no. 1, pp. 53–61, 2003.

[24] P. Yadmellat and M. R. Kermani, "Adaptive modeling of a magnetorheological clutch," *IEEE/ASME Transactions on Mechatronics*, vol. 19, no. 5, pp. 1716–1723, 2014.

[25] J. An and D.-S. Kwon, "Modeling of a magnetorheological actuator including magnetic hysteresis," *Journal of Intelligent Material Systems and Structures*, vol. 14, no. 9, pp. 541–550, 2003.

[26] C. Jędryczka, P. Sujka, and W. Szeląg, "The influence of magnetic hysteresis on magnetorheological fluid clutch operation," *COMPEL—International Journal for Computation and Mathematics in Electrical and Electronic Engineering*, vol. 28, no. 3, pp. 711–721, 2009.

[27] P. Guo, J. Xie, and X. Guan, "Dynamic model of MR dampers based on a hysteretic magnetic circuit," *Shock and Vibration*, vol. 2018, Article ID 2784950, 13 pages, 2018.

[28] J. Goldasz, B. Sapinski, and L. Jastrzebski, "On the application of Bouc-Wen hysteresis approach for modeling of MR actuators," in *Proceedings of the Actuator 16th International Conference on New Actuators*, pp. 1–5, Breme, Germany, June 2018.

[29] S. M. Chen, W. A. Bullough, and J. Hart, "CFD study of the flow in a radial electrorheological fluid clutch," *Journal of Physics: Conference Series*, vol. 21, no. 15, pp. 1569–1574, 2010.

[30] D. Lin, P. Zhou, and A. Bergqvist, "Improved vector play model and parameter identification for magnetic hysteresis materials," *IEEE Transactions on Magnetics*, vol. 50, no. 2, pp. 18–21, 2014.

[31] J. Goldasz and B. Sapinski, "Nondimensional characterization of flow-mode magnetorheological/electrorheological fluid dampers," *Journal of Intelligent Material Systems and Structures*, vol. 23, no. 14, pp. 1545–1562, 2012.

[32] Lord Company, http://www.lordmrstore.com/lord-mr-products/mrf-132dg-magneto-rheological-fluid.

[33] M. Rosu, P. Zhou, D. Lin et al., *Multiphysics Simulation by Design for Electrical Machines, Power Electronics, and Drives*, John Wiley & Sons, Hoboken, NJ, USA, 2018.

[34] D. Lin, P. Zhou, C. Lu, N. Chen, and M. Rosu, "Construction of magnetic hysteresis loops and its applications in parameter identification for hysteresis models," in *Proceedings of the 2014 International Conference on Electrical Machines (ICEM)*, pp. 1050–1055, Berlin, Germany, September 2014.

[35] M. Rosu, *Advanced Hysteresis Modeling*, Ansys, Canonsburg, PA, USA, 2017.

[36] N. M. Wereley and L. Pang, "Nondimensional analysis of semi-active electrorheological and magnetorheological dampers using approximate parallel plate models," *Smart Materials and Structures*, vol. 7, no. 5, pp. 732–743, 1998.

[37] W. Hu and N. M. Wereley, "Nondimensional damping analysis of flow-mode magnetorheological and electrorheological dampers," in *Proceedings of the ASME 2003 International Mechanical Engineering Congress and Exposition*, pp. 265–272, American Society of Mechanical Engineers, Washington, DC, USA, November 2003.

[38] R. W. Phillips, *Engineering Applications of Fluids with a Variable Yield Stress*, University of California, Berkeley, CA, USA, 1969.

[39] J. Goldasz and B. Sapinski, "Verification of magnetorheological shock absorber models with various piston configurations," *Journal of Intelligent Material Systems and Structures*, vol. 24, no. 15, pp. 1846–1864, 2013.

[40] Mathworks Matlab, https://www.mathworks.com.

[41] M. Kubík, O. Machacek, Z. Strecker, J. Roupec, P. Novak, and
     I. Mazurek, "Transient magnetic model of magnetorheological
     damper and its experimental verification," *MATEC Web of
     Conferences*, vol. 153, article 06002, 2018.

[42] Z. Strecker, M. Kubík, P. Vítek, J. Roupec, D. Paloušek, and
     V. Šreibr, "Structured magnetic circuit for magneto-
     rheological damper made by selective laser melting tech-
     nology," *Smart Materials and Structures*, vol. 28, no. 5, article
     055016, 2019.

[43] M. Kubík, O. Macháček, Z. Strecker, J. Roupec, and
     I. Mazůrek, "Design and testing of magnetorheological valve
     with fast force response time and great dynamic force range,"
     Smart Materials and Structures, vol. 26, no. 4, article 047002,
     2017.

Research Article

Modelling Magnetorheological Dampers in Preyield and Postyield Regions

E. Palomares ⓘ, A. L. Morales ⓘ, A. J. Nieto ⓘ, J. M. Chicharro ⓘ, and P. Pintado ⓘ

Universidad de Castilla-La Mancha, ETSI Industriales, Departamento de Mecánica Aplicada e Ing. de Proyectos,
Avda. Camilo José Cela, 13071 Ciudad Real, Spain

Correspondence should be addressed to E. Palomares; eduardo.palomares@uclm.es

The use of magnetorheological dampers has rapidly spread to many engineering applications, especially those related to transportation and civil engineering. The problem arises upon modelling their highly nonlinear behaviour: in spite of the huge number of apparently accurate models in the literature, most fail when considering the overall magnetomechanical behaviour. In this study, a brief but broad review of different magnetorheological damper models has been carried out, which includes characterisation, modelling, and comparison. Unlike many other studies, the analyses cover the behaviour from preyield to postyield regions of the MR fluid. The performance of the different models has been assessed by means of numerous experimental tests and by means of simulations in a simple and straightforward semiactive control case study. The results obtained prove that most models usually fail in predicting accurate low-velocity behaviour (before iron chains yield) and, as a result, may lead to bad estimations when used in control schemes due to modelling errors and chattering.

1. Introduction

Traditional materials and fluids are being replaced by smart materials and fluids which enhance features for cutting edge technological challenges. May be the most common example of smart fluid is magnetorheological (MR) fluids, which were discovered and developed by Rabinow at the U.S. National Bureau of Standards in the late 1940s [1]. These fluids modify their rheological behaviour as a response to applied magnetic fields [2–4]. They are noncolloidal suspensions where the continuous phase is mineral oil and the dispersed phase consists of high purity iron particles on the order of a few microns in volume fractions from 20% up to 50%. The magnetically-induced dipoles form chain-like structures parallel to the applied field, which restricts the motion of the fluid and increases viscosity. The higher the magnetic field, the higher the energy needed to break those chains and hence reduce viscosity. Several studies have been carried out not only to characterise pre- and postyield regions [5–7] but also many other aspects such as particle shape, which affects durability and abrasion [8], or the type of mineral oil, which

influences behaviour as proven by Lim et al. [9] and Park et al. [10].

Carlson and Jolly showed the huge variety of commercial applications that these fluids open up [11]. They are used in many fields and devices but one should emphasize their use as active dampers or shock absorbers [12] in applications which may range from civil engineering (buildings and bridges [13–16]) to transportation (vehicle seats [17, 18], automobiles [19–24], railway vehicles [25–27], and even landing gears [28]).

The authors have found in the literature a huge number of studies dealing with modelling of MR dampers as a function of excitation and current supplied. Topical reviews, such as that carried out by Wang and Liao [29], provide support for this statement. The simplest and most widely known model is the Bingham model [30] where the MR fluid is treated as a Newtonian fluid only from a specific threshold force or yield stress [31]. Later, Wang and Gordaninejad [32] used a Herschel–Bulkley fluid model which considers a pseudoplastic behaviour in the postfluence region [33]. More intricate models also take into account the preyield

region, such as the biviscous model [34, 35] or those developed by Soltane et al. [36] which model a soft transition between pre- and postyield regions based on a Papanastasiou fluid model [37].

None of these models consider the inherent and characteristic hysteresis of the force vs. velocity cycles in MR dampers despite having been thoroughly studied. Among many other authors, one can mention Soltane et al., who used a nonhysteretic model as a base [36]; Guo et al., who modified the Bingham model and considered displacement along with velocity [38]; Pang et al., with a version with branches of the biviscous model [39]; Choi et al., with a brute-force polynomial fitting [40, 41]; or Spencer et al. who linked a phenomenological model with a general solution for a large class of hysteretic systems [42].

The great number of scientific papers related to modelling MR dampers clearly indicates that this is a topic far from being solved. Although almost all the proposed models show accurate behaviour, none of them seem to hit the nail on the head. In general, characterisation, modelling, and validation tests are carried out in a relatively short range of medium velocities, so neither the lower nor the higher velocities can be successfully simulated. In addition, some significant aspects such as frictions, accumulator stiffness, and even hysteresis are usually neglected, which leads to over or underestimate the goodness of the proposed active or semiactive control technique. Nevertheless, one should not overcomplicate the models since that could hinder applicability in certain fields. A good example is the use of MR models in closed-loop control systems [43], which often demand concise and robust direct models (free from instabilities, chattering, and high computational costs), as well as effective and easily derivable inverse models.

The authors present in this work a brief but broad review of different MR damper models as well as a thorough experimental comparison of all the models considered. Indeed, these comparisons are fair because not only are they quantitative but they are also based on the same commercial MR damper. The experiment design also permits a better understanding of the MR damper behaviour from quasistatic to wide-range dynamic conditions and serves to figure out advantages and drawbacks of the different models. A case study of semiactive control is also shown to obtain a fair and useful comparison between models.

2. Characterisation of a MR Damper

Experimental characterisation and the following model comparisons have been made on a commercial magnetorheological damper RD-8040-1 manufactured by the Lord Corporation. It is a monotube shock containing high-pressure nitrogen gas (300 psi). Experimental tests have been carried out in a Material Testing System MTS-810 where the damper, in the midstroke position, was jointed in order to avoid misalignment.

MR fluid can accumulate sediment if it remains in the same static position for long periods. Thus, the specimen must be excited in order to obtain a homogeneous suspension of the iron particles prior to the tests. Moreover, temperature of the fluid may affect the obtained results. Figure 1(a) shows the variation of temperature of the damper body while working (sinusoidal excitation of amplitude 8 mm at 0.5 Hz) at different currents applied (0, 0.5, and 1 A). The higher the current, the higher the steady temperature and the time required to achieve it. The significance of the working temperature is shown in Figure 1(b) where the damper force is shown to be temperature dependent. Differences are noticeable (up to 40%) and the behaviour of the MR damper becomes more symmetric and predictable once the steady working temperature has been achieved.

Quasistatic tests were carried out in order to characterise the stiffness due to the compressed nitrogen gas chamber along with friction forces. Figure 2 shows the force vs. displacement curve after contracting and extending the shaft for 3 hours (aprox. $10 \, \mu$m/s). One may observe that there is a slope which defines the stiffness of the nitrogen gas chamber as well as hysteresis due to friction forces. The friction is noticeable higher when reaching the top and bottom ends of the stroke, which suggests a more complicated source of friction than the usual Coulomb friction. Both stiffness and friction can explain the nonsymmetric force-velocity curves which appear when low velocities are tested.

Dynamic tests are obtained by subjecting the damper to a sinusoidal excitation, where the amplitude is 4, 8, 12, or 16 mm, whereas the frequency is set to 0.1, 0.5, 1, 2, or 4 Hz. The resulting 20 combinations cover a wide range of velocities from 2.5 to 400 mm/s, which is considerably higher than those studied by other authors. These tests allows for studying different phenomenological situations:

(a) Low (L) velocity tests where preyield region dominates (up to 15 mm/s)

(b) Medium (M) velocity tests where pre- and postyield regions are balanced (up to 100 mm/s)

(c) High (H) velocity tests where postyield region dominates (over 100 mm/s)

In addition, five different intensities have been considered (0, 0.25, 0.50, 0.75, and 1 A) which leads to a total of 100 different characterisation tests.

The tests conducted permit the usual force-velocity hysteresis features (well described in [29]) to be characterised: it progresses along a counter-clockwise path, is strong only in the preyield domain, exhibits roll-off in the vicinity of zero velocity, and seems to depend on several parameters. Leaving aside the obvious intensity dependence, Wang and Liao argued that hysteresis shows displacement amplitude and frequency dependence for sinusoidal experimental tests where $z = d \sin(2\pi f t)$ [29], but this means that hysteresis depends on maximum velocity: $2\pi \, df$. In order to determine dependences different from velocity, Figure 3 compares tests in which maximum velocity remains constant. Whether differences should be attributed to displacement (d), acceleration ($4\pi^2 df^2$), or both of them is not clear, but not taking this behaviour into account would deteriorate model performance.

(a)

(b)
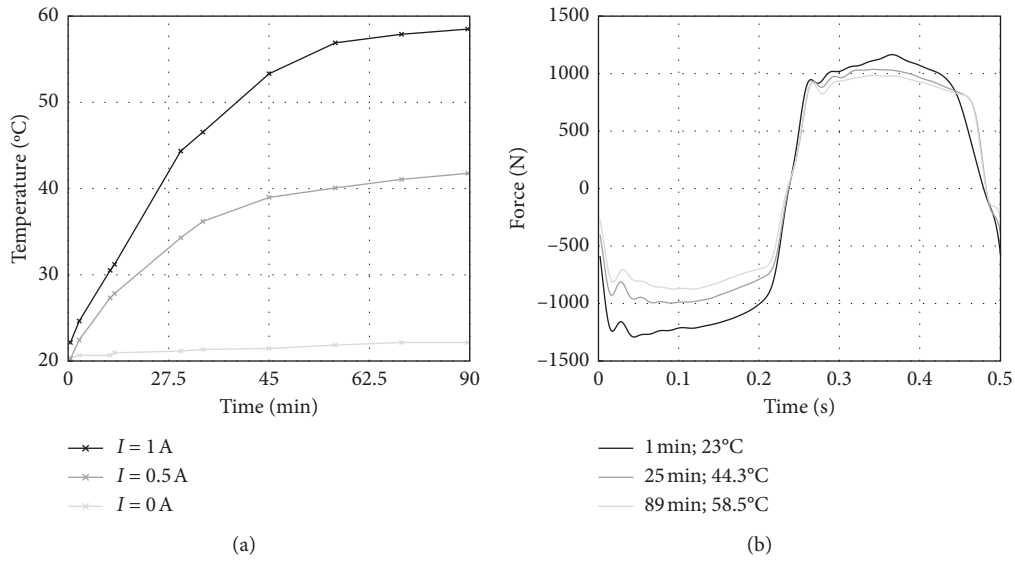
Figure 1: (a) Time response of the MR damper body temperature for three different currents (0, 0.5, and 1 A) and (b) sample of a damper force cycle with a constant current of 1 A after different elapsed times (1, 25, and 90 minutes). In both cases, the excitation is a sinusoidal excitation of 8 mm amplitude and 2 Hz frequency.

Figure 2: Quasistatic force-displacement cycle of the MR damper (3 hours per cycle).

(a)

(b)

Figure 3: Force-velocity hysteresis cycles for different experimental sinusoidal tests. (a) $I = 0$ A, (b) $I = 1$ A.

3. Review of MR Damper Models

In order to carry out a straightforward description of the state of the art related to modelling of MR dampers, all the parametric models referred to are expressed with the same (if possible) nomenclature. Figure 4 shows the most recurrent variables in the parametric models. F is the actual damper force, but the models will describe the net force $F - f_0$, that is, the force after subtracting the contribution of the nitrogen gas accumulator when the shaft remains in the midstroke position (f_0). z refers to the shaft displacement from the midstroke position, where a positive value means a contraction of the rod. C_0 and C_∞ are usual damping constants which would linearly define the force-velocity curves in the preyield and postyield regions. In fact, these regions have a frontier in the velocity $\dot{z}_y$, whereas f_y refers to the force that makes the iron chains yield (f_y) in the Bingham model (that is, the origin ordinate for the C_∞ line). For those models which predict hysteresis, $\dot{z}_h$ means the zero force velocity intercept. Adopting such a nomenclature for all the models will shed some light on the currently fuzzy state of the art and will demonstrate that proposed models are not as different as they may initially seem.

In 1922, Eugene C. Bingham proposed the mathematical form of a viscoplastic model for those materials that behave as a rigid body at low stresses and as a viscous fluid at high stresses [31]. Perhaps from the works of Stanway et al. in the late 1980s [30], the so-called Bingham model has been used to model the rheological behaviour of MR fluids easily. The idealised mechanical model consists of a Coulomb friction element (related to the fluid yield stress) in parallel with a viscous damper:

$$F - f_0 = f_y \operatorname{sign}(\dot{z}) + C_\infty \dot{z}. \tag{1}$$

Wang and Gordaninejad in [32] argued that the postyield viscoplastic behaviour in MR fluids is not constant as assumed by the Bingham model but agrees with a non-Newtonian Herschel–Bulkley fluid model [33]. Although the mathematical form of this model was developed to describe MR fluid dynamics through pipes and parallel plates, this behaviour can be used to predict the MR damper force:

$$F - f_0 = f_y \operatorname{sign}(\dot{z}) + C_\infty |\dot{z}|^n \operatorname{sign}(\dot{z}). \tag{2}$$

This formulation provides a nonlinear behaviour in the postyield region which more closely resembles experimental data.

Rather than assuming that the MR fluid is rigid in the preyield condition, as the Bingham model does, Stanway et al. [35] adopted the nonlinear biviscous model where the MR fluid is plastic in both the pre- and postyield conditions:

$$F - f_0 = \begin{cases} C_0 \dot{z}, & \text{if } |\dot{z}| < \dot{z}_y, \\ f_y \operatorname{sign}(\dot{z}) + C_\infty \left(\dot{z} - \operatorname{sign}(\dot{z}) \dot{z}_y \right), & \text{if } |\dot{z}| \geq \dot{z}_y, \end{cases} \tag{3}$$

where continuity in the piecewise function is given by the fact that $f_y = C_0 \dot{z}_y$. In fact, the Bingham model can be

Figure 4: Main MR model parameters.

regarded as a limiting case of this model in which $\dot{z}_y \longrightarrow 0$ and hence $C_0 = f_y/\dot{z}_y \longrightarrow \infty$.

Soltane et al. returned to the starting point very recently and proposed a new modification of the Bingham model which also includes a preyield region [36]. Unlike the biviscous model, the regularised Bingham model (RB in the following) proposes a continuous equation based on the Papanastasiou fluid model that smoothes the yield criterion [37], that is,

$$F - f_0 = f_y \operatorname{sign}(\dot{z}) \left[1 - e^{-\operatorname{sign}(\dot{z})(\dot{z}/\dot{z}_y)} \right] + C_\infty \dot{z}, \tag{4}$$

where $\dot{z}_y$, although it can be still be considered as the transition velocity, is more properly an artificial regularisation parameter with the dimension of velocity which controls the exponential growth of the damping force. The smaller the parameter, the more similar the approximation to the initial Bingham model.

Until now, the models described have shown an evolution which tends to model a biviscous behaviour with a soft transition between pre- and postyield regions, leaving aside the hysteretic behaviour of the MR damper. One of the first approaches to the hysteresis modelling was carried out by Gamota and Filisko with an extension of the Bingham model [44]. It is a viscoelastic-plastic model (viscoelastic in preyield region and plastic in postyield region) based on the Bingham model in series with a standard model of a linear solid [45]. Nevertheless, this model is usually discarded because its governing equations are extremely stiff.

A simpler solution to include the hysteretic phenomenon is to duplicate any nonhysteretic model into two different branches: one for contraction and another for extension. May be the easiest approach (which includes pre- and postdomains) is the hysteretic biviscous model developed by Pang et al. in 1998 [39]. It is an extension of Stanway et al.'s biviscous model with an improved representation of the preyield hysteresis. This is accomplished by adding a fourth parameter, that is, the zero force velocity

intercept $\dot{z}_h$ which causes a translation in the axis of abscissas ($\dot{z}$) as indicated by the following piecewise continuous function:

$$F - f_0 = \begin{cases} C_\infty \dot{z} - f_y, & \text{if } \left(\dot{z} < -\dot{z}_{yc} \right) \text{ and } \left(\ddot{z} > 0 \right), \\ C_0 \left(\dot{z} - \dot{z}_h \right), & \text{if } \left(-\dot{z}_{yc} \leq \dot{z} \leq \dot{z}_{ye} \right) \text{ and } \left(\ddot{z} > 0 \right), \\ C_\infty \dot{z} + f_y, & \text{if } \left(\dot{z}_{ye} < \dot{z} \right) \text{ and } \left(\ddot{z} > 0 \right), \\ C_0 \dot{z} + f_y, & \text{if } \left(\dot{z}_{yc} < \dot{z} \right) \text{ and } \left(\ddot{z} < 0 \right), \\ C_\infty \left(\dot{z} + \dot{z}_h \right), & \text{if } \left(-\dot{z}_{ye} \leq \dot{z} \leq \dot{z}_{yc} \right) \text{ and } \left(\ddot{z} < 0 \right), \\ C_0 \dot{z} + f_y, & \text{if } \left(\dot{z} < -\dot{z}_{ye} \right) \text{ and } \left(\ddot{z} < 0 \right), \end{cases} \tag{5}$$

where the contraction yield velocity $\dot{z}_{yc}$ and the extension yield velocity $\dot{z}_{ye}$ are also introduced and given by the expressions:

$$\dot{z}_{yc} = \frac{f_y - C_0 \dot{z}_h}{C_0 - C_\infty},$$
$$\dot{z}_{ye} = \frac{f_y + C_0 \dot{z}_h}{C_0 - C_\infty}. \tag{6}$$

In the same vein, Soltane et al. proposed the hysteretic regularised Bingham model (HRB) which modifies the nonhysteretic version by translating pre- and postyield regions to the left or right (a quantity defined by the zero force velocity intercept $\dot{z}_h$) depending on the compression or extension [36]:

$$F - f_0 = \begin{cases} C_\infty \left(\dot{z} - \dot{z}_h \right) + f_y \left(1 - e^{-\text{sign} \left(\dot{z} - \dot{z}_h \right) \left(\left(\dot{z} - \dot{z}_h \right) / \dot{z}_y \right)} \right) \text{sign} \left(\dot{z} - \dot{z}_h \right), & \text{if } \ddot{z} < 0, \\ C_\infty \left(\dot{z} + \dot{z}_h \right) + f_y \left(1 - e^{-\text{sign} \left(\dot{z} + \dot{z}_h \right) \left(\left(\dot{z} + \dot{z}_h \right) / \dot{z}_y \right)} \right) \text{sign} \left(\dot{z} + \dot{z}_h \right), & \text{if } \ddot{z} > 0. \end{cases} \tag{7}$$

Guo et al. took a leap forward in 2006 when they developed a more concise and non-piecewise model which describes not only a smooth biviscous behaviour but also the hysteretic behaviour of MR dampers [38]:

$$F - f_0 = f_y \tanh \left(C_0 \left(\dot{z} + \Omega z \right) \right) + C_\infty \left(\dot{z} + \Omega z \right), \tag{8}$$

Ω is defined as the absolute value of the hysteretic critical velocity divided by the absolute value of the hysteretic critical displacement, that is, $z_h / \dot{z}_h$. The authors of this model emphasize its ability to predict the performance of MR dampers accurately with parameters which have a definite physical meaning while avoiding the inconveniences of other more complicated models.

Some authors have opted to use nonparametric modelling methods based upon analytical expressions which avoid any physical interpretation. This is the case with the validated multifunction model [46], black-box model [47], query-based model [48], neural network model [49], fuzzy model [50], Ridgenet model [51], or the common polynomial model [40, 41]. This latter consists of a brute-force polynomial fitting process, the piecewise expression of which is as simple as

$$F - f_0 = \begin{cases} \sum_{i=0}^{n} a_i \left(\dot{z} \right)^i, & \text{if } \ddot{z} < 0, \\ \sum_{i=0}^{n} b_i \left(\dot{z} \right)^i, & \text{if } \ddot{z} > 0. \end{cases} \tag{9}$$

This model leads to $2 \left(n + 1 \right)$ coefficients, which is a huge number considering that it has been proven that at least 6th order polynomials are required, and at least 12th order polynomials are recommended [41]. In addition, it is well known that these polynomials are extremely sensitive to velocities which exceed the fitting domain.

Returning to parametric models, hysteresis operator-based dynamic models are also very common in the literature. They are conceived to represent a large class of hysteretic behaviour by means of a mathematical formulation which usually includes differential equations. One can find the Dahl hysteresis operator [52, 53], LuGre hysteresis operator [54, 55], the hyperbolic tangent function operator [56], and the well-known Bouc–Wen hysteresis operator (initially formulated by Bouc [57] and later generalised by Wen [58]). A modification of the Bouc–Wen model (the so-called modified Bouc–Wen model or Spencer model [42]) is widely used in the literature obtaining high accuracy in its force predictions. This phenomenological model is governed by the following equations:

$$F - f_0 = C_0 \dot{z}_{mr} + K_0 z,$$
$$\dot{z}_{mr} = \frac{1}{C_0 + C_\infty} \left(\alpha z_{bw} + C_\infty \dot{z} + K_\infty \left(z - z_{mr} \right) \right),$$
$$\dot{z}_{bw} = -\gamma \left| \dot{z} - \dot{z}_{mr} \right| \left| z_{bw} \right|^{n-1} z_{bw} - \beta \left(\dot{z} - \dot{z}_{mr} \right) \left| z_{bw} \right|^n$$
$$+ A \left(\dot{z} - \dot{z}_{mr} \right), \tag{10}$$

where z_{mr} is an intermediate variable for modelling pre- and postyield behaviour, K_0 is the accumulator stiffness, K_∞ controls stiffness at large velocities, and α, β, γ, A, and n, as well as the evolutionary variable z_{bw}, define a general Bouc–Wen hysteresis [58]. Despite its proven accuracy, the extended number of model parameters (10 without considering the influence of the current applied) leads to difficulties in parameter identification.

Intensity dependence has not yet been mentioned, but all the authors deal with this problem in the same way: they fit the proposed model for different intensities and the resulting parameters are subsequently fitted through polynomials with

the power of applied current. The order of these polynomials varies with the author. Some of them use a simple first-order polynomial for all the current-dependent variables [36, 41, 42], whereas other authors carry out a more detailed study leading from second- to fourth-order polynomials depending on the variable considered [39]. In general, experimental force-velocity data for MR dampers suggest a nonlinear dependence of the force on the current applied.

In any case, magnetic solenoid dynamics (usually modelled simply as an inductor in series with a resistor) should be included in order to obtain realistic results. This can be simply achieved by including a first-order differential equation in terms of voltage (or current) as Spencer et al. proposed [42]:

$$\dot{u} = -\eta(u - v), \tag{11}$$

where v is the voltage applied to the current driver, u the instantaneous voltage in the magnetic solenoid, and η a time constant.

4. Experimental Comparison of MR Damper Models

In order to carry out a fair comparison among MR models, all of them were fitted by using the same experimental data from a RD-8040-1 damper. The fitting procedure of the different models was conducted with a nonlinear least-squares method in Matlab software. Quantitative comparisons will be carried out by measuring the normalised root mean square error (NRMSE), that is, the usual root mean square error normalised by the range (maximum value minus minimum value).

A first approach to the models confirms that they are all capable of predicting to a greater or lesser extent the experimental behaviour of a MR damper. That fact can be proven by fitting individually several experimental tests. Figure 5 shows how the nonhysteretic models behave for four cases: a low velocity test at $I = 0$ A (Figure 5(a)), a low velocity test at $I = 1$ A (Figure 5(b)), a high velocity test at $I = 0$ A (Figure 5(c)), and a high velocity test at $I = 1$ A (Figure 5(d)). The same tests are later replicated with the hysteretic models in Figure 6.

Differences in the parameters when different currents are applied (0 or 1 in these cases) are easily modelled by fitting a polynomial. The main problem arises when the parameters of the models, for a constant current, are different depending on the range of velocities that needs to be covered. That is what happens in Figures 5 and 6: low velocity tests (where preyield dominates) and high velocity tests (where postyield dominates), for the same current, require very different values of the model parameters to provide an accurate performance.

The influence of the range of velocities in the fitting procedure has been analysed by taking into account two different sets of experimental data:

(a) All the experimental results, which comprise low, medium, and high velocity tests (in the following LMH fitting)

(b) Only the habitual medium and high velocity tests, that is, discarding those where the postyield region is not fully developed and the preyield region dominates (in the following MH fitting).

Predictions obtained from LMH fitting and LM fitting are later compared to six experimental results which cover three different maximum velocities (low, medium, and high) and two applied intensities ($I = 0$ A and $I = 1$ A). The sinusoidal excitation is set to $A = 4$ mm and $f = 0.5$ Hz for the low velocity test, $A = 4$ mm and $f = 4$ Hz for the medium velocity test, and $A = 16$ mm and $f = 2$ Hz for the high velocity test.

The Bingham model (Figure 7) stands out because of its simplicity and plainness, but returns high errors in general because it neglects both hysteresis and the preyield region. MH fitting obtains errors up to 24% in low velocity validations and up to 16% otherwise, whereas LMH fitting slightly improves those results (up to 19% and 16%, respectively).

Herschel–Bulkley model (Figure 8) behaves reasonably well in all the velocity ranges since it smoothes the yield transition, but the lack of hysteresis also leads to medium errors. For MH fitting, NRMSEs are between 6% and 12%, whereas LMH fitting slightly improves predictions if yield transition has not totally developed yet but also slightly worsens predictions otherwise.

The biviscous model (Figure 9) and regularised Bingham model (Figure 10) behave very similarly to the Herschel–Bulkley model. For MH fitting, they provide slightly lower errors except for low velocity predictions where these predictions clearly fail and NRMSEs rise to 23% and 28%, respectively. For LMH fitting, these two models fix their problems in the low velocity range (NRMSE around 10%) but the preyield region almost disappears if high velocities are reached. Thus, these models degenerate into the Bingham model when fitted this way.

Low NRMSEs do not appear until hysteretic models are used. On the one hand, for MH fitting, the hysteretic biviscous model (Figure 11), the hysteretic regularised Bingham model (Figure 12), or the Shuqi-Guo model (Figure 13) significantly improves errors if the postyield domain is well developed (between 2.5% and 6.5%) but their behaviour is erratic if the preyield region dominates (NRMSE up to 40%). On the other hand, for LMH fitting, said erratic behaviour when preyield region dominates disappears but this is very harmful when simulating high velocities: NRMSEs increase (6–13%) because hysteresis almost vanishes and these models degenerate into the Bingham model.

The nonparametric 12th order polynomial model (Figure 14) is capable of obtaining low NRMSEs but only if the postyield domain is well developed. In addition, it presents a wavy shape and errors may be huge if velocities leave the fitting domain. NRMSEs are between 4% and 30% for MH fitting and 6% and 24% for LMH fitting. Lower polynomial order would compromise prediction accuracy, whereas higher orders would enhance its drawbacks.

(a)

(b)

(c)

(d)
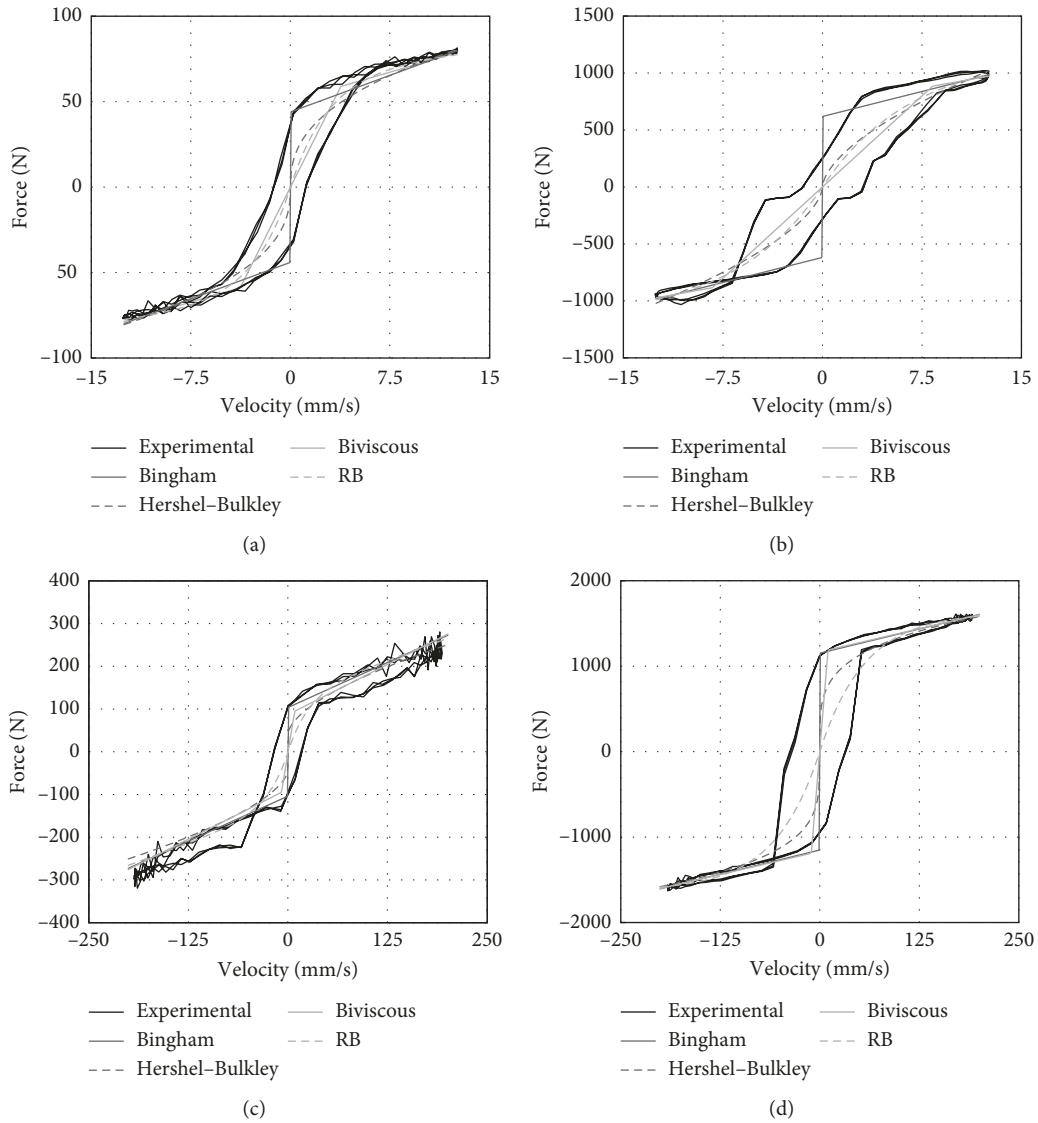
Figure 5: Nonhysteretic model predictions for four different experimental tests: (a) low velocity without intensity; (b) low velocity with $I = 1$ A; (c) high velocity without intensity; (d) high velocity with $I = 1$ A.

(a)

(b)
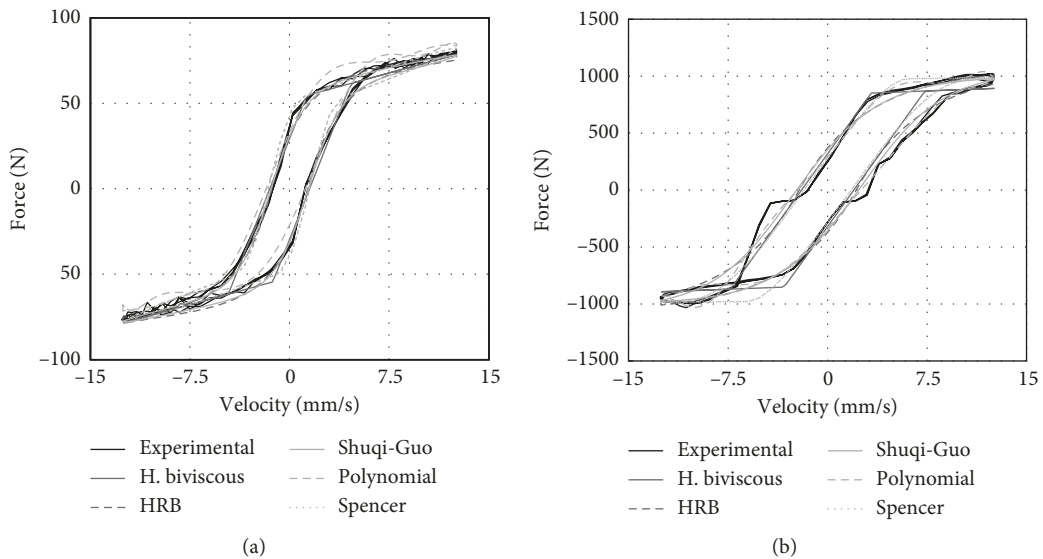
Figure 6: Continued.

(c)

(d)
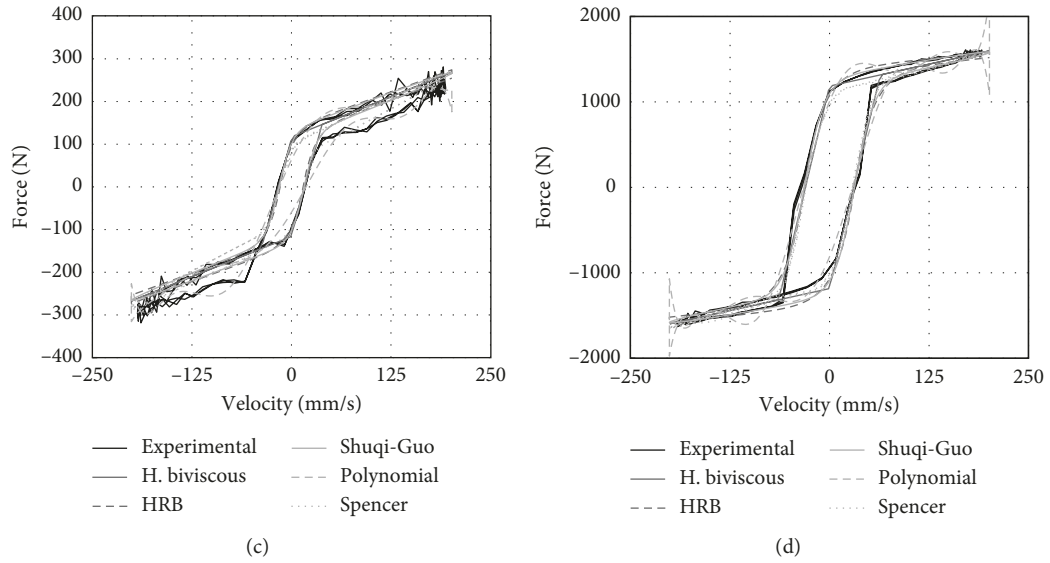
Figure 6: Hysteretic model predictions for four different experimental tests: (a) low velocity without intensity; (b) low velocity with $I = 1$ A; (c) high velocity without intensity; (d) high velocity with $I = 1$ A.

(a)

(b)

(c)

(d)
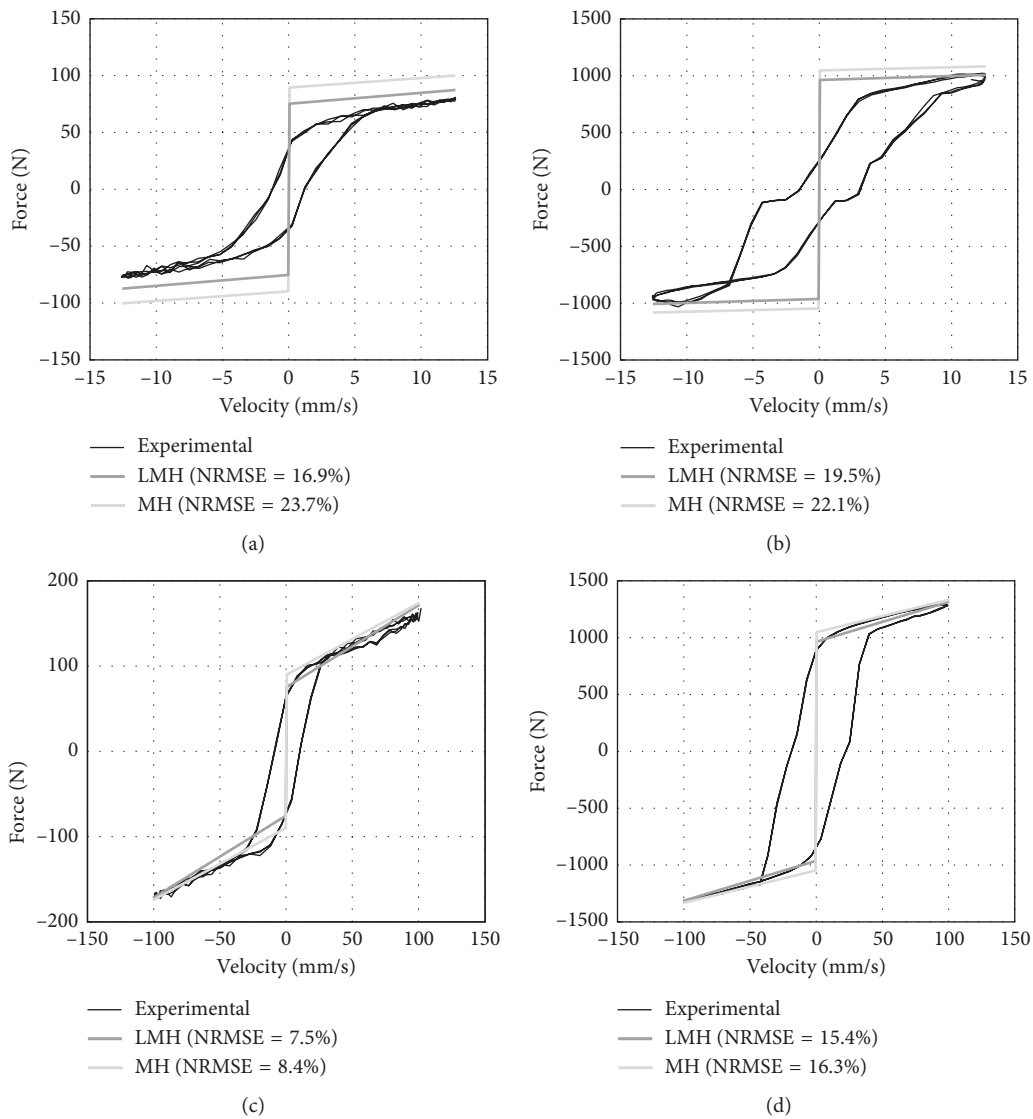
Figure 7: Continued.

(e)

(f)
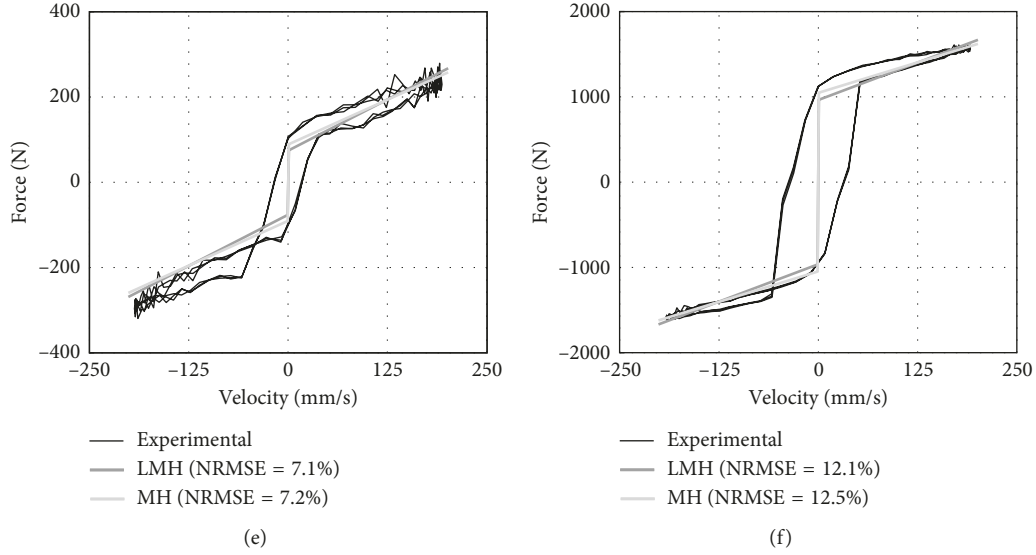
FIGURE 7: Bingham model (fitted with LMH and MH tests) predictions for six different tests: (a) low velocity without intensity; (b) low velocity with $I = 1$ A; (c) medium velocity without intensity; (d) medium velocity with $I = 1$ A; (e) high velocity without intensity; (f) high velocity with $I = 1$ A.

Finally, the Spencer model (Figure 15) stands out from the others for providing the best qualitative and quantitative predictions when the postyield region dominates (NRMSEs between 1.7% and 4.4% for any fitting method). Predictions when the preyield region dominates are still accurate (between 4% and 8.1% for any fitting method), and they show no erratic behaviour in any case. Nevertheless, the fitting procedure is too complicated due to the high number of parameters: it requires a very precise seed and a trial-and-error procedure is usually worthwhile.

Tables 1 and 2 show the fitted parameters which have a physical meaning and are shared by the different models. One can observe that not only are the values obtained similar in the different models but also close to those expected by inspection. Only one exception arises when analysing f_y in the Herschel–Bulkley model: the least-squares fitting procedure leads to a low (and even zero if $I = 1$ A) value of f_y because parameter n seems to be enough to model the pre- and postyield domains; nevertheless, if one sets an estimated fix value of f_y, NRMSE and the qualitative behaviour of this model are equivalent.

In short, one may come to the following main conclusions:

(i) If one uses MH fitting, the behaviour of the model when yield transition is not fully developed is clearly poor because predictions underestimate MR damper forces in the preyield region. This compromises the simulation results of control systems which, in fact, are specifically designed to achieve low vibration velocities (or accelerations).

(ii) If one uses LMH fitting, the models provide an accurate performance if the postyield domain is not fully developed but hysteresis almost vanishes and force is overestimated otherwise. This diminishes the claimed good performance of the complex and

refined models, degenerating into the old Bingham model.

(iii) The Spencer model provides the best qualitative and quantitative behaviour, but the seed for the fitting procedure must be so accurate that least-squares methods are almost unnecessary.

5. Case Study: Skyhook Control of a Quarter-Car Suspension System

A quarter-car semiactive suspension system (shown in Figure 16) with an on-off skyhook control strategy has been numerically analysed in order to determine the influence of the selected MR model. The chosen suspension parameters were $M = 500$ kg and $K = 78000$ N/m together with the characterised and modelled magnetorheological damper RD-8040-1.

Figure 17 shows the excitement in the base which replicates a speed bump. The mathematical expression is

$$z_0(t) = \begin{cases} \dfrac{H}{2}\left[\sin\left(2\pi\dfrac{v}{L}(t-0.5)-\dfrac{\pi}{2}\right)+1\right], & 0.5 \le t \le \dfrac{L}{v}+0.5, \\ \\ 0, & \text{otherwise,} \end{cases}$$

(12)

where H and L are the bump height and length, respectively, and v is the vehicle velocity (constant).

The on-off skyhook control strategy can be defined as follows [59]:

$$F_{sa} = \begin{cases} F_{\max}, & \dot{z}(\dot{z}-\dot{z}_0) \ge 0, \\ F_{\min}, & \dot{z}(\dot{z}-\dot{z}_0) < 0, \end{cases}$$

(13)

where $F_{\max}$ and $F_{\min}$ are the MR damper forces when a current $I = 1$ A and $I = 0$ A, respectively, is supplied. An
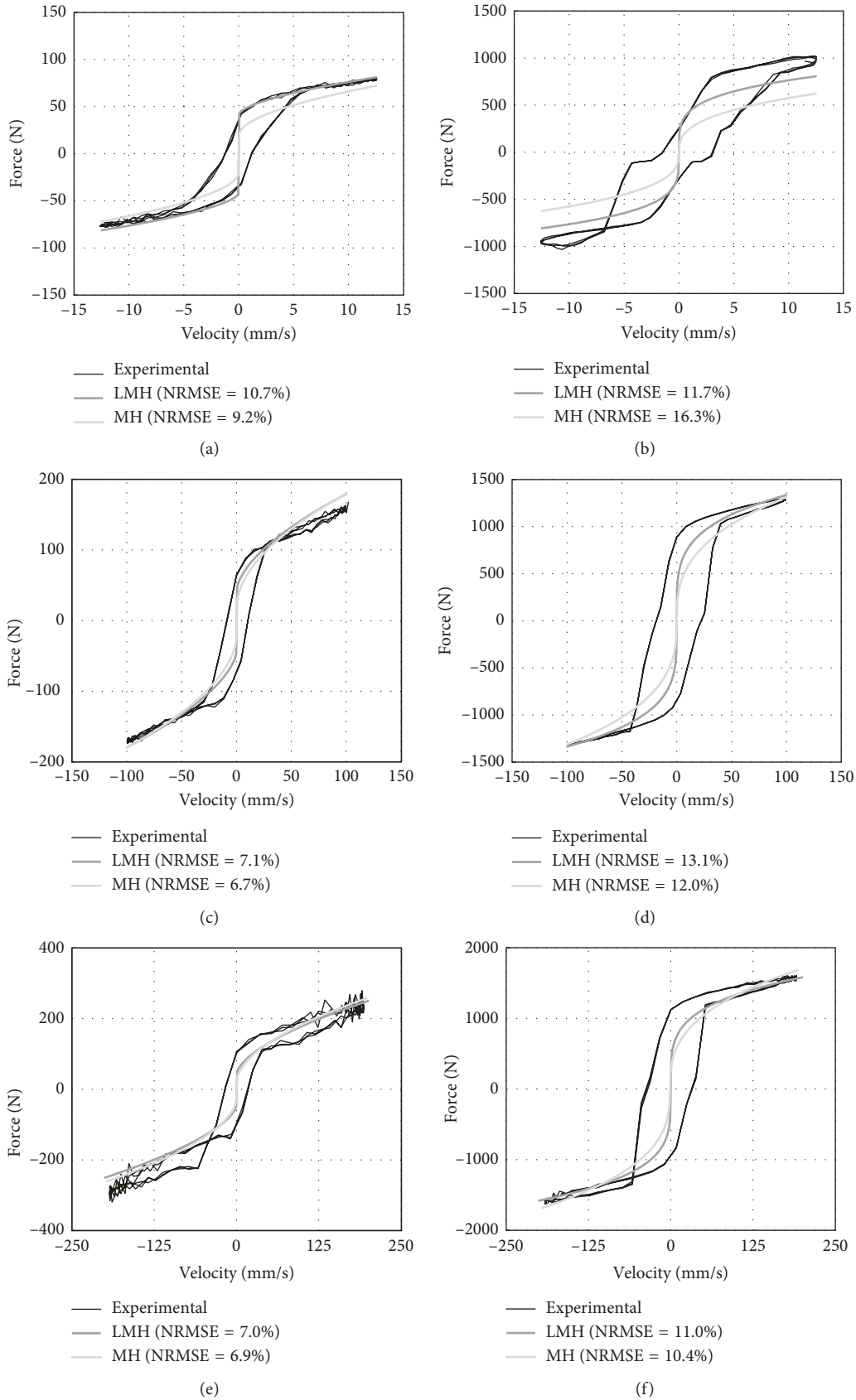
FIGURE 8: Herschel–Bulkley model (fitted with LMH and MH tests) predictions for six different tests: (a) low velocity without intensity; (b) low velocity with $I = 1$ A; (c) medium velocity without intensity; (d) medium velocity with $I = 1$ A; (e) high velocity without intensity; (f) high velocity with $I = 1$ A.
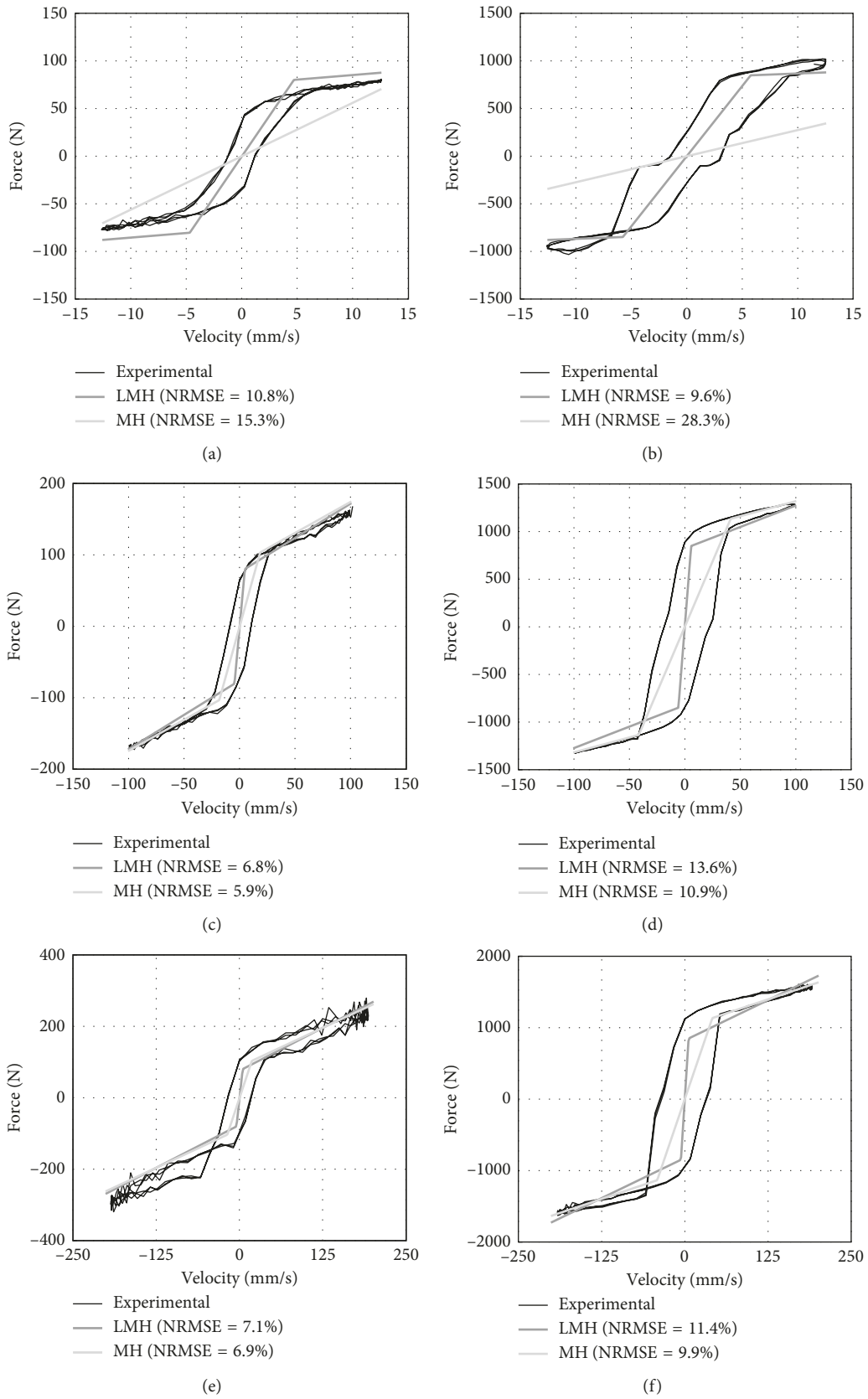
FIGURE 9: Biviscous model (fitted with LMH and MH tests) predictions for six different tests: (a) low velocity without intensity; (b) low velocity with $I = 1$ A; (c) medium velocity without intensity; (d) medium velocity with $I = 1$ A; (e) high velocity without intensity; (f) high velocity with $I = 1$ A.
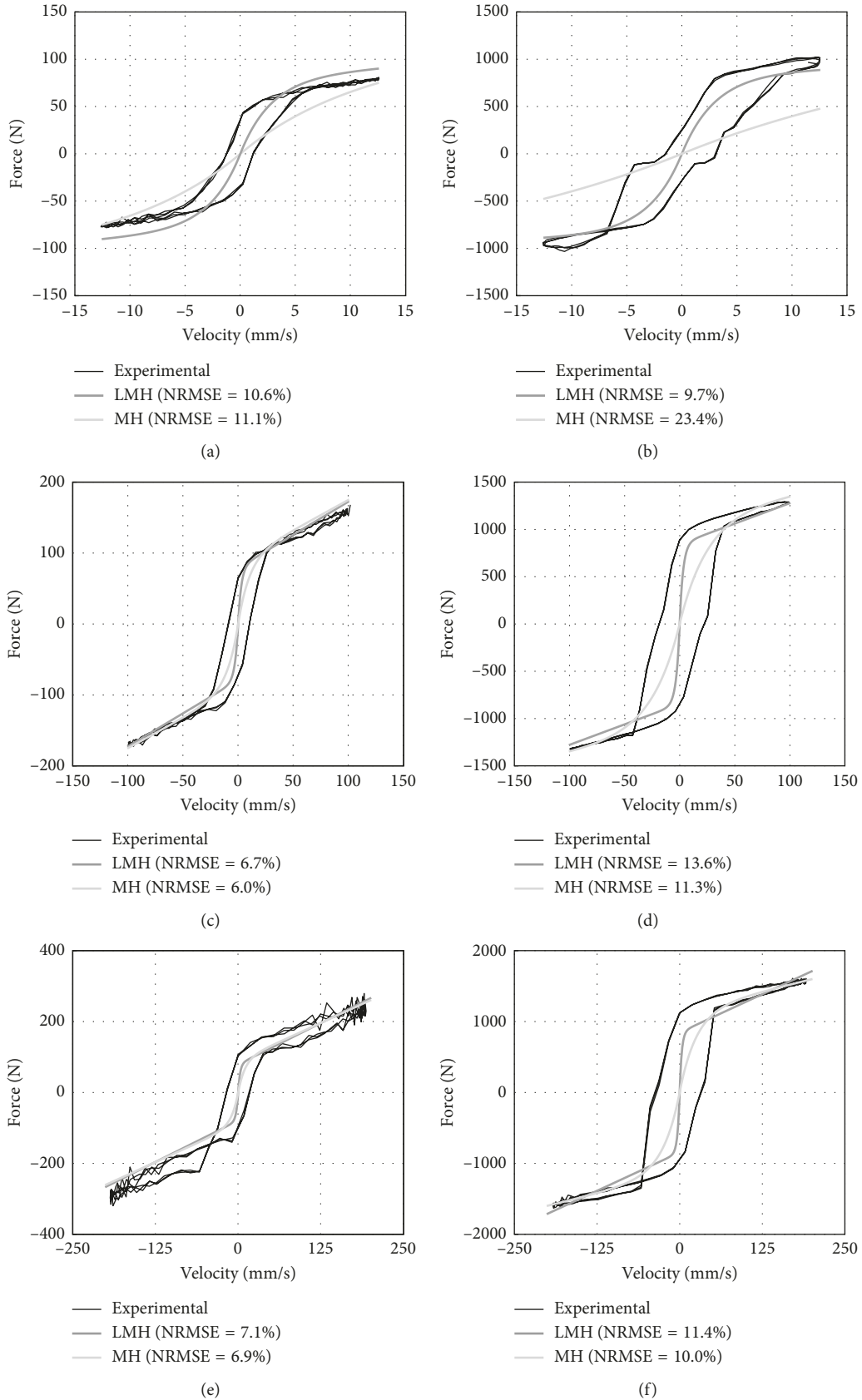
FIGURE 10: Regularised Bingham model (fitted with LMH and MH tests) predictions for six different tests: (a) low velocity without intensity; (b) low velocity with $I = 1$ A; (c) medium velocity without intensity; (d) medium velocity with $I = 1$ A; (e) high velocity without intensity; (f) high velocity with $I = 1$ A.
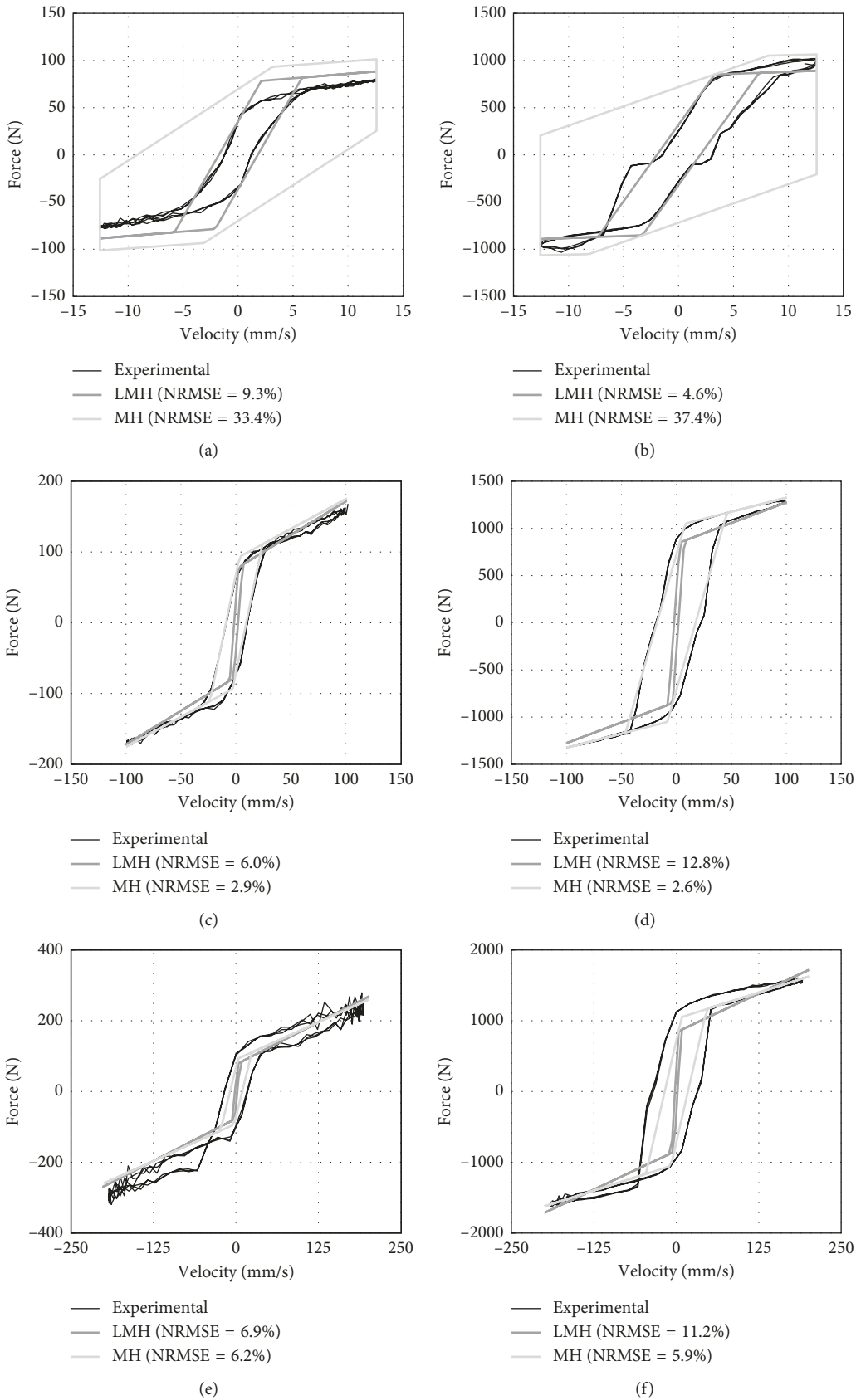
FIGURE 11: Hysteretic biviscous model (fitted with LMH and MH tests) predictions for six different tests: (a) low velocity without intensity; (b) low velocity with $I = 1$ A; (c) medium velocity without intensity; (d) medium velocity with $I = 1$ A; (e) high velocity without intensity; (f) high velocity with $I = 1$ A.
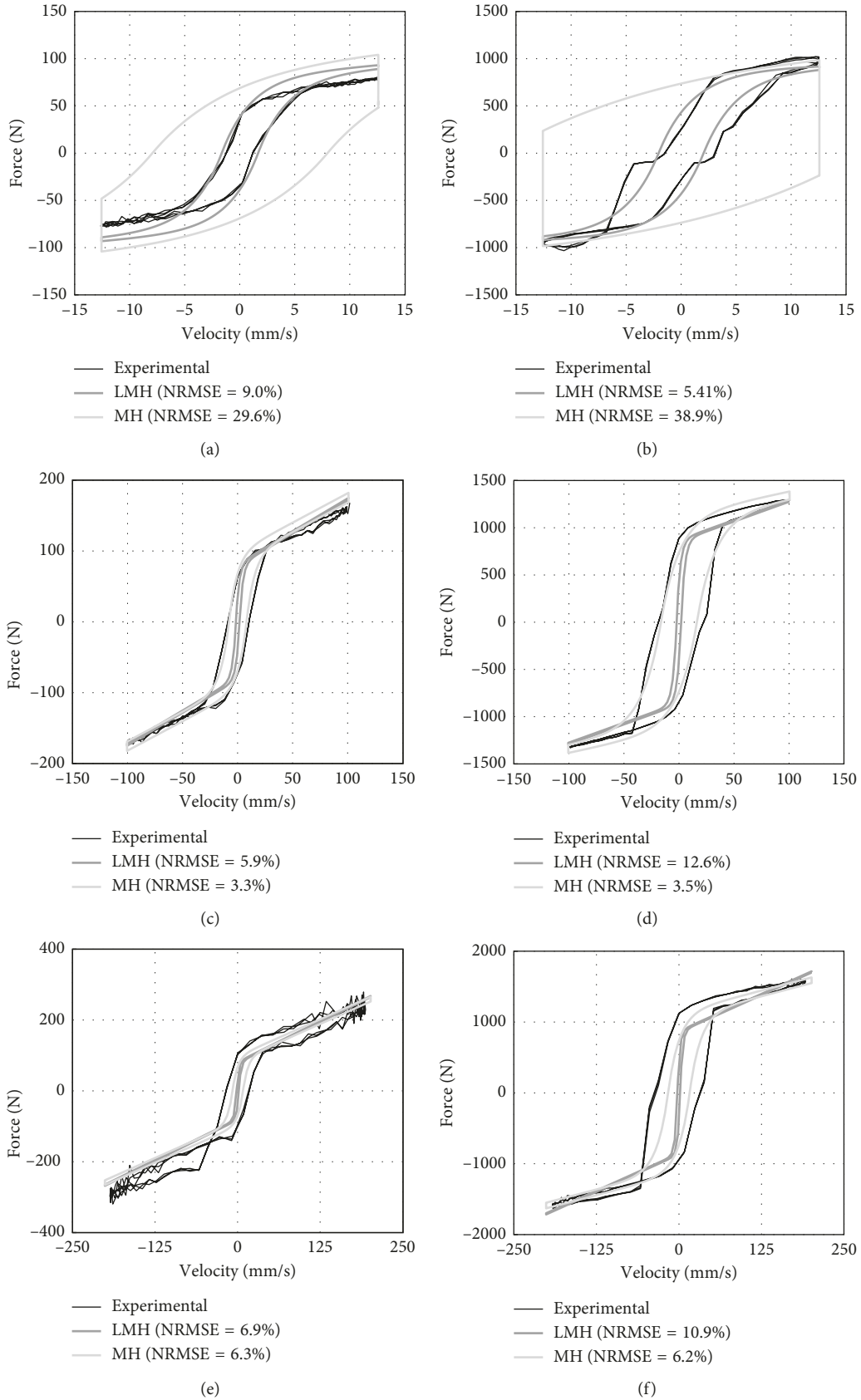
FIGURE 12: Hysteretic regularised Bingham model (fitted with LMH and MH tests) predictions for six different tests: (a) low velocity without intensity; (b) low velocity with $I = 1$ A; (c) medium velocity without intensity; (d) medium velocity with $I = 1$ A; (e) high velocity without intensity; (f) high velocity with $I = 1$ A.
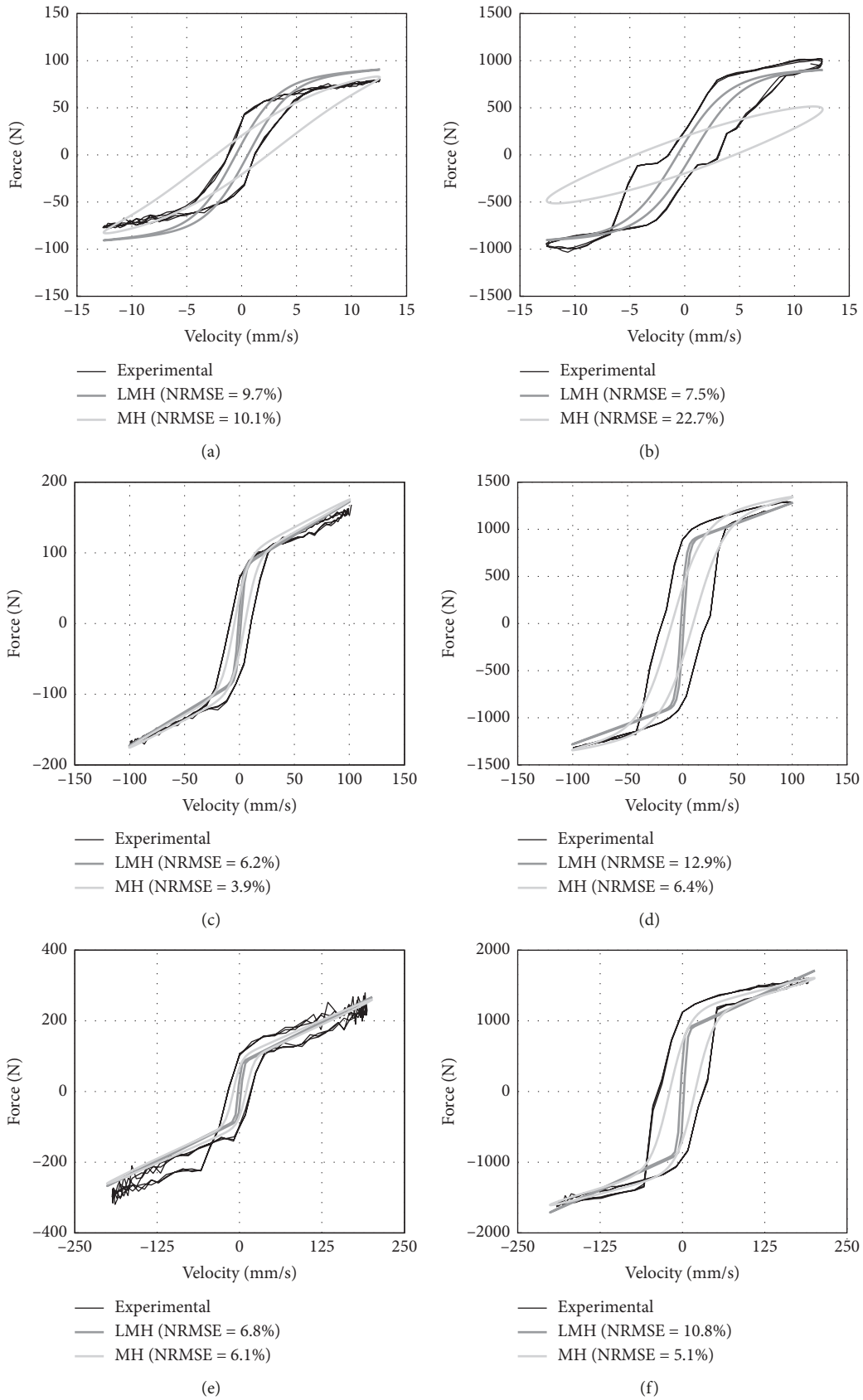
Figure 13: Shuqi-Guo model (fitted with LMH and MH tests) predictions for six different tests: (a) low velocity without intensity; (b) low velocity with $I = 1$ A; (c) medium velocity without intensity; (d) medium velocity with $I = 1$ A; (e) high velocity without intensity; (f) high velocity with $I = 1$ A.
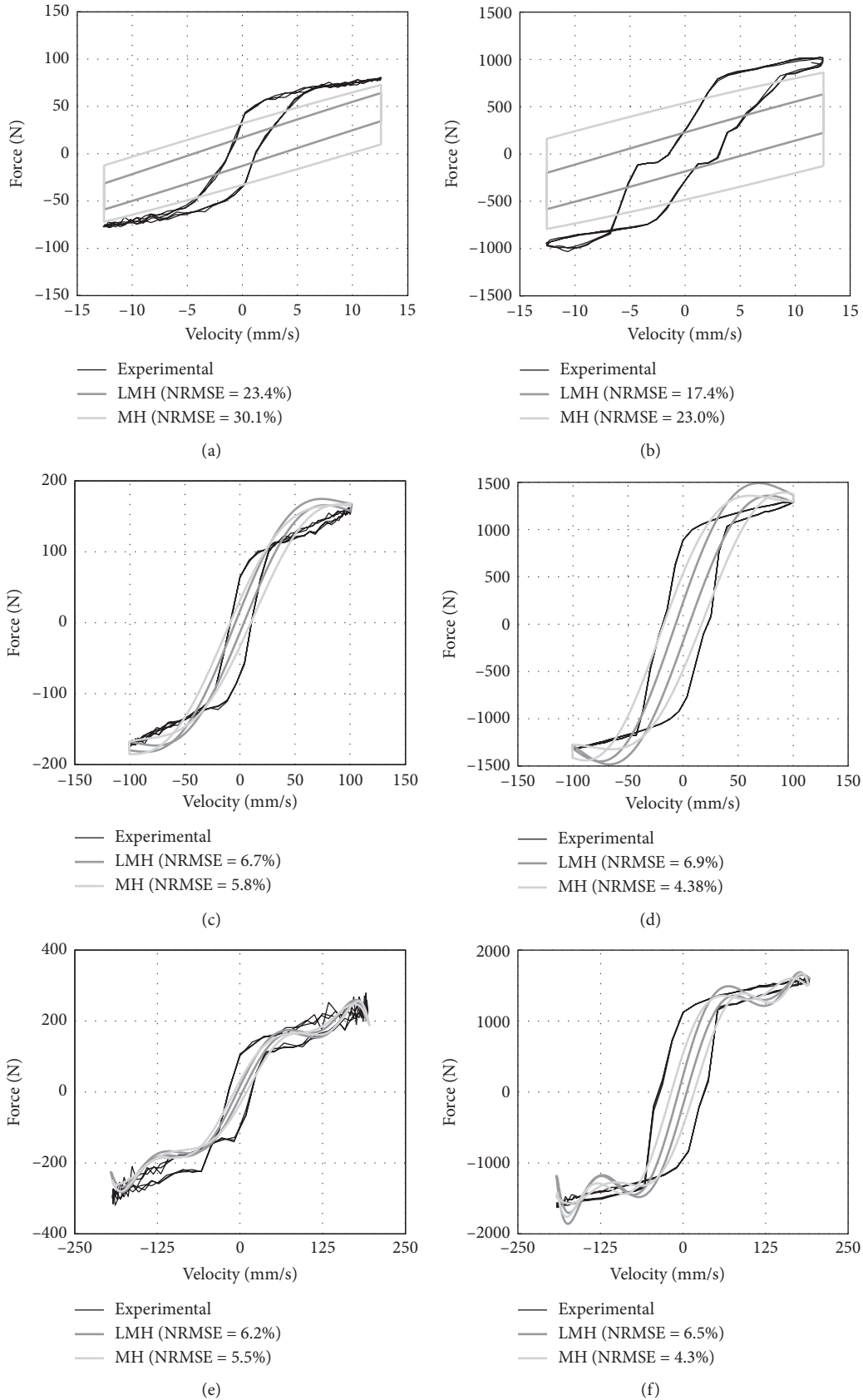
FIGURE 14: Polynomial model (fitted with LMH and MH tests) predictions for six different tests: (a) low velocity without intensity; (b) low velocity with $I = 1$ A; (c) medium velocity without intensity; (d) medium velocity with $I = 1$ A; (e) high velocity without intensity; (f) high velocity with $I = 1$ A.
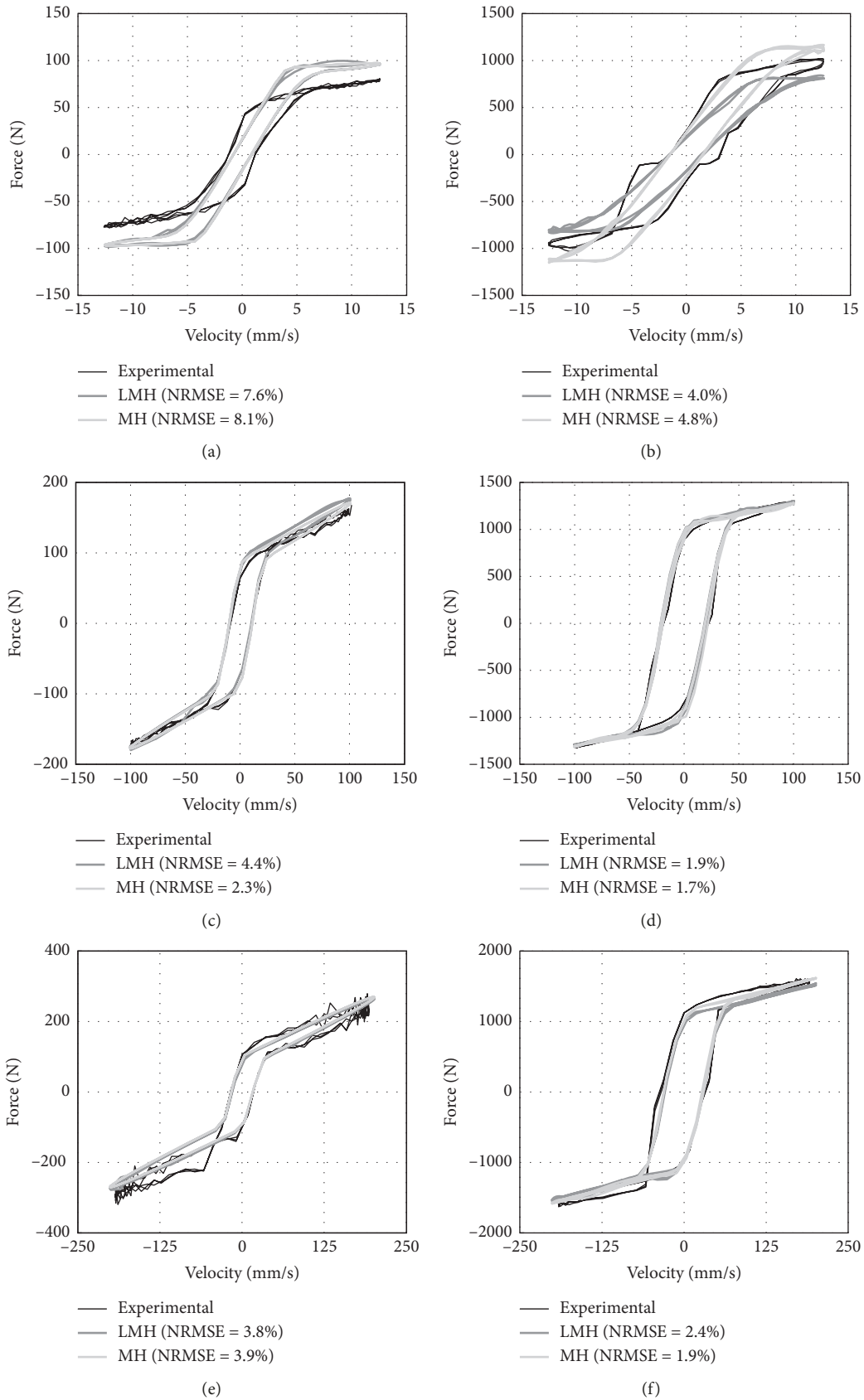
FIGURE 15: Spencer model (fitted with LMH and MH tests) predictions for six different tests: (a) low velocity without intensity; (b) low velocity with $I = 1$ A; (c) medium velocity without intensity; (d) medium velocity with $I = 1$ A; (e) high velocity without intensity; (f) high velocity with $I = 1$ A.

TABLE 1: Model parameters after fitting with $I = 0$ A.

	Model	f_y (N)	C_∞ (Ns/m)	C_0 (Ns/m)	$\dot{z}_y$ (mm/s)	$\dot{z}_h$ (mm/s)
LMH	Bingham	75.26	961.87	—	—	—
	Herschel–Bulkley	41.62	548.00	—	—	—
	Biviscous	75.80	961.25	17124	4.7	—
	Regularised Bingham	79.26	933.13	—	2.8	—
	Hysteretic biviscous	76.44	955.97	20330	2.1	1.8
	Hysteretic regularised Bingham	80.40	924.53	—	2.7	1.7
	Shuqi-Guo	79.11	934.93	263	—	—
	Spencer	—	961.25	20330	—	—
MH	Bingham	89.67	842.82	—	—	—
	Herschel–Bulkley	19.69	549.58	—	—	—
	Biviscous	86.28	869.84	5612	1.8	—
	Regularised Bingham	89.80	851.50	—	9.9	—
	Hysteretic biviscous	90.76	842.74	7579	3.1	9.2
	Hysteretic regularised Bingham	92.09	829.93	—	7.0	7.9
	Shuqi-Guo	90.60	844.22	85	—	—
	Spencer	—	964.31	20156	—	—

TABLE 2: Model parameters after fitting with $I = 1$ A.

	Model	f_y (N)	C_∞ (Ns/m)	C_0 (Ns/m)	$\dot{z}_y$ (mm/s)	$\dot{z}_h$ (mm/s)
LMH	Bingham	963.1	3508.5	—	—	—
	Herschel–Bulkley	0.0	2333.8	—	—	—
	Biviscous	823.5	4503.7	147230	5.8	—
	Regularised Bingham	845.5	4324.1	—	3.0	—
	Hysteretic biviscous	837.4	4385.8	162000	3.3	2.0
	Hysteretic regularised Bingham	863.7	4195.1	—	3.0	2.0
	Shuqi-Guo	855.8	4293.8	222	—	—
	Spencer	—	2401.3	162640	—	—
MH	Bingham	1046.7	2858.9	—	—	—
	Herschel–Bulkley	0.0	2997.5	—	—	—
	Biviscous	1005.0	3135.9	27392	4.1	—
	Regularised Bingham	1137.0	2302.4	—	25.0	—
	Hysteretic biviscous	1027.5	2974.6	40831	8.2	17.6
	Hysteretic regularised Bingham	1099.9	2436.5	35	16.3	16.2
	Shuqi-Guo	1084.7	2589.6	—	—	—
	Spencer	—	2412.1	160680	—	—
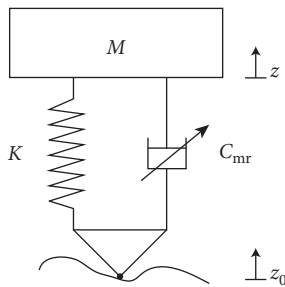
FIGURE 16: The quarter-car suspension system.

example of the current required by the skyhook control system, superimposed on the bump, is shown in Figure 17 (differences depending on the MR model are imperceptible). Note that, though not seen in Figure 17, the damper will switch off after the sprung mass has reached its equilibrium position again.

Figures 18 and 19 show the sprung mass acceleration (related to comfort in vehicles), both controlled and passive, for all the MR models considered after either MH fitting and LMH fitting. In all the analysed models, passive results for the two fitting cases are almost identical because the damper remains in the postyield region, where differences are limited. Nevertheless, controlled results highlight noticeable differences.

Results in the control with the Bingham model (Figure 18(a)) show chatter in the controlled sprung mass acceleration. This is due to the fact that this model does not consider a preyield region and there is a discontinuity between positive and negative postyield regions (see Figure 7). This occurs using both MH fitting and LMH fitting.

Controls with nonhysteretic Herschel–Bulkley, biviscous, and regularised Bingham models show a similar behaviour (Figures 18(b)–18(d)). Both the first peak (around 0.15 s), which corresponds to the ascent to the top of the bump, and the second (around 0.25 s), which is due to the
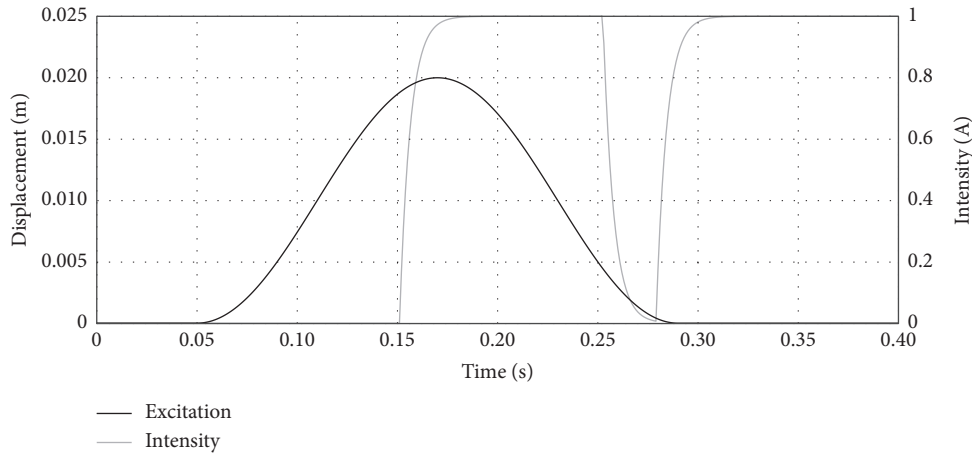
FIGURE 17: Temporal excitation corresponding to a bump with $H = 0.02$ m and $L = 1$ m travelled at $v = 15$ km/h and example of the current required by the skyhook control system.

(a)

(b)

(c)

(d)
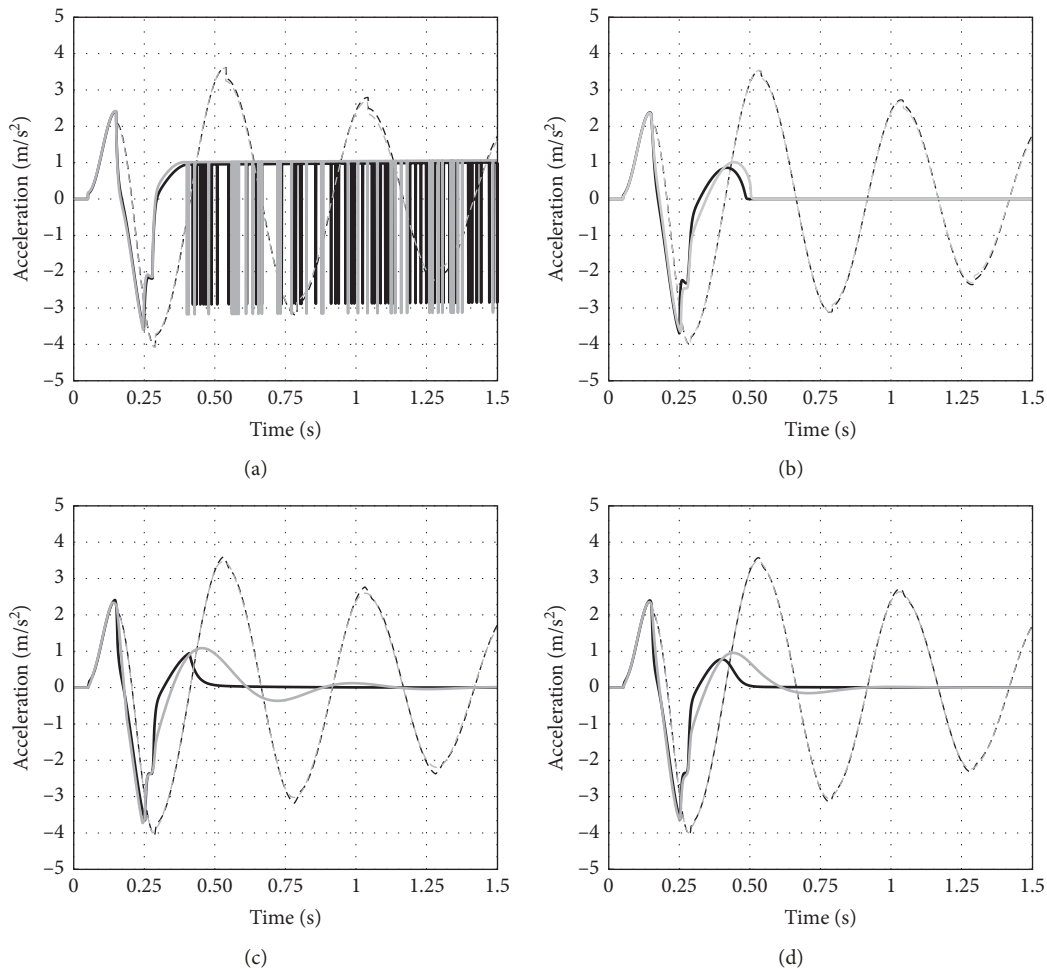
FIGURE 18: Time response of the controlled (solid line) and passive (dotted line) sprung mass acceleration for the (a) Bingham model, (b) Herschel–Bulkley model, (c) biviscous model, and (d) regularised Bingham model, after LMH fitting (black) and MH fitting (grey).

drop from the top of the bump, are almost identical notwithstanding the tests which were used to fit the models. This happens because the relative velocity of the MR damper is still high and the postyield region (very similar in all the cases) dominates dynamics. Nevertheless, the third peak (around 0.40 s), which is due to a rebound, happens at lower velocities where yield transition is not fully developed and models have been proven to disagree. These three models, if
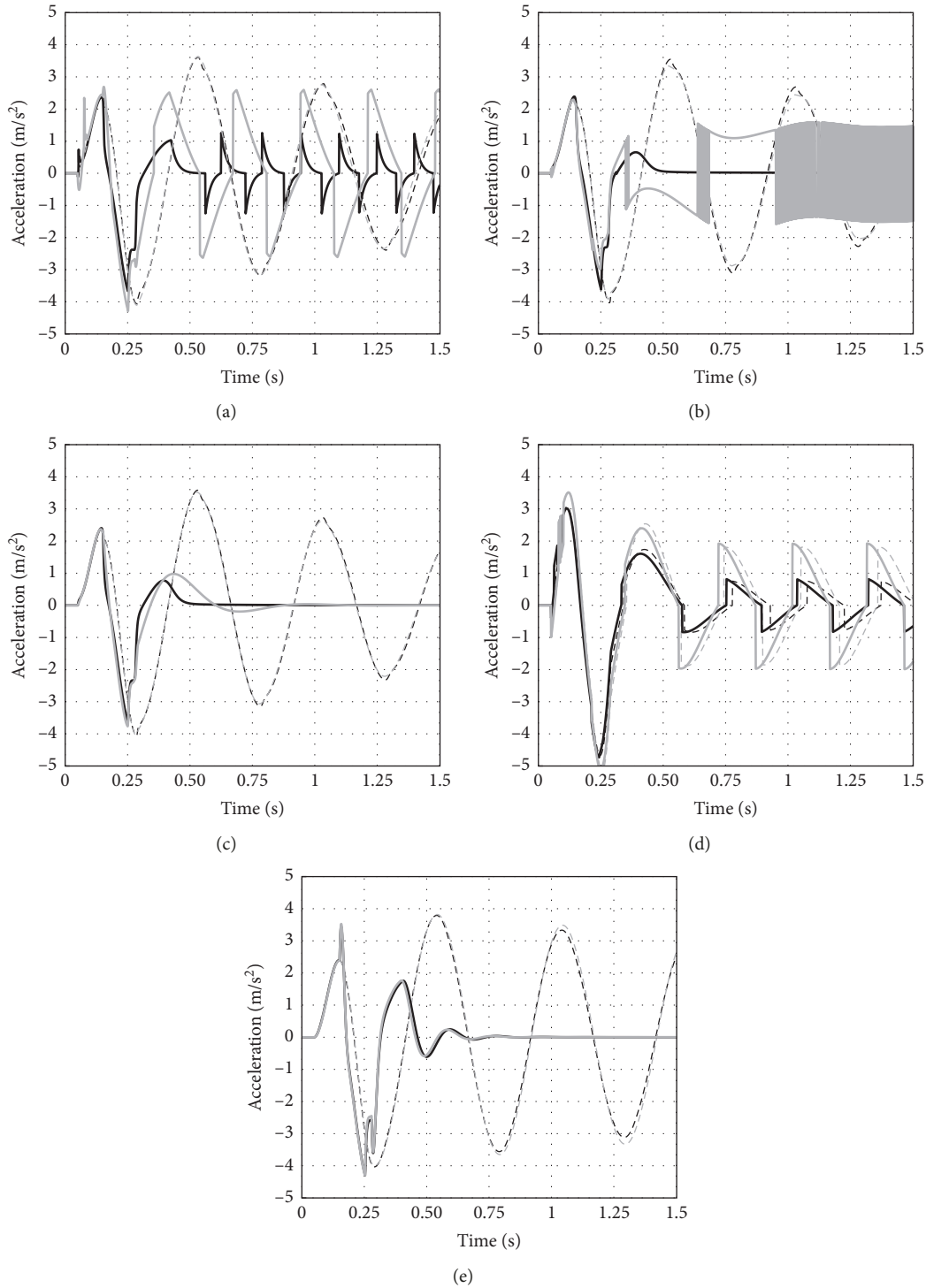
Figure 19: Time response of the controlled (solid line) and passive (dotted line) sprung mass acceleration for the (a) hysteretic biviscous model, (b) hysteretic regularised Bingham model, (c) Shuqi-Guo model, (d) polynomial model, and (e) Spencer model, after LMH fitting (black) and MH fitting (grey).

MH fitted, predict a slower attenuation of the sprung mass acceleration because the dissipative force is underestimated (see Figures 8–10, subplots (a) and (b)). This fact is especially noticeable when considering the regularised Bingham model because it is the one which underestimates the force in a

greater extent. Thus, the faster attenuation predicted by the model after LMH fitting would be more reliable.

The use of hysteretic models such as the hysteretic biviscous, HRB, and 12th order polynomial models (Figures 19(a), 19(b), and 19(d), respectively) does not

contribute perceptible improvements in comparison to the results obtained with the previous nonhysteretic models. Indeed, they are hysteresis models based on two different branches (depending on the sign of the relative acceleration of the damper), which may lead to low velocity chatter and discontinuities as shown in Figures 19(a), 19(b), and 19(d). In addition, since there is no branch which replicates the static state of the MR damper (that is, zero force when zero velocity), the sprung mass will achieve a different static position depending on either the supplied intensity and the active branch when it stops. As a consequence, these models provide acceleration time responses which are far from being acceptable.

Results for the Shuqi-Guo model (Figure 19(c)) avoid the control drawbacks inherent in the branched hysteresis models (chatter, static position, etc.,) but results are almost identical to those obtained with the nonhysteretic models: if MH fitting is used, the low velocity force is underestimated; if LMH fitting is used, hysteresis almost vanishes.

Finally, results for the Spencer model (Figure 19(e)) show a lower dissipation than the predicted by the rest of the models (rebounds reach slightly higher acceleration levels) and almost identical predictions in both fitting cases. Note that the Spencer model was proven to provide the most accurate behaviour in all the velocity ranges and for the two considered fittings.

Tables 3 and 4 show the rms value of the sprung mass acceleration. It is not a surprise that, even discarding chattering models, predicted rms values are in the range of 0.541–$0.734 \, \text{m/s}^2$, which means variations up to 36% depend on the model one decides to use.

We draw the following conclusions about the influence of the MR model on semiactive control simulations:

(i) Systems including discontinuous or piecewise models (such as the Bingham model, hysteretic biviscous model, HRB model, or polynomial model) are prone to chatter, discontinuities, and variations in the static deflection.

(ii) Nonhysteretic models provide similar predictions to hysteretic models because hysteresis actually affects a small fraction of an oscillation.

(iii) Differences between MH fitting and LMH fitting are mainly noticeable at low-velocity oscillations, where MH fitting underestimates the damping force and leads to a slower attenuation.

(iv) The Spencer model shows a lower dissipation (and hence worse rms accelerations) than the predicted by the other models, but it was shown to be the most accurate model.

(v) Nonnegligible influences such as friction are not included in the models, which mainly compromises low velocity predictions.

6. Conclusions

This article performs an updated review of the main MR damper models. Unlike other studies, this review includes a broad and thorough experimental comparison of nine models to predict the behaviour of the same Lord RD-8040-1 MR damper.

The variety of experimental tests used for the fitting process has been proven to be a key decision: if tests where the preyield region dominates are discarded, low-velocity predictions are either poor or erratic; if these tests are also considered, hysteresis at higher velocities almost vanishes. The Spencer model avoids this problem and stands out for accurately predicting pre- and postyield regions with NRMSE lower than 8% in all cases.

These models have also been used in a straightforward semiactive control case study. Several problems have arisen: on the one hand, discontinuous or piecewise models produce chatter, discontinuities, and even variations in the static deflection; on the other hand, MH fitting underestimates damping forces and predicts slower attenuations. The a priori accurate Spencer model predicts a slower attenuation in comparison to the rest of the models.

In the light of these results, there is still room for further research on MR models. NRMSE should be reduced in all the range of velocities which cover pre- and postyield domains, and proposed models must guarantee the lack of habitual problems such as chatter, discontinuities, or inaccuracies prior to claiming the goodness of any control scheme.

Data Availability

The simulation data used to support the findings of this study are available from the corresponding author upon request. The experimental data used for the magneto-rheological damper characterisation and fitting procedure of the different models are available from the corresponding author upon request.

Disclosure

The authors approve the final article submitted to Shock and Vibration.

TABLE 3: Root mean square (rms) value of the sprung mass acceleration for simulations with nonhysteretic models (units in m/s^2).

	MR model			
	Bingham	Herschel–Bulkley	Biviscous	Regularised Bingham
LMH	1.123	0.559	0.543	0.542
MH	1.178	0.582	0.627	0.596

TABLE 4: Root mean square (rms) value of the sprung mass acceleration for simulations with hysteretic models (units in m/s^2).

	MR model				
	Hysterical biviscous	HRB	Shuqi-Guo	Polynomial	Spencer
LMH	0.674	0.531	0.541	0.944	0.734
MH	1.516	1.274	0.607	1.456	0.729

Conflicts of Interest

Authors' Contributions

All the authors participated in the experimental tests, the numerical data processing, the scientific discussions, and the preparation of the manuscripts and the figures.

Acknowledgments

References

[1] J. Rabinow, "The magnetic fluid clutch," *Transactions of the American Institute of Electrical Engineers*, vol. 67, no. 2, pp. 1308–1315, 1948.

[2] A. G. Olabi and A. Grunwald, "Design and application of magneto-rheological fluid," *Materials & Design*, vol. 28, no. 10, pp. 2658–2664, 2007.

[3] L. Zipser, L. Richter, and U. Lange, "Magnetorheologic fluids for actuators," *Sensors and Actuators A: Physical*, vol. 92, no. 1–3, pp. 318–325, 2001.

[4] M. R. Jolly, J. W. Bender, and J. D. Carlson, "Properties and applications of commercial magnetorheological fluids," *Journal of Intelligent Material Systems and Structures*, vol. 10, no. 1, pp. 5–13, 1999.

[5] J. Claracq, J. Sarrazin, and J.-P. Montfort, "Viscoelastic properties of magnetorheological fluids," *Rheologica Acta*, vol. 43, no. 1, pp. 38–49, 2004.

[6] G. Bossis, S. Lacis, A. Meunier, and O. Volkova, "Magnetorheological fluids," *Journal of Magnetism and Magnetic Materials*, vol. 252, pp. 224–228, 2002.

[7] B. J. Park, F. F. Fang, and H. J. Choi, "Magnetorheology: materials and application," *Soft Matter*, vol. 6, no. 21, pp. 5246–5253, 2010.

[8] J. De Vicente, D. J. Klingenberg, and R. Hidalgo-Alvarez, "Magnetorheological fluids: a review," *Soft Matter*, vol. 7, no. 8, pp. 3701–3710, 2011.

[9] S. T. Lim, M. S. Cho, I. B. Jang, and H. J. Choi, "Magnetorheological characterization of carbonyl iron based suspension stabilized by fumed silica," *Journal of Magnetism and Magnetic Materials*, vol. 282, pp. 170–173, 2004.

[10] J. H. Park, B. D. Chin, and O. O. Park, "Rheological properties and stabilization of magnetorheological fluids in a water-in-oil emulsion," *Journal of Colloid and Interface Science*, vol. 240, no. 1, pp. 349–354, 2001.

[11] J. D. Carlson and M. R. Jolly, "MR fluid, foam and elastomer devices," *Mechatronics*, vol. 10, no. 4-5, pp. 555–569, 2000.

[12] G. Z. Yao, F. F. Yap, G. Chen, W. H. Li, and S. H. Yeo, "MR damper and its application for semi-active control of vehicle suspension system," *Mechatronics*, vol. 12, no. 7, pp. 963–973, 2002.

[13] S. J. Dyke, B. F. Spencer, M. K. Sain, and J. D. Carlson, "Modeling and control of magnetorheological dampers for seismic response reduction," *Smart Materials and Structures*, vol. 5, no. 5, pp. 565–575, 1996.

[14] G. W. Housner, L. A. Bergman, T. K. Caughey et al., "Structural control: past, present, and future," *Journal of Engineering Mechanics*, vol. 123, no. 9, pp. 897–971, 1997.

[15] B. F. Spencer and S. Nagarajaiah, "State of the art of structural control," *Journal of Structural Engineering*, vol. 129, no. 7, pp. 845–856, 2003.

[16] H. J. Jung, B. F. J. Spencer, Y. Q. Ni, and I. W. Lee, "State-of-the-art of semiactive control systems using MR fluid dampers in civil engineering applications," *Structural Engineering and Mechanics*, vol. 17, no. 3-4, pp. 493–526, 2004.

[17] S.-B. Choi, M.-H. Nam, and B.-K. Lee, "Vibration control of a MR seat damper for commercial vehicles," *Journal of Intelligent Materials Systems and Structures*, vol. 11, no. 12, pp. 936–944, 2000.

[18] S. J. McManus, K. A. Boileau, P. E. Boileau, J. Boutin, and S. Rakheja, "Evaluation of vibration and shock attenuation performance of a suspension seat with a semi-active magnetorheological fluid damper," *Journal of Sound and Vibration*, vol. 253, no. 1, pp. 313–327, 2002.

[19] K. Kim and D. Jeon, "Vibration suppression in an MR fluid damper suspension system," *Journal of Intelligent Material Systems and Structures*, vol. 10, no. 10, pp. 779–786, 1999.

[20] H.-S. Lee and S.-B. Choi, "Control and response characteristics of a magneto-rheological fluid damper for passenger vehicles," *Journal of Intelligent Materials Systems and Structures*, vol. 11, no. 1, pp. 80–87, 2000.

[21] F. Gordaninejad and S. P. Kelso, "Fail-safe magneto-rheological fluid dampers for off-highway, high-payload vehicles," *Journal of Intelligent Materials Systems and Structures*, vol. 11, no. 5, pp. 395–406, 2000.

[22] M. Ahmadian and C. A. Pare, "A quarter-car experimental analysis of alternative semiactive control methods," *Journal of Intelligent Materials Systems and Structures*, vol. 11, no. 8, pp. 604–612, 2000.

[23] C. Y. Lai and W. H. Liao, "Vibration control of a suspension system via a magnetorheological fluid damper," *Modal Analysis*, vol. 8, no. 4, pp. 527–547, 2002.

[24] A. H.-F. Lam and W.-H. Liao, "Semi-active control of automotive suspension systems with magneto-rheological dampers," *International Journal of Vehicle Design*, vol. 33, no. 1–3, pp. 50–75, 2003.

[25] W. H. Liao and D. H. Wang, "Semiactive vibration control of train suspension systems via magnetorheological dampers," *Journal of Intelligent Material Systems and Structures*, vol. 14, no. 3, pp. 161–172, 2003.

[26] D. H. Wang and W. H. Liao, "Semi-active suspension systems for railway vehicles using magnetorheological dampers. Part I: system integration and modelling," *Vehicle System Dynamics*, vol. 47, no. 11, pp. 1305–1325, 2009.

[27] D. H. Wang and W. H. Liao, "Semi-active suspension systems for railway vehicles using magnetorheological dampers. Part II: simulation and analysis," *Vehicle System Dynamics*, vol. 47, no. 12, pp. 1439–1471, 2009.

[28] D. C. Batterbee, N. D. Sims, R. Stanway, and Z. Wolejsza, "Magnetorheological landing gear: 1. A design methodology," *Smart Materials and Structures*, vol. 16, no. 6, pp. 2429–2440, 2007.

[29] D. H. Wang and W. H. Liao, "Magnetorheological fluid dampers: a review of parametric modelling," *Smart Materials and Structures*, vol. 20, 2011.

[30] R. Stanway, J. L. Sproston, and N. G. Stevens, "Non-linear modelling of an electro-rheological vibration damper," *Journal of Electrostatics*, vol. 20, no. 2, pp. 167–184, 1987.

[31] E. C. Bingham, *Fluidity and Plasticity*, McGraw Hill, New York, NY, USA, 1922.

[32] X. Wang and F. Gordaninejad, "Study of field–controllable, electro– and magnetorheological fluid dampers in flow mode using Herschel-Bulkey theory," in *Proceedings of the SPIE's 7th Annual International Symposium on Smart Structures and Materials*, vol. 3989, pp. 244–252, Newport Beach, CA, USA, April 2000.

[33] W. H. Herschel and R. Bulkley, "Konsistenzmessungen von Gummi-benzollösungen," *Kolloid-Zeitschrift*, vol. 39, no. 4, pp. 291–300, 1926.

[34] E. W. Williams, S. G. Rigby, J. L. Sproston, and R. Stanway, "Electrorheological fluids applied to an automotive engine mount," *Journal of Non-Newtonian Fluid Mechanics*, vol. 47, pp. 221–238, 1993.

[35] R. Stanway, J. L. Sproston, and A. K. El-Wahed, "Applications of electro-rheological fluids in vibration control: a survey," *Smart Materials and Structures*, vol. 5, no. 4, pp. 464–482, 1996.

[36] S. Soltane, S. Montassar, O. B. Mekki, and R. El Fatmi, "A hysteretic Bingham model for MR dampers to control cable vibrations," *Journal of Mechanics of Materials and Structures*, vol. 10, no. 2, pp. 195–206, 2015.

[37] T. C. Papanastasiou, "Flows of materials with yield," *Journal of Rheology*, vol. 31, no. 5, pp. 385–404, 1987.

[38] S. Guo, S. Yang, and C. Pan, "Dynamic modeling of magnetorheological damper behaviors," *Journal of Intelligent Material Systems and Structures*, vol. 17, no. 1, pp. 3–14, 2006.

[39] L. Pang, G. M. Kamath, and N. M. Wereley, "Dynamic characterization and analysis of magnetorheological damper behavior," in *Proceedings of the 5th Annual International Symposium on Smart Materials and Structures*, vol. 3327, pp. 284–302, San Diego, CA, USA, June 1998.

[40] S.-B. Choi, S.-K. Lee, and Y.-P. Park, "A hysteresis model for the field-dependent damping force of a magnetorheological damper," *Journal of Sound and Vibration*, vol. 245, no. 2, pp. 375–383, 2001.

[41] H. Du, K. Yim Sze, and J. Lam, "Semi-active control of vehicle suspension with magneto-rheological dampers," *Journal of Sound and Vibration*, vol. 283, no. 3–5, pp. 981–996, 2005.

[42] B. F. Spencer Jr., S. J. Dyke, M. K. Sain, and J. D. Carlson, "Phenomenological model of a magnetorheological damper," *Journal of Engineering Mechanics*, vol. 123, no. 3, pp. 230–238, 1996.

[43] M. Boada, B. Boada, and V. Diaz, "A novel inverse dynamic model for a magnetorheological damper based on network inversion," *Journal of Vibration and Control*, vol. 24, no. 15, pp. 3434–3453, 2018.

[44] D. R. Gamota and F. E. Filisko, "Dynamic mechanical studies of electrorheological materials: moderate frequencies," *Journal of Rheology*, vol. 35, no. 3, pp. 399–425, 1991.

[45] I. H. Shames and F. A. Cozzarelli, *Elastic and Inelastic Stress Analysis*, Prentice-Hall, Inc., Englewood Cliffs, NJ, USA, 1992.

[46] X. Song, M. Ahmadian, and S. C. Southward, "Modeling magnetorheological dampers with application of non-parametric approach," *Journal of Intelligent Material Systems and Structures*, vol. 16, no. 5, pp. 421–432, 2005.

[47] G. Jin, M. K. Sain, K. D. Pham, F. S. Jr Billie, and J. C. Ramallo, "Modeling MR–dampers: a nonlinear blackbox approach," in *Proceedings of the 2001 American Control Conference*, vol. 1, pp. 429–434, Arlington, VA, USA, June 2001.

[48] M. Mori and A. Sano, "Local modeling approach to vibration control by MR damper," in *Proceedings of the SICE Annual Conference*, vol. 3, pp. 2572–2577, Sapporo, Japan, 2004.

[49] D. H. Wang and W. H. Liao, "Modeling and control of magnetorheological fluid dampers using neural networks," *Smart Materials and Structures*, vol. 14, no. 1, pp. 111–126, 2005.

[50] K. C. Schurter and P. N. Roschke, "Fuzzy modeling of a magnetorheological damper using ANFIS," in *Proceedings of the 9th IEEE International Conference on Fuzzy Systems*, vol. 1, pp. 122–127, San Antonio, TX, USA, May 2000.

[51] G. Jin, M. K. Sain, and B. F. Spencer Jr., "Modeling MR-dampers: the ridgenet estimation approach," in *Proceedings of the 2002 American Control Conference*, vol. 3, pp. 2457–2462, Anchorage, AK, USA, May 2002.

[52] P. R. Dahl, "Solid friction damping of mechanical vibrations," *AIAA Journal*, vol. 14, no. 12, pp. 1675–1682, 1976.

[53] Q. Zhou, S. R. K. Nielsen, and W. L. Qu, "Semi-active control of three-dimensional vibrations of an inclined sag cable with magnetorheological dampers," *Journal of Sound and Vibration*, vol. 296, no. 1-2, pp. 1–22, 2006.

[54] C. C. de Wit, H. Olsson, K. J. Astrom, and P. Lischinsky, "A new model for control of systems with friction," *IEEE Transactions on Automatic Control*, vol. 40, no. 3, pp. 419–425, 1995.

[55] P. Lischinsky, C. C. de Wit, and G. Morel, "Friction compensation for an industrial hydraulic robot," *IEEE Control Systems*, vol. 19, no. 1, pp. 25–32, 1999.

[56] N. M. Kwok, Q. P. Ha, T. H. Nguyen, J. Li, and B. Samali, "A novel hysteretic model for magnetorheological fluid dampers and parameter identification using particle swarm optimization," *Sensors and Actuators A: Physical*, vol. 132, no. 2, pp. 441–451, 2006.

[57] R. Bouc, "Mathematical model for hysteresis," *Acustica*, vol. 24, pp. 16–25, 1971.

[58] Y. K. Wen, "Method for random vibration of hysteretic systems," *Journal of the Engineering Mechanics Division ASCE*, vol. 102, pp. 249–263, 1976.

[59] Y. Liu, T. P. Waters, and M. J. Brennan, "A comparison of semi-active damping control strategies for vibration isolation of harmonic disturbances," *Journal of Sound and Vibration*, vol. 280, no. 1-2, pp. 21–39, 2005.

Research Article

Experimental Approach to Active Mounts Using Electromagnetic Actuator and Rubber with Consideration of Shock Resistance for Naval Shipboard Equipment

Yun-ho Shin [ID],[1] Seok-jun Moon,[1] Woo-jin Jung,[2] and Soo-ryong Bae[2]

[1]*Department of System Dynamics, Korea Institute of Machinery and Materials, 156 Gajeongbuk-ro, Yuseong-gu,*
 Daejeon 305-343, Republic of Korea
[2]*Agency for Defense Development, Seoul, Republic of Korea*

Correspondence should be addressed to Yun-ho Shin; shinyh77@kimm.re.kr

There is demand for stringent vibration isolation within machine installations in order to achieve maximum performance or to satisfy otherwise extreme criteria, particularly, when there is a strong source of vibration such as a motor pump. It is frequently necessary to prevent the transmission of these vibrations to other parts of the system for passenger comfort in vehicles, ships, trains, etc., or for the protection of delicate electronic equipment. In the defense sector, the need for equipment which is better at avoiding detection has led researchers to focus more on improving vibration isolation. In this paper, an active mount combined with a passive rubber mount and an electromagnetic actuator is proposed and examined for use in naval shipboard equipment. The electromagnetic actuator is suggested for improving performance and overcoming its inherent limitations which are caused by the friction between the magnet and coil. The design specifications of an active mount, such as required force, displacement, and frequency characteristics, are identified for the self-excited pump system, and then an electromagnetic actuator active mount is redesigned with considering the shape of the passive rubber mount and shock resistance. The performance was examined on the single active mount using an external exciter, which could be simplified as two-degree-of-freedom system, and also confirmed experimentally on an active mount system with four mounts using a motor system. From the results of applying the proposed electromagnetic active mount, a vibration reduction of about 20 dB for the motor equipment was observed for the excited frequency components of 1,600 rpm and its two harmonic components.

1. Introduction

Vibration isolation is an important requirement throughout many areas of engineering, particularly when there is a strong source of vibration such as a motor pump. It is frequently necessary to prevent the transmission of these vibrations to other parts of the system for reasons such as passenger comfort in vehicles, ships, trains, etc., or for the protection of delicate electronic equipment [1]. In the defense sector, the need for equipment which can better avoid detection has led researchers to focus more on improving vibration isolation [2]. Passive vibration isolators separate objects of interest from external vibrations without using power or a control system. Compared with active isolators that use active or semiactive technologies, passive vibration isolators are suitable for applications in which compactness, cost, and reliability are primary concerns [3]. However, the high performance vibration isolation that is required for more sensitive applications, and in defense equipment, necessitates active isolation technology. Active isolators can perform at a higher level than passive isolators through the incorporation of an active component. Collette et al. have reviewed several patented developments in the field of active vibration isolation [4]. They demonstrated that active suspension does not suffer from the two fundamental trade-offs between the settling time caused by the

direct excitation of payload and the transmissibility by the base excitation through the isolator which are inherently given to passive suspension design. Then, the main active strategies were presented and compared using single-degree-of-freedom models. Cho et al. have focused on configurations of active mounts which are combined with passive and active components [5]. The seven configurations are presented according to the connection of an active element to a passive element. Shin et al. [2] have proposed an active mount that uses an electromagnetic actuator to reduce vibrations transmitted from naval shipboard equipment to the structure of the ship's hull. The active mount combines a proven rubber mount and a moving magnetic-based electromagnetic actuator. It is ideal for reducing vibrations at a low frequency range (under 300 Hz) and has fail-safe capabilities that protect the equipment at the top of the mount from external shock. Kaal et al. [6] have presented the development, simulation, and experimental investigation for a proof of concept of active vibration isolation with dielectric elastomers. It can support large masses because it is capable of withstanding compressive forces without stability drawbacks. The actuator design can easily be adjusted to specific requirements by changing the size of the active area or the number of layers. Lee et al. [7] have presented the design, simulation, and manipulation of a 6-axis hybrid vibration isolation system. This vibration isolation system is composed of four spiral metal springs for passive isolation and eight voice coil motors for active isolation.

This paper discusses an active mount which combines a passive rubber mount and an electromagnetic actuator that can be applied to naval shipboard equipment. While it is similar with the actuator in reference [2], this electromagnetic actuator is modified for improved performance and to overcome its inherent limitations. First, the design specifications for active mounts, such as required force, displacement, and frequency characteristics, are identified for the self-excited pump system. Second, an electromagnetic actuator active mount is designed, over and over, with consideration for the shape of the passive rubber mount and for shock resistance. Third, the performance of the single active mount is examined experimentally by using an external exciter. Finally, the control performance is also confirmed experimentally on an active mount system with four mounts using a motor system.

2. Design of an Active Mount with Consideration for Shock Resistance

2.1. Required Force to Control the Objective Pump-Motor System. A schematic diagram of the target system is described in Figure 1 of this study. Based on basic information and the measurements of the target system (pump-motor and piping systems), the required control force was calculated. After applying only the resilient mount corresponding to the passive part of the active mount to the bottom of the pump motor, the vibrations were measured and analyzed. At the bottom of the pump, four passive

mounts are installed (locations 1 to 4), and the average of the measured accelerations at each installed location is obtained to calculate the required control force to select or design the proper actuator. Figure 2 shows the results of vertical acceleration, when the instrument's rotational speed was set to 1,600 rpm in each installation location, in terms of 1/3 octave band and compares them with the vibration tolerance specification (MIL-STD-740) [8]. It is possible to confirm that the frequency range of interest corresponds with the configured purpose of the active mount, and high frequency vibration reductions can be observed through the passive mount.

It is relatively difficult to estimate the excitation force of the system by using the measured vibration signals for the target system. However, by calculating the force transmitted to the hull or other equipment when the specifications of the viscoelastic mount, such as stiffness and damping, are known, the force can be estimated using this simple calculation. The force transmitted from the equipment to the hull is calculated using equation (1) after measuring absolute acceleration (or velocity, displacement) information at the top and bottom of the mount.

$$F_T = c_r \left(\dot{x}_e - \dot{x}_b \right) - k_r \left(x_e - x_b \right). \tag{1}$$

In equation (1), k and c denote the stiffness and damping coefficients, respectively, and subscripts e and b denote the top and bottom of mount, respectively. The specifications of stiffness and damping, used for calculating the transmitted force, are 5.27×10^5 N/m and 1.58×10^3 Ns/m.

The required control force calculated from the relevant frequency components and the averaged values obtained from the viscoelastic mounts (locations 1 to 4) at the bottom of the pump system are described in Table 1. The frequency components that differ by more than 20 dB from the maximum value of the measured transmitted force are regarded as sufficiently small and excluded from the frequency component to be controlled. In order to conservatively design the actuator, the maximum required operating force of the actuator is set to 120 N based on the transmitted force in the time domain, and the maximum displacement is ±1 mm. It is how the target performance in designing the electromagnetic actuator together with the constraints on space is designated.

2.2. Electromagnetic Actuator Design of Hybrid Mount considering Shock Resistance: Phase I. In previous research [2], the design of the electromagnetic actuator was based on a three-level concept, as shown in Figure 3, which took into consideration the type of moving coil and the type of moving permanent magnet. In addition to the design proposed previously, the detailed proposal and the conceptual design are presented in the additional, detailed design plan.

The results of determining the detailed specifications for production are as follows: the ferro-metal for the electromagnetic actuator is SS400 ferrite chrome steel and the permanent magnet is a N42H sintered neodymium zinc boron magnet. Because permanent magnets are difficult to
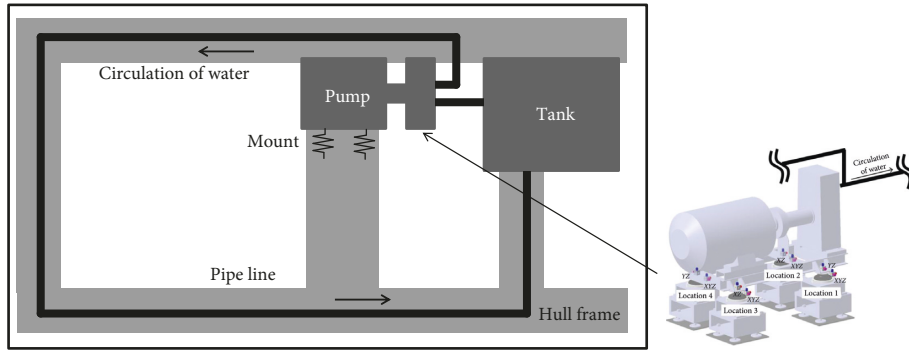
FIGURE 1: Overall schematic of target system.

(a)

(b)

(c)

(d)
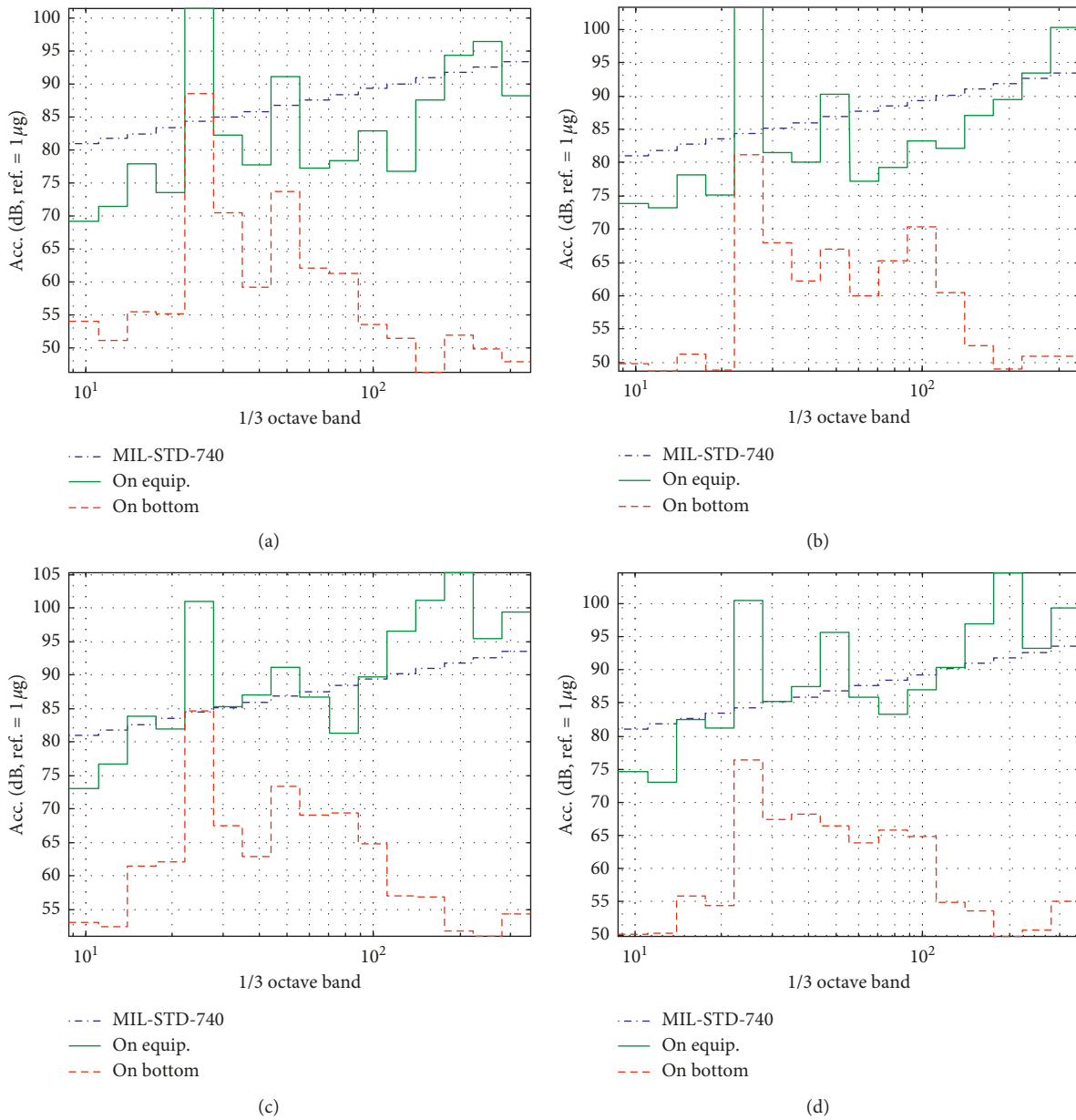
FIGURE 2: Acceleration signals at supported location: 1/3 octave scale. (a) Location 1. (b) Location 2. (c) Location 3. (d) Location 4.

TABLE 1: Required design specification of the electromagnetic actuator.

Domain	Required force or displacement
Frequency domain	41.5 N_{peak} @ 26.5 Hz 3.3 N_{peak} @ 53.3 Hz
Time domain	Max. 120 N_{peak} (force) Max. ±1 mm (displacement)
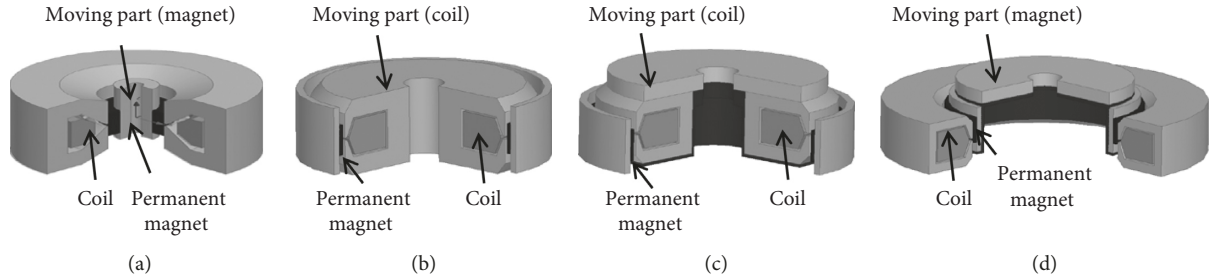
FIGURE 3: Design of electromagnetic actuator. (a) 1st concept design. (b) 2nd concept design. (c) Detailed design-I. (d) Detailed design-II.

produce in one circular form, they are made in a toric shape by attaching pieces in a circumferential direction. The coil used in this study is self-bound type which suffers over time from the partial melting of the sheath covering it, once the current begins to run through it. The diameter of coil material, copper, is determined by 1.3 mm (AWG #16), and the coil is wrapped with 270 turns, respectively. When the current flows through, the coil is peeled off and wound. The materials of the joints used to fix the mover and the stator and the passive mounts attached to the actuator are made of stainless steel to reduce magnetic flux leakage during control; Figure 4 shows the schematic drawings of the prototype including the mover, the stator, and the viscoelastic passive mount for the electromagnetic actuators types I and II which are described in Table 2. The final assembly of the passive mount element and the assembled electromagnetic actuator is shown in Figure 5 along with the coil and the permanent magnet parts.

The designed gap between the mover and the stator of the actuator for the horizontal direction was 2 mm. However, the gap was relatively small and difficult to be realized because when the mount is installed, a force acts between the permanent magnet and the metal forming a magnetic pole and that makes it difficult to align the center of gravity. This is because there is a high possibility of adhesion between the metal and the mover after the center is installed, and the viscoelastic material, being in a thin layer (1.8 mm), is used in the pore to maintain the pore distance. The measured resistance value of the manufactured electromagnetic actuator I is 1.1 Ω, and it shows a 6.4% error according to the analytical results (1.17 Ω) of the commercial program used in the electromagnetic field analysis of this study, and the resistance measurement results of the electromagnetic actuator II is 2.1 Ω according to the results of the commercial program's analysis (2.23 Ω) with an error of 6.2%. The analysis results for both actuators I and II including resistances by ANSYS Maxwell are described in Table 3.

The block diagram of experimental configurations required for the performance evaluation of the manufactured hybrid mount is shown in Figure 6. It is the equipment configuration to measure the force generated when the current is applied to the hybrid mount; the overall equipment configuration is shown in Figure 7, and the test conditions are described in Table 4. The satisfaction of the requirements for each actuator, based on measurement results, is also described in Table 5.

Based on the results of the performance tests of the two proposed electromagnetic actuator designs, it was confirmed that the required actuating force was satisfied. However, it was also observed that the actuator is likely to cause friction when the actuator is not made ideally (eccentricity 0) due to the force applied in the horizontal direction as shown in Figure 7. In order to compensate for that, the modified electromagnetic actuator design is proposed in the next section.

2.3. Electromagnetic Actuator Design of Hybrid Mount with Consideration for Shock Resistance: Phase II. The new design of the actuator is being proposed in order to eliminate the harmonics present at low frequencies, below 50 Hz, caused due to the electromagnetic actuator friction mentioned before. The following are the specific points related to actuator design modifications:

(1) The permanent magnets and the metal for forming the magnetic path are integrated so that no attractive force acts between the magnet and the metal

(2) The coil part is designed to be connected with the hull so that the magnet part and the coil part do not pull out, even if eccentricity exists

(3) Modifying the design so that the mover can move up and down without contact in order to secure shock resistance
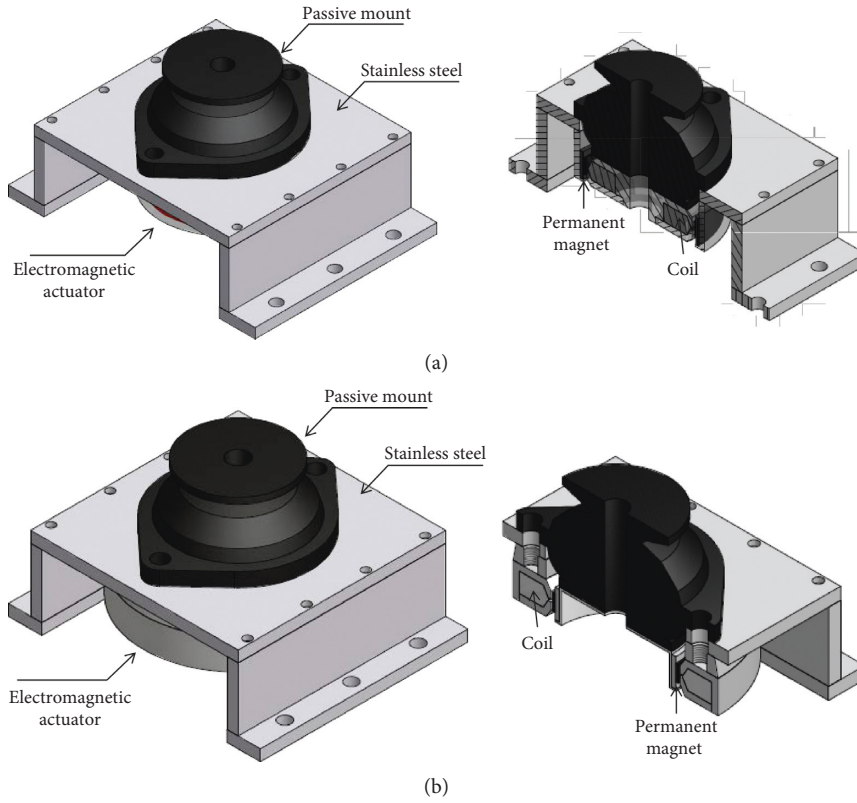
Figure 4: Schematic drawings for detailed design. (a) Detailed design-I. (b) Detailed design-II.

Table 2: Details of suggested actuator.

	Detailed design-I	Detailed design-II
Electrical gap	5 mm	5 mm
Mechanical gap	2 mm	2 mm
Coil specification	Ø1.3 mm × 270 turns	Ø1.3 mm × 270 turns
Weight	Abt. 6.5 kg	Abt. 10 kg
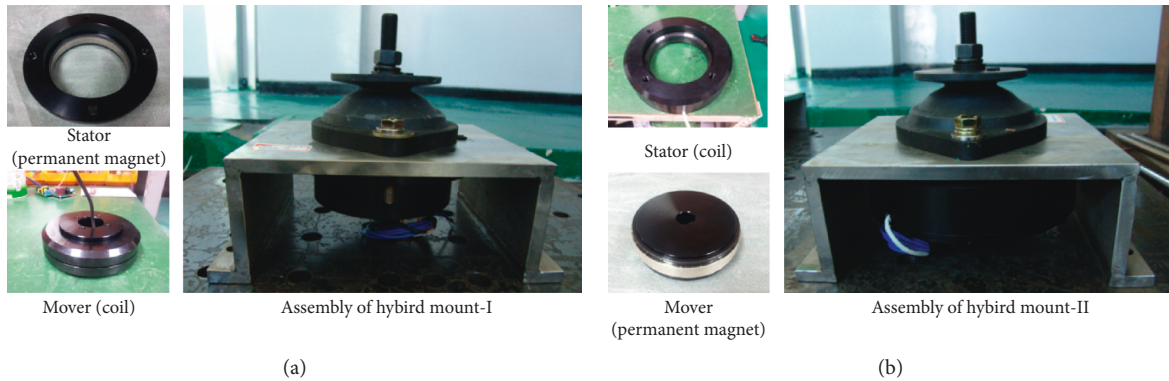
Figure 5: Electromagnetic active mount. (a) Detailed design-I. (b) Detailed design-II.

Considering the maximum deflection in the compression-tension direction (about 50 mm) based on the results of the impact test run according to the procedures of MIL-S-901D [9] for the hybrid mount hand part (6K900) shown in Figure 8, the design was carried out in order to solve the friction problem mentioned above, and the final suggested design is shown in Figure 9. The hammer of 3,000 lb is impacted to the mount-equipped naval

TABLE 3: Analysis results of suggested actuator.

	Detailed design-I	Detailed design-II
Resistance	1.17 Ω	2.33 Ω
Inductance	0.20 H	0.22 H
Input voltage	150 V	150 V
Time constant	0.17 sec	0.09 sec
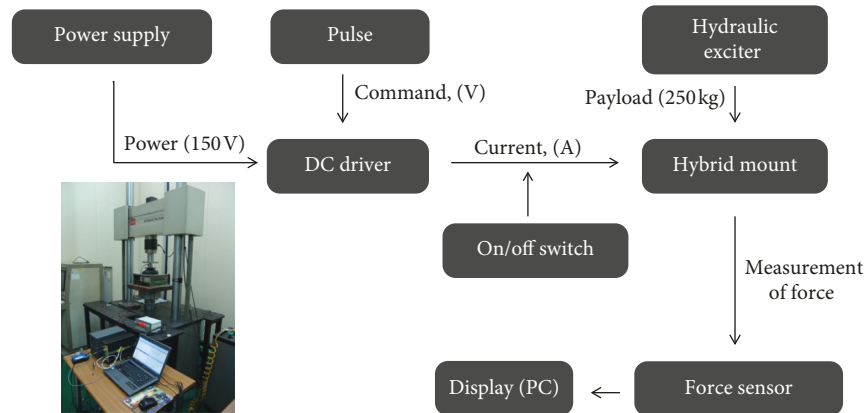
FIGURE 6: Configuration of blocking force measurements [2].
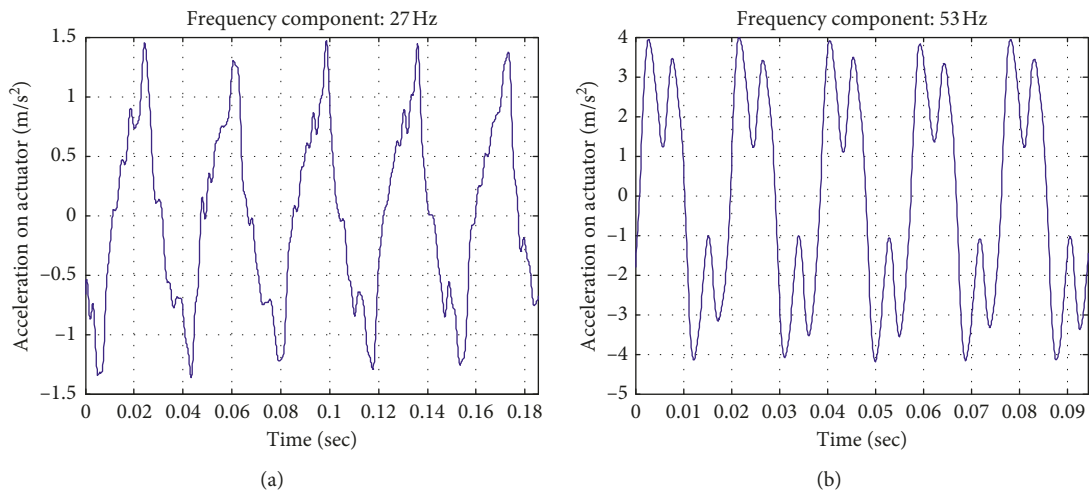
FIGURE 7: Acceleration of suggested actuator for command input voltage of pure sine. (a) 27 Hz. (b) 53 Hz.

TABLE 4: Experiment condition for measurement of blocking force.

Frequency range	Step size of frequency	Input current	Remarks
10–100 Hz	Δ10 Hz	1 A$_{Peak}$, 2 A$_{Peak}$	Additional measurement at 26.7 Hz, 53.4 Hz
100–300 Hz	Δ25 Hz	1 A$_{Peak}$, 2 A$_{Peak}$	

shipboard equipment, and it must be able to withstand the impact imposed by the weight of the hammer for given height in reference [9]. To consider the impact, 10 mm is determined as the vertical gap between coil and magnet, and the integrity was confirmed from the test for the final design.

The electromagnetic field analysis was performed using a commercial electromagnetic analysis program to calculate the force and the electromagnetic characteristic parameters for the improved design. The detailed design specifications are described in Table 6, and the modeling results and the analysis results are shown in Figure 10. The parameters of

TABLE 5: Measurement results of blocking force compared with required force.

Experimental setup	Required	Detailed design-I	Detailed design-II
@ 26.5 Hz	41.5 N_{peak}	930 N_{peak}	405 N_{peak}
@ 53.3 Hz	3.3 N_{peak}	548 N_{peak}	124 N_{peak}
Max. value	120 N_{peak}	1,200 N_{peak}	900 N_{peak}

(a)　　　　　(b)
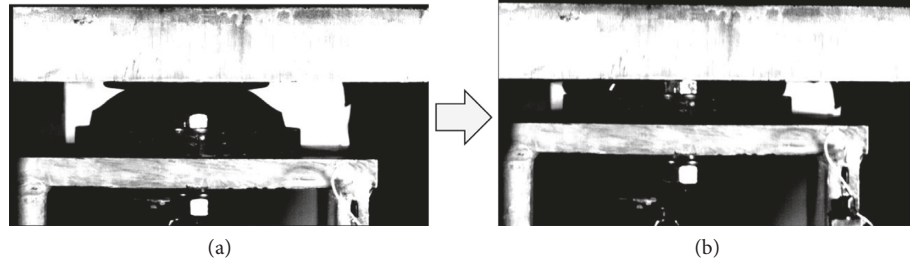
FIGURE 8: Maximum deflection of passive rubber mount applying required shock based on MIL-S-901D. (a) Equilibrium state. (b) Maximum deflection.

(a)　　　　　(b)

(c)
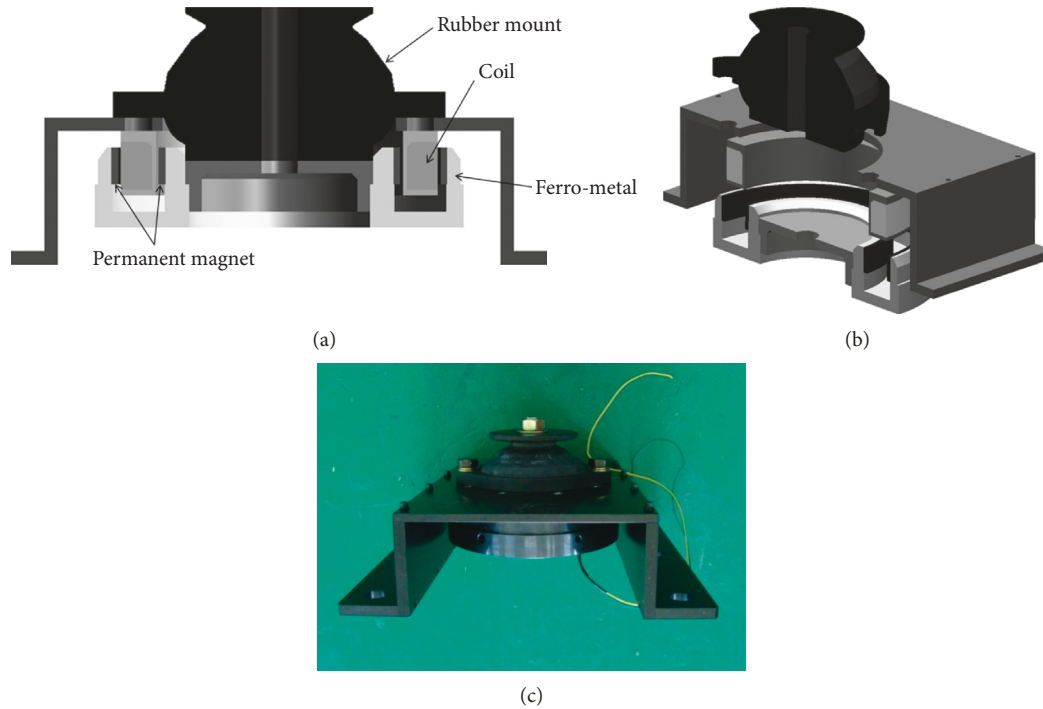
FIGURE 9: Assembly of modified electromagnetic actuator. (a) Sectional view. (b) Assembly schematic. (c) Prototype.

the actuator derived from the analysis are summarized in Table 7.

The sinusoidal input current is applied to the manufactured actuator, and the measured acceleration on the top of mount is shown in Figure 11. Compared with the previous results in Figure 7, it was confirmed that the high frequency or the peripheral frequency component due to the friction had been removed, and the harmonic component was not observed.

In order to examine the satisfaction of the required control force of the proposed electromagnetic actuator, a current which has a sinusoidal waveform of a single frequency is applied, and the force generated at that time is measured by MTS-810 (material property test machine) and ICP 208C02 (piezo-type force sensor) as shown in Figure 12 and Table 4. The experimental results are summarized in Figure 13, and the required control force magnitudes for the 26.7 Hz and 53.4 Hz target frequency components for the unit current are described in Table 8. It is confirmed that a force greater than the required actuation force for vibration reduction can be generated for the target frequency components. A section where the force rises above 200 Hz is observed from the experimental results, and it seems that the relatively increased measurement result is obtained due to the ductility effect of the material testing machine structure.

TABLE 6: Design specification for suggested electromagnetic actuator.

	Suggested design
Electrical gap	40 mm
Mechanical gap	2 mm
Coil specification	Ø1.3 mm × 310 turns
Weight	Abt. 7.2 kg

Coil

Ferro-metal

Permanent magnet

(a)

(b)
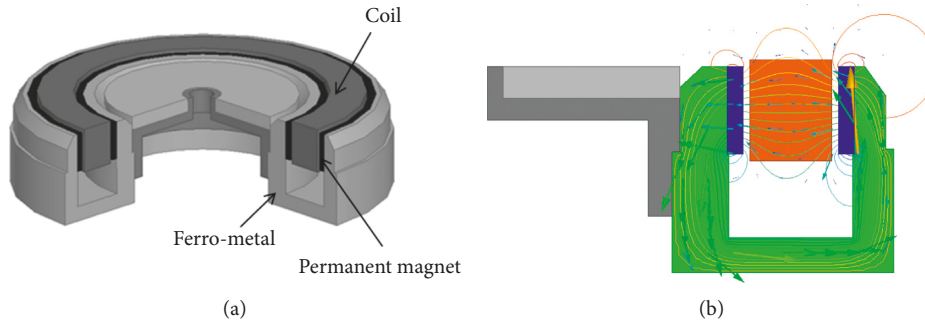
FIGURE 10: FE analysis of electromagnetic actuator for electromagnetic field by Maxwell. (a) Analysis model. (b) Analysis results of ANSYS Maxwell.

TABLE 7: Major parameters of suggested electromagnetic actuator.

	Suggested design
Resistance	2.00 Ω
Inductance	0.93 H
Input voltage	150 V
Time constant (L/R)	0.33 sec
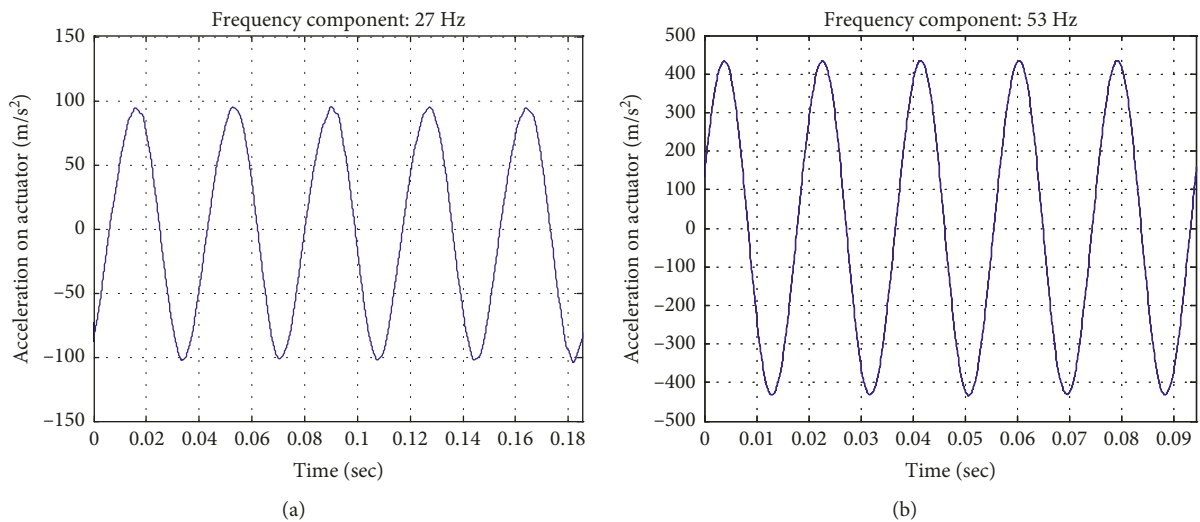
FIGURE 11: Acceleration of modified actuator for command input voltage of pure sine. (a) 27 Hz. (b) 53 Hz.

3. Experimental Verification of the Reduction of Transmitted Force by Active Hybrid Mount

3.1. Application of Control Algorithm to a Simplified 2-DOF System. The effect of applying the Filtered-X LMS algorithm is verified by the simulation of a 2-degree-of-freedom system including the electric field as described in reference [2]. The

Filtered-X LMS algorithm is a kind of adaptive filter that eliminates disturbances by using the reference inputs responsively within the system [10–12]. First, by passing the reference input through a filter whose coefficients are adapted, the convergence and stability of the original LMS algorithm characteristics are dramatically improved, the necessary control force is obtained, and the influence of the

(a)   (b)
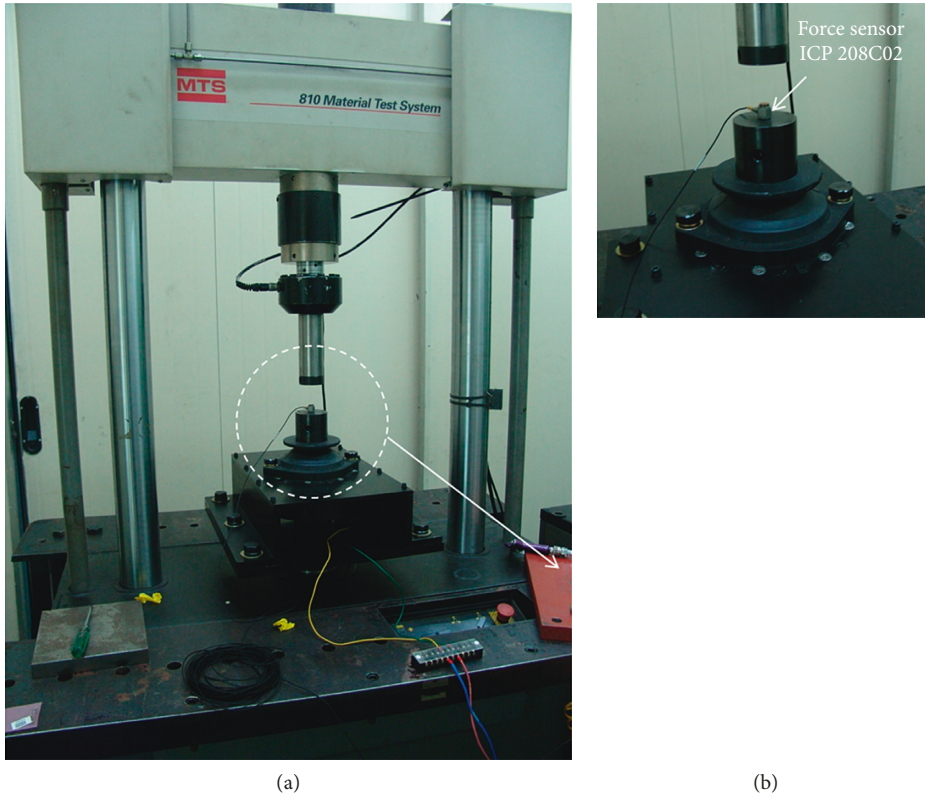
FIGURE 12: Experimental setup for blocking force measurement.
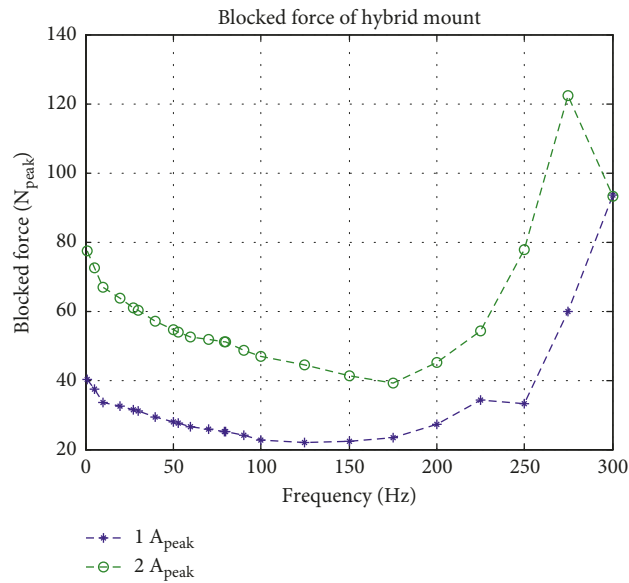
FIGURE 13: Measurement of blocking force for modified electromagnetic actuator.

TABLE 8: Measurement results of blocking force compared with required force.

	26.7 Hz	53.4 Hz
Required operating force	40.3 N_{peak}	3.3 N_{peak}
Measurement results	61.0 N_{Peak} @ 2.0 A_{Peak}	53.9 N_{Peak} @ 2.0 A_{Peak}
Satisfied/not satisfied	Satisfied	Satisfied

(a)   (b)
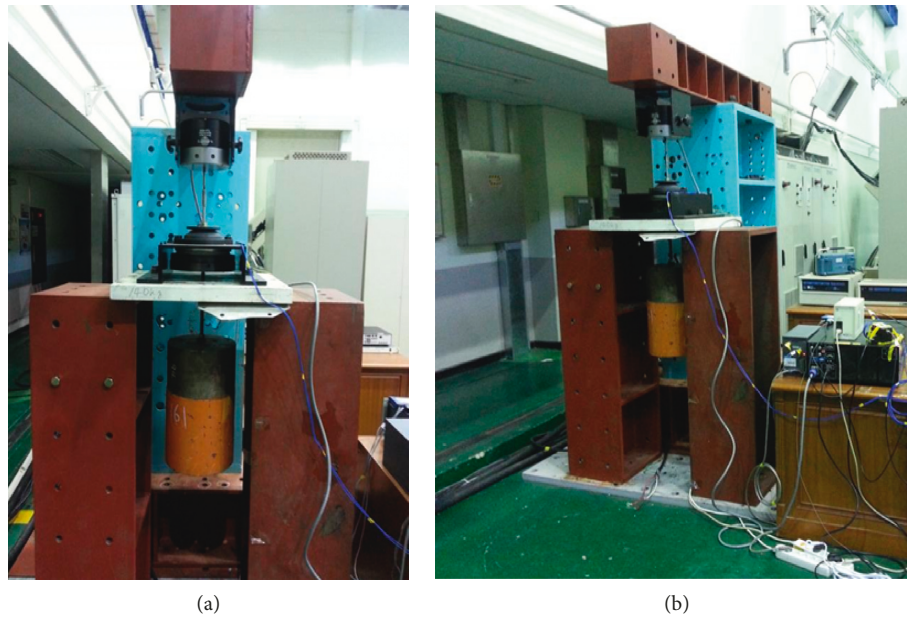
FIGURE 14: Experimental setup for 2-DOF system with electromagnetic hybrid mount.
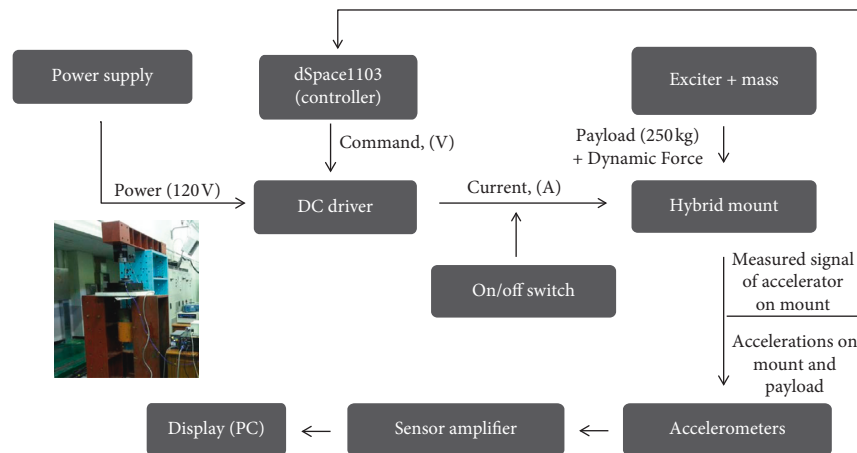
FIGURE 15: Schematic diagram for 2-DOF system with electromagnetic hybrid mount.

disturbance is removed from the system. Because the Filtered-X LMS algorithm uses feedforward control, it is very effective when the frequency characteristics of a target system are known. Finally, experimental apparatus were constructed for the performance test of 2-DOF hybrid mount (electromagnetic actuator) system. A 250 kg hanging payload is installed so that the center of gravity is low, as shown in Figure 14, and the exciter for generating disturbance is installed directly on the mount. Figure 15 outlines the experimental setup of the final 2-DOF hybrid mount system.

Two kinds of experiments with two different input frequency sets for the Filtered-X LMS algorithm were performed. Both results of 30, 60, and 90 Hz harmonics and 90, 180, and 270 Hz harmonics all show a reduction of more than 20 dB as shown in Figure 16, and the effectiveness of the proposed electromagnetic hybrid mount is confirmed. The results are summarized in Table 9.

3.2. Application of Control Algorithm to a 7-DOF System for a Motor System.

In addition to the 2-DOF performance test for the hybrid mount (electromagnetic actuator) system, a 7-DOF hybrid mount system for confirming the effectiveness of an actual motor system was constructed as shown in Figure 17, and a schematic diagram of the corresponding system in Figure 17(a) is described in Figure 18. An unbalanced mass (10 kg) was installed at the end of the motor system to implement the driving force of the machine. Four hybrid mounts with electromagnetic actuators were installed supporting four points, and an accelerometer for observing the vibration reduction was attached to the lower end of each mount. Figure 17(b) shows an amplifier, a DC driver, and an analog filter for a 7-DOF system. The control using the Filtered-X LMS algorithm for the target system was implemented by designing and applying an independent controller for each point as shown in Figure 19. The experimental results of a 1,600 rpm (26.7 Hz) primary
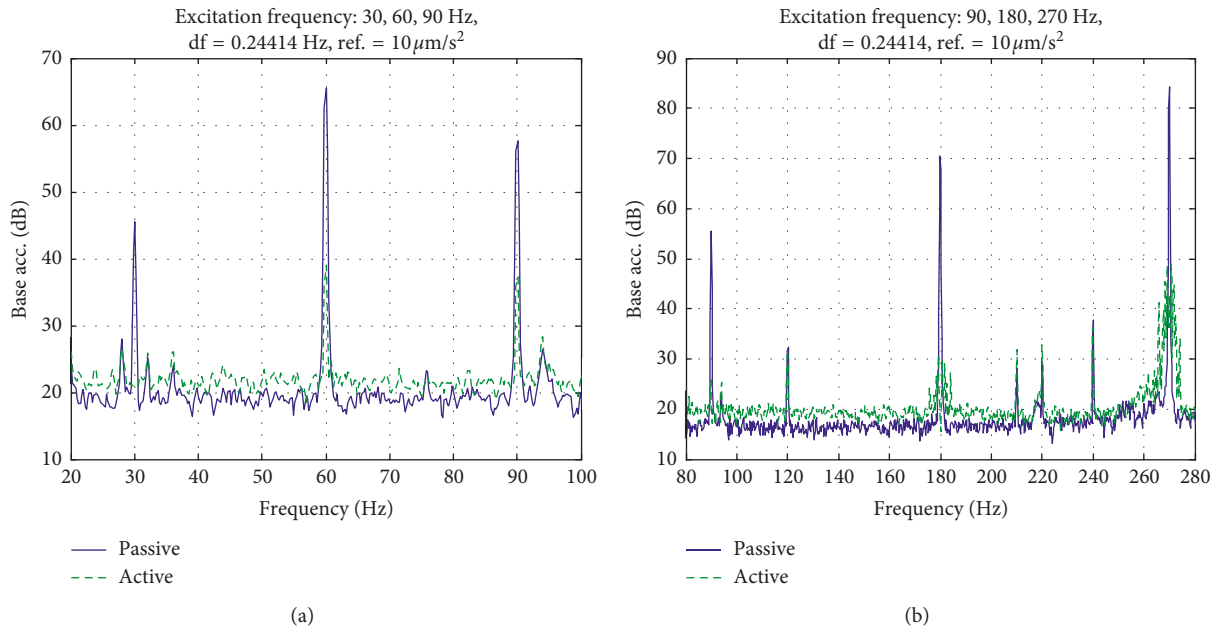
Figure 16: Experimental results of vibration reduction while applying hybrid mount. (a) Set #1: 30, 60, and 90 Hz. (b) Set #2: 90, 190, and 270 Hz.

Table 9: Measurement results of vibration reduction when applying the hybrid mount.

#	Frequency (Hz)	Passive (dB)	Active (dB)	Difference (dB)
	30 Hz	45.5	20.9	24.6
Set #1	60 Hz	65.5	39.0	26.5
	90 Hz	57.7	37.3	20.4
	90 Hz	57.5	28.0	29.5
Set #2	180 Hz	72.7	32.9	39.8
	270 Hz	86.5	44.8	41.7

(a)

Figure 17: Continued.

Analog filter

Total controller scheme

dSpace 1103

Power suplly

Sensor amp.

DC driver

(b)
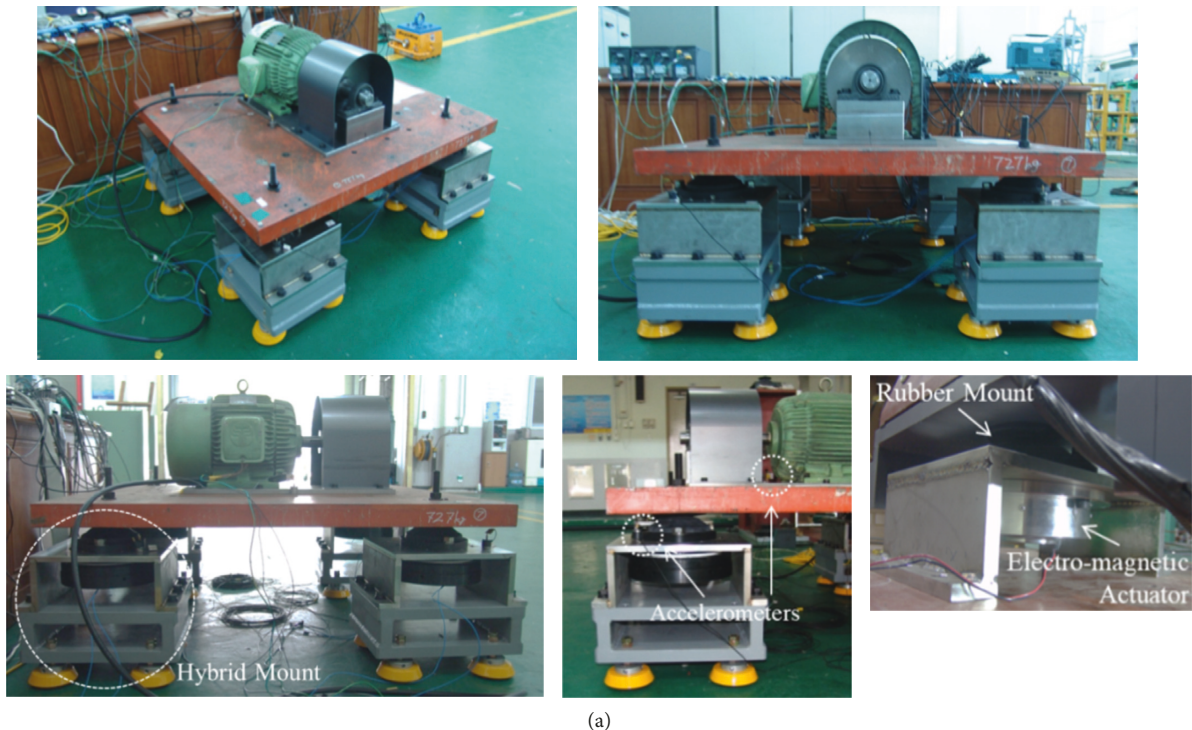
FIGURE 17: Experimental setup for 7-DOF system with electromagnetic hybrid mount. (a) Overall experimental setup for 7-DOF system. (b) Components for control.

Total payload: 836 kg
Four hybrid mounts

Motor: 109 kg, 220V/30A

Imbalance mass: 10 kg

M_p (727 Kg)

F_a K_r C_r

m_b

K_b C_b

F_a K_r C_r

m_b

K_b C_b

(a)
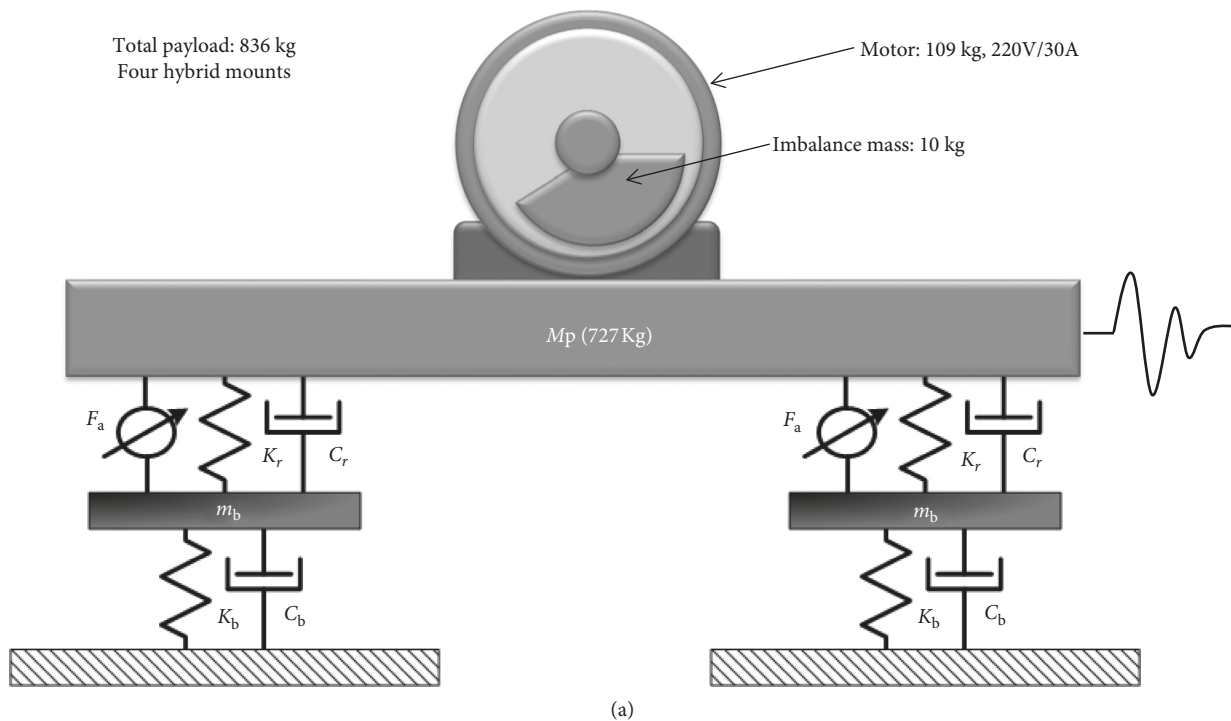
FIGURE 18: Continued.

(b)
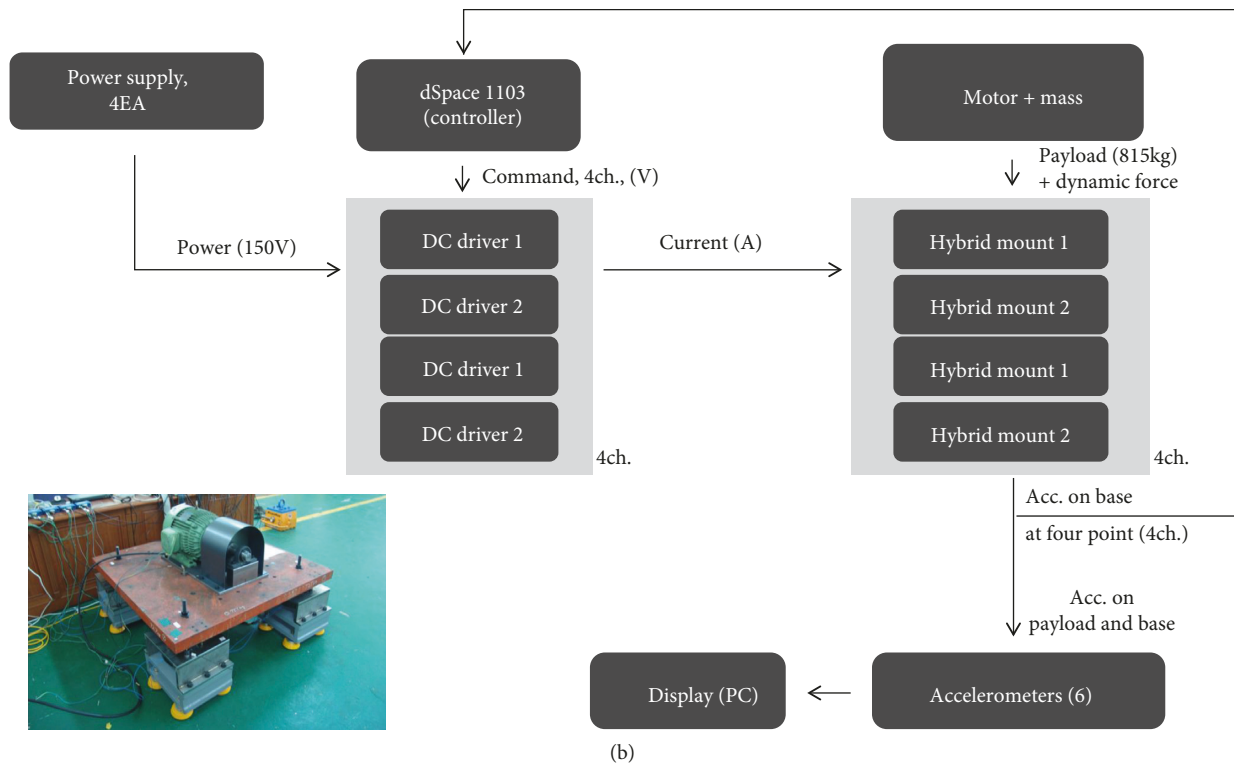
FIGURE 18: Schematic diagram of the experimental setup for the 7-DOF system. (a) Schematic diagram of the 7-DOF system. (b) Control scheme.

(a)   (b)
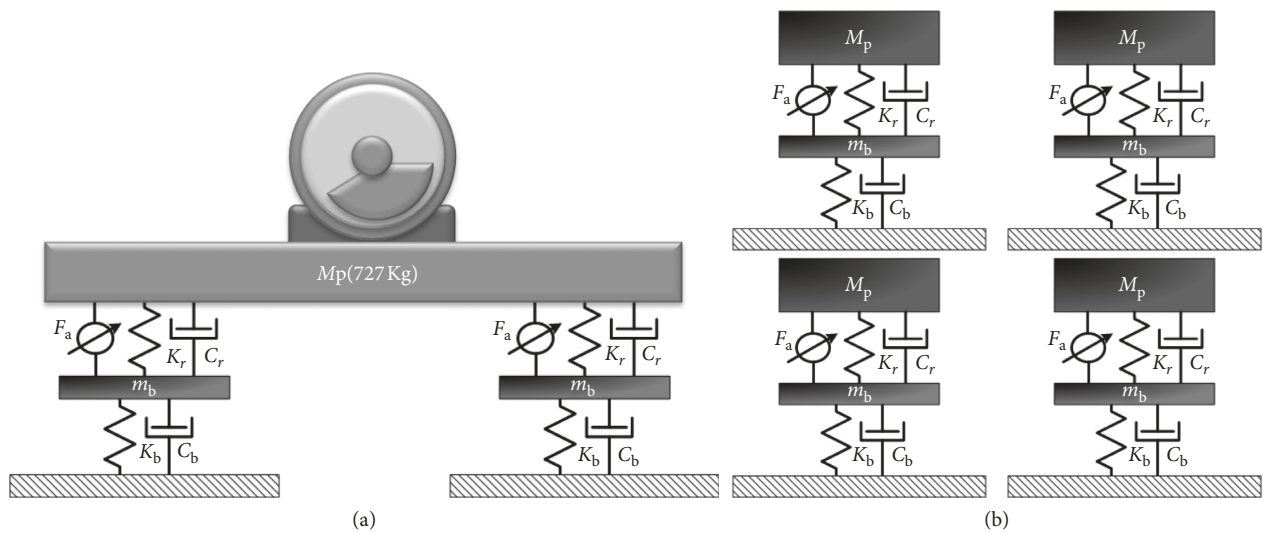
FIGURE 19: Design schematics of a controller for the 7-DOF system with a hybrid mount. (a) Original system. (b) Control scheme.

component, with consideration of the initial operating frequency and two harmonic components (53.4 Hz, 80.1 Hz), are shown in Figure 20 and Table 10. From the results of applying the proposed electromagnetic hybrid mount, the average vibration reduction of about 19.7 dB was observed for the excited frequency components.

4. Conclusion

An active mount combined with a passive rubber mount and an electromagnetic actuator has been proposed and examined through the rigorous experiment laid out in this paper. It can be applied to naval shipboard equipment. Based on the designs of previous research [2], the electromagnetic actuator was modified and re-suggested in order to improve the performance and overcome its inherent limitations which were caused by the friction between the mover and stator. The design specification of an active mount, such as required force, displacement, and frequency characteristics, was identified for the self-excited pump system, and then an electromagnetic actuator active mount is redesigned with consideration for the shape of the passive rubber mount and
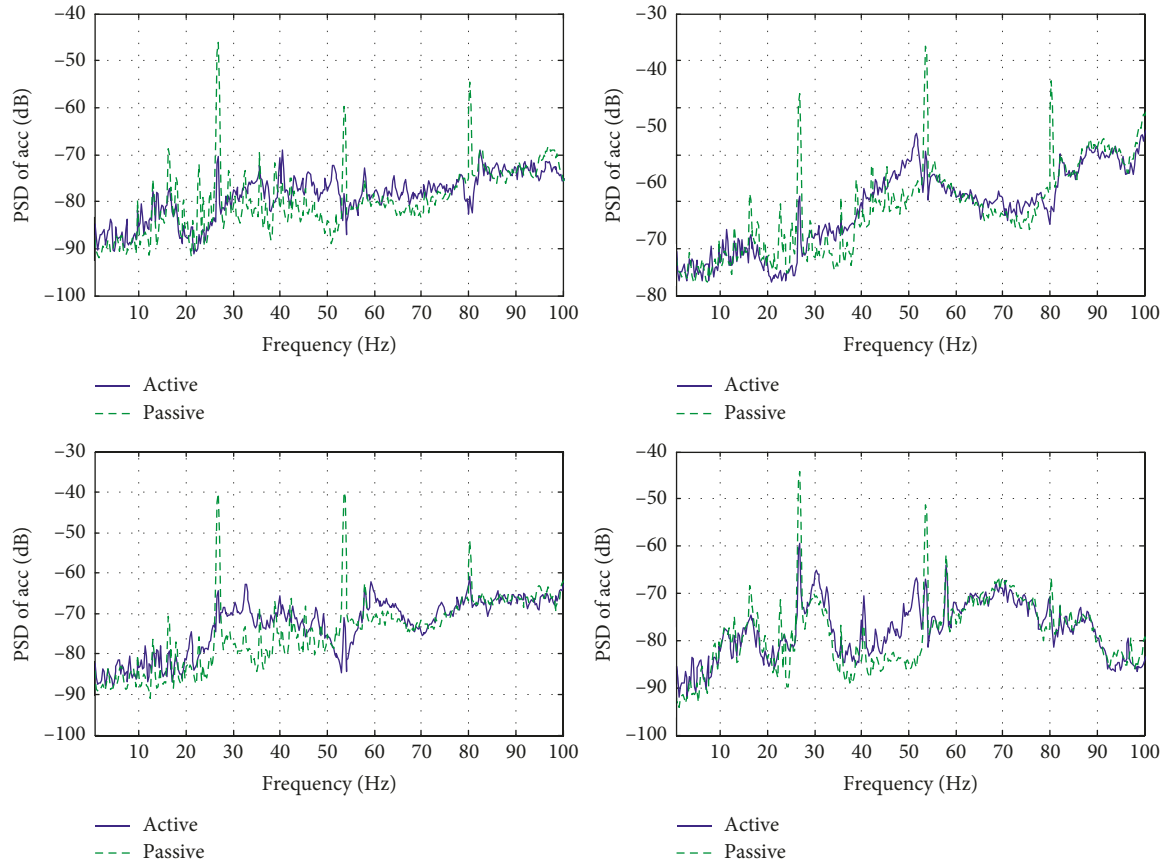
Figure 20: Control results for a 7-DOF system with hybrid mount. (a) Pt. #1, $dB_{ref} = 1$ g. (b) Pt. #2, $dB_{ref} = 1$ g. (c) Pt. #3, $dB_{ref} = 1$ g. (d) Pt. #4, $dB_{ref} = 1$ g.

Table 10: Control results for a 7-DOF system with the hybrid mount.

#		26.7 Hz	53.4 Hz	80.1 Hz	Average (dB)
Point 1	Passive	−46.2	−59.9	−54.7	
	Active	−70.3	−78.3	−79.0	
	Difference	−24.1	−18.4	−24.3	−22.3
Point 2	Passive	−47.0	−36.9	−44.4	
	Active	−68.9	−59.4	−71.2	
	Difference	−21.9	−22.5	−26.8	−23.7
Point 3	Passive	−40.4	−39.9	−51.9	
	Active	−64.4	−70.9	−61.0	
	Difference	−20.0	−31.0	−9.1	−20.0
Point 4	Passive	−44.1	−51.2	−66.8	
	Active	−59.4	−66.9	−73.9	
	Difference	−15.3	−15.7	−7.1	−12.7
Average (dB)					−19.7

shock resistance. The performance was examined experimentally on the single active mount using an external exciter and also confirmed experimentally on an active mount system with four mounts using a motor system. From the results of applying the proposed electromagnetic hybrid mount, there was an observed reduction in recorded vibrations to the floor of 23.8 dB on the single mount system, which is modelled as a 2-DOF system, and 19.7 dB on the four-mount system, modelled as a 7-DOF system, observed, respectively, for the three harmonic components of vibration.

Data Availability

The data used to support the findings of this study are available from the corresponding author upon request.

Conflicts of Interest

The authors declare that they have no conflicts of interest.

Acknowledgments

References

[1] A. D. Shaw, S. A. Neild, and D. J. Wagg, "Dynamic analysis of high static low dynamic stiffness vibration isolation mounts," *Journal of Sound and Vibration*, vol. 332, no. 6, pp. 1437–1455, 2013.

[2] Y.-H. Shin, S.-J. Moon, J.-I. Kwon, W.-J. Jung, and J.-J. Jeon, "A new mount with moving-magnet type electromagnetic actuator for naval shipboard equipment," *International*

Journal of Naval Architecture and Ocean Engineering, vol. 7, no. 1, pp. 41–55, 2015.

[3] C.-C. Lan, S.-A. Yang, and Y.-S. Wu, "Design and experiment of a compact quasi-zero-stiffness isolator capable of a wide range of loads," *Journal of Sound and Vibration*, vol. 333, no. 20, pp. 4843–4858, 2014.

[4] C. Collette, S. Janssens, and K. Artoos, "Review of active vibration isolation strategies," *Recent Patents on Mechanical Engineering*, vol. 4, no. 3, pp. 212–219, 2011.

[5] H. Y. Cho, S. J. Moon, Y. H. Shin, W. J. Jung, and M. C. Won, "A comparative study on the dynamic characteristics and control performances of hybrid mounts according to element configuration," *Transaction on Korean Society for Noise and Vibration Engineering*, vol. 22, no. 6, pp. 556–563, 2012.

[6] W. Kaal, T. Bartel, and S. Herold, "Active vibration isolation with a dielectric elastomer stack actuator," *Smart Materials and Structures*, vol. 26, no. 6, article 055016, 2017.

[7] J. H. Lee, H. Y. Kim, K. H. Kim, M. H. Kim, and S. W. Lee, "Control of a hybrid active-passive vibration isolation system," *Journal of Mechanical Science and Technology*, vol. 31, no. 12, pp. 5711–5719, 2017.

[8] Military Specification MIL-STD-740-2, *Structureborne Vibratory Acceleration Measurements and Acceptance Criteria of Shipboard Equipment*, Department of the Navy, Washington, DC, USA, 1986.

[9] Military Specification MIL-S-901D, *Shock Tests High Impact Shipboard Machinery Equipment and Systems*, Department of the Navy, Washington, DC, USA, 1989.

[10] F. Kerber, S. Hurlebaus, B. M. Beadle, and U. Stobener, "Control concepts for an active vibration isolation system," *Mechanical System and Signal Processing*, vol. 21, no. 8, pp. 3042–3059, 2007.

[11] B.-H. Lee and C.-W. Lee, "Model based feed-forward control of electromagnetic type active control engine-mount system," *Journal of Sound and Vibration*, vol. 323, no. 3–5, pp. 574–593, 2009.

[12] B. Widrow and S. D. Stearns, *Adaptive Signal Processing*, Prentice-Hall, Upper Saddle River, NJ, USA, 1985.